Monopile Response to Scour and Scour Protection

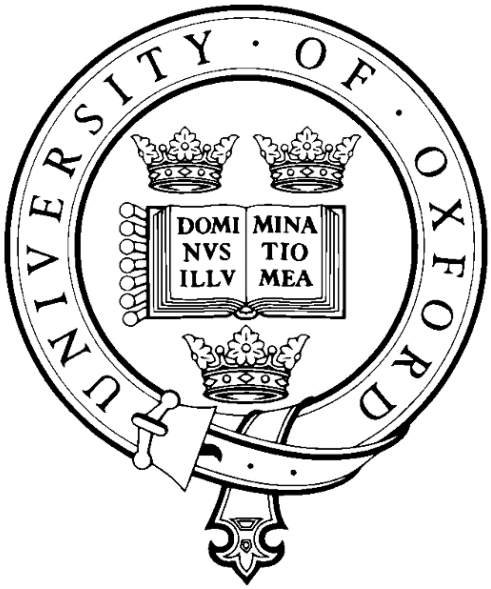

Russell Mayall

St Catherine's College

University of Oxford

A portfolio submitted for the degree of

Doctor of Engineering

Trinity Term

October 2019

Supervised by

Harvey Burd, Byron Byrne, Ross McAdam,

Phillipa Slater, and Richard Whitehouse

For my family

Epigraph

Human activities are estimated to have caused approximately 1.0°C of global warming above pre-industrial levels, with a likely range of 0.8°C to 1.2°C. Global warming is likely to reach 1.5°C between 2030 and 2052 if it continues to increase at the current rate.

An average warming of 1.5°C across the whole globe raises the risk of heatwaves and heavy rainfall events, amongst many other potential impacts. Limiting warming to 1.5°C rather than 2°C can help reduce these risks, but the impacts the world experiences will depend on the specific greenhouse gas emissions 'pathway' taken.

Pathways limiting global warming to 1.5°C with no or limited overshoot would require rapid and far-reaching transitions in energy, land, urban and infrastructure (including transport and buildings), and industrial systems. These systems transitions are unprecedented in terms of scale, but not necessarily in terms of speed, and imply deep emissions reductions in all sectors, a wide portfolio of mitigation options and a significant upscaling of investments in those options.

In 1.5°C pathways with no or limited overshoot, renewables are projected to supply 70–85% (interquartile range) of electricity in 2050.

Intergovernmental Panel on Climate Change (IPCC) Special Report: Global Warming of 1.5 ºC, 2018

Abstract

Scour of seabed sediments can occur around offshore structures, the resultant reduction in strength and stiffness of the structure's foundations presents operational challenges for monopile-supported offshore wind turbine structures. Turbines are at risk of reduced operation or even premature decommissioning if scour causes the natural frequency of a wind turbine to drop too close to the loading frequency, or if the foundation capacity is compromised. In practice scour protection systems are used to mitigate the development of scour itself. Scour protection may also have a restorative influence on the natural frequencies of the structure and capacity of the foundation. This portfolio presents the results of a DEng research project exploring the interactions between scour development, scour protection, foundation stiffness and strength, and structural dynamics of offshore wind turbine structures.

Flume experiments were performed, where a scale monopile – tower system exposed to realistic scour development in the Fast Flow Facility flume at HR Wallingford was subjected to structural dynamics testing and lateral loading. Three scour protection systems were modelled in the experiments: pre-installed rock-armour, remedial rock fill, and remedial tyre-filled net options.

Numerical modelling is presented, using a one-dimensional (1D) finite element model developed for the analysis of natural frequencies for monopile-supported turbines with scour and scour protection. A 1D finite element approach was also used to explore the results of the lateral loading experiments. The numerical modelling produces results that are consistent with data from the flume experiments and from a case study of field data from a high scour offshore wind farm.

The research confirms that there is potential for scour protection systems to enhance the stiffness and capacity of monopile foundations. These gains are negligible for tyre-filled net scour protection systems due to the low stiffness and density of the tyres. The stiffness contribution of rock-type scour protection systems is further enhanced if sand accumulates in the scour protection matrix, but these positive contributions become diminished if extreme global scour causes the scour protection to become unstable. Pre-installed rock armour scour protection systems provide the most reliable solution in terms of seabed stability and foundation response.

Note on the Format of this Portfolio

This portfolio contains three scientific papers (total of 54 pages) of joint authorship, two of which are published in conference proceedings, and one which is forthcoming for journal publication:

Paper 1 (9 pages): **Mayall, R.O.**, Byrne, B.W., Burd, H.J., McAdam, R.A., Cassie, P. and Whitehouse, R.J.S. (2019). Modelling of foundation response to scour and scour protection for offshore wind turbine structures. Scour and Erosion IX - Proceedings of the 9th International Conference on Scour and Erosion, ICSE 2018, pp. 405.

Paper 2 (6 pages): **Mayall, R.O.**, McAdam, R.A., Byrne, B.W., Burd, H.J., Sheil, B.B., Cassie, P. and Whitehouse, R.J.S. (2018). Experimental modelling of the effects of scour on offshore wind turbine monopile foundations. In: 9th International Conference Physical Modelling in Geotechnics (ICPMG 2018). London, UK, July. (c109 pp. 725-730).

Paper 3 (39 pages): **Mayall, R.O.**, McAdam, R.A., Whitehouse, R.J.S., Burd, H.J., Byrne, B.W., Heald, S.G., Sheil, B.B., and Slater, P.L. [Forthcoming]. Flume tank testing of offshore wind turbine dynamics with foundation scour and scour protection. Journal of Waterway, Port, Coastal, and Ocean Engineering. DOI: 10.1061/(ASCE)WW.1943-5460.0000587.

The work described in these papers was conducted by me in the course of my DEng research project, with academic contributions from my academic and industry supervisors. The papers themselves were drafted by me, with editorial contributions from my co-authors. I confirm that the remainder of the portfolio is wholly my own work except where stated otherwise.

Funding

This research was supported through funding from E.ON and HR Wallingford, and by grant EP/L016303/1 for Cranfield University, the University of Oxford and Strathclyde University, Centre for Doctoral Training in Renewable Energy Marine Structures - REMS (http://www.rems-cdt.ac.uk/) from the UK Engineering and Physical Sciences Research Council (EPSRC).

Table of Contents

List of Appendices

Notation

The following is a list of the notation that appears in multiple locations in the main body of this portfolio. The papers contain internal notation sections. Notation that appears only in the Appendices is defined in the Appendix text.

Latin Symbols

a	Shape function coordinate
A	Cross-sectional area
B	Small strain shear modulus fitting parameter
B_v	Hermitian shape function
C	Damping
C_a	Added mass coefficient
d_{XX}	Soil particle diameter (XXth percentile)
D	Pile outer diameter
D_R	Relative density
e	Voids ratio
E	Young's modulus
f_m	Natural frequency of the m^{th} mode
g	Acceleration due to gravity (9.81 m/s^2)
G	Shear modulus
G_0	Small strain shear modulus
G_s	Specific gravity
h	Lever arm
h_L	Height of local bed level above global bed level
h_w	Water depth
H	Horizontal load
I	Second moment of area
j	Distributed moment of inertia
J	Moment of inertia
k	Non-dimensional stiffness coefficient
K	Stiffness
L	Pile embedment length
L_e	Element length
m	Vibration mode number (structural dynamics)
m	Distributed moment reaction (soil-structure interaction)
M	Moment load (structure loading)
M	Mass (structural dynamics)
M_{top}	Top mass
n	Porosity (soil characterisation)
n	Power fitting parameter (small strain shear modulus)
n	Curvature parameter (soil-structure interaction)
$n_{els,req}$	Target number of elements
N_M	Number of top masses
p	Pressure
p	Distributed lateral reaction (soil-structure interaction)
p'	Effective stress
p_{atm}	Atmospheric pressure

q_c	CPT cone tip resistance
r	Radial distance from pile centreline
R_{gyr}	Radius of gyration
s_u	Undrained shear strength
S_{eq}	Equilibrium scour depth
S_L	Local scour depth
S_G	Global scour depth
S_T	Total scour depth
t	Time
t_{sp}	Scour protection thickness adjacent to the pile wall
t_w	Pile wall thickness
T_f	Elapsed flow time
v	Lateral displacement
v_0	Displacement amplitude
$\dot{v}$	Velocity
$\ddot{v}$	Acceleration
V	Mode shape
w	Vertical displacement
w_g	Gauss point weighting
x	Horizontal coordinate
y	Horizontal coordinate
z	Vertical coordinate
z'	Height above ground level
z_{BSF}	Depth below seafloor before scour
z_{CD}	Height above chart datum
z_G	Depth below global seabed level
z_L	Elevation

Greek Symbols

$\alpha_{a,b}$	Fitting parameter, gradient of a with respect to b (scour effects on structural dynamics)
α_L	Local scour influence factor
β	Modal coefficient
γ	Unit weight
γ'	Effective submerged unit weight
δ_L	Non-dimensional overburden reduction depth
Δf_m	Proportional change in natural frequency
Δz_O	Overburden reduction depth
ε_f	Natural frequency error
$\varepsilon_{\Delta f}$	Error in change of natural frequency
ζ	Damping ratio
θ	Shields parameter (sediment mobility)
θ	Beam neutral axis rotation (beam analysis)
κ	Timoshenko shear coefficient
λ	Eigenvalue
ν	Poisson's ratio
ρ	Material density
ρ_w	Density of water
σ_v'	Effective vertical stress
$\sigma_{v,A}'$	Apparent effective vertical stress adjacent to pile wall

$\sigma'_{v,G}$	Effective vertical stress relative to the global bed level
$\sigma'_{v,L}$	Effective vertical stress relative to the local bed level
ϕ'	Internal angle of friction
ψ	Beam cross-section rotation
ω	Circular frequency
Ω	Factor on natural frequency

Abbreviations, Subscripts and Superscripts

0	Initial value
1D	One-dimensional
3D	Three-dimensional
B	Value at the pile base
BSF	Below seafloor
CD	Chart datum
CDF	Cumulative density function
CPT	Cone penetrometer
Eig	Output of numerical analysis programme *EigPile*
FFF	Fast Flow Facility
G	Value at ground level
i	Initial value
i	Intercept
LVDT	Linear variable differential transformer
max	Maximum value
Meas	Measured value
min	Minimum value
OCR	Overconsolidation ratio
OWF	Offshore wind farm
ref	Reference value
R	Reference value
P-RA	Pre-installed rock armour scour protection
R-RF	Remedial tock fill scour protection
R-TFN	Remedial tyre-filled net scour protection
SHM	Structural health monitoring
SP	Scour protection

Acknowledgements

I would like to thank Scott Whyte and Jude Mayall for encouraging me to apply.

For their guidance in my research I would like to thank Harvey Burd, Byron Byrne, and Ross McAdam at Oxford, Steve Heald and Phillipa Slater at E.ON, and Richard Whitehouse at HR Wallingford.

The flume experiments described in this portfolio would not have been possible without the immense support received from colleagues at Oxford, E.ON and HR Wallingford. I am grateful for the hard work of Amelia Couldrey, Andrew Huckstep, Barrie Aldridge, Ben Holland, Brian Sheil, Chris Brett, Clive Baker, Dave Webb, David Todd, Esther Gomes, Ian Payne, Iona Richards, James Sutherland, Joe Mitchell, John Harris, Neil Crossouard, Ollie Douglas, Ollie Harris, Patrick Rainey, Teodor Totev, Toby Balaam, and Tom Rigden (also Phillipa, Richard, Ross, and Steve) in their support of my work in the flume. I am especially grateful for the occasions when the work entailed shovelling several tonnes of sand, pile driving, or working at antisocial hours.

I am grateful to Ross McAdam and Brian Sheil for developing the CPT and monotonic loading equipment used in the experiments.

I am grateful to both Clive Baker at Oxford and Brian Thomas at Thomas Fabrications Ltd for fabricating the majority of the equipment used in the experiments. I would like to thank Italeri for fulfilling an order of 700 model scale truck tyres. I would like to thank Mike Rattley, Darren Burbury and Amin Rismanchian at Fugro for performing triaxial tests.

For provision of field data, I would like to thank Phillipa, Steve, and Richard, and numerous others behind the scenes.

For contributions to morale I would like to thank my wife Jude, my daughter Felicity, my friends, my cats, my colleagues at Oxford, my colleagues in the REMS programme, and colleagues at conferences in Cranfield, Oxford, London, Taipei, and Glasgow.

I would like to thank my parents Eirwen and Peter for raising me.

I would like to thank friends and family who facilitated our wedding. I am grateful to the John Radcliffe Hospital, Oxford University Hospitals, and the NHS for helping to deliver Felicity into the world. I would like to thank Philip Hamp at InHouse estate agents, Melanie Griffiths at Peter Clarke & co estate agents, and Karen Peacock at Truemans solicitors for helping us move to our new home.

Finally, thank you Fizzy for being so nice. I love you.

Section 1 – Introduction and Background

1.1 Introduction

Offshore wind energy is a large part of the renewable energy market, one that has undergone rapid growth over the past 10 years (Figure 1.1). Installed offshore wind turbine structures are supported by a variety of substructures identified in Figure 1.2 – the research presented in this portfolio is concerned with monopile foundations, which represent the vast majority of installed structures.

The presence of structures in the offshore environment can result in scour (erosion of the sediments) due to the interaction between the structure and the water flow around it (e.g. Figure 1.3; Figure 1.4). Scour presents potential problems for monopile wind turbine structures including decreases in foundation capacity and stability, decreases of the structural natural frequency, increases in bending moments due to the larger loading lever arm, increases in structural fatigue, and loss of support for connecting cables. In practice, scour protection systems are frequently installed to mitigate the effects of scour. The research presented in this portfolio aims to address some of the uncertainty in the geotechnical design of monopile foundations under the influence of scour, and with the associated scour protection systems.

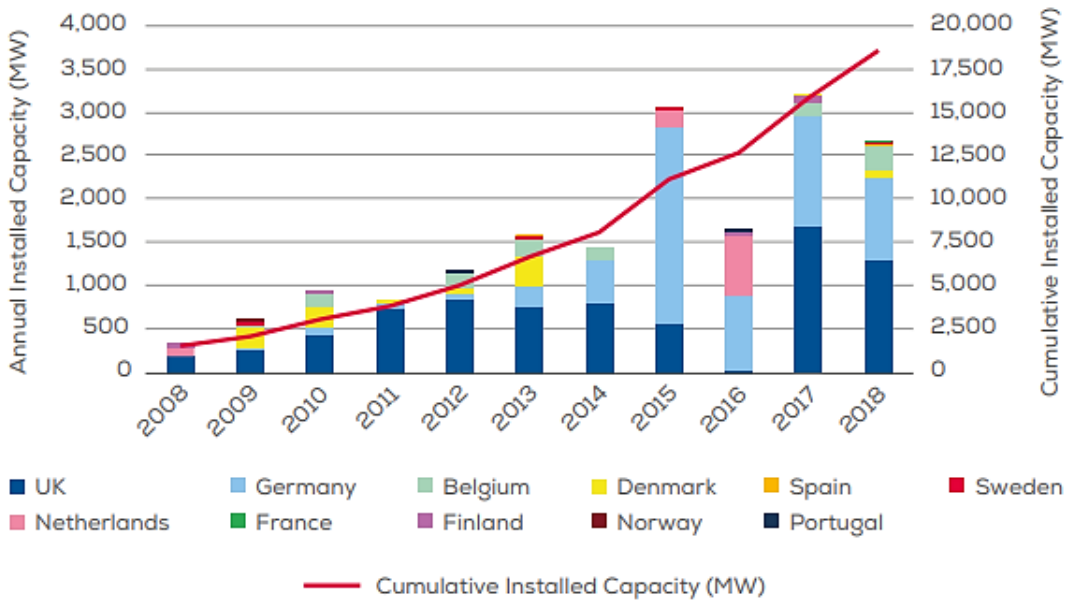

Figure 1.1. Annual wind installations in Europe (from WindEurope, 2019).

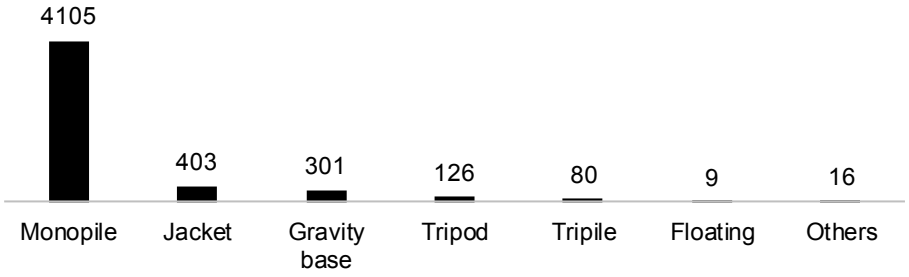

Figure 1.2. Type and number of substructures for grid connected wind turbines in Europe at the end of 2018 (data from WindEurope, 2019).

(a) (b)

Figure 1.3. (a) Global scour beneath an elevated coastal building (photo credit: FEMA); (b) Local scour at a bridge pier (photo credit: USGS).

Figure 1.4. Sediment plumes at Thanet offshore wind farm viewed from space, white dots are wind turbines (photo credit: NASA Earth Observatory)

1.2 Motivation

1.2.1 Design Drivers

Monopile foundations for offshore wind turbines have large diameters (D > 4 m) with embedment ratios in the range 2 < L/D < 6 (where L is the pile embedment). The critical loading frequencies are rotor frequency (frequently terms 1P), the frequency at which the blades pass in from of the tower (termed 3P for a three-bladed turbine), as well as the wave and wind loading of the structure. To minimise fatigue damage from the dynamic amplification of loads, monopile wind turbine structures are designed to have a natural frequency at between the 1P and blade passing 3P loading bands (e.g. Figure 1.5).

Scour around offshore foundations can take the form of global scour or local scour, or a combination of both; Figure 1.6 presents a schematic of typical scour definitions. A typical design scour depth is 1.5 D (API, 2011), and higher values have been observed in the field. Scour presents the potential for loss of a significant portion of the design pile embedment and hence capacity, which must either be accounted for in design or mitigated using scour protection. Scour has the effect of reducing the natural frequency of the structure, which compromises the margin above the 1P loading frequency.

The development of scour in excess of the design values can lead to reduced turbine operation due to concerns over the foundation capacity and fatigue damage. This has significant commercial impacts, for example the monthly revenue of a 3 MW turbine can be estimated as follows (assuming a capacity factor of 38% (Energy Numbers, 2016) and an example energy price of £100/MWh):

$$R_{turb} = 0.38 * 24\text{h/day} * 365\text{day/year} * 3\text{MW} * £100/\text{MWh} \cong £0.98 \text{ million/year} \cong £82{,}000/\text{month}$$

The aim of the research is to enable the design life of wind farms in high scour environments to be maximised by improving analysis methods for monopiles with scour and scour protection.

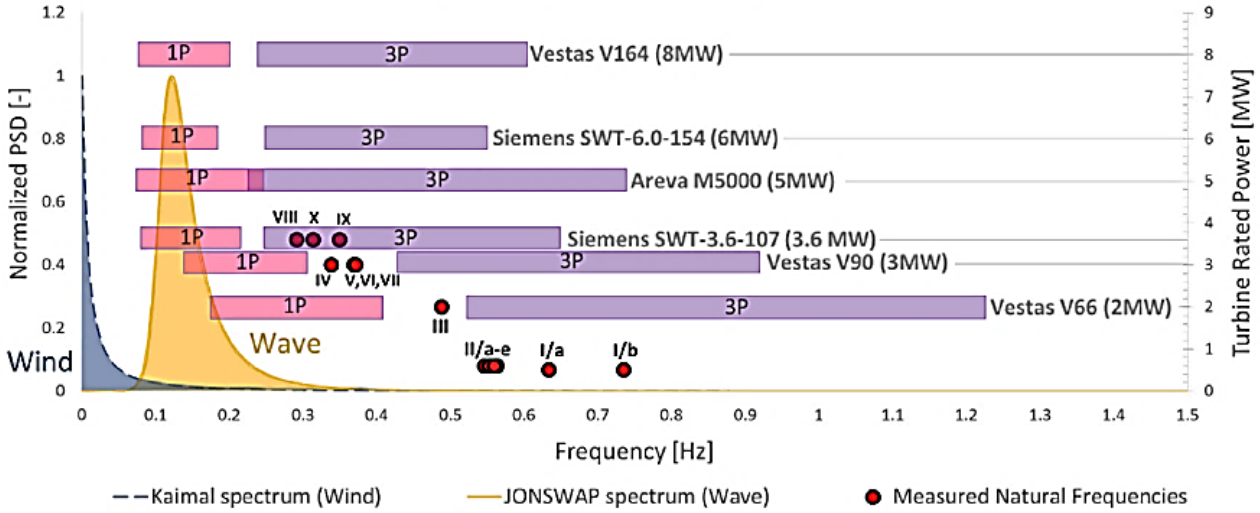

Figure 1.5. Excitation frequencies of commercial offshore wind turbines (from Arany et al., 2016). 1P is the turbine rotor frequency at rated wind speeds, and 3P is the frequency of turbine blades passing in front of the tower. Red dots are measured structural natural frequencies at operating offshore wind farms.

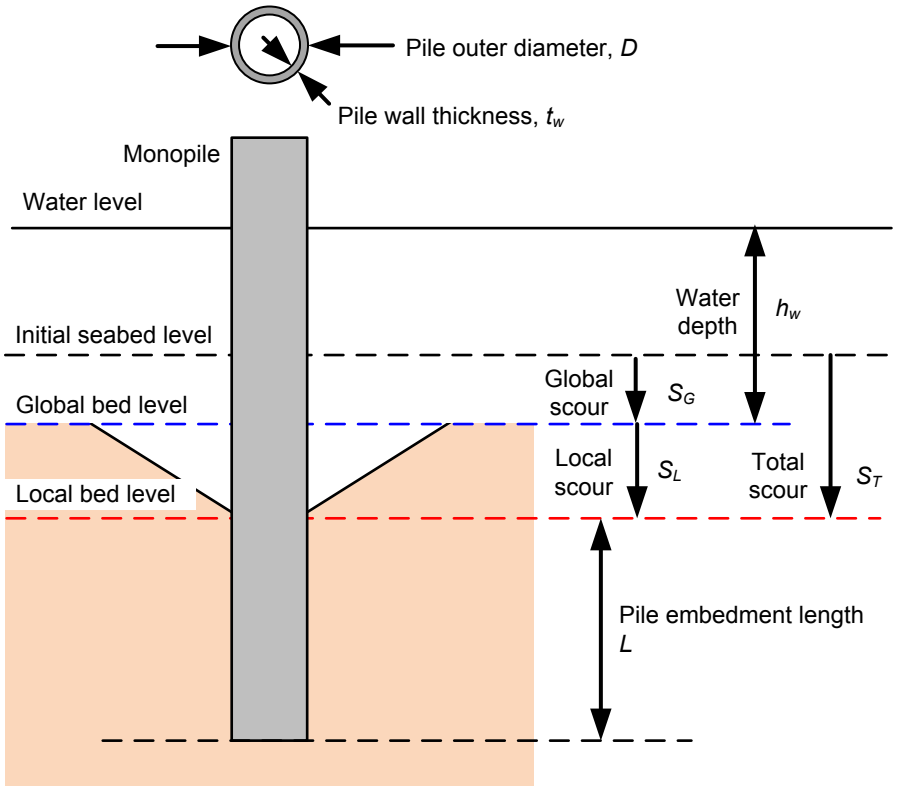

Figure 1.6. Idealised schematic of scour around a monopile

1.2.2 Robin Rigg Offshore Wind Farm

Robin Rigg Offshore Wind Farm comprises 60 x Vestas V90-3.0 MW wind turbines, located in the Solway Firth offshore UK (Figure 1.7 & Figure 1.8). The wind turbines are supported by monopiles with D = 4.3 m, in medium dense to dense sand overlying normally consolidated clay.

The foundation design for Robin Rigg did not include scour protection, but the pile length was designed to accommodate local scour on the basis of design codes. During operation, reductions in the natural frequency of wind turbine structures were linked to unexpected global scour, due to a migrating channel to the north of the site; Figure 1.9 presents the site bathymetry developments. The operational concerns relating to this global scour led to the premature decommissioning of two wind turbines, with remedial scour protection installed at other locations as mitigation against further global scour.

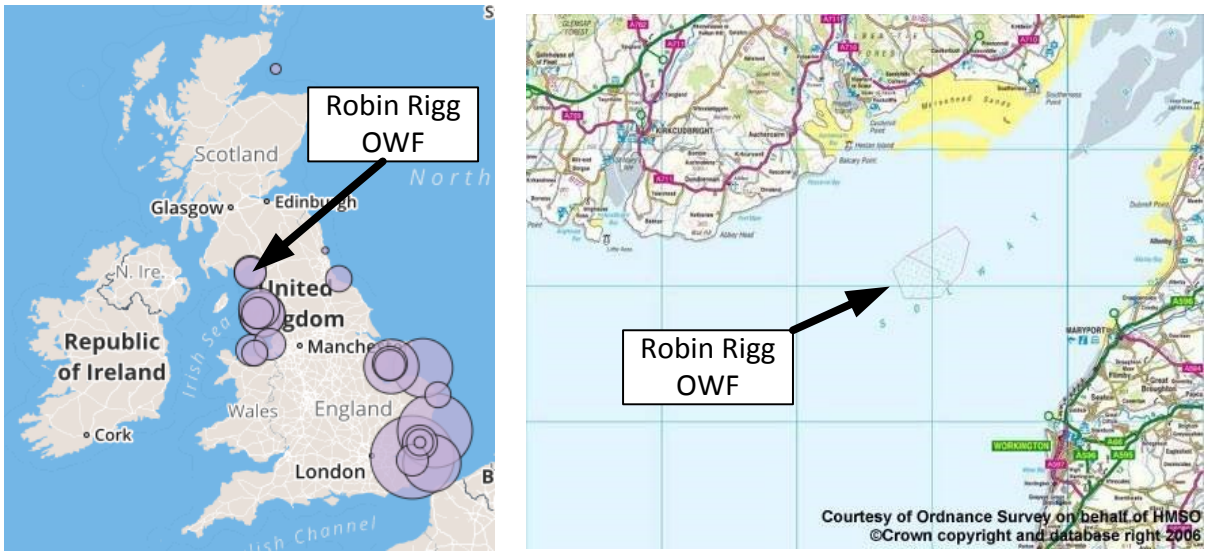

Figure 1.7. Robin Rigg offshore wind farm location map

Figure 1.8. Wind turbines at Robin Rigg offshore wind farm (courtesy of E.ON)

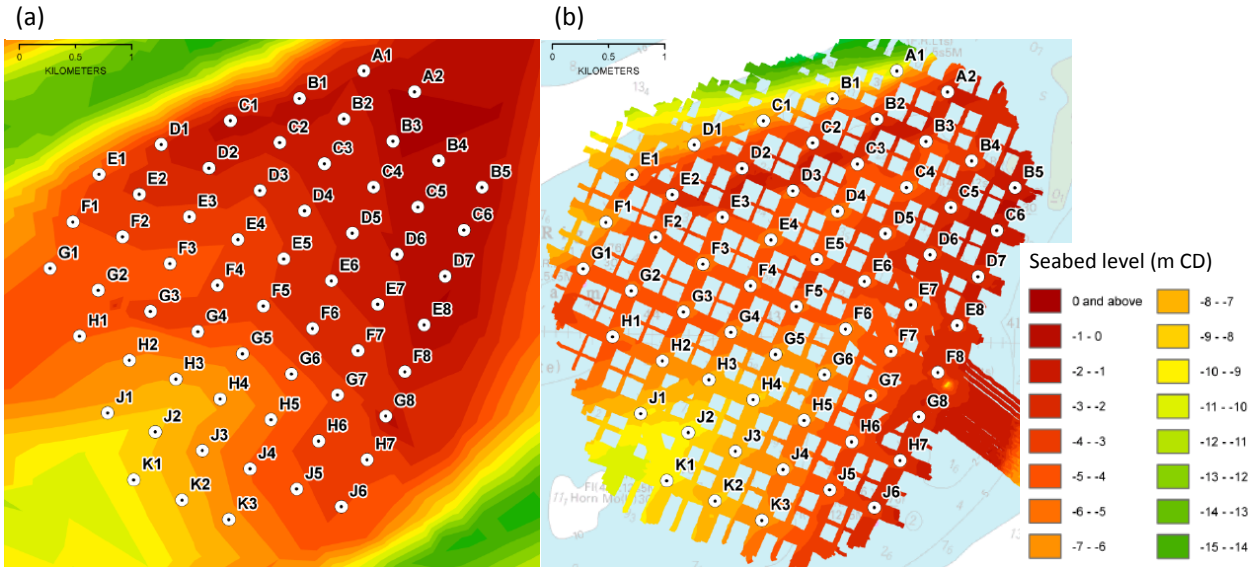

Figure 1.9. Evolution of Robin Rigg site bathymetry (from HR Wallingford, 2015): (a) 5 years before pile installation; (b) 5 years after pile installation. Labelled points (e.g. A1) indicate turbine locations; colour indicates seabed level relative to local chart datum (CD); pale blue/white fill indicates no data.

1.3 Research Project Overview

1.3.1 Research Questions

Three key research questions were posed in a research and development proposal at the outset of the project:

i. What is the effect of scour protection on foundation stiffness and strength?

ii. What is the effect of global seabed lowering and can stiffness be regained with scour protection?

iii. Does local or global scour dominate foundation response and hence structural natural frequency?

1.3.2 Research Participants

The research presented in this portfolio was the result of a collaboration between Oxford University, E.On Energy, and HR Wallingford. The key participants are shown in Figure 1.10. This works forms part of a wider set of research activities at Oxford University working towards optimisation of foundation design for the offshore wind sector.

1.3.3 Portfolio Outline

The research questions were explored through flume experiments and numerical modelling. Figure 1.11 presents an outline of these research activities and their location in this portfolio.

Section 1 sets the context for the research, presenting the motivation for the study and a review of the background literature.

Section 2 presents the flume experiments developed and executed in this research project. A monopile – tower system was modelled in HR Wallingford's Fast Flow Facility flume tank. The experiments explore the influence of scour and scour protection on monopile natural frequencies and lateral capacity. A scientific paper is presented (Paper 3: Mayall et al., [Forthcoming]), followed by further detailed results and discussion.

Section 3 presents the development of a numerical model *EigPile* for the analysis of natural frequencies. *EigPile* uses a one-dimensional finite element approach, the soil reactions are modelled as linear elastic using the results of the PISA and PISA2 projects. Models to account for the stress and stiffness effects of scour and scour protection are implemented in *EigPile*.

Section 4 presents numerical modelling of the flume experiments. The structural dynamics tests are used to calibrate the *EigPile* scour and scour protection models. The monotonic lateral loading tests are modelled to provide insight into the influence of scour protection on monopile capacity.

Section 5 presents a case study of two turbine locations at Robin Rigg offshore wind farm. The case study considers monopiles that have been exposed to combined local and global scour, and subsequently remediated using rock fill scour protection. The calibrated models from Section 4 are applied for computations of natural frequencies and lateral capacities in the case study.

Section 6 concludes the research, presenting the contributions, key findings, recommendations, and responses to the research questions.

Appendix A (Paper 1: Mayall et al., 2019) and **Appendix B** (Paper 2: Mayall et al., 2018) are scientific papers published in conference proceedings, these present further details on some aspects of the research and are included for completeness. **Appendix C**, **Appendix D** and **Appendix E** present supplementary information and analysis methods, which is mostly factual in nature.

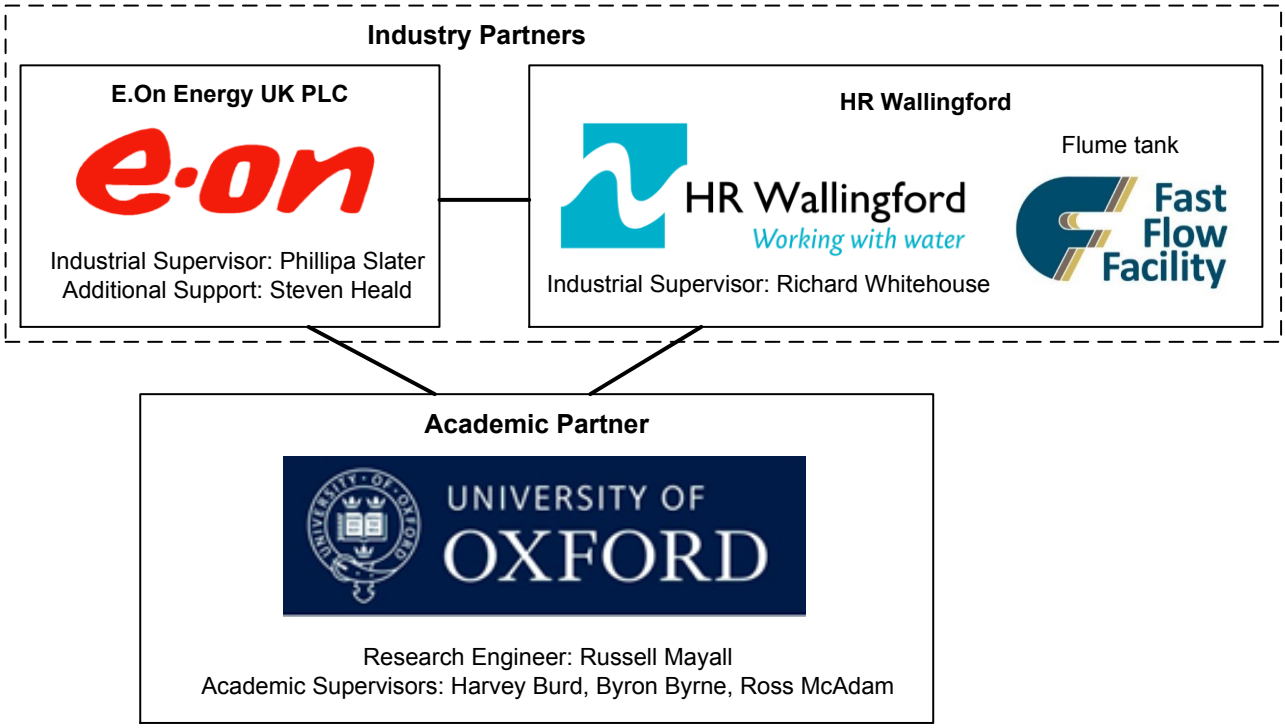

Figure 1.10. Organogram of research participants

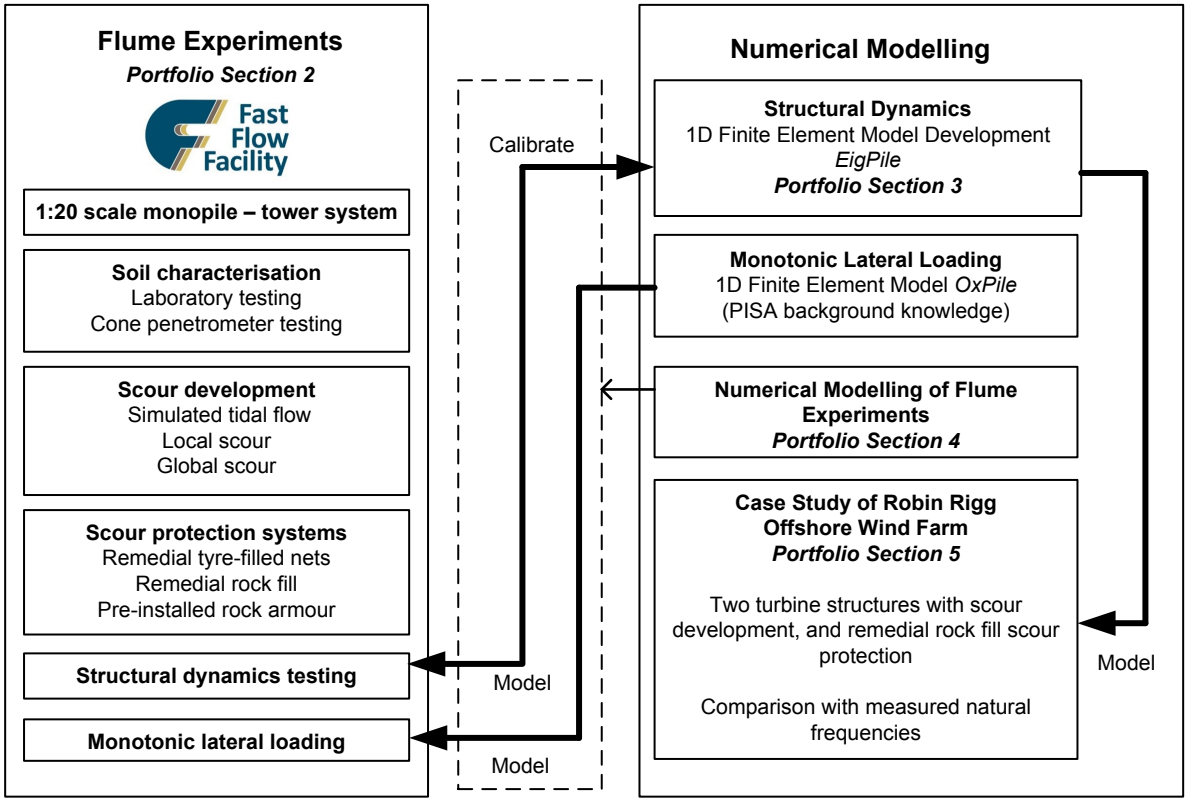

Figure 1.11. Research Project Structure

1.4 Background Literature

1.4.1 Monopile Foundation Stiffness and Stability Analysis Methods

1.4.1.1 Design Standards

The offshore wind industry design guidance (e.g. DNVGL, 2016) is derived from standards for oil and gas structures (e.g. API, 2011; ISO 2004; ISO, 2007). Compared with oil and gas structures, wind turbine foundations are subjected to a high number of load cycles, with a high ratio of lateral and moment loads to vertical loads. The analysis methods for piles derived from API (2011) and its predecessors are not entirely suitable for the design of monopiles due to differences in the pile geometry and loading. Previous research has identified opportunities for optimisation of design practices for monopile foundations (Kallehave et al., 2015), which has been addressed in part through subsequent research such as the PISA and PISA2 projects.

1.4.1.2 Macro Element Soil Model Analysis Method

In a macro-element model the structure is modelled resting on a set of elastic springs (lateral, rotational, cross-coupling, and vertical) acting at a single node representing the foundation. This method has the benefit of providing a quick method to analyse the natural frequency of structures, without the requirement of a full finite element analysis of the foundation.

Arany et al. (2016) presented a simplified mathematical model for an offshore wind turbine using a macro element methodology (Figure 1.12). The basis of the Arany et al. (2016) model consists of modifying the natural frequency of a fixed base cantilever tower, f_{FB}, and applying empirical rotational and lateral foundation flexibility coefficients, C_R and C_L,

$$f_1 = C_R C_L f_{FB} \tag{1.1}$$

The Arany et al. (2016) model was found to have errors up to 3.5% compared to measured natural frequencies from ten offshore wind farms, which is a reasonable match for preliminary design purposes. However, this prediction method does not model the behaviour of higher vibration modes, or model the deformation of the pile below ground level which prevents the analysis of pile fatigue. Furthermore, the method assumes fairly simplistic distribution of stiffness along the pile (constant or

linearly increasing with depth), which may limit the applicability in more complicated layered soil conditions, or require modification to incorporate scour and scour protection effects.

1.4.1.3 PISA and PISA2 Projects

The design standards (e.g. DNVGL, 2016) recommend that the load-displacement behaviour of piles is predicted using a nonlinear Winkler spring method in one-dimensional (1D) finite element analysis, where the soil is represented by discrete nonlinear lateral 'springs' termed p-y curves. For monopile wind turbine foundations the p-y approach is generally considered overly simplistic, since this method excludes the contribution of distributed moment due to the rotation of the pile cross-section, and also excludes the shear and moment forces acting at the pile base.

The PISA project (PISA Final Report, 2016) and subsequent PISA2 project (PISA2 Final Report, 2018) were joint industry projects, which aimed to improve the design methodology for laterally-loaded monopiles. The results are published in conference proceedings (e.g. Byrne et al., 2015; Zdravković et al., 2015; Burd et al., 2017), and the knowledge has recently been consolidated in a series of papers published in *Géotechnique* (Zdravković et al., 2019a; Burd et al., 2019; Byrne et al., 2019; McAdam et al., 2019; Zdravković et al., 2019b; Taborda et al., 2019).

The PISA project proposed the 1D design model shown in Figure 1.13((a)&(b)); the PISA model incorporates the distributed lateral resistance, vertical tractions causing a distributed moment along the pile (Figure 1.13(c)), plus moment and shear resistance at the base of the pile. A 1D finite element analysis approach offers the benefit of speed, which allows a large number of calculations to be performed in a short period of time and is a key benefit in the analysis of offshore wind farms. Figure 1.14 presents the normalised soil reaction curves in the PISA 1D model, and Table 1.1 presents the soil reaction normalisations employed in the PISA 1D model. Three-dimensional (3D) finite element analyses were performed to calibrate the soil reactions in the 1D model (Figure 1.13(d)), the 3D analyses are described in Zdravković et al. (2019b) and Taborda et al. (2019).

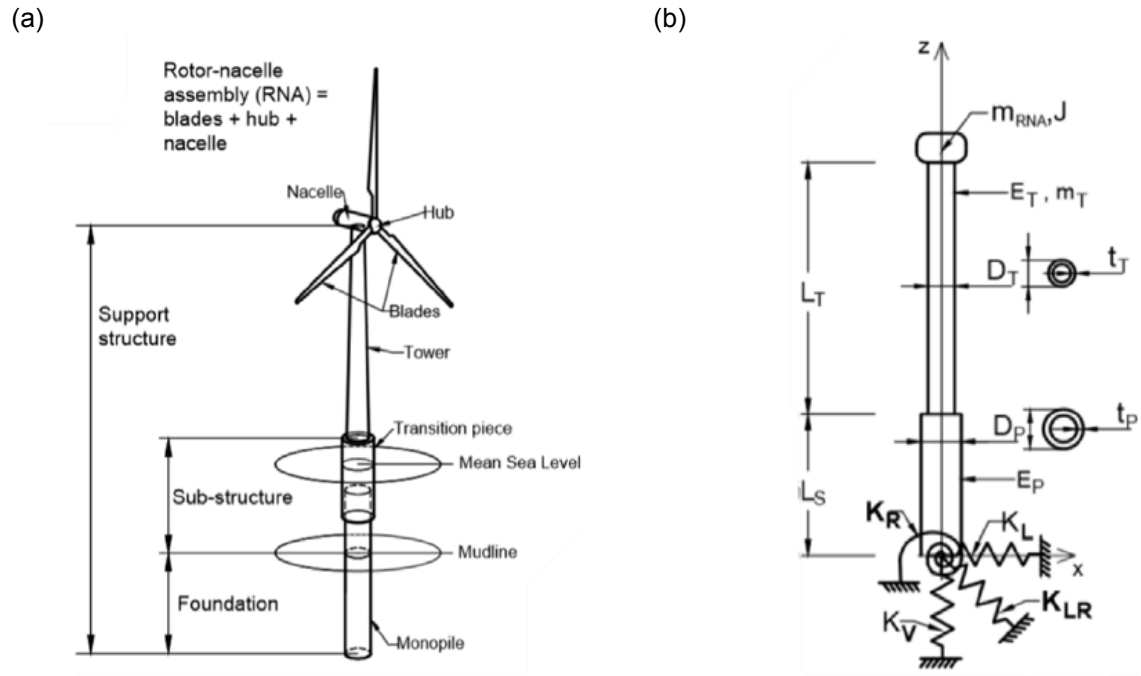

Figure 1.12. Basic model of a wind turbine (edited from Arany et al., 2016): (a) Main components of the structure; (b) Mathematical model with a macro element pile foundation model; L_T is the tower length, L_S is the sub-structure length, m denotes mass, J denotes inertia, E denotes Young's Modulus, D is the average diameter of an element, t is the average wall thickness of an element; items with subscript T are tower elements, items with subscript P are pile elements.

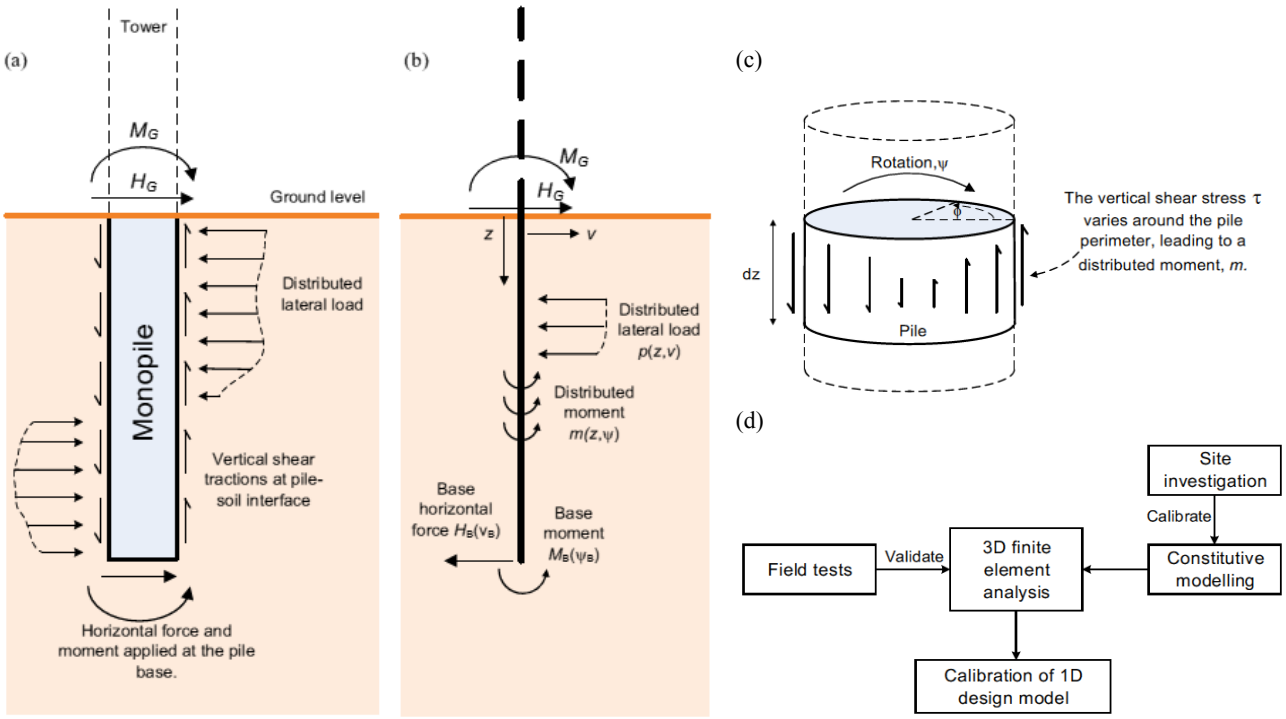

Figure 1.13. Construction of the PISA model for laterally loaded monopiles (from Burd et al., 2017). (a) Assumed soil reactions; (b) 1D design model; (c) View of vertical tractions for an elemental length of pile, which are assumed equivalent to a distributed moment reaction, m; (d) design model development process.

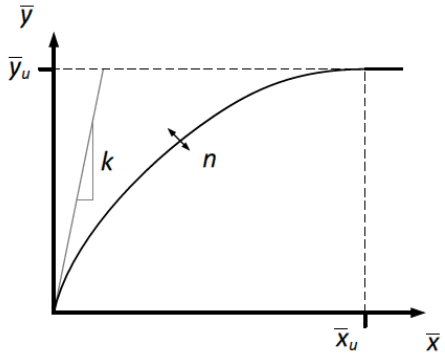

Figure 1.14. General form of normalised soil reaction curves (from PISA Final Report, 2016); specified in terms of an initial stiffness, k, curvature, n, ultimate value, $\bar{y}_u$, and displacement at the ultimate value, $\bar{x}_u$

Table 1.1. Definition of non-dimensional forms employed in PISA design model (PISA Final Report, 2016)

Component	Notation	Clay framework	Sand framework
Distributed lateral load	$\bar{p}$	$\frac{p}{s_u D}$	$\frac{p}{\sigma'_{vi} D}$
Lateral displacement	$\bar{v}$	$\frac{v}{D}\frac{G}{s_u}$	$\frac{v}{D}\frac{G}{\sigma'_{vi}}$
Distributed moment	$\bar{m}$	$\frac{m}{s_u D^2}$	$\frac{m}{pD}$
Pile rotation	$\bar{\psi}$	$\psi\frac{G}{s_u}$	$\psi\frac{G}{\sigma'_{vi}}$
Base horizontal force	$\bar{H}_B$	$\frac{H_B}{s_u D^2}$	$\frac{H_B}{\sigma'_{vi} D^2}$
Base moment	$\bar{M}_B$	$\frac{M_B}{s_u D^3}$	$\frac{M_B}{\sigma'_{vi} D^3}$

In the PISA project 3D analyses were performed for one sand site (Dunkirk) and one clay site (Cowden till); the constitutive models in the 3D analysis were calibrated using site data (Zdravković et al., 2019a) and the results were validated against medium scale field testing (described in Burd et al., 2019; Byrne et al., 2019; McAdam et al., 2019).

In the PISA2 project the PISA design methodology was applied to a broader set of geotechnical conditions, by producing calibrated soil reactions for the 1D model on the basis of further 3D finite element analyses. The additional analyses in the PISA2 project included: generalised sand sites for a range of relative densities, D_R, of 45% to 90% (using the Dunkirk sand constitutive models), three clay sites (Cowden till, Bothkennar clay, London clay), and scenarios with layered soil conditions.

The calibrated 1D soil reactions models (PISA Final Report, 2016; PISA2 Final Report, 2018) provide a useful basis for preliminary analysis of offshore structures, but are limited in several ways: (1) the reactions are limited to the modelled geotechnical conditions; (2) the reactions are only limited to the modelled pile geometry, such as the diameter, wall thickness, and embedment; (3) the reaction models vary with depth below ground level, and this variation depends on the deformed shape of the pile, which may differ for a change of soil conditions or with a difference in the height of the applied lateral load. The *MATLAB* program *OxPile* was developed by the University of Oxford as an implementation of the PISA 1D FE model, including the soil reaction curves.

The PISA and PISA2 projects showed that the new design methodology produces more accurate predictions of lateral pile capacities with reduced conservatism when compared to the design standard p-y approach (e.g. API, 2011), provided the 1D soil reactions are calibrated from 3D analyses using appropriate constitutive soil models. The PISA methodology has been widely adopted by the industry partners on the PISA project. The reduced conservatism has allowed monopile foundations to be more economically designed, and adopted for wind farms in higher water depths than was previously anticipated.

1.4.1.4 Shear Modulus

Soil stiffness is non-linear, and reduces with increases in strain. Several authors have made efforts to define the relationship between the secant shear modulus, G, and the level of shear strain (e.g. Hardin and Drnevich, 1972; Vardanega and Bolton, 2013; Hanssen, 2015), as shown in Figure 1.15. These methods involve empirical fitting of large sets of measured data, such as the test database presented by Vardanega and Bolton (2013).

At very small strains (typically < 10^{-5}) the shear modulus of a soil can be assumed constant (see Figure 1.15), allowing the soil to be treated as an elastic material with small strain shear modulus, G_0. For lateral pile analysis methods, such as the PISA model, G_0 is a key parameter for initial stiffness calculations (see Section 3), and hence natural frequency assessments.

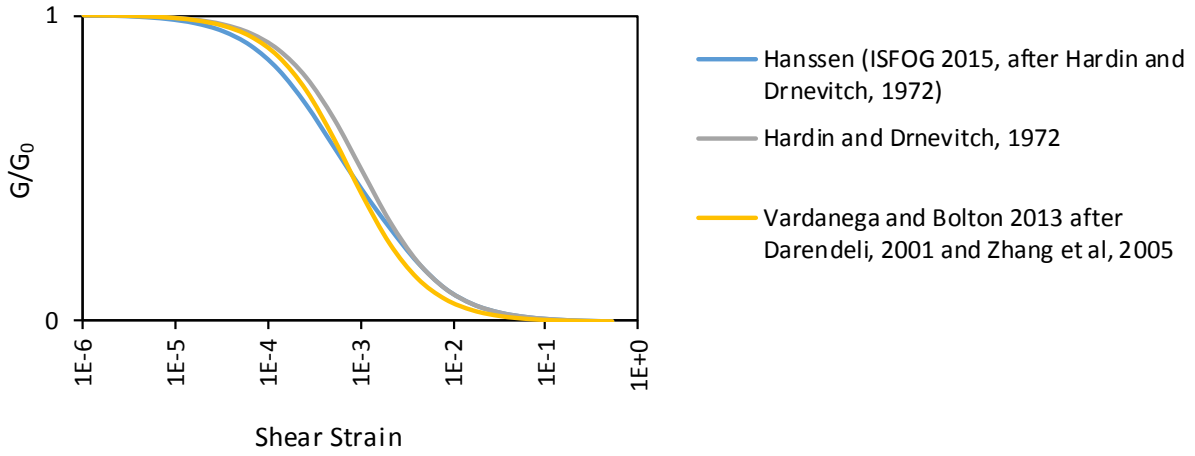

Figure 1.15. Soil secant shear modulus degradation curves

Viggiani and Atkinson (1995) noted that empirical G_0 prediction methods are often in the form:

$$G_0 = B.f(e)OCR^k p_{ref}\left(\frac{p'}{p_{ref}}\right)^n \tag{1.2}$$

where B is an empirical shear stiffness coefficient that depends on the soil composition, $f(e)$ is a function of void ratio, OCR is the overconsolidation ratio, k is a plasticity index coefficient, p_{ref} is a reference stress, and p' is the effective stress. Table 1.2 presents a selection of empirical G_0 calculation methods, presented in a form similar to (1.1) where possible.

Tami and Jaapar (2015) compared G_0 data from *in situ* tests, laboratory tests, and empirical methods. They observed that *in situ* test data generally represent an upper bound to the laboratory test data, and empirical methods vary from measured values by up to 75%, generally as a lower bound with outliers higher than the measured data; this variation is reasonably consistent with the accuracies cited elsewhere (e.g. +/- 50% in Rix and Stokoe, 1992).

As with other empirical methods of determining soil conditions, the assumed relationships should be calibrated based on site-specific data. The soil stiffness around a foundation may also be affected by rate effects, hysteresis and anisotropy; which are not discussed further here.

Table 1.2. Empirical methods for estimating small strain shear modulus

Reference	Soil Type	Empirical Calculation	Coefficients
Hardin and Richart (1963)	Sand	$B.f(e)p_{atm}\left(\frac{p'}{p_{atm}}\right)^{0.5}$	$f(e)=\frac{1}{0.3+0.7e^2}$
Bui (2009) in Clayton (2011)	Sand and clay	$G_0=B.f(e)p_{atm}\left(\frac{p'}{p_{atm}}\right)^{0.5}$	Pluviated sands and reconstituted clays: B = 3000 to 6000; $f(e)=(1+e)^{-3}$
Vardanega and Bolton (2013)	Clay	$G_0=B.f(e)p_{atm}\left(\frac{p'}{p_{atm}}\right)^{0.5}$	B = 1500 to 5000 (typical 2000 $f(e)=(1+e)^{-2.4}$
Zuccarino et al. (2015)	Clay	$G_0=B.f(e)OCR^k p_{atm}\left(\frac{p'}{p_{atm}}\right)^{0.5}$	B = 445; $f(e)=e_0^{-1.3}$ k from Hardin and Black (1968)
DNVGL (2016)	Clay	$G_0=\frac{300s_{u,dss}}{(I_P/100)}$	$s_{u,dss}$ = Undrained shear strength from direct simple shear tests I_P = Plasticity index
	Clays	$G_0=600s_u-170s_u(OCR-1)^{0.5}$	-
	Sands	$G_0=\frac{m(\sigma_{atm}\sigma_v)^{0.5}}{2(1+\nu)}$	$m=1000\tan\phi'$ ϕ' = Angle of friction

1.4.2 Scour at Monopile Foundations

1.4.2.1 Sediment Mobility Criteria

The development of scour is influenced by the site wave and current environment, the character of the seabed sediments, the local geology, and the properties of the structures and infrastructure placed on the seabed. The phenomenon of gaps forming around foundations (slotting) due to the foundation loading is distinct from scour, and is not considered in the current research.

The susceptibility of a site to scour is typically assessed in terms of sediment mobility. Figure 1.16 presents example sediment mobility curves, defining the relationship between soil particle size and flow velocity required to cause erosion and transportation. Note that for fine soils the velocity for erosion increases with decreasing particle size, which is attributed to cohesive effects. For this reason cohesive soils are often considered as resistant to scour. The Shields curve (Figure 1.16 (b)) is generally a preferred approach to the Hjulström curve (Figure 1.16 (a)), since the Shields parameter (θ) is dimensionless.

An offshore site can have either live bed or clear water conditions (Lesny, 2010). In clear water conditions the undisturbed flow velocity is less than the critical flow velocity required to cause sediment transport (i.e. $\theta < \theta_c$), and the scour level is likely to reach a steady equilibrium. In live bed

conditions the undisturbed flow velocity is greater than the critical flow velocity required to cause sediment transport (i.e. $\theta > \theta_c$), causing the sediments to move naturally without the structure's influence. As a result the scour level in live bed conditions may fluctuate after the initial development rather than reach a steady equilibrium.

An offshore site environment can be wave-dominated or current-dominated. The scour depth is generally larger in current-dominated conditions than in wave-dominated conditions (Sørensen and Ibsen, 2013).

1.4.2.2 Global Scour

Global scour refers to a global lowering of the seabed, such as overall seabed movement, migrating sandwaves and sandbanks (Figure 1.17), migrating channel features, or dishpan scour around jacket structures. In the case of sandwaves, an offshore wind farm can be anticipated to have changes in global bed level throughout the project; sandwaves have heights in the range of 1 m to 5 m and can have mobility in the order of 10 m per year (Larsen et al., 2016), which would equate to 0.25 km movement for a 25-year design life.

1.4.2.3 Local Scour

Local scour is the formation of a scour pit around a foundation caused by the formation of horseshoe vortices around the pile in a flow, as illustrated in Figure 1.18(a). As a scour pit develops an equilibrium depth can be reached, where the depth of the scour pit does not increase any further in the given wave and current conditions. Local scour pits are often asymmetric due to prevailing current directions (e.g. Figure 1.18(b)).

Empirical calculation methods for predicting local scour depth have been developed by several authors (e.g. Breusers et al., 1977; Høgedal and Hald, 2005). The experimental data of Sumer et al. (1992b) is commonly cited, with a mean equilibrium S_L/D = 1.3, and standard deviation of 0.7; the experimental work of Ram Babu et al. (2003) suggests a limiting S_L/D = 1.0 for cohesive sediments. The design standards from the petroleum industry (API, 2011; ISO, 2007) recommend a design S_L/D = 1.5; and DNVGL (2016) guidance suggests a design S_L/D = 1.3. Other research suggests higher

values, e.g. Den Boon et al. (2005) yielded values of S_L/D = 1.75. Mostafa (2012) remarks that the maximum scour depth considered in design practice is generally S_L/D = 2.0.

1.4.2.4 Natural Backfilling of Scour Holes

Scour holes can be backfilled naturally in some cases. Sørensen et al. (2010) assessed the characteristics of soil material that has backfilled scour holes in a large wave channel model. CPT measurements were used to explore the relative density of backfill material in wave-dominated environments. The backfill material was found to have a relative density of 60% to 80%, with higher density near the surface.

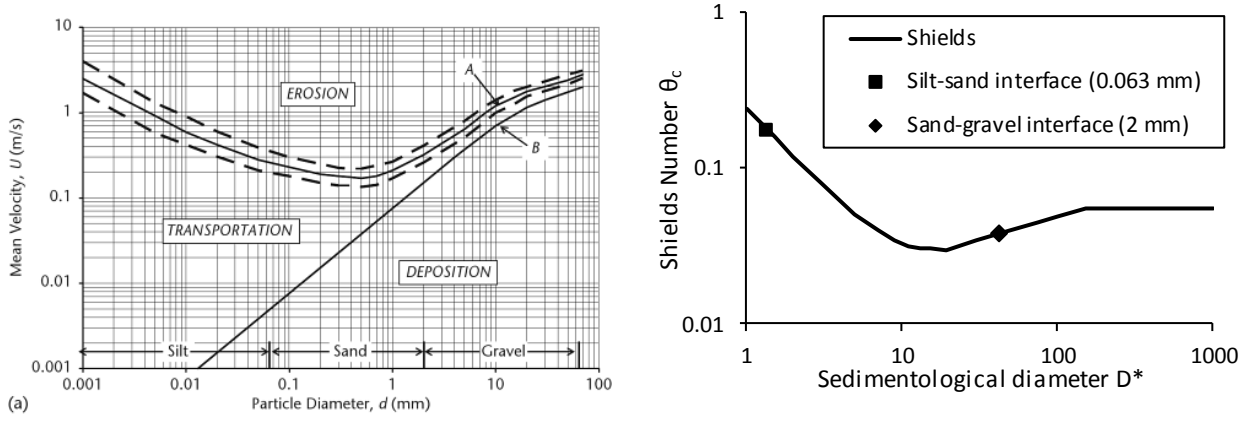

Figure 1.16. Sediment mobility curves: (a) Hjulström sediment mobility curve (from Dingam, 2009); (b) Parameterised Shields curve (after Van Rijn, 1984).

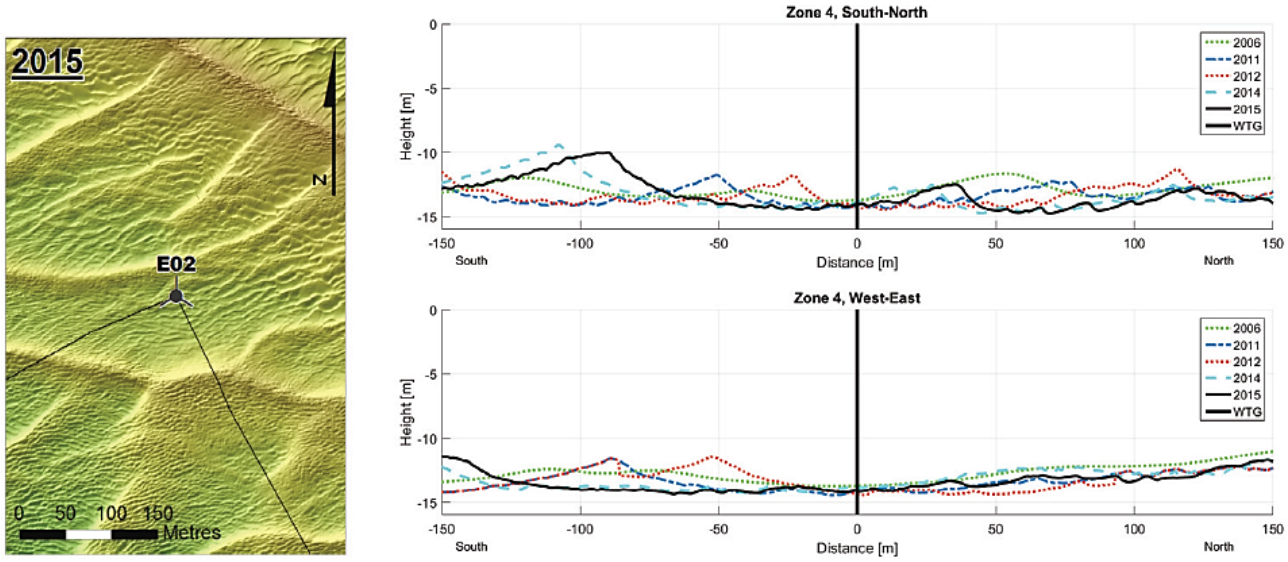

Figure 1.17. Sand waves at Race Bank offshore wind farm (from Larsen et al., 2016).

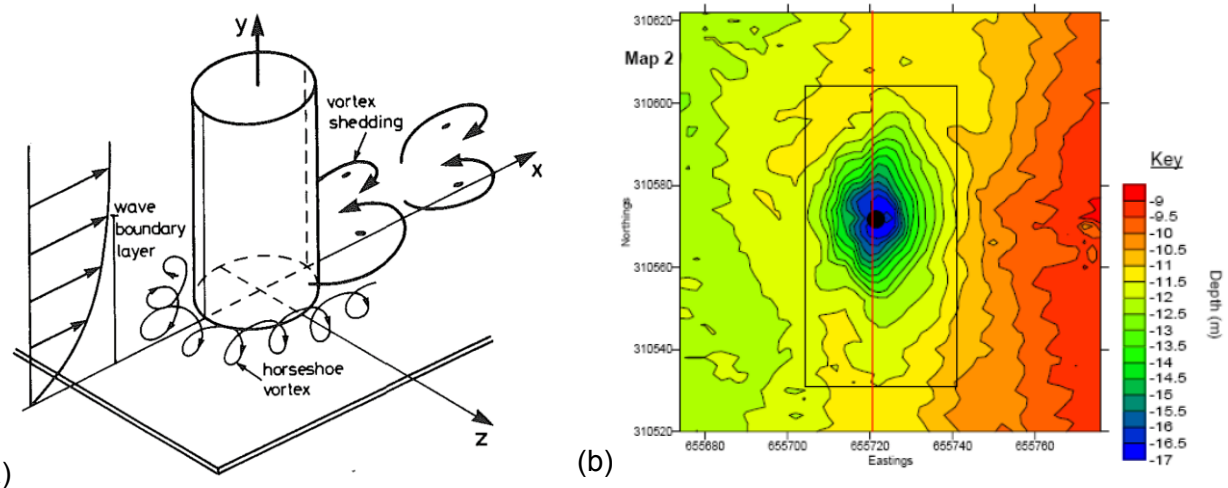

Figure 1.18. Local scour phenomena: (a) Flow patterns around a pile in wave-dominated conditions (from Sumer et al., 1992a); (b) Measured scour pit around a 4.2 m monopile at Scroby Sands offshore wind farm (from Høgedal and Hald, 2005).

1.4.3 Scour Protection Systems

1.4.3.1 Scour Mitigation Strategies

The design standards (e.g. DNVGL, 2016) state that scour should be considered in pile design, but give limited guidance on how to do so. At sites where scour is expected, one of the following pile design approaches might be adopted:

iv. Design scour protection to be either pre-installed or placed shortly after pile installation to minimise the risk of scour developing. This mitigates the risk at the outset. This approach is generally considered the best practice, and is most commonly adopted for wind farms recently in development (e.g. Horns Rev, Race Bank, Walney Extension).

v. Design the pile length to accommodate an extreme prediction of scour depth. As with design approach (i.), this approach also reduces the risk at the outset. However, the additional pile length for a design scour depth of, say, S_L/D = 2 would account for additional 33% to 50% pile embedment for a typical monopile embedment of $4 \leq L/D \leq 6$. The additional pile length requirement of this approach adds significant material costs, but also contributes logistical concerns such as requirements for larger vessels and increased resistance to pile driving.

vi. 'Monitor and react', where the pile length is designed to accommodate modest scour depths and scour protection is installed only if needed (Riezebos et al., 2016). This approach has the benefit

of a lower upfront capital cost, but carries risk of possible remediation requirements during operation. This approach is adopted for some offshore wind farms due to the potential for cost reduction (e.g. Robin Rigg, Scroby Sands, Arkona).

1.4.3.2 Scour Protection Options

Scour protection can generally take the form of rock fill, filled bags or nets, or mattresses. Rock fill is most commonly used (Figure 1.19(a)), typically installed via side-dump vessel (Figure 1.19(b)) or by fall pipe. Alternative scour protection systems such as bags or nets (e.g. Figure 1.19(c)&(d)), or mattresses (e.g. Figure 1.19(e)&(f)) offer potential for cost reduction, but also introduce uncertainty to the operation of the wind turbine since these systems are often at a prototype stage. There are inevitable environmental risks associated with all scour protection types, such as installing tyres offshore or quarrying activities for the acquisition of rock fill, these have not been accounted for in the current work.

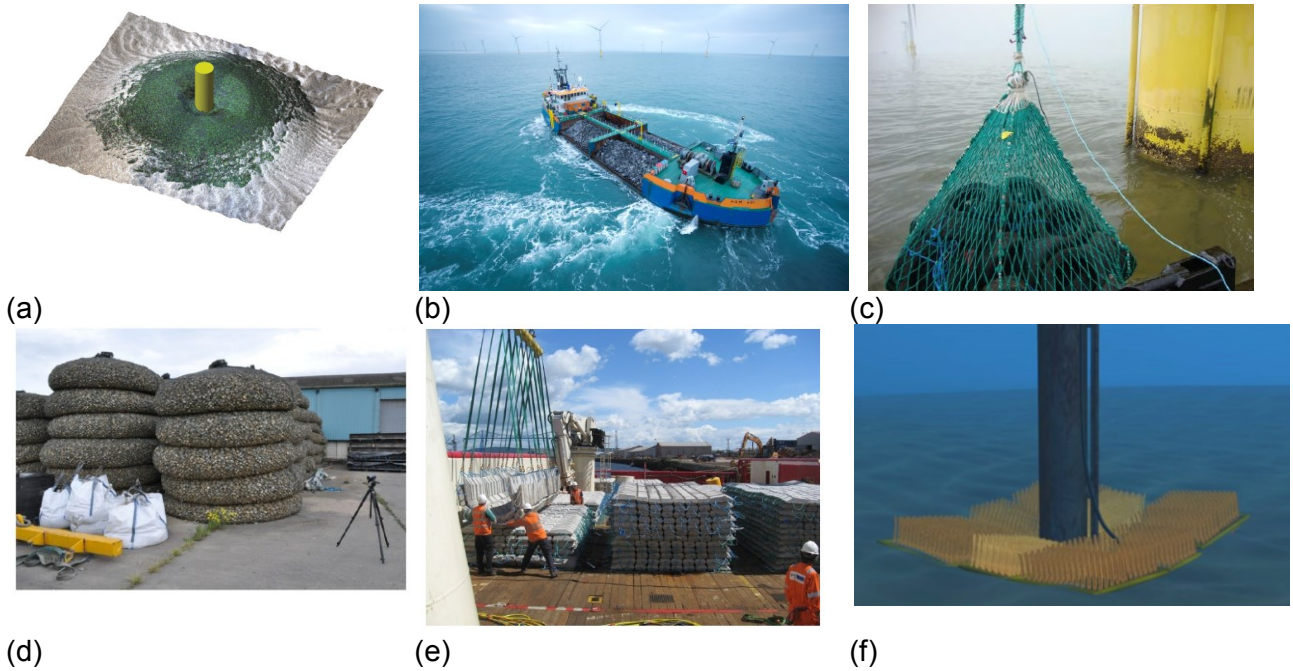

Figure 1.19. Some example scour protection systems: (a) Pre-installed rock armour in model testing (from Riezebos et al., 2016); (b) Typical side dump vessel used for rock placement (photo credit: Van Oord); (c) Tyre-filled nets being installed at Scroby Sands offshore wind farm (photo credit: Norfolk Marine); (d) Filter unit rock-filled nets (photo credit: HR Wallingford); (e) Articulating concrete block mattress (photo credit: Pipeshield Ltd); (f) Fronded mats (credit: Seabed Scour Control Systems Ltd).

1.4.3.3 Scour Protection Failure Mechanisms

The design standards do not offer guidance on the design of scour protection. Design typically relies on the expertise and knowledge of the designers (e.g. Whitehouse et al., 2011; De Vos et al., 2011), with design activities often accompanied by scale model testing in a flume tank. There have been recent attempts to apply computational fluid dynamics to the study of scour protection systems (e.g. Tavouktsoglou et al., 2019), the results of this studies correspond well with flume tank test testing. Figure 1.20 illustrates the four basic failure mechanisms considered for scour protection.

The design drivers for the scour protection failure mechanisms are typically based on hydraulic stability criteria, for example: to avoid erosion of the top layer (Figure 1.20(a)) requires rocks of sufficient size and mass to avoid being transported; to avoid loss of bed material (Figure 1.20(b)) the rock layer is often placed on top of a gravel filter layer; and to avoid edge scour problems (Figure 1.20(c)&(d)) the toe of the scour protection can be placed sufficiently distant from the pile.

There is an ongoing joint industry research project aiming to produce a handbook for scour protection design (HaSPro JIP) (Raaijmakers, 2019). The HaSPro JIP is not due to complete until mid 2020; it is likely that the results will not be publicly available for at least 2 years beyond that date. It is noted that the project aims to provide best practices for scour protection design.

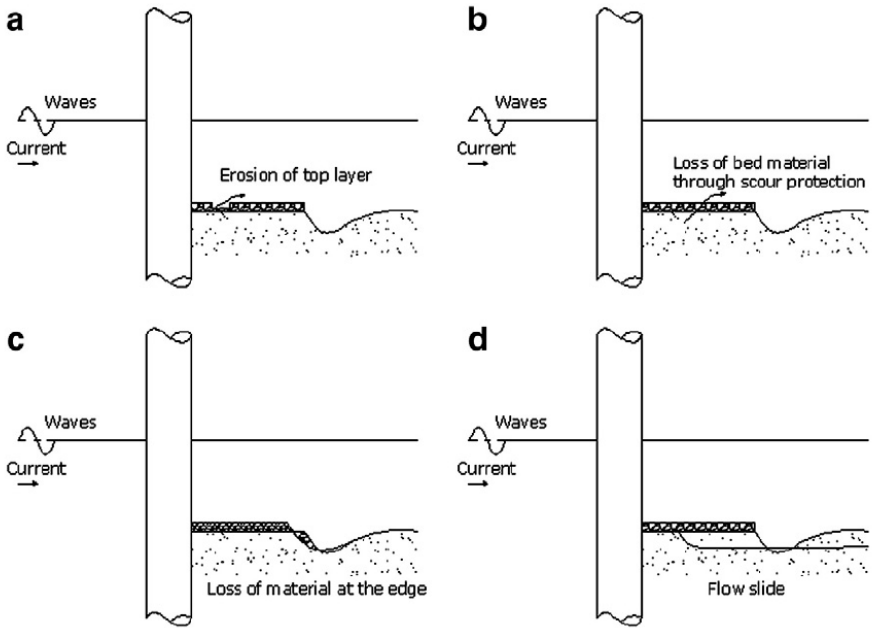

Figure 1.20. Scour Protection Failure Mechanisms (from De Vos et al., 2011, after Hoffmans and Verheij, 1997)

1.4.3.4 Edge Scour Seabed Morphology Effects

The formation of edge scour (Figure 1.20(c)) has been studied to some extent using flume experiments and based on field observations (e.g. Whitehouse et al., 2011; Petersen et al., 2012; Petersen et al., 2015). It is noted that edge scour is occasionally referred to as secondary scour in practice. Figure 1.21 shows some of the findings published by Petersen et al. (2015).

The field measurements in Figure 1.21(b) (flow direction oriented at 180° to Figure 1.21(a)) shows that the greatest depth of edge scour tends to form on the downstream side due to the wake and vortex effects, where the apparent upstream side is caused by asymmetry of the flood and ebb tidal current velocities. The experimental results of Petersen et al. (2015) suggested an equilibrium depth for secondary scour depth on the transverse and downstream sides (Figure 1.21(c)&(d)), that is to be consistent with field measurements.

Experimental testing presented by Riezebos et al. (2016) showed that pre-installed scour protection could be designed to form a 'falling apron' over time (Figure 1.19(a)), and showed that in such cases the scour protection can reach a stable condition over time without necessarily inducing failure.

1.4.3.5 Flow-Induced Changes in Scour Protection Grading

The apparent grading of scour protection material has been shown in several experimental studies to have been affected by flow – where finer sediments were either depleted or accreted from the scour protection layer.

An et al. (2014) performed experiments to explore the susceptibility of rock berms to suction scour (Figure 1.20(b)), the tests were for live bed conditions with a high level of suspended sediments in the flow. The study found that suction did not occur in cases where there was a high sediment supply, instead there was an accumulation of sand in the rock berm due to deposition (Figure 1.22).

Petersen et al. (2019) present an experimental study on the hydraulic stability of single layer widely-graded scour protection options (as opposed to a coarse grade underlain by a filter layer).

The study found that the flow had caused fines to be removed close to the surface of the scour protection layer, and had also induced internal erosion adjacent to the pile wall, shown in Figure 1.23.

The observed internal changes in scour protection condition have potential implications for geotechnical design that have not been explored in the literature. The submerged unit weight and extent of particle interlocking are both likely to be affected by the loss or gain of fines, and hence influence the reactions at the pile-soil interface.

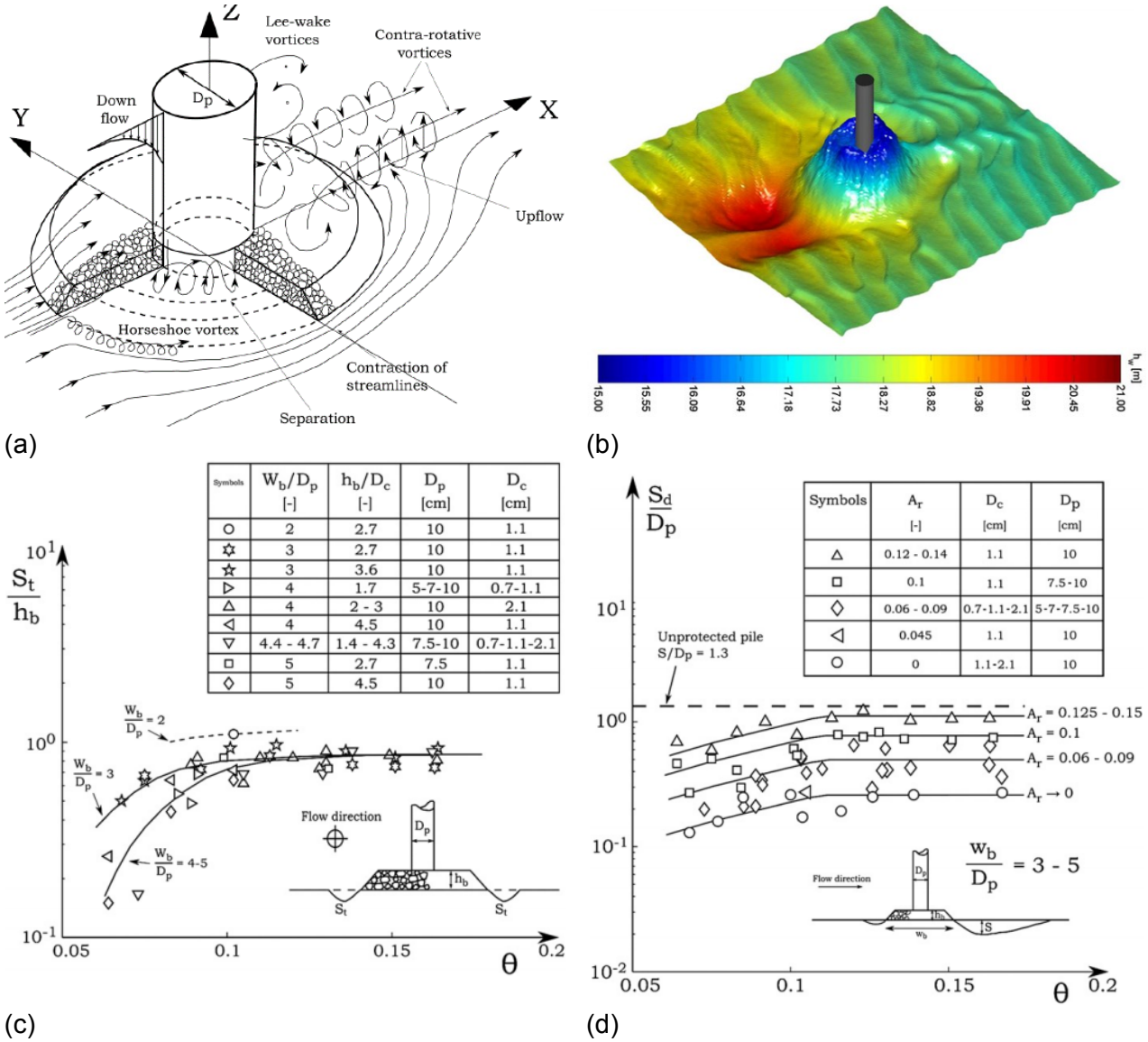

Figure 1.21. Edge scour around pre-installed rock armour scour protection (from Petersen et al., 2015): (a) Flow patterns in steady flow conditions; (b) Bathymetry data showing edge scour around scour protection at Offshore Windpark Egmond aan Zee, presented with exaggerated vertical scale; (c) Normalised equilibrium edge scour depth, transverse side, data from flume experiments; (d) Normalised equilibrium edge scour depth, downstream side, data from flume experiments.

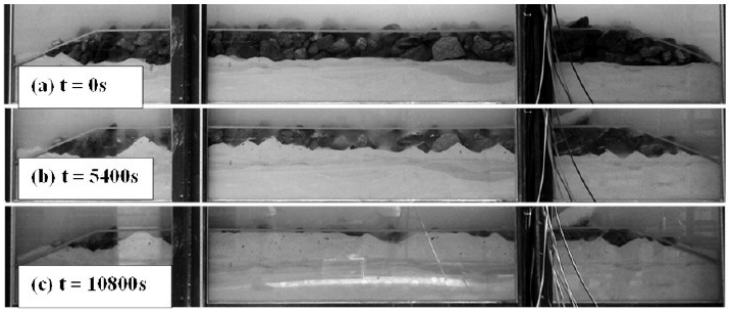

Figure 1.22. Accumulation of sand in a rock berm in live bed conditions (from An et al., 2014)

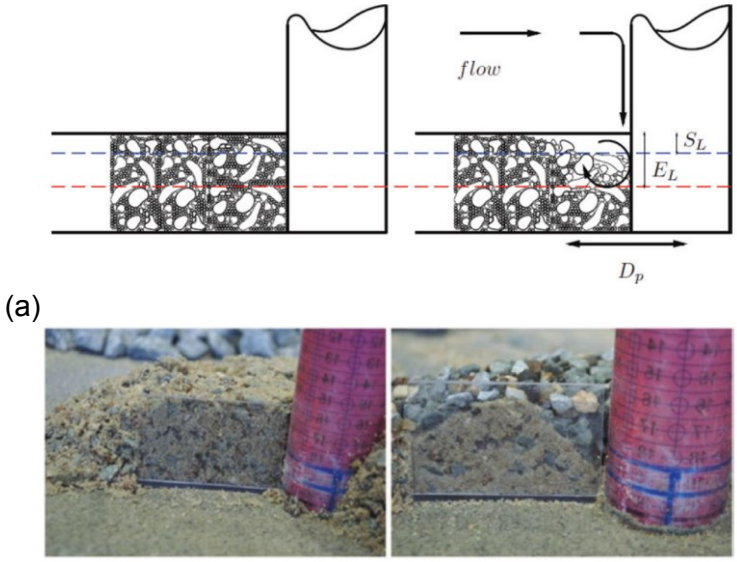

Figure 1.23. Settlement and erosion adjacent to the pile in single layer widely-graded rock armour scour protection (from Petersen et al., 2019): (a) definition of equilibrium and scour levels; (b) observations in flume experiments. (left panels: initial condition, right panels: equilibrium condition).

1.4.4 Scour and Scour Protection Interaction with Pile Behaviour

1.4.4.1 Vertical Effective Stresses

Where scour occurs at a pile, the behaviour is affected by two key mechanisms: (A) a loss of pile-soil contact, and (B) a presumed reduction in the vertical effective stresses in the remaining soil due the removed overburden. Accounting for Mechanism (A) is straightforward, but does introduce the uncertainty of the scour depth predictions; accounting for Mechanism (B) introduces additional uncertainty in the assumed distribution of vertical effective stresses below the scour hole.

For global scour it is generally accepted that soil stresses can be calculated assuming that the removed layers have no residual effect on the stresses (e.g. DNVGL, 2016; Qi et al., 2016). For local scour conditions the design standards (e.g. API, 2011) suggest a bi-linear distribution, shown in Figure 1.24.

Qi et al. (2016) proposed an alternative empirical vertical effective stress distribution, as a hyperbolic tan function (adapted for consistency with notation in Figure 1.24),

$$\sigma'_{va} = \gamma' \left[z + S_d \tanh\left(f \frac{z}{D} \right) \right] \tag{1.3}$$

where f is an empirical parameter, optimised as f = 1.5 based on centrifuge lateral load tests on model piles in the sand with a scour slope, $\beta = 30°$, and zero scour base width ($S_{wb} = 0$). Qi et al. (2016) hypothesise that f would be higher for increasing scour slope β.

Lin (2017) proposed a theoretical vertical effective stress distribution based on Boussinesq's point load equation to capture the additional scour hole dimensions in Figure 1.24(a),

$$\sigma'_{va} = \gamma' z \left[1 + (\tan\beta) \left(\frac{\frac{S_d}{\tan\beta} + S_{wb}}{\sqrt{\left(\frac{S_d}{\tan\beta} + S_{wb} \right)^2 + z^2}} - \frac{S_{wb}}{\sqrt{S_{wb}^2 + z^2}} \right) \right] \tag{1.4}$$

Lin and Jiang (2019) performed a comparison of the performance of the FHWA-DP, FHWA-DS, API (Figure 1.24(b)), and Lin (2017) (1.4) methods for pile capacity in axial tension predictions from finite element modelling with full surface interface roughness. The study found that the FHWA-DS approach was preferred for dense sands and FHWA-DP was preferred for loose sands. the study also concluded that that the Lin (2017) expression produced conservative results (i.e. under-predictions), but offered an improvement over the bilinear approaches when considering finite element analyses with varying scour base and slope dimensions. The finite element results showed the tension capacities became relatively insensitive to the slope angle, β, for $\beta > 15°$. Both the finite element results and the Lin (2017) expression (1.4) showed sensitivity (of tensile capacity) to the scour hole base width S_{wb}.

There is inconsistency between the vertical effective stress profiles produced using the various approaches for local scour conditions. In practice the API (2011) approach is most likely to be used for offshore wind turbine design, but this may not be the most appropriate as indicated by Qi et al (2016). The Lin and Jiang (2019) study also raises some interesting questions, such as the potential for the soil condition and scour hole width to influence the vertical effective stress condition. However it is unclear how relevant the conclusions from tensile capacity analysis are for laterally loaded piles.

A further limitation of the knowledge base in this area is how to handle vertical effective stresses in the presence of scour protection. There is also a knowledge gap in how to account for realistic scour hole asymmetry (e.g. Figure 1.18(b)) in the vertical effective stress profiles.

1.4.4.2 Change in Soil Properties with Scour

As scour develops, the change in stress results in a change in the soil properties. For example, Lin et al. (2010) discusses how as soil is unloaded by scour the remaining soil can be considered as overconsolidated compared to the remaining stress state. No guidance is offered in the design standards (e.g. DNVGL, 2016) relating to change in soil strength and stiffness due to scour. It is generally assumed that if the stress can be defined then parameters such as G_0 can be calculated.

The effect of scour on CPT measurements was observed in the centrifuge test measurements of Qi et al. (2016), reproduced in Figure 1.25. The results in Figure 1.25 show that for local scour conditions the cone tip resistance, q_c, recovers to the no scour value with increasing depth, and for global scour (termed general scour in Figure 1.25) the cone tip resistance, q_c, does not recover to the no scour condition.

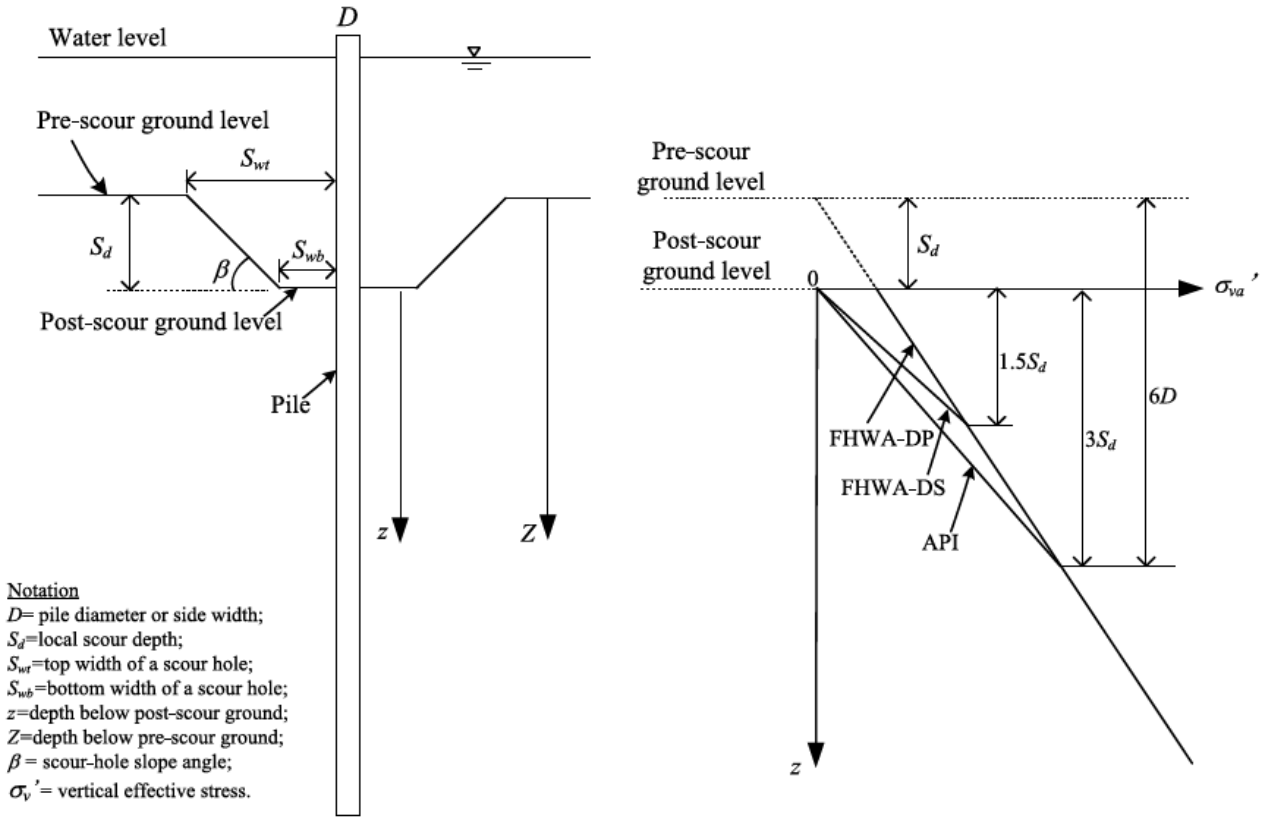

(a) (b)

Figure 1.24. Vertical effective stress models under the influence of scour (from Lin and Jiang, 2019): (a) Scour hole dimensions; (b) Schematic of vertical effective stress distribution by different methods: FHWA-DP = US Federal Highway Administration-Driven Piles (Hannigan et al., 2006), FHWA-DS = US Federal Highway Administration-Drilled Shafts (Brown et al., 2010), API = American Petroleum Institute (API, 2011)

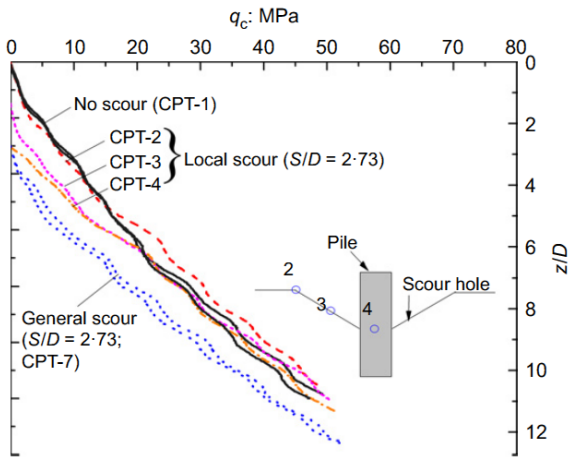

Figure 1.25. Centrifuge measurements of cone tip resistance q_c in a scour pit (from Qi et al., 2016)

1.4.4.3 Influence of Scour on Pile Foundation Behaviour

The specific subject of how scour affects monopile performance has been studied in a small number of numerical and experimental research projects.

Several studies are presented in the literature using 1D numerical analyses to predict the effect of scour on the natural frequency of monopile wind turbines, a selection of such results are collated in Figure 1.26. The predicted reduction in f_m with scour depth is greater for the second mode of vibration than for the first in the Sørensen and Ibsen (2013) study (Figure 1.27). These studies use 1D finite element approaches, and use the initial stiffness of p-y springs to represent the soil stiffness. In the case of Damgaard et al. (2013) and Sørensen and Ibsen (2013) the initial stiffness is using the p-y spring formulations. It is noted that the predictions of f_m with scour lack validation, and do not include the distributed moment, base shear and base moment components suggested in the PISA methodology.

Figure 1.27 presents the predicted frequencies from Sørensen and Ibsen (2013) for a monopile with local scour and varying relative density, D_R, of backfill material. The relative density of scour hole backfill in the Sørensen and Ibsen (2013) study (Figure 1.27) has a significant effect on the soil stiffness and also the recovered natural frequency, f_m. The backfill material was assumed to have a lower stiffness than the original material, hence f_m remained lower than the unscoured case.

Experimental testing was performed by Prendergast et al. (2013; 2015) in which driven piles at a sand test site were subjected to scouring and impact loading (Figure 1.28); the piles were instrumented with accelerometers to provide data for natural frequency analysis. The results indicate that monitoring of natural frequencies could be used for the detection of scour.

There are relatively few analyses of the lateral capacity of piles under the influence of scour. Lin et al. (2014) presented a study of laterally loaded slender piles, and a modified p-y formulation based on the expected failure wedge geometry with a local scour pit. Li et al. (2018) presented a numerical analysis of laterally loaded monopiles with varying soil conditions and with scour, and found the natural frequencies to depend strongly on both the soil conditions and the scour depth; although this study is limited in that the soil was modelled using the API p-y approach.

Overall the published numerical analyses of scour effects on the natural frequency of wind turbine structures lack validation against either full scale structures or experiments that model of a wind turbine tower and rotor-nacelle assembly (these components influence the dynamic behaviour of the structure).

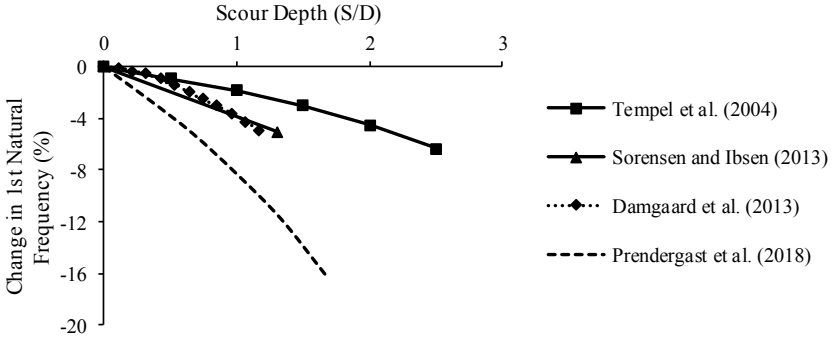

Figure 1.26. Numerical predictions of monopile wind turbine natural frequency variation with scour

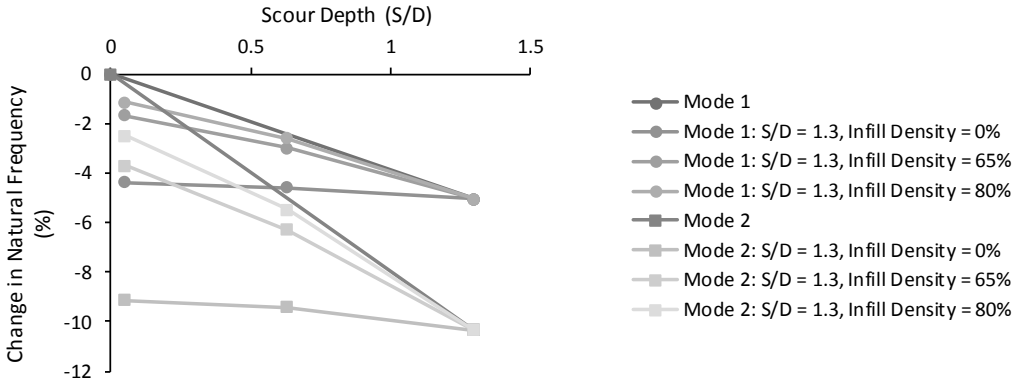

Figure 1.27. Numerical predictions of the effect of scour hole infilling on monopile wind turbine natural frequencies (data from Sørensen and Ibsen, 2013)

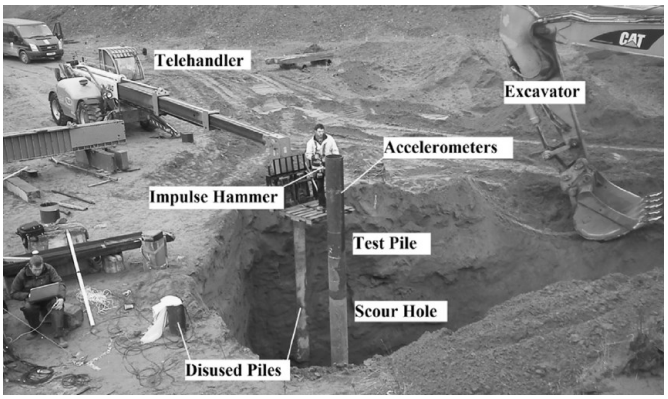

Figure 1.28. Impact testing of a driven pile with an excavated scour hole (from Prendergast et al., 2013)

1.4.4.4 Influence of Scour Protection on Pile Foundation Behaviour

The influence of scour protection on pile behaviour has received limited research attention, but is intuitively expected to have a positive effect on natural frequencies and lateral capacity.

Yang et al. (2019) present a study of a laterally loaded hybrid monopile-gravel wheel foundation using centrifuge testing and 3D finite element analysis (Figure 1.29). The hybrid monopile-gravel wheel of Yang et al. (2019) bears similarity to monopiles with pre-installed rock armour scour protection – a key difference is that the gravel is confined at the outside edge in the gravel wheel case but unconfined for rock armour. The study confirms a positive contribution of scour protection, and also showed that the lateral capacity increased with wheel diameter which approached the response for a uniform gravel layer for a wheel diameter greater than 6.5 times the pile diameter, D.

Hucker et al. (2019) present natural frequency monitoring data for the Greater Gabbard offshore wind farm for over 6 years (Figure 1.30), including data for monopiles without scour protection and with rock dump scour protection. In general the data shows that the natural frequencies tended to reduce over time for unprotected foundations, and to increase over time for foundations with scour protection; seasonal variations are also observed in the data. Hucker et al. (2019) suggest that a 'settlement and densification' mechanism is likely to have caused the scour protection stiffness to increase over time, resulting in the observed natural frequency gain. Perhaps the scour protection at this site has undergone some internal changes in composition due to sediment accretion similar to the observations of An et al. (2014) (Figure 1.22).

It is understood that in design the influence of scour protection on pile behaviour is often disregarded as a conservative assumption. There is scope for further optimisation of monopile design methodologies by defining methods to incorporate the contribution of scour protection.

(a) (b)

Figure 1.29. Modelling of a hybrid monopile-gravel wheel foundation (from Yang et al., 2019): (a) Centrifuge lateral loading tests; (b) Finite element model

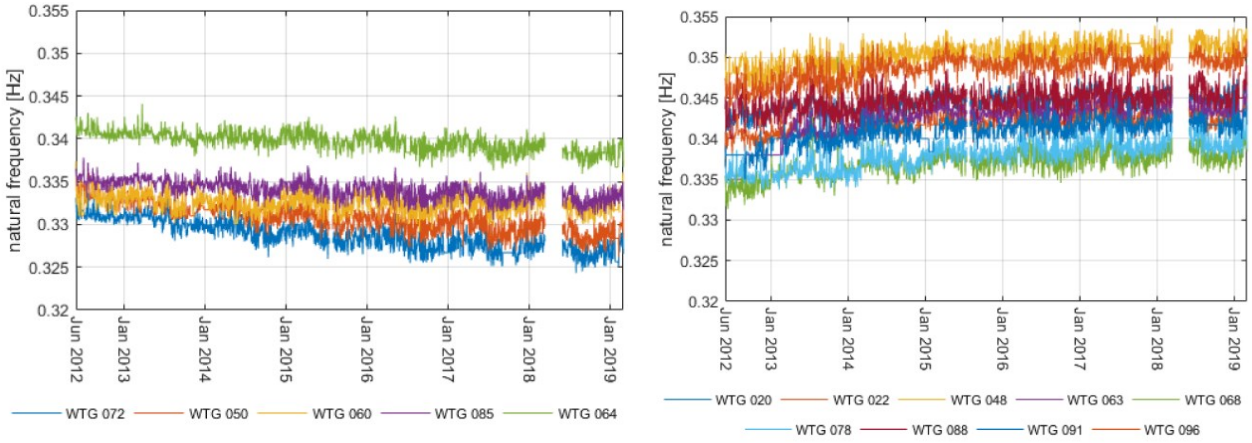

(a) (b)

Figure 1.30. Natural frequency monitoring data at Greater Gabbard offshore wind farm (from Hucker et al., 2019): (a) Foundations without scour protection; (b) Foundations with scour protection

1.4.5 Summary of Background Literature

1.4.5.1 Summary of the Present Situation

This literature review has considered the current situation for the design of monopile-supported offshore wind turbines with scour and with scour protection:

i. The PISA and PISA 2 projects have led to the potential for significant cost reductions for offshore wind farms in development by producing a less conservative and more reliable prediction methodology for the analysis of laterally-loaded monopiles.

ii. Published natural frequency predictions for monopile offshore wind turbines tend to use either macro element models or p-y approaches, the PISA methodology may offer potential optimisation of these analyses.

iii. Scour depth prediction and scour protection design is an empirical activity that is concerned with hydraulic stability to avoid failure of any scour protection systems.

iv. Scour protection is likely to induce a complicated seabed morphology due to secondary scour effects, the influence on the performance of monopile foundations has not been explored.

v. Scour protection has been shown to be susceptible to internal grading changes due to either deposition or accretion of finer materials in certain site conditions, the potential to influence the soil-structure interaction has not been explored.

vi. Monopile performance under the influence of scour has been studied to some extent, but there is conflicting guidance over the methods of assessing vertical effective stresses in scoured conditions.

vii. There is almost no guidance on the effects of scour protection on monopile foundation performance.

1.4.5.2 Research Opportunities

There is an opportunity to perform research in the following areas:

i. Expand upon the PISA model for monopile lateral load-displacement behaviour to include the effects of scour and scour protection.

ii. Develop a numerical framework for assessing the effects of scour and scour protection on the natural frequency of monopile offshore wind turbine structures, on the basis of the PISA model.

iii. Experimental testing of the natural frequency of offshore wind turbine structures subject to scour and scour protection, to provide validation data for numerical models.

iv. Assess the effect of scour protection on the lateral loading response of monopile foundations.

Section 2 – Flume Experiments

2.1 Introduction

This Section presents a description of the flume experiments programme performed at the Fast Flow Facility (FFF) at HR Wallingford from June to August 2017. The aim of these experiments was to monitor the foundation behaviour of a model monopile – tower system exposed to scour and with scour protection. The foundation behaviour effects were inferred from structural dynamics measurements and monotonic lateral loading tests.

Data from the flume experiments were previously described in two reports (Mayall, 2018; 2019). A separate report (HR Wallingford, 2018) describes aspects of the experiments relating to the flume operation, including specification and measurement of the flow regime, access scaffold, and bathymetry data acquisition. A small number of elements from the HR Wallingford report that are relevant to the interpretation of the results have been incorporated.

2.2 Journal Paper

The following scientific paper (Paper 3) is a manuscript for journal publication. Paper 3 includes detail on the experiment scope, experimental setup, characterisation of the sand test bed, cone penetrometer testing, pile installation, flow regime for scouring, scour depth measurements, scour protection details, and natural frequency results. Appendix B presents Paper 2, which was published in conference proceedings, which presents further detail on some aspects of the physical modelling.

Section 2.3 provides further detailed results and discussion of the bathymetry data in terms of scour development and scour protection stability. Section 2.4 provides further detailed results and discussion of the structural dynamics data, including analysis of the mode shapes. Section 2.5 presents the monotonic lateral loading tests. Supplementary information on the experimental setup and data analysis methods is provided for reference in Appendix C.

Section 2.6 presents a discussion of the experimental results and conclusions drawn from the experiment results.

Monopile Response to Scour and Scour Protection

Paper 3

Flume tank testing of offshore wind turbine dynamics with foundation scour and scour protection

Mayall, R.O., McAdam, R.A., Whitehouse, R.J.S., Burd, H.J.,

Byrne, B.W., Heald, S.G., Sheil, B.B., and Slater, P.L. [Forthcoming]

Flume tank testing of offshore wind turbine dynamics with foundation scour and scour protection

Russell O. Mayall[1], Ross A. McAdam[2], Richard J.S. Whitehouse[3], Harvey J. Burd[4], Byron W. Byrne[5], Steven G. Heald[6], Brian B. Sheil[7], Phillipa L. Slater[8]

[1] Doctoral Candidate, Department of Engineering Science, University of Oxford, Parks Road, OX1 3JP, UK. russell.mayall@eng.ox.ac.uk

[2] Associate Professor, Department of Engineering Science, University of Oxford, Parks Road, OX1 3JP, UK. ross.mcadam@eng.ox.ac.uk

[3] Chief Technical Director (Sediment Dynamics), HR Wallingford, Howbery Park, Wallingford, Oxfordshire, OX10 8BA, UK. R.Whitehouse@hrwallingford.com

[4] Associate Professor, Department of Engineering Science, University of Oxford, Parks Road, OX1 3JP, UK. harvey.burd@eng.ox.ac.uk

[5] Professor, Department of Engineering Science, University of Oxford, Parks Road, OX1 3JP, UK. byron.byrne@eng.ox.ac.uk

[6] Offshore Technical Support Manager, RWE Renewables UK Ltd, Greenwood House, Westwood Way, Coventry, CV4 8LG, UK. Steven.Heald@eon.com

[7] Royal Academy of Engineering Research Fellow, Department of Engineering Science, University of Oxford, Parks Road, OX1 3JP, UK. brian.sheil@eng.ox.ac.uk

[8] Technical Head, Development Offshore Wind, RWE Renewables UK Ltd, Greenwood House, Westwood Way, Coventry, CV4 8LG, UK. Phillipa.Slater@eon.com

ABSTRACT

Scour erosion processes can occur at seabed level around offshore wind turbine monopile foundations. These scour processes are often especially severe at sites where mobile sediments, such as sands, are present in the superficial seabed soils. Loss of local soil support to the monopile, caused by scour erosion, can lead to significant changes in the dynamic characteristics of the wind turbine support structure. This can result in accelerated fatigue damage due to the applied cyclic loads from the wind turbine generator, especially at the rotor frequency. Although scour erosion can be controlled by appropriate scour protection systems, there is a lack of knowledge to support the design and optimisation of these protection measures, to ensure that the dynamic performance of the wind turbine support structure remains within acceptable limits. This paper describes an experimental campaign conducted on a 1:20 scale model of a driven

monopile foundation and wind turbine support structure, founded in a prepared sand test-bed in the Fast Flow Facility flume (HR Wallingford, UK). Scour processes were induced by applying cycles of flow. Experiments were conducted to investigate the influence that these scour processes, and selected concepts for preventative and remedial scour protection, have on the dynamic characteristics of the monopile-tower system. The paper describes the experimental procedures that were adopted, and provides an assessment of the results.

INTRODUCTION

Many offshore wind turbine support structures, in operation or under development, employ monopiles with diameter D in the range 4 - 10m and embedment ratios L/D (where L is embedded length) in the range 2 - 6. Scour erosion processes, due to wave and current action, can often occur in the seabed soils around foundations, especially at sites where the superficial soil is sand-dominated. These erosion processes can cause significant loss of soil support to the foundation, with consequential reductions in stiffness and ultimate capacity. Moreover, the depth of local scour erosion holes that develop around monopiles scales with pile diameter; monopiles with larger diameters cause greater depths of local scour. The relatively large diameter but low embedment ratio wind turbine monopiles are therefore potentially vulnerable to the effects of scour.

Reductions in foundation stiffness due to scour cause corresponding reductions in the natural frequencies of the combined foundation - wind turbine support structure. This change to the dynamic characteristics of the structural system can cause accelerated fatigue damage due to the action of cyclic loads, especially those associated with the rotor frequency. Accelerated fatigue damage can lead to significant reductions in design life and asset value. In extreme cases, reductions in the ultimate capacity of the foundation, due to scour processes, may trigger concerns about the ability of the structure to operate safely within serviceability limits.

Scour processes that develop around offshore foundations are commonly categorised as (i) ‘local scour’ in which erosion of the soil occurs by the action of downflow and horseshoe vortices around the pile (e.g. Sumer et al., 1992), and (ii) ‘general scour’ in which effects such as migrating sand waves, basin-wide erosion or loss of upstream soil supply cause changes in the original sea bed level on a length scale that is considerably larger than the dimensions of the foundation (general scour is sometimes referred to in projects as leading to a change in the global seabed level). It should be noted that 'global' sedimentation can also occur, e.g. due to the passage of a sand wave crest past the pile, or due to regional accretion. An idealised

seabed profile around a monopile foundation, indicating general scour of magnitude S_G, and an additional conical local scour hole of depth S_L, is illustrated in Fig. 1.

Various approaches have been proposed to predict the depth and extent of local scour at a piled foundation (e.g. Whitehouse, 1998). Practical guidance on design values of S_L are provided in standard guidance documents (e.g. API 2011, DNVGL 2016). Recommended design values of S_L are typically proportional to the pile diameter; $S_L = 1.5D$ in API 2011 and $S_L = 1.3D$ in DNVGL 2016. Local scour equilibrium depths and development rates are influenced by the site wave and current conditions. Design values for S_G need to be determined on the basis of local site conditions, including an assessment of the way in which the seabed conditions might develop over the lifetime of the foundation.

In commercial wind farm projects, if at the design stage the risk of scour is considered to be significant, pre-installed preventative scour protection systems may be incorporated as the foundation is installed. Alternatively, when unexpected scour processes occur during the working life of a wind turbine structure, post-construction remedial scour protection systems may be employed. Rock fill scour protection - installed from a side-dump vessel or via a fall pipe - is most commonly used; and is placed either as a layer of certain thickness using a single grading or underlain with a filter layer of smaller rock. Alternative scour protection concepts such as filter units (rock-filled nets) or tyre-filled nets can be installed by lowering from a crane vessel; these offer potential cost reductions and opportunities for easier decommissioning.

Scour protection systems are primarily designed on the basis of the need to control physical scour erosion processes around the monopile, including failure mechanisms such as (i) erosion of the placed material, (ii) suction scour-induced loss of seabed sediments through scour protection layers, and (iii) instability due to secondary/edge scour at the extremity of the scour protection (e.g. Whitehouse et al., 2011; De Vos et al., 2011). Previous experimental studies on scour protection have tended to explore these hydrodynamic aspects with recent developments including: (i) allowing a ‘falling apron’ of rock to develop at the edge of scour protection with an unstable initial condition representing global scour (Riezebos et al., 2016), (ii) observations of sediment accumulation in suction scour tests (An et al., 2014), and (iii) observations of internal scouring adjacent to the pile wall in widely-graded scour protection systems (Petersen et al., 2019). However, there is a separate, but equally important, requirement to consider the influence of scour and scour protection systems on the structural performance of the monopile-tower system. Consideration of these structural performance issues might also provide opportunities to actively control the dynamic characteristics of the monopile-tower via appropriate scour protection systems.

This paper describes an experimental investigation on the influence of scour and scour protection systems on the dynamic characteristics of a model monopile - tower system (see summary in Mayall et al., 2018). Previous experimental work in this area, with a focus on structural performance of foundations, has been mainly limited to the influence of scour on response rather than extending to scour protection systems. Such testing typically employs artificially-generated scour holes (e.g. Prendergast et al., 2013; Prendergast et al. 2015; Qi et al., 2016), which provides a useful means of investigating idealised forms of the problem, but does not incorporate realistic aspects of actual scour erosion processes. The influence that the presence of scour protection systems has on the structural performance of monopile foundations has received limited previous attention.

The experimental campaign was conducted in the 4m wide Fast Flow Facility (FFF) flume at HR Wallingford, UK (Whitehouse et al., 2014). A model monopile - tower system at reduced scale was impact driven into a prepared sand bed in the flume test section. Water currents were employed to generate controlled scour processes around the monopile, eroding the soil in a manner representative of that at full scale in the field. The effect of these scour erosion processes on the dynamic characteristics of the monopile-tower system was assessed through dynamic testing. The influence of pre-installed rock armour scour protection, and separate remedial rock fill and tyre-filled net systems, were also investigated. The test program generated a significant amount of data, which are collated and interpreted in this paper.

It is recognised that achieving similarity between field scale structures and laboratory scale models presents difficulties due to the competing scaling of the geometric, structural, and dynamic properties of the structure, soil, fluid, and body forces. Where possible the work described in this paper has adopted appropriate scaling of geometry, structural stiffness, and mass, but it is accepted that it was not possible to achieve scaling of factors such as the mass and stiffness/viscosity of the soil and water. The data therefore support a qualitative indication of the influence that scour and scour protection systems have on the dynamic characteristics of the full scale monopile - tower systems. They provide a basis for the calibration of new scalable design models that can be applied to predict the effects of scour and scour protection systems on the dynamic performance of full-scale structures. A preliminary design model for this purpose, based on the one dimensional (1D) finite element framework, is described in Mayall et al. (2019); the experimental data presented here will be used to inform future developments of this framework.

EXPERIMENTAL SETUP

The experiments employed a sand bed prepared within a 1.0m deep and 4.0m x 4.0m plan area sediment pit located inside the FFF flume, as illustrated in Fig. 2. Initially, a 75mm thick gravel layer and a distributed perforated pipe system and permeable geotextile membrane cover were placed in the pit to provide controlled saturation and drainage. The sand bed was then built up with a fine silica sand (Bathgate psf) in 50mm thick layers using a 26kg plate compactor. Physical properties of the Bathgate sand employed in the tests are listed in Table 1.

Steel retaining beams of 100mm height, spanning across the flume width, were used to extend the height of the sand bed up to 0.7m above the flume base. A sand slope of 1:3 gradient was placed outside of the retaining steel beams to provide fairing to the flow entering and exiting the test area. Once the sand bed had been prepared, it was saturated via the distributed pipe system at a gradual rate to minimise the risk of piping.

A gloss-painted glass fibre reinforced plastic (GFRP) tube and aluminium tube were used to construct the monopile and tower sections respectively. The geometry and properties of the tube sections are listed in Table 2. The GFRP monopile was produced by CompoTech and the longitudinal modulus and shear modulus were calculated using classical lamination theory. A stiff aluminium transition piece of 0.2m length, mounted within the top of the GFRP tube, was used to provide a rigid connection between the foundation and tower. A set of brass discs were mounted on the top of the tower to represent the mass of the rotor-nacelle assembly. The number N_M of brass discs employed in the tests was varied to allow the influence of the top mass on the system dynamics to be investigated. The geometry and material of the monopile - tower structure were carefully selected to ensure similar physical behaviour to full scale structures using the dimensionless groups described in Table 3. The dimensionless properties were compared against two datasets for full scale structures; (i) Robin Rigg offshore wind farm in the UK (data supplied by E.On Energy), and (ii) using wind turbine parameters compiled by Arany et al. (2016) for ten offshore wind farms across the Netherlands, Belgium and UK. Further detail on the typical loading and structural natural frequencies of varied scale offshore wind turbines can also be found in Arany et al. (2016).

Dynamic tests were conducted by exciting the structure with a finger tap on the tower at z = 5.47m, above the pile tip. The applied force was measured using a PCB Piezotronics 208C01 type IEPE force sensor. The response of the structure was measured in the streamwise and crossflow directions at six positions along the tower using twelve PCB Piezotronics 333B50 type IEPE uniaxial accelerometers. The accelerometers were

mounted on cruciform brackets inside the tower section (see Mayall et al., 2018). All test control and data acquisition processes were carried out using National Instruments compact DAQ instrumentation. The masses and locations of the peripheral pile/tower assembly components, including the force sensor and accelerometers are listed in Table 4.

TEST MATRIX

Six tests were performed to explore the influence of various global scour, local scour and scour protection systems on the dynamic characteristics of the model monopile – tower system. Table 5 lists these tests, including the target depths of local and global scour and the generic forms of the scour protection systems that were applied. The scour depths actually achieved in the tests varied from these targets, and is discussed later in the paper. The following common routine was adopted for the testing programme:

1. Prepare sand bed.
2. Conduct cone penetrometer tests.
3. Install preventative scour protection (Test 5 only).
4. Fill flume to target water depth.
5. Drive pile to target depth.
6. Develop local scour via two-way water flow.
7. Install remedial scour protection (Tests 2,3,4,6 only).
8. Develop global scour by incremental removal of steel retaining beams and two-directional water flow.
9. Conduct lateral monotonic loading test (outside scope of current paper).
10. Drain flume
11. Inspect the scour protection condition (Tests 2 to 6)

Test 1 did not employ a scour protection system; it therefore provided a scour-only reference case.

SAND BED CHARACTERISATION

Cone penetrometer testing

Cone penetrometer tests (CPT) were conducted on the prepared sand bed, at the centre of the pile installation location, after the sand had been saturated. This provided a check on the repeatability of the bed preparation process as well as data to support future modelling exercises. A cone 8 mm in diameter with 60° angle cone tip was employed, with load measurements at the cone tip and the jacking point. The rate of cone advance was 4 mm/s. Fig. 3(a) shows the depth variation of the measured cone end bearing, q_c for all of the

tests. A separate calibration exercise was conducted using samples of saturated Bathgate sand at known relative density D_R to obtain the correlation (based on a previously-suggested form e.g. Jamiolkowski et al., 1985):

$$D_R\ [\%] = -37.53 + 23.97 \ln \frac{\left(q_c/p_{ref}\right)}{\left(\sigma_v'/p_{ref}\right)^{0.5}} \quad (1)$$

where the reference stress is p_{ref} = 100 kPa and σ_v' is the initial vertical effective stress in the soil at the level of the cone tip.

The variation of relative density with depth for each test, on the basis of the correlation in Equation (1), is plotted in Fig. 3(b), which can be applied within numerical and design methodologies, such as the PISA design model (Burd et al., 2019).

Small strain shear modulus

The initial lateral resistance of the pile is likely to be highly dependent on the shear stiffness of the soil. Various published correlations between CPT end bearing and small strain stiffness can be chosen (e.g. Rix and Stokoe, 1991; Baldi et al., 1989), which result in significant variance in the derived stiffness. In order to address this uncertainty, data on small strain shear modulus (G_0) were measured in bender element and resonant column tests of known relative density (Table 6) performed by Fugro, Wallingford, UK.

G_0 was measured in the bender element tests for isotropic stress conditions at values of mean effective stress, p', in the range 5 kPa to 50 kPa, and in the resonant column tests at mean effective stresses of between 10 kPa and 50 kPa. Data are shown in Fig. 4. It is clear that G_0 increases significantly with stress level; there is also a small apparent dependency on relative density.

These shear modulus data can be represented to a reasonable accuracy using $B = 478$ in the Hardin and Richart (1963) correlation,

$$G_0 = \frac{B p_{ref}}{0.3 + 0.7e^2}\left(\frac{p'}{p_{ref}}\right)^{0.5} \quad (2)$$

where p' is mean effective stress and p_{ref} = 100 kPa. This correlation is indicated on Fig. 4 and the inferred variance of small strain stiffness for the tests are shown in Fig. 3(c), where it has been assumed that the mean effective stress can be approximated by the vertical effective stress (i.e. K_0 = 1). Little difference is observed between the small strain stiffness profiles for each test, with Test 1 presenting the lowest cone tip resistance and resulting stiffness, likely due to small variations in the bed preparation process. However, the

analysis of measured natural frequency (see Fig. 13) does not indicate any subsequent influence and the repeatability of the sand bed preparation is therefore considered sufficiently consistent.

It is recognised that the pile driving process is likely to result in changes to the soil stresses and density local to the pile, and the resulting soil stiffness (Jardine et al., 2005). However, further research is required to assess the lateral extent of these changes and their impact on the small strain behaviour of monopiles under dynamic loading.

Soil friction angle

Triaxial compression tests were conducted in undrained conditions on BE1 and drained conditions on BE2, see Table 6. The critical state triaxial compression friction angle was determined as 34.3^{o} from these tests.

FOUNDATION INSTALLATION

The fully assembled monopile and tower was impact driven into the prepared sand bed to a tipping depth of $3D$ above the sand bed base (H_B = 600mm in Fig. 2) using a 7.75kg annular drop weight applied to a polyethylene cushion on top of the monopile. The selected drop weight and height was found to achieve a penetration rate of at least 0.25 mm per blow during trials performed prior to the FFF experiment campaign. The soil plug length z_{plug} was measured by a plumb line lowered through a hole in the transition piece. The total driving energy was calculated as the product of the hammer weight, hammer stroke, and number of blows.

Fig. 5 shows the cumulative number of blows, hammer drop heights, and driving energy applied during installation; Table 7 lists the length of the soil plug at the end of driving for each test. In all cases there was drawdown of the soil inside the pile. The increased blow count and associated total energy for Test 2 resulted in a refinement of the strategy for the driving of subsequent tests, to move to longer hammer strokes at lower blow counts, resulting in the consistent profiles of blow count and driving energy for subsequent tests. In Test 3 it was found that the pile had twisted during driving and was misaligned by 7° anticlockwise (viewed from above) about the vertical axis at the end of driving.

FLOW REGIME FOR SCOURING

An approximately square wave pattern of reversing flow was used to simulate a tidal current for the development of local and global scour, as illustrated in Fig. 6. Current speeds were selected on the basis of sediment transport scaling, to represent live-bed conditions in the field (i.e. where sediment transport occurs

generally across the seabed). The FFF allows recirculation of suspended sediments to allow representative modelling of live bed conditions, including a replenishing upstream sediment supply. Depth averaged current velocities ($\overline{U}$), measured using an acoustic Doppler current profiler, exceeded the critical threshold of sediment motion ($\overline{U}_{crit}$) of 0.3 m/s, calculated using Equation 3 (Soulsby, 1997).

$$\overline{U}_{crit} = 7\left(\frac{h_w}{d_{50}}\right)^{\frac{1}{7}}\left[g(G_s-1)d_{50}f(D_*)\right]^{1/2} \quad \text{For } D_* > 0.1 \qquad (3)$$

$$f(D_*) = \frac{0.30}{1+1.2D_*} + 0.055[1-\exp(-0.02D_*)]$$

$$D_* = \left[\frac{g(G_s-1)}{\nu^2}\right]^{\frac{1}{3}} d_{50}$$

where ν is the kinematic viscosity of fresh water used in testing, assumed to be 1.23x10^{-6} m^2/s for 12°C.

The adopted phases of flow are listed in Table 8. Phase 1 indicates the conditions employed to develop local scour, and Phase 2 specifies the flow processes employed to develop global scour. The morphodynamics for Phase 1 was selected using local scour prediction methods (Whitehouse, 1998). Phase 2 was designed on the basis of sediment transport considerations (Soulsby, 1997) both to increase the overall sediment transport rate in the test section and to generate bed lowering through net loss from the test section.

LOCAL AND GLOBAL SCOUR ANALYSIS

The bathymetry local to the pile and scour hole was measured periodically during the tests using an underwater laser scanner (ULS), with a typical spatial resolution of approximately 0.001 – 0.003m. The scanner was mounted on a traverser located at y = 0.3m, see Fig. 7(a). Fig. 7(a) also shows a typical plan layout of bathymetry obtained from the ULS system.

The local bed level, (i.e. the level adjacent to the pile), used to define the total scour depth S_T, was determined as the median of the data for 0.5 ≤ r/D ≤ 0.75, where r is radial distance from the pile centre. The global bed level, used to establish the global scour depth S_G, was determined as the median of the data for 4.5 ≤ r/D ≤ 7.5, as shown in Fig. 7(b). To account for shadowing effects of the pile on the ULS measurements, only data for $y \geq 0$ were considered. Symmetry of the bed levels about $y = 0$ was assumed for the median and percentile calculations described later. Based on the bathymetry comparison for y ≥ 0 and y ≤ 0 on Fig. 7(a) this is shown to be a reasonable assumption. Scour depths were determined relative to the global bed level at the start of each test.

The scour depths for each test, determined using the procedures outline above, are listed in Table 9. These data are presented in terms of total scour and global scour (rather than local scour) since total scour is measured more directly than local scour. The local scouring process produced repeatable results in terms of depth of fully-formed local scour holes (Tests 1, 2, 3, and 6). It is noted that the Phase 1 flow process induced a small amount of unintended global scour as indicated in the table. The global scour depths achieved in the tests were significantly less than the target values (specified in Table 5 based on values observed in the field). The discrepancy between target and achieved global scour was due to the experimental difficulty in naturally removing sand from the test section by sediment transport. Since the tests were in the live bed regime there was loss of sediment at the test section as well as replenishment on reversing flow cycles.

The actual value of global scour achieved was greatest in Test 6 when, as noted below Table 8, the flow time series was modified to increase the lowering. In the earlier tests even though smaller than target global scour had been achieved it was important to keep a consistent approach so that the effects of other parameters could be evaluated. The obtained local and global scour provide sufficient range for the purpose of the current study.

INSTALLATION OF SCOUR PROTECTION SYSTEMS

Three types of scour protection system were investigated: pre-installed rock armour, remedial rock fill and remedial tyre-filled nets.

Fig. 8 illustrates the geometric definitions adopted to characterise these scour protection systems, including geometries before and after further scour erosion. Note that when scour protection is present, the total scour depth S_T is defined with respect to the level of the scour protection adjacent to the pile. This is in contrast to schemes for the case where scour protection is absent, illustrated in Fig. 1.

For Test 2 the configuration of the tyre-filled nets (TFNs) was specified to match that installed for five monopiles at Scroby Sands offshore wind farm in the UK (data provided by E.On Energy). Two rings of six tethered TFNs were lowered into position in the local scour hole Fig. 9(a). The TFNs consisted of nylon mesh bags filled with 50 rubber model truck tyres (Italeri 1:24 scale model 3889 truck rubber tyres, G_S = 1.2, outside diameter = 42mm, inside diameter = 26mm, tread width = 11mm, wall thickness = 1mm).

The selected scour protection rock material consisted of an angular narrow-graded limestone gravel of median diameter d_{50} = 18.3mm with G_S = 2.8 (re-analysed since Mayall et al., 2019); the density of the rock is similar to the 'normal' density rock used offshore and sometimes 'high' density rock is used where G_S ~ 3, .

The rock scour protection grading curve was selected from those available for geometric similarity to that installed at selected full size structures at Robin Rigg offshore wind farm (data provided by E.On Energy); Fig. 10 presents a comparison of the full scale and experiment scale rock grading curves.

For Tests 3, 4 and 6, the limestone gravel (representing rock fill material for scour protection) was placed underwater using an inclined fall pipe as shown in Fig. 9(b), with its opening located close to the surface of the scour hole to facilitate placement accuracy. The fall pipe simulates rock installation in the field and removes the risk of any operator induced bed disturbance which would change the stress field. From observations during rock installation the rocks embedded about 20% of their diameter in the sand bed and the target thickness of rockfill was between 2/3 and 3/4 of the local scour hole depth.

For Test 5, the limestone gravel was placed immediately following the bed preparation using a template with geometry defined in Fig. 8(a) and edge slope of rock 1V:3H. This was intended to represent a pre-installed scour protection configuration. Fig. 9(c) shows the pre-installed rock after placement. A thin steel retaining collar was used for Test 5 only to create a small annular space between the rock and pile wall and hence prevent damage to the pile during driving; the collar was removed prior to flow Phase 1.

Table 10 lists the installed characteristics of the scour protection system employed for each test. The width b (Fig. 8) was estimated from the post-installation bathymetry plots. The in-place dry density of the scour protection material ρ_d was calculated using the installed mass of material and the volume of the scour protection material determined from the bathymetry measurements. The bulk voids ratio *e* and porosity n for the scour protection material were calculated from the dry densities using standard methods (e.g. Craig, 1992). The installed scour protection material has a lower density and higher voids ratio than the original sand that has been scoured.

STRUCTURAL DYNAMICS MEASUREMENTS

Measurements of the dynamic response of the monopile - tower system were conducted during scheduled pauses in the flume flow (i.e. with standing water), concurrent with bathymetry measurements. In the pause periods the number of top masses was varied. After each change the structure was excited with a finger tap impulse applied to the mounted force sensor (close to the tower top), with signals allowed to decay naturally. Data were sampled at a frequency of 3012Hz logged for 32s periods.

Fig. 11 shows a typical measured acceleration signal and the corresponding power spectral density (PSD); this indicates first, second and third mode peaks in PSD at frequencies of 6.6, 19.7 and 48.6Hz; these peaks are close to but not identical to the natural frequencies due to the influence of damping. For

each test a minimum of three impulses were logged in each of the streamwise (x-axis) and spanwise (y-axis) directions.

Values of the first three natural frequencies and corresponding mode shapes and modal damping ratios, were determined from the measured acceleration time series starting 0.5s after the peak measured force. It was assumed that the modes were uncoupled, and that each mode could therefore be considered as a single degree of freedom system:

$$\ddot{v}_m(t) + 2\zeta_m\omega_{n,m}\dot{v}_m(t) + \omega_{n,m}^2 v_m(t) = 0 \quad (4)$$

where $v(t)$ is the displacement at an arbitrary point on the tower, $\omega_{n,m}$ and ζ_m are circular natural frequency and damping ratio respectively for the m^{th} mode.

For damped free vibration, the solution for the displacement is

$$v_m(t) = v_{0,m}e^{-\zeta\omega_{n,m}t}\sin(\omega_{n,m}\sqrt{1-\zeta_m^2}\,t + \phi_m) \quad (5)$$

where $v_{0,m}$ is a constant (that depends on the initial conditions), and ϕ_m is a phase angle.

The data were initially smoothed to remove high frequency noise, using a moving average method with window length of 30, and linear trends were removed. Values of $\omega_{n,1}$ and ζ_1 were then determined by fitting the model in Equation (5), by least squares, to each accelerometer data, adopting sample lengths of approximately 20 cycles. Values of $\omega_{n,1}$, ζ_1 and $\phi_1$were common, whilst v_1 varied between accelerometers. The distribution of v_1 along the tower was used to determine the mode shape. Moving average filters were more consistent in fitting results to Equation (5), (when compared to alternatives, such as Savitzky-Golay filters) and were selected as the preferred approach.

After fitting the first mode, the residual acceleration signals were calculated by subtracting the first mode signal estimated from the model, and further linear detrending. A similar fitting process to that adopted for the first mode was then conducted on the residual accelerations to determine ($\omega_{n,2}$, ζ_2). The process was then repeated to determine the third mode data ($\omega_{n,3}$, ζ_3). Example data obtained from this procedure are shown in Fig. 12 in terms of natural frequency $f_{n,m}$, where $f_{n,m} = \omega_{n,m}/2\pi$. The mode shapes are presented using the normalisation $V_0/|V_0|_{max}$ as indicated in Fig. 12(d), this is the accepted method of presenting mode shapes in modal analyses (for the example shown in Fig. 12(d), in the case of modes 1 and 2 $|V_0|_{max}$ occurs at the same location z = 5.5 m, in the case of mode 3 this is at a different location z = 3.6 m).

For each top mass and vibration mode, the natural frequency was inferred as the mean fitted value across multiple impulse taps from both streamwise and spanwise directions. The inferred natural frequency and damping ratio of the first, second and third modes are plotted in Fig. 13 at the start of each test (un-

scoured conditions) for all values of top mass M_{Top} (Table 4) where M_{Top} includes the brass top mass discs, force sensors and mounting.

Fig. 13 shows that, as expected, there is a tendency for the natural frequencies to reduce with increased top mass. This effect is particularly marked for the first mode. Data for the second and, to a lesser extent the third mode, exhibit a certain amount of variability. This is a likely indication that these modes are especially sensitive to the soil conditions such that minor difference in the stiffness of the prepared sand bed have a significant effect on the natural frequencies. Test 5 has the pre-installed rock armour scour protection and Test 6 has a larger initial pile embedment.

EXPERIMENTAL RESULTS

Unremediated scour development; Test 1

Fig. 14(a) shows the measured global and local levels throughout Test 1 (in which scour protection systems were absent). During flow Phase 1 a significant amount of local scour, accompanied by some unplanned global scour, develops. In Phase 2, the global scour is seen to continue. A small rise in the local scour level is apparent at T_f = 25 hours suggesting that the scour hole had been partially backfilled by deposited sand, presumably caused by a sand wave moving through the test area during the global lowering process.

Changes in the inferred first three natural frequencies (relative to the un-scoured conditions) are plotted in Fig. 14(b). It is interesting to note that the second mode natural frequencies exhibits the greatest sensitivity to local scour; indeed the rise in the local scour level at T_f = 25 hours is concurrent with a peak in the second mode natural frequency.

Remedial tyre-filled net scour protection; Test 2 (R-TFN)

The variations of bathymetry and natural frequency during Test 2, in which tyre-filled nets were installed in a fully-developed local scour hole, are shown in Fig. 15. The natural frequencies show negligible change when the tyre-filled nets were initially placed, shown in Fig. 16 for the first mode. This is attributed to the low stiffness and bulk density of the tyre-filled nets relative to the undisturbed sand.

The variability of local bed level measurements immediately after installing the tyre-filled nets (5th and 95th centiles) is greater than that seen in rock fill remedial scour protection tests (discussed in subsequent sections). This is due to the presence of gaps between the nets and varying levels of the nets around the pile. The local levels reduced by about 0.5D in the global scour flow phases; this is associated with settlement and deformation of the tyre-filled nets. During these global scour phases there was no significant

further local scour compared with Test 1, and the natural frequencies remained relatively unchanged. Examination of the tyre-filled nets at the end of the test indicated that sand had accumulated in them to various degrees, with some nets sitting on the soil surface, some partially buried, and some fully buried, as shown in Fig. 17.

Remedial rock fill scour protection; Tests 3 (R-RF1), 4 (R-RF2) and 6 (R-RF3);

Remedial scour protection in the form of rock fill in the locally scoured hole was installed in three tests. In Tests 3 and 6, rock was installed in a fully-formed scour hole. In Test 4 rock was installed in a partially-formed scour hole, resulting in a thinner deposit of rock.

Fig. 18(a),(c)&(e) show the measured local and global bathymetry during the three tests. The first three natural frequencies generally show a step increase after installing scour protection (Fig. 18(b),(d)&(f)), with a small relative change observed for Test 4 (R-RF2), in which the remediation of a shallower scour hole has less influence on the natural frequency recovery. The frequencies corresponding to the equivalent embedment in undisturbed sand were not fully recovered, shown in Fig. 19 for the first mode. Fig. 20 shows excavated cross-sections through the scour protection material at the end of each test. These excavations were performed after the pile had been subjected to monotonic loading to failure; the pile is therefore displaced from the original position.

During the global scour phases in Tests 3 and 6, the local bed level remained stable. In Test 3 and 6 the natural frequencies increased in the initial global scour phases ($8 < T_f < 25$), and approach the natural frequencies of the equivalent scour depths during local scouring Fig. 19(a & c). This rise in natural frequency is considered to be due to sand accretion in the rock matrix. Fig. 20(a & c) show that at the end of the tests the rock matrix is seen to be packed with sand. The process by which this sand accretion occurs was not directly observed during the tests.

Continued flow in Phase 2 of Tests 3 and 6 induced further global scour and resulted in reducing natural frequencies. Since the local bed level was stable, this suggests that changing surcharge from the global bed level has influenced the scour protection stiffness contribution.

In Test 4, where scour protection was placed in a partially-formed scour hole, the local pile embedment gradually reduced during global scour flow phases as the scour protection material was consumed by formation of a falling apron, and the rock level at the pile wall was lowered as shown in Fig. 18(c) and observed in the excavations in Fig. 20(b). This loss of support around the pile caused a reduction in the natural frequencies shown in Fig. 18(d).

Considerable accretion of sand in the rock matrix was observed in all cases (Fig. 20). This infilling may be due to the combined effects of deposition at the ground surface and from suction scour of the sand beneath the scour protection. However, the base of the scour protection material in excavations of Tests 3 and 6 was observed to be unchanged since installing the rock, suggesting sand deposition due to the high sediment supply in the live-bed test conditions was the dominant process (supported by results of An et al., 2014).

It was observed in all cases that sand accretion did not occur in the rock material close to the pile wall near the surface. This local absence of accreted sand, apparent in all of the images in Fig. 20, is considered to be due to local horseshoe vortex action around the base of the pile.

Falling aprons of scour protection material were observed in Tests 4 and 6, indicating a dominant erosion of the underlying sand at the periphery of the scour protection. The falling aprons were typically one to three stones in thickness; the edges of the scour protection material and the falling aprons were partially buried by sand bedforms. The thickness of the scour protection layers was predominantly maintained throughout the global scouring stages of Test 3, as shown in Fig. 21. However, the development of significant falling aprons and the transport of rock away from the pile resulted in reductions in scour protection thickness for Tests 4 and 6, most significantly for the partially filled scour hole of Test 4.

Excavations following Test 4 indicated that the base of the scour protection layer had lowered by $0.46D$, and the thickness of scour protection material at the pile wall had reduced by 39%. It is possible that suction scour may have caused settlement of the scour protection in Test 4, after most of the rock had been depleted by formation of the falling apron.

Pre-installed rock armour scour protection; Test 5 (P-RA)

During the flow cycles that followed the pre-installation of rock scour protection (Test 5) there was negligible change in the bathymetry levels close to the pile wall at all test stages, as shown in Fig. 22(a). However, a moderate increase in the natural frequencies is observed in Fig. 22(b). indicating some stiffening of the soil-structure interaction, possibly due to the effect of sand accretion in the scour protection layer. Following the global scour phases, a falling apron developed at the toe of the scour protection, and rock infilled with sand was observed during excavation at the end of the test shown in Fig. 23. Similar to Tests 3, 4 and 6 excavations (Fig. 20) a zone of rock near the pile wall remained clear of sand. In the current case, the competing effects of the sand accretion and falling apron formation appear to have a net effect of marginally increasing the natural frequencies.

At the end of the test a small depression was observed in the level of scour protection close to the pile wall (Fig. 23). This feature appears to relate to pile installation processes rather than being caused by scour.

DISCUSSION

An experimental campaign is described in which the influence of scour erosion, and scour protection systems, on the dynamic characteristics of a reduced-scale monopile-wind turbine support system is investigated. Scour processes were modelled by conducting the tests in a flume, employing two-way flow to represent tidal cycles and live-bed scour, where global scour development was initiated mid flume test. A consequence of this approach (instead of alternative procedures in which scoured bed profiles are formed artificially) was that the scoured bed profiles exhibited considerable spatial variability (as it would in reality). The complexity of the bathymetry data necessitated a detailed and careful analysis to infer appropriate characteristic dimensions for the scoured seabed, to support an analysis of the dynamic test results.

Since the global scour is created by flow during the test (rather than by an initial unstable condition, e.g. in Riezebos et al., 2016) the current experiments are considered to incorporate a degree of realism that is absent in alternative experimental approaches involving artificial seabed and scour protection profiles. The 'live bed' conditions employed in the tests induced various complex interactions involving the accretion of sand in the scour protection systems and 'falling apron' deformations of rock scour protection material. These interactions are consistent with other laboratory studies (Arboleda Chavez et al., 2019 and Riezebos et al., 2016) and presumed to be representative of field conditions. Field data presented by Hucker et al. (2019) shows natural frequency increases over time for wind turbines with scour protection installed in mobile sandy seabeds potentially due to settlement and densification of the scour protection and, in our view, sediment accretion.

Tests conducted for cases where scour protection systems were absent allowed the influence of scour processes on the dynamic performance of the system to be observed in isolation. Scour processes were observed to significantly reduce the first three natural frequencies of the monopile-tower system. Reductions in the first natural frequency have a particular practical significance for working wind turbine structures, because of concerns that excessive accumulation of fatigue damage might occur if the first natural frequency were to drift into the turbine rotor frequency band. The results demonstrate that the second natural frequency is especially sensitive to scour effects, which is broadly in agreement with published numerical studies (e.g. Zaaijer, 2006; Sørensen and Ibsen, 2013). This feature is likely due to the mode shape for this mode, in which relatively large amplitudes occur at bed level. For working wind turbine support structures,

measurements of the second natural frequency are likely to provide a particularly sensitive indication of the presence of scour.

The scour-only tests confirm that scour processes invariably cause significant reductions in the stiffness of the foundation (as indicated by the lowering of the natural frequencies). Two distinct mechanisms are considered to occur; (A) scour processes remove soil that would otherwise contribute lateral stiffness to the pile hence increasing the free length; and (B) scour processes reduce the effective stresses in the remaining soil adjacent to the pile due to loss of overburden. Since the stiffness (small strain shear modulus) of the sand is known to depend on the magnitude of the *in situ* stresses, the loss of overburden in Mechanism B causes the stiffness of the soil adjacent to the pile to reduce. Scour protection systems (when present) are considered to modify the dynamic characteristics of the system by reversing these two detrimental mechanisms. Effective reversal of Mechanism A requires that scour protection systems are stiff and well-compacted against the monopile. The reversal of Mechanism B relies only on the surcharge applied by the scour protection material.

The installation of remedial rock fill scour protection was found to increase the natural frequencies, although the magnitude of the effect was variable. In all cases the installation of rock fill did not restore the natural frequencies to values corresponding to an equivalent additional pile embedment in undisturbed sand. Although it can be confidently assumed that the additional surcharge provided by the rock will have contributed to additional foundation stiffness via the reversal of Mechanism B, the effectiveness of the direct stiffness contribution (reversal of Mechanism A) is in this case uncertain. It is considered likely that the direct stiffness contribution is relatively modest in the current experiments since – following normal practice in the field – no attempt was made to compact the rock against the pile. A smaller diameter rock (d_{50}/D ~ 0.05) with high density may be beneficial for Mechanism B (not explored in these tests).

There was an observed tendency in some cases for the natural frequencies to increase slightly after the rock fill material had been placed and further flow cycles had been conducted. It is considered that this effect is a consequence of the sand accretion within the rock material that was invariably observed at the end of each test. This accreted sand is likely to have (i) slightly increased the local surcharge and (ii) developed a stiffer interface between the rock material and the pile by the filling of voids. Sand accretion in rock berms has previously been observed in the laboratory by An et al. (2014) but it is believed that the current tests provide the first published observation of this mechanism in connection with scour protection systems for monopile foundations. The role of suction scour has been assessed in the current tests on the basis of the

results of An et al. (2014, Figure 5) which delimits when suction is in operation. The sediment ratio d_{50}(sand)/d_{50}(rock) = 0.161 mm/18.3 mm = 8.8 10^{-3} and the bed mobility θ is estimated at 0.33 for the global scour phase of the current tests. When plotted on the diagram of An et al. we are in the 'no motion' region of the diagram and hence suction scour is ruled out.

The effectiveness of the remedial rock fill scour protection configuration, in terms of the influence of further global scouring, depended on the installed thickness. For thin layers of limited extent, subsequent global scouring caused substantial further reductions in the observed natural frequencies. This is considered to be associated with the 'falling apron' mechanism that was observed in the tests. More substantial rock fill layers with further recovery of the foundation stiffness (presumably due to the additional effects of sand accretion) also had the potential for reductions in natural frequency during subsequent global scouring.

Tyre-filled net remedial scour protection was shown to provide relatively small increases in both foundation stiffness and subsequent recovery with sand accretion. It appears that the relatively lightweight low stiffness nature of this system does not reverse Mechanisms A and B in any significant way. However, the tyre-filled nets were shown to be successful in achieving a stable local bed level, thereby maintaining the dynamic characteristics of the structure against further erosion.

Pre-installed rock armour scour protection was shown to provide significant protection from local and global scouring. Some increase in the natural frequency of the structure was observed, attributed to sand accretion within the rock matrix during flow cycles.

CONCLUSIONS

Analysis of the structural dynamics of a scaled wind turbine monopile-tower system exposed to local and global scour, and scour remediation, in large-scale laboratory tests has demonstrated the changes that can occur in the first three natural frequencies. The mode 1 frequency is especially sensitive to tower top mass and the mode 2 frequency is most sensitive to scour effects.

The results of this study inform the site by site assessment and modelling of scour effects and their impact on structural performance. The main conclusions are:

(1) Pre-installed scour protection systems have the principal purpose of preventing local erosion around the monopile. Pre-installed rock – intended to mimic typical systems employed in practice – was shown to provide effective protection in the current tests.

(2) Remedial scour protection systems typically have the dual purpose of preventing further erosion and restoring the dynamic characteristics of the system to acceptable levels. The current experiments

demonstrate that the effectiveness of remedial scour protection systems in controlling further erosion is variable. Relatively thick rock fill layers are shown to be effective; tyre-filled nets also demonstrated a significant erosion control capability. None of the remedial configurations that were tested, however, provided a wholly effective means of restoring the system dynamics. The rock fill material provided some stiffness recovery, but the rock appears to have been deposited in a loose state with the consequence that the stiffness of the deposited material is lower than that of the *in situ* sand. The stiffness contribution of tyre-filled nets was observed to be low.

(3) The test results imply the following tentative conclusions for full-scale structures:

(i) Employing pre-installed scour protection is likely to be a more effective way of controlling scour processes than by managing the erosion via post-construction remedial scour protection measures.

(ii) Tyre-filled nets provide an effective means of slowing the erosion processes although they are otherwise ineffective in improving the system dynamics.

(iii) Rock fill remedial scour protection is effective in both arresting further scour and adding stiffness to the system, although a sufficiently large volume of material needs to be installed for these two actions to be effective. The benefit of installing high density rock (not tested) in adding stiffness to the system could be considered.

(iv) Sand accretion within the scour protection systems can provide a useful enhancement of performance in terms of system dynamics. However, with no known published excavations of offshore scour protection systems known to the authors, it is unclear to what extent this sand accretion would occur in the field and therefore what potential stiffness increases might be expected. There may be scope to specify the grading of scour protection systems to maximise the effectiveness of the sand accretion mechanism.

ACKNOWLEDGEMENTS

This research project is supported through funding from E.On Climate and Renewables (recently renamed to RWE Renewables) and HR Wallingford, and by grant EP/L016303/1 for Cranfield University, the University of Oxford and Strathclyde University, Centre for Doctoral Training in Renewable Energy Marine Structures - REMS (http://www.rems-cdt.ac.uk/) from the UK Engineering and Physical Sciences Research Council (EPSRC). Byrne is supported by the Royal Academy of Engineering under the Research Chairs and Senior Research Fellowships scheme.

The Authors gratefully acknowledge the work of team members at HR Wallingford, E.On and Oxford University, who aided in the implementation and execution of the testing program. In addition, the Authors gratefully acknowledge Fugro for triaxial testing performed as input to the soil characterisation for the experiments.

DATA AVAILABILITY

The following data are available on request from ross.mcadam@eng.ox.ac.uk: detail of model monopile – tower system, soil characterisation results, bathymetry results, natural frequency results.

NOTATION LIST

The following symbols are used in this paper:

A = Cross-sectional area;

b = Scour protection width;

B = Small strain shear modulus coefficient;

d_{xx} = Sand particle diameter coefficient (xx^{th} percentile);

D = Pile diameter;

D_R = Sand relative density;

e = Soil voids ratio;

E = Young's modulus;

EI = Flexural stiffness;

$f_{n,m}$ = Natural frequency for mode m;

G_0 = Soil small strain shear modulus;

G_S = Soil specific gravity;

h_w = Water depth;

H_B = Depth of sand below pile tip;

L = Pile embedment length;

L_X = Geometric length (of structure component X);

M = Bending moment;

M_{Top} = Structure top mass;

n = Soil porosity;

N_{cyc} = Number of flow cycles;

N_M = Number of top masses;

p' = Mean effective stress;

p_{ref} = Reference stress;

q_c = CPT bearing stress;

r = Radial distance from pile centerline;

S_G = Global scour bathymetry reduction;

S_L = Local scour bathymetry reduction;

S_T = Total scour bathymetry reduction;

t_w = Pile wall thickness;

t_{sp} = Scour protection thickness adjacent to the pile wall;

T_f = Elapsed flow time;

$\overline{U}$ = Depth averaged flow velocity;

v = Displacement;

x = Coordinate in the streamwise direction;

y = Coordinate in the spanwise direction;

z = Distance above pile toe;

γ = Soil unit weight;

$\omega_{n,m}$ = Circular natural frequency for mode m;

ζ_m = Damping ratio for mode m;

ϕ_m = Phase angle for mode m;

ρ = Material density;

ρ_w = Water density, assumed 1000 kg.m^{-3};

σ_v' = Soil effective vertical stress;

ν = Kinematic viscosity of water;

REFERENCES

Abadie, C.N., Byrne, B.W. and Levy-Paing, S. (2015). “Model pile response to multi-amplitude cyclic lateral loading in cohesionless soils”. In: International Symposium on Frontiers in Offshore Geotechnics, 2015-6-10 to 2015-6-12, ISFOG, Oslo, Norway pp. 681-686.

An, H., Cheng, L., Luo, L., Draper, S., White, D. and Jas, E. (2014). "Effect of sediment supply on suction scour under a rock berm". In Proceedings of the 7th International Conference on Scour and Erosion, ICSE 2014. vol. 1, Taylor & Francis, London, UK, pp. 265 - 273, 7th International Conference on Scour and Erosion, Perth, Australia, 2/12/14.

API (2011). RP 2GEO - Recommended Practice for Geotechnical Foundation Design Consideration. Washington: American Petroleum Institute.

Arany, L., Bhattacharya, S., Macdonald, J.H. and Hogan, S.J. (2016). "Closed form solution of Eigen frequency of monopile supported offshore wind turbines in deeper waters incorporating stiffness of substructure and SSI". Soil Dynamics and Earthquake Engineering, 83, pp.18-32.

Arboleda Chavez, C., Stratigaki, V., Wu, M., Troch, P., Schendel, A., Welzel, M., Villanueva, R., Schlurmann, T., De Vos, L., Kisacik, D., Taveira Pinto, F., Ferradosa, T., Santos, P.R., Baelus, L., Szengel, V., Bolle, A., Whitehouse, R. and Todd, D. (2019). "Large scale experiments to improve monopile scour protection design adapted to climate change – The PROTEUS project." Energies 2019, 12(9), 1709; https://doi.org/10.3390/en12091709

Baldi, G., Bellotti, R., Ghionna, V.N., Jamiolkowski, M. and Lo Presti, D.C.F., (1989), August. Modulus of sands from CPTs and DMTs. In Proc. 12th ICSMFE (Vol. 1, pp. 165-170).

Burd, H.J., Taborda, D.M.G. Zdravković, L. Abadie, C.N., Byrne, B.W., Houlsby, G.T., Gavin, K.G., Igoe, D.J.P., Jardine, R.J., Martin, C.M., McAdam, R.A., Pedro, A.M.G., and Potts, D.M. (2019). PISA Design Model for Monopiles for Offshore Wind Turbines: Application to a Marine Sand. Geotechnique doi.org/10.1680/jgeot.18.P.277

Craig, R.F. (1992). Craig's Soil Mechanics. London, Spon Press.

De Vos, L., De Rouck, J., Troch, P. and Frigaard, P. (2011). "Empirical design of scour protections around monopile foundations Part 1: Static approach". Coastal Engineering 58 540-553.

DNVGL (2016). Standard DNVGL-ST-0126, Support structures for wind turbines, Edition April 2016.

Hardin, B.O., and Richart Jr, F.E. (1963). "Elastic wave velocities in granular soils". Journal of Soil Mechanics & Foundations Div, 89 (Proc. Paper 3407).

Hucker, N., Ward, I. and Manceau, S. (2019). "Measured changes in the natural frequency of offshore wind turbines with monopile foundations". Proceedings SECED 2019 Conference, 9-10 September 2019, Greenwich, London.

Jamiolkowski, M., Ladd, C.C., Germaine, J.T. and Lancelotta, R. (1985). “New developments in field and laboratory testing of soils. State-of-the-art report”. Proceedings of the 11th International Conference on Soil Mechanics and Foundation Engineering, San Francisco, 1, 57-153, Balkema Pub., Rotterdam.

Jardine, R.J., Chow, F.C., Overy, R. and Standing, J. R. (2005). “ICP design methods for driven piles in sands and clays”. Thomas Telford Ltd, London, p 105.

Mayall, R.O., Byrne, B.W., Burd, H.J., McAdam, R.A., Cassie, P. and Whitehouse, R.J.S. (2019), "Modelling of foundation response to scour and scour protection for offshore wind turbine structures", Scour and Erosion IX - Proceedings of the 9th International Conference on Scour and Erosion, ICSE 2018, pp. 405.

Mayall, R.O., McAdam, R.A., Byrne, B.W., Burd, H.J., Sheil, B.B., Cassie, P. and Whitehouse, R.J.S. (2018), "Experimental modelling of the effects of scour on offshore wind turbine monopile foundations", Physical Modelling in Geotechnics, pp. 725.

Petersen, T.U., Nielsen, A.W., Hansen, D.A., Pedersen, A.V., Christensen, E.D. and Fredsøe, J. (2019). “Stability of single-graded scour protection around a monopile in current”. Scour and Erosion IX - Proceedings of the 9th International Conference on Scour and Erosion, ICSE 2018, pp. 405.

Poulos, H. G. and Davis, E. H. (1980). Pile foundation analysis and design, John Wiley & Sons, New York.

Prendergast, L.J., Hester, D., Gavin, K. and O'Sullivan, J.J. (2013). "An investigation of the changes in the natural frequency of a pile affected by scour", Journal of Sound and Vibration, vol. 332, no. 25, pp. 6685-6702.

Prendergast, L.J., Gavin, K. and Doherty, P. (2015). "An investigation into the effect of scour on the natural frequency of an offshore wind turbine", Ocean Engineering, vol. 101, pp. 1-11.

Qi, W.G., Gao, F.P., Randolph, M.F. and Lehane, B.M. (2016). "Scour effects on p–y curves for shallowly embedded piles in sand", Geotechnique, vol. 66, no. 8, pp. 648-660.

Riezebos, H., Raaijmakers, T., Tönnies-Lohmann, A.,Waßmuth, S. and Van Steijn, P. (2016). “Scour protection design in highly morphodynamic environments”. In: ICSE 2016 (8th International Conference on Scour and Erosion), 12-15 September 2016, Oxford, UK. (2016)

Rix, G.J. and Stokoe, K.H. (1991), "Correlation of initial tangent modulus and cone penetration resistance", Huang, A.B. (Ed.), Calibration Chamber Testing: Proceedings of the First International Symposium on Calibration Chamber Testing ISOCCTI, Potsdam, New York, 28-29 June 1991, Elsevier Science Publishing Company, New York, pp. 351-362.

Sørensen, S.P.H. and Ibsen, L.B. (2013). "Assessment of foundation design for offshore monopiles unprotected against scour". Ocean Engineering 63 17-25.

Soulsby, R.L. (1997). Dynamics of marine sands, London: Thomas Telford.

Sumer, B.M, Christiansen, N. and Fredsøe, J. (1992). "Time scale of scour around a vertical pile". In: Proc. 2nd Int. Offshore and Polar Eng. Conf., ISOPE, San Francisco, USA, Vol. 3, pp. 308 – 315.

Whitehouse, R.J.S. (1998). Scour at marine structures, London. Thomas Telford.

Whitehouse, R.J.S., Harris, J.M., Sutherland, J. and Rees, J. (2011). "The nature of scour development and scour protection at offshore windfarm foundation". Marine Pollution Bulletin 62 73-88.

Whitehouse, R., Sutherland, J., Powell, K. and Harris, J. (2014). "Fast flow facility for sediment and morphology testing". In: Coastlab 14, 29 September – 2 October 2014, Varna, Bulgaria (eds. V. Penchev and F.T. Pinto), pp 104-113.

Zaaijer, M. B. (2006). "Foundation modelling to assess dynamic behaviour of offshore wind turbines". Applied Ocean Research, 28, 45–57.

TABLES

Table 1. Properties of Bathgate sand

d_{10} (mm)	d_{50} (mm)	d_{90} (mm)	G_s	e_{min}	e_{max}
0.077	0.161	0.282	2.65	0.502	0.753

Table 2. Pile and tower geometry and properties

Component	Material	Length (m)	Outer diameter D (m)	Wall thickness t_w (mm)	Longitudinal modulus E (GPa)	Density ρ (kg/m^3)
Monopile	GFRP	2.5	0.197	3.5	31.235	1855
Tower	Aluminium	3.2	0.1016	1.6	69	2700

Table 3. Monopile-tower structure dimensionless groups at full scale and experiment scale

Dimensionless group		Robin Rigg[a]	Arany et al. (2016) dataset	Experiment design
Pile slenderness	L/D	4.6 – 6.3	4.3 – 9.4	4.5 – 5.5
Pile wall thickness	D/t_w	57 – 96	50 – 106	56
Tower height	L_t/L_{pile}	1.09 – 1.24	0.74 – 1.73	1.2
Pile relative stiffness (Poulos & Davis, 1980; Abadie et al., 2015)	$E_p I_p/E_s L^4$	8E-4 – 5E-3	(not assessed)	2E-3 – 5E-3
Tower relative stiffness (Arany et al., 2016)	$E_t I_t/E_p I_p$	0.11 – 0.18	0.12 – 0.71	0.15
Mass ratio (Arany et al., 2016)	M_{Top}/M_t	1.0	0.5 – 1.3	0.04 – 1.6 (0.83 for N_M = 3)

Where: L_t is the tower length excluding the transition piece, $E_p I_p$ is the flexural stiffness of the monopile, E_s is a reference soil stiffness estimated at the pile tip using the relationship $E_s = 2(1+\nu)G_0$ where ν is the Poission's ratio (assumed as 0.5) and G_0 is the small strain shear modulus calculated using Equation (2), $E_t I_t$ is the average flexural stiffness of the tower, M_{Top} is the mass attached to the top of the tower, M_t is the mass of the tower excluding attachments

[a] Robin Rigg offshore wind farm data supplied by E.On Energy

Table 4. Mass and location of pile/tower assembly peripherals

Component	Height of centre of gravity above pile tip z (m)	Mass (kg)
Transition piece	2.38	2.83
Accelerometers and mounting	2.33, 2.83, 3.18, 3.53, 4.13, 5.38	0.07 (per height)
Force sensors and mounting	5.47	0.30
Top masses (N_M = 1)	5.49	1.11
Top masses (N_M = 3)	5.51	3.32
Top masses (N_M = 6)	5.54	6.64

Table 5. Test matrix and target scour depths

Test	Initial condition		Local scour phase	Global scour phase		
	Target pile embedment L/D	Target water depth h_w/D	Target local scour S_L/D	Target global scour S_L/D	Scour protection system	Target global scour S_G/D
1	4.5	4.5	1.5	0	None	1.5
2	4.5	4.5	1.5	0	Tyre-filled nets (remedial) (R-TFN)	1.5
3	4.5	4.5	1.5	0	Rock fill (remedial) (R-RF1)	1.5
4	4.5	4.5	0.75	0	Rock fill in partial scour hole (remedial) (R-RF2)	1.5
5	4.5	4.5	0.0	0	Pre-installed rock armour (P-RA)	1.5
6	5.5	3.5	1.5	0	Rock fill (remedial) (R-RF3)	2.5

Table 6. Small strain shear modulus tests

Test ID	Test Type	e	D_R [%]
BE1_Loose	Bender Element	0.665	35.1
BE2_Medium	Bender Element	0.599	61.3
BE3_Dense	Bender Element	0.531	88.5
RC1_Medium	Resonant Column	0.582	68.0

Table 7. Pile embedded lengths and plug lengths

Test	Installed embedded length L/D	Plug length z_{plug}/D
1	4.56	4.04
2	4.61	4.29
3	4.57	4.43
4	4.55	4.33
5	4.57	4.37
6	5.61	5.33

Table 8. Definition of flow regimes for scouring phases. N_{cyc} is the total number of symmetrical flow cycles employed

Phase	1a	1b	2a	2b	2c	2d[e]	2e[e]
$\overline{U}$ (m/s)	0.35[a]	0.55[b]	0.70	0.70	0.70	0.70	0.70
Flow time (mins)	166	332[c]	498	498	498	498	498
N_{cyc}	1	2[c]	3	2[d]	2	2	2
Scour type	Local	Local	Global	Global	Global	Global	Global
Target $\Delta S/D$	0.75	0.75	0.5	0.5	0.5	0.5	0.5

Exceptions:

[a] Test 1, Phase 1a: $\overline{U}$ = 0.40 m/s

[b] Test 6, Phase 1b: $\overline{U}$ = 0.50 m/s

[c] Test 4, Phase 1b: Flow time = 0, N_{cyc} = 0

[d] Test 3, Phase 2b: N_{cyc} = 3 repeating Phase 2a

[e] Phase 2d and 2e: Only used for Test 6, with a 3:1 asymmetry in the duration of forward flow to transport more sediment from test bed

Table 9. Overview of achieved scour depths

Test	After local scour development (End of flow Phase 1)		After global scour development (End of flow Phase 2)
	Total scour S_T/D	Global scour S_G/D	Global scour S_G/D
1	1.58	0.14	0.57
2 (TFN)	1.58	0.09	0.43
3 (R-RF1)	1.49	0.21	0.30
4 (R-RF2)	0.66	-0.02	0.36
5 (P-RA)	-	0.14	0.46
6 (R-RF3)	1.51	0.15	1.79

Table 10. In-place scour protection system characteristics

Test		Installed height at pile wall t_{sp}/D	Width b/D	Bulk unit weight γ (kN/m^3)	Bulk voids ratio e	Bulk porosity n
2 (R-TFN)	Tyre-filled nets	1.23	0.7	10.14	4.960	0.832
3 (R-RF1)	Rock fill	0.82	2.2	18.85	0.953	0.488
4 (R-RF2)	Rock fill in partial scour hole	0.54	1.1	18.99	0.923	0.480
5 (P-RA)	Preinstalled rock	0.28[a]	3.2	18.04	1.146	0.534
6 (R-RF3)	Rock fill	1.02	1.7	18.60	1.008	0.502

Note: [a] this is the measured thickness at the pile wall once the protective collar had been removed after pile driving analysed according to Fig. 7(b).

FIGURES

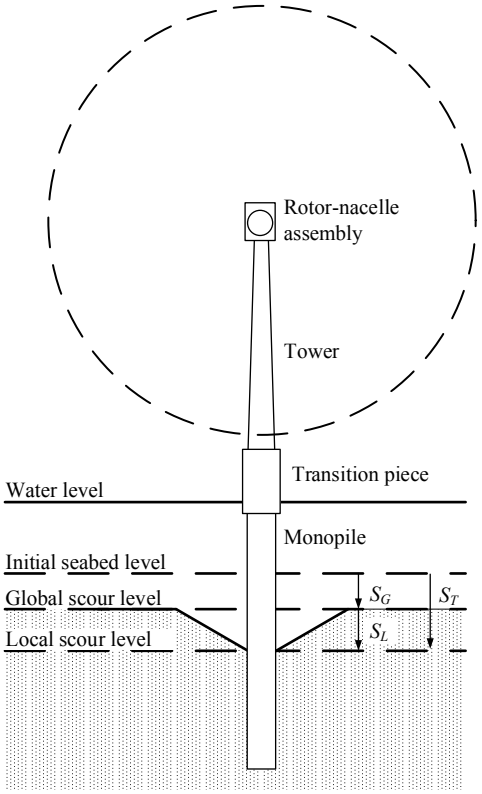

Fig. 1. Idealised seabed profile due to local and global scour (after Mayall et al., 2018)

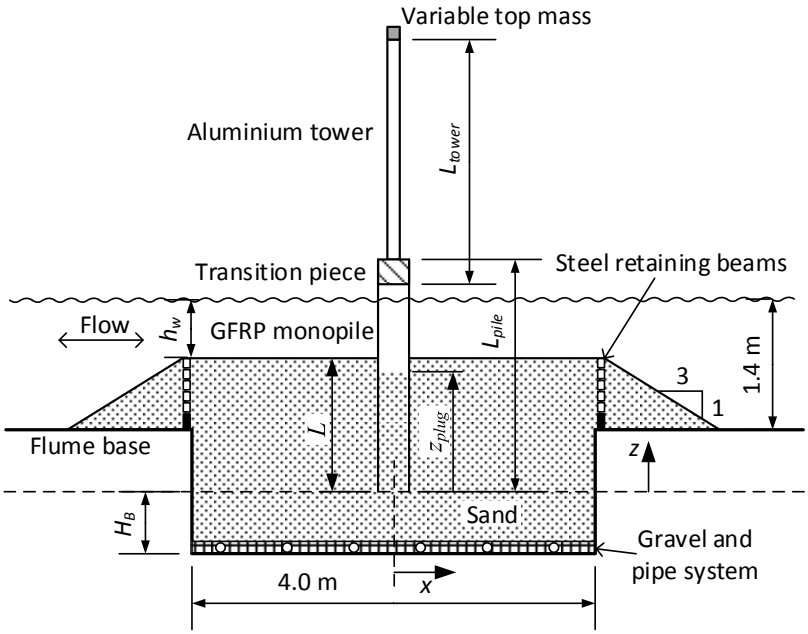

Fig. 2. Annotated section view of the prepared sand bed and monopile - tower system (not to scale)

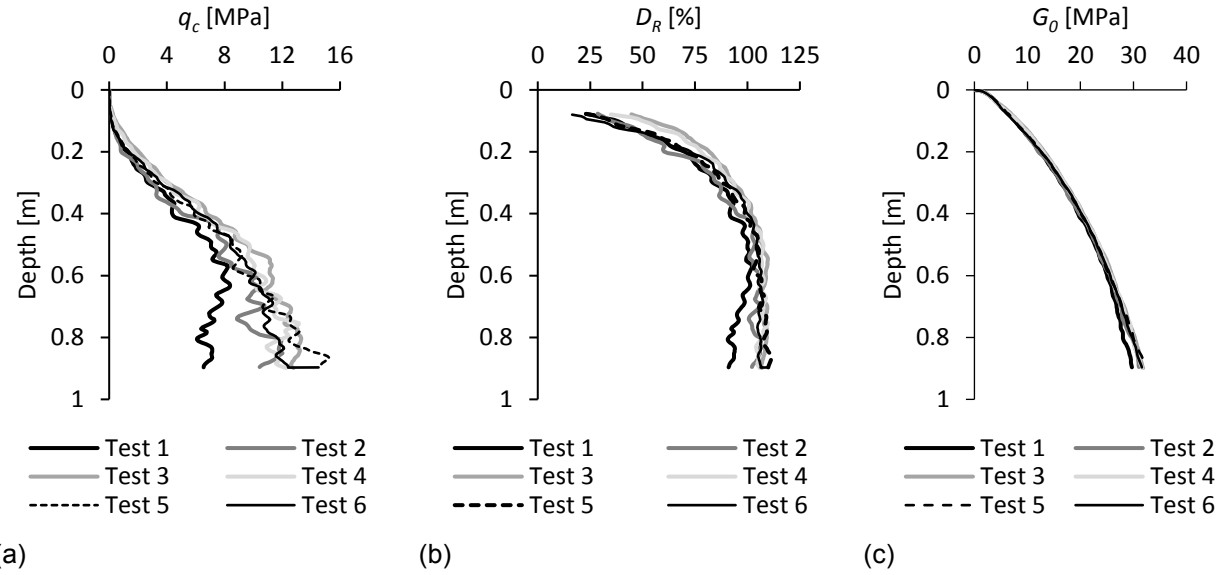

(a) (b) (c)

Fig. 3. Test bed CPT measurements on (a) end bearing, q_c; (b) inferred relative density D_R; (c) inferred small strain shear modulus, G_0

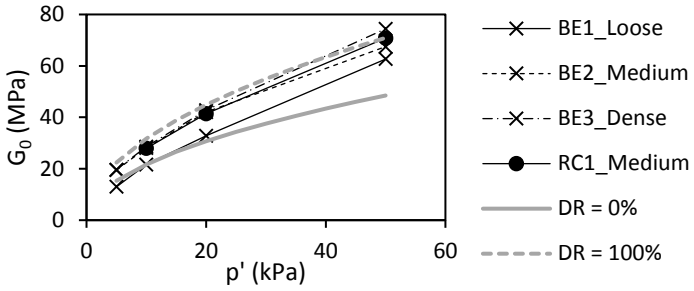

Fig. 4. Measured small strain shear modulus, G_0. Also shown is the correlation in Equation (2) with $B = 478$ for $D_R = 0$ and 100%

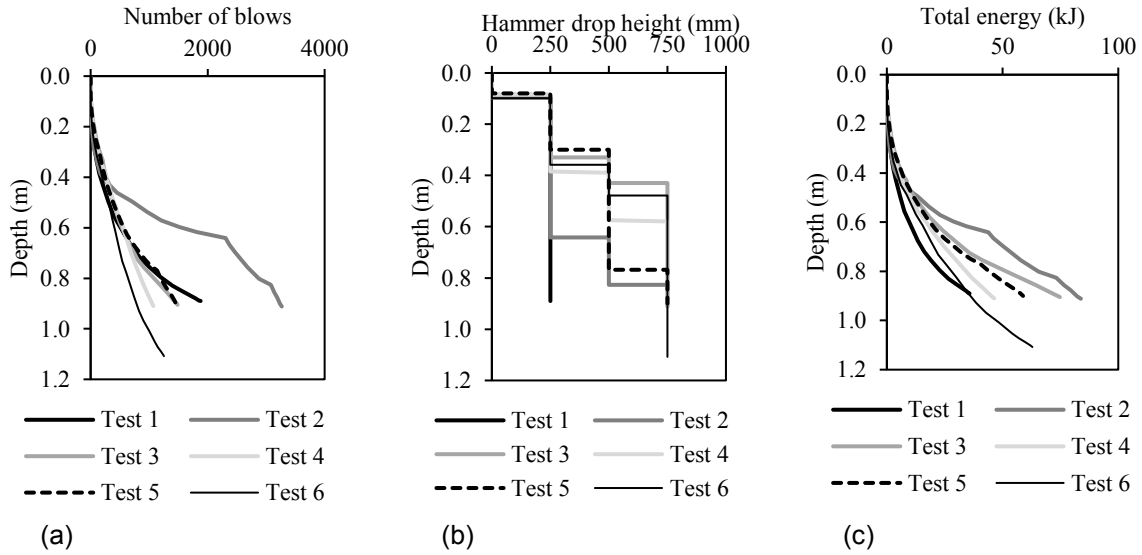

Fig. 5. Driving records (a) Driving number of blows; (b) Hammer drop height; (c) Driving energy

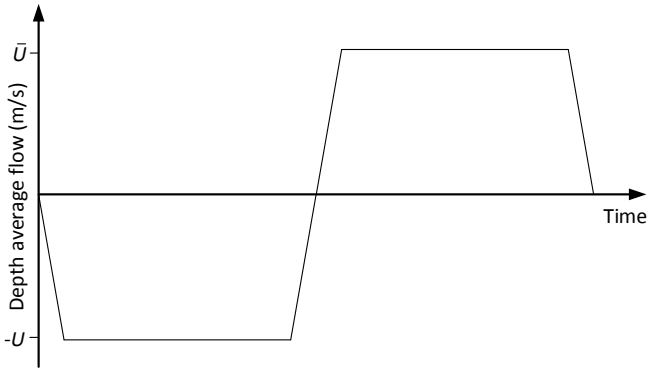

Fig. 6. Illustration of a typical symmetrical flow cycle

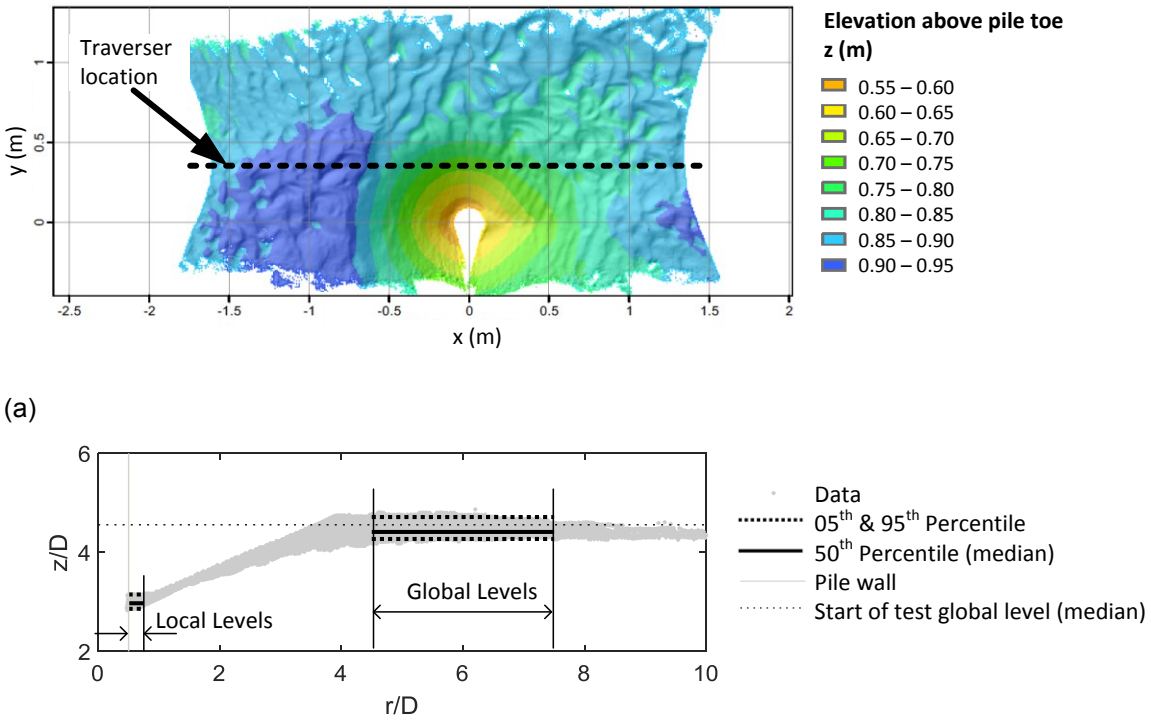

Fig. 7. Typical profile of scour (Test 1, end of flow Phase 1b) (a) Plan bathymetry plot with hillshade to highlight detail, indicating the underwater laser scanner traverser location; (b) Bathymetry section interpretation, individual data points appear as a grey band

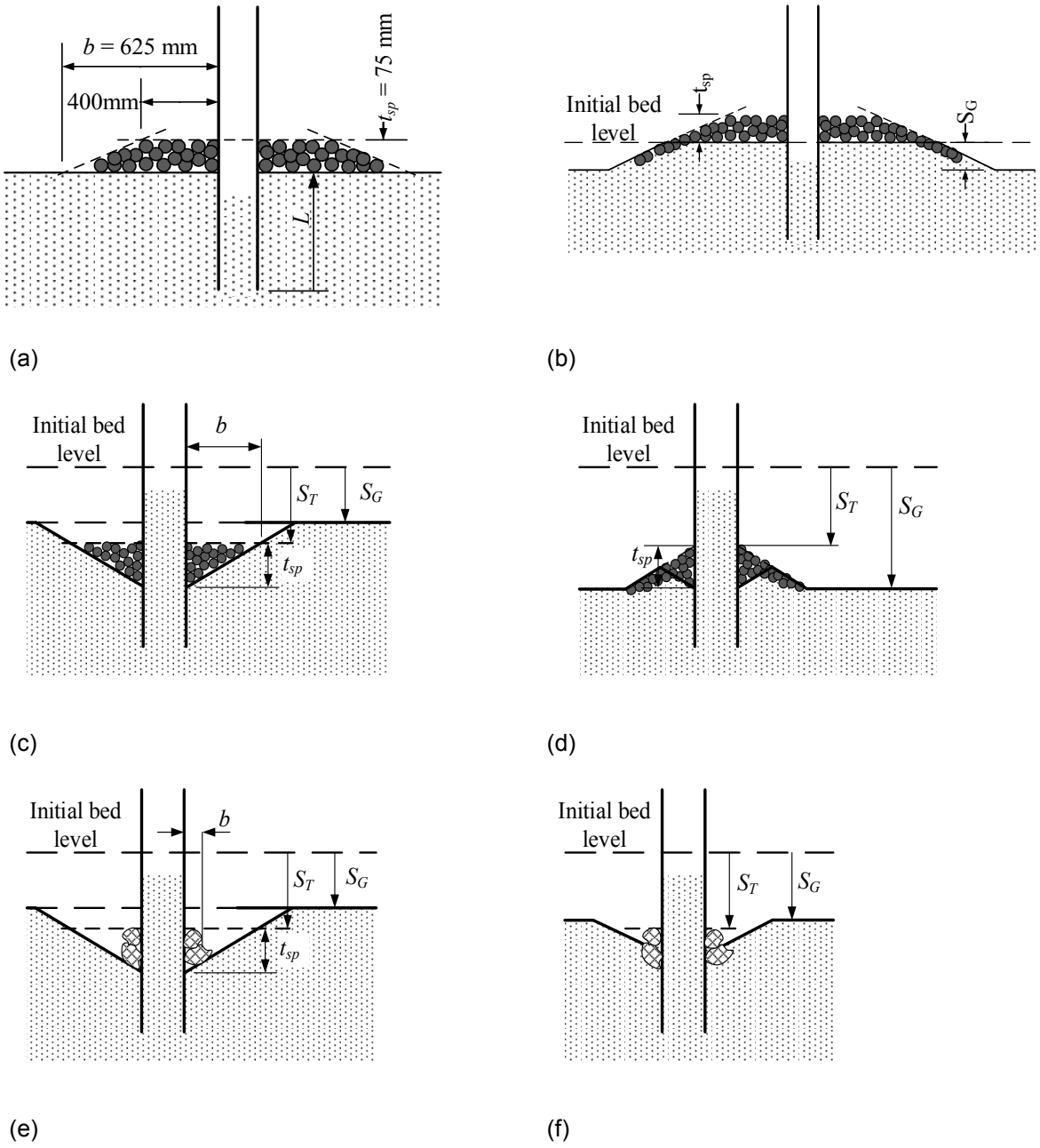

Fig. 8. Geometric definitions for scour protection systems (a) Preinstalled rock armour (Test 5); (b) Pre-installed rock armour following global scour; (c) Rock fill in scour hole (Tests 3, 4 & 6); (d) Rock fill following global scour; (e) Tyre-filled nets (Test 2); (f) Tyre-filled nets following global scour

(a) (b) (c)

Fig. 9. Photographs of installed scour protection systems; (a) Tyre-filled nets (Test 2); (b) Rock fill (Tests 3, 4, 6); (c) Pre-installed rock (Test 5)

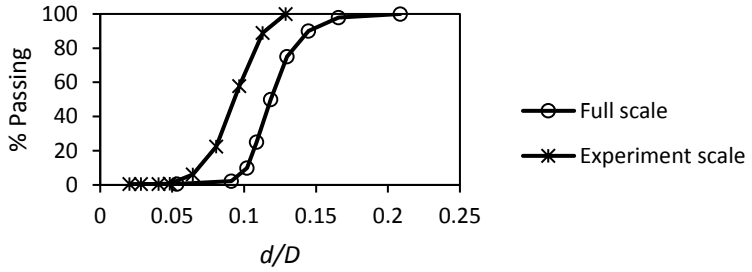

Fig. 10. Dimensionless rock scour protection grading curves at full scale and experiment scale

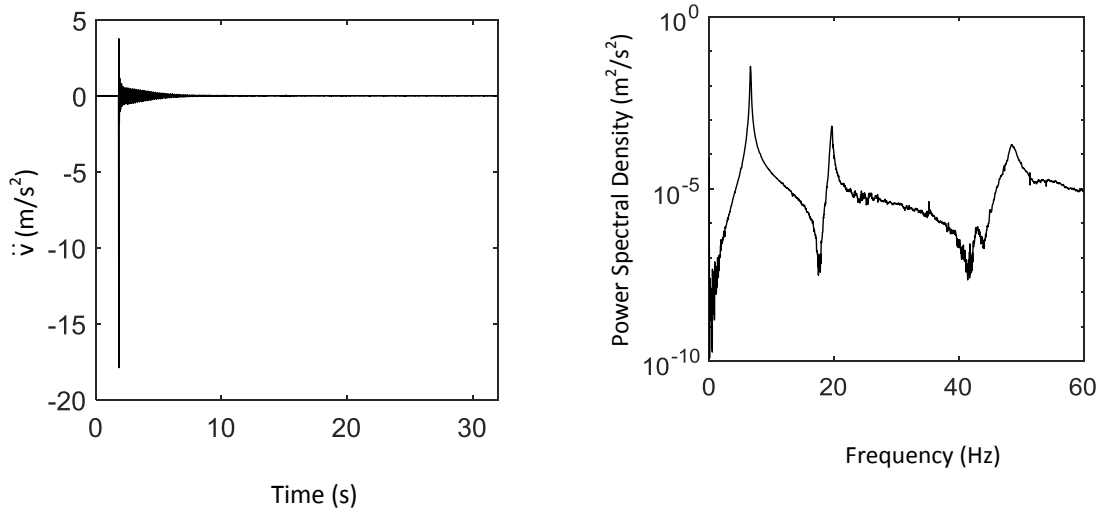

(a) (b)

Fig. 11. Example signal and power spectral density (start of Test 3, N_M = 0, top accelerometer, streamwise); (a) Recorded acceleration; (b) Power spectral density

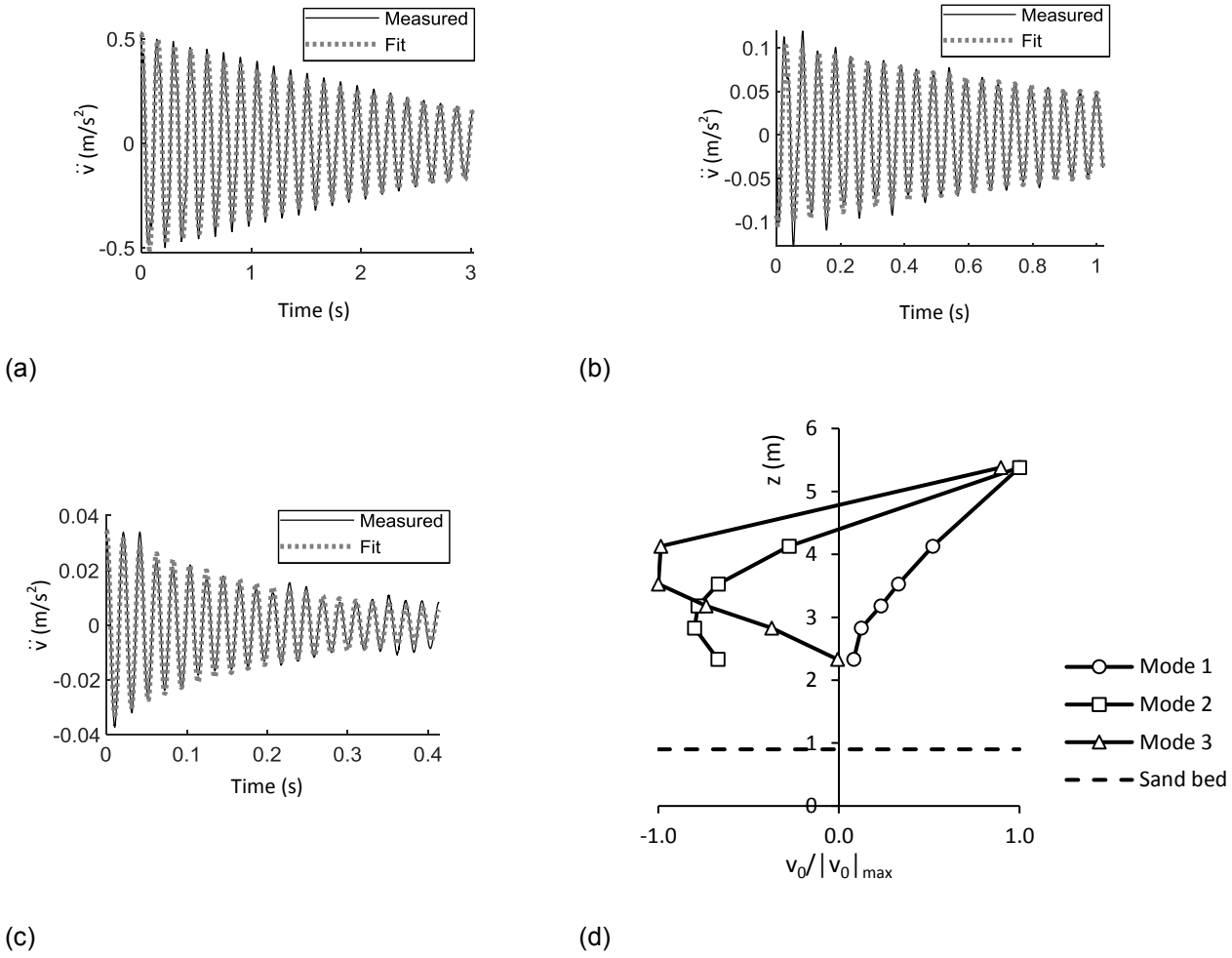

Fig. 12. Example calculation of natural frequencies (start of Test 3, N_M = 0, top accelerometer, streamwise). Also shown are the mode shapes. (a) First mode measured signal fitting (f_n = 6.63 Hz, ζ = 0.9 %); (b) Second mode residual signal fitting (f_n = 19.6 Hz, ζ = 0.6 %); (c) Third mode residual signal fitting (f_n = 48.4 Hz, ζ = 1.4 %); (d) Mode shapes with height above pile tip – initial sand bed at z = 0.9 m

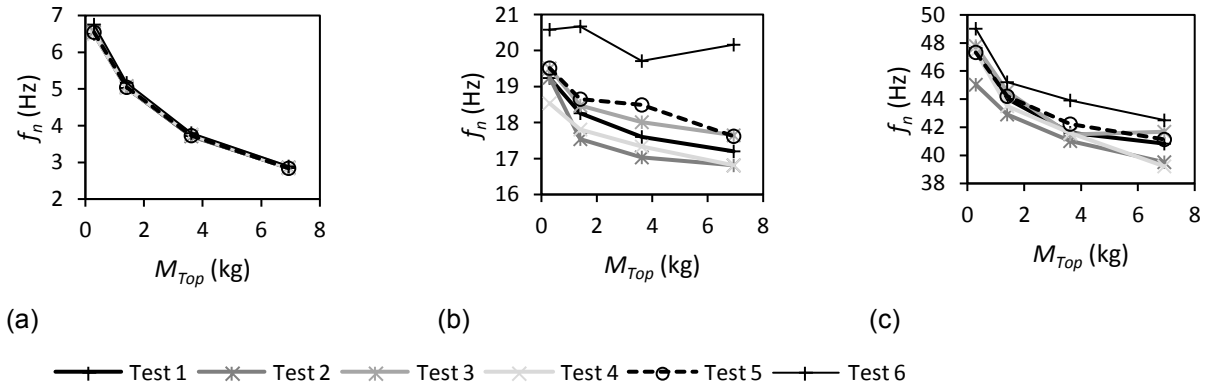

Fig. 13. Influence of top mass on the inferred natural frequency at the start of each test; (a) Mode 1 natural frequency; (b) Mode 2 natural frequency; (c) Mode 3 natural frequency

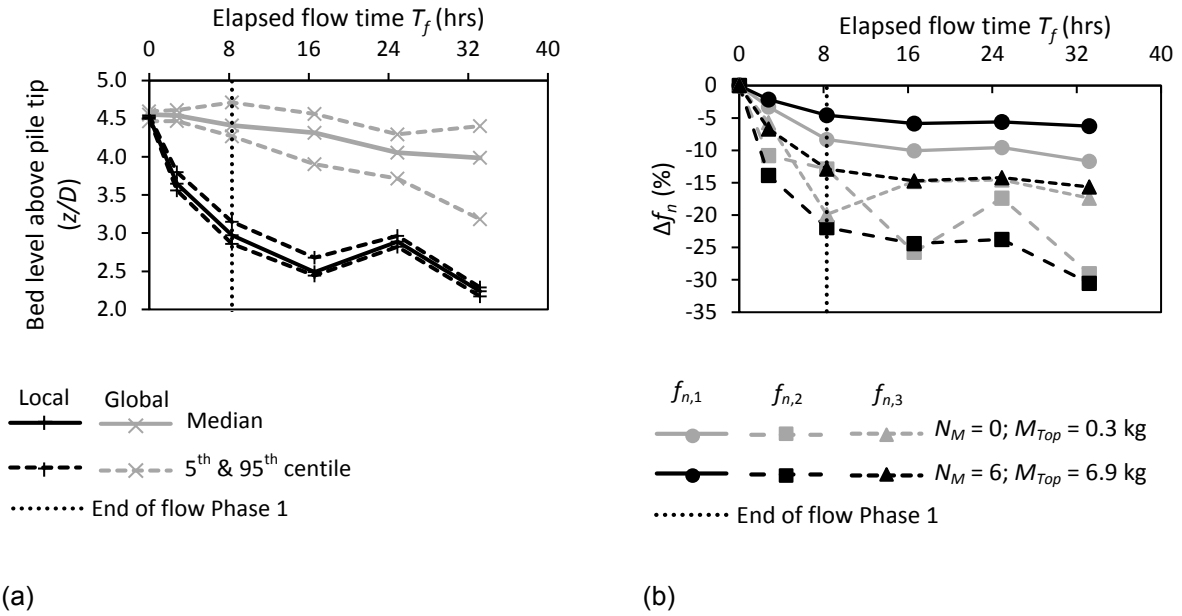

(a) (b)

Fig. 14. Experiment results – measured bathymetry and inferred natural frequencies for experiment with unremediated scour (Test 1); (a) Bathymetry outputs; (b) Change in natural frequency

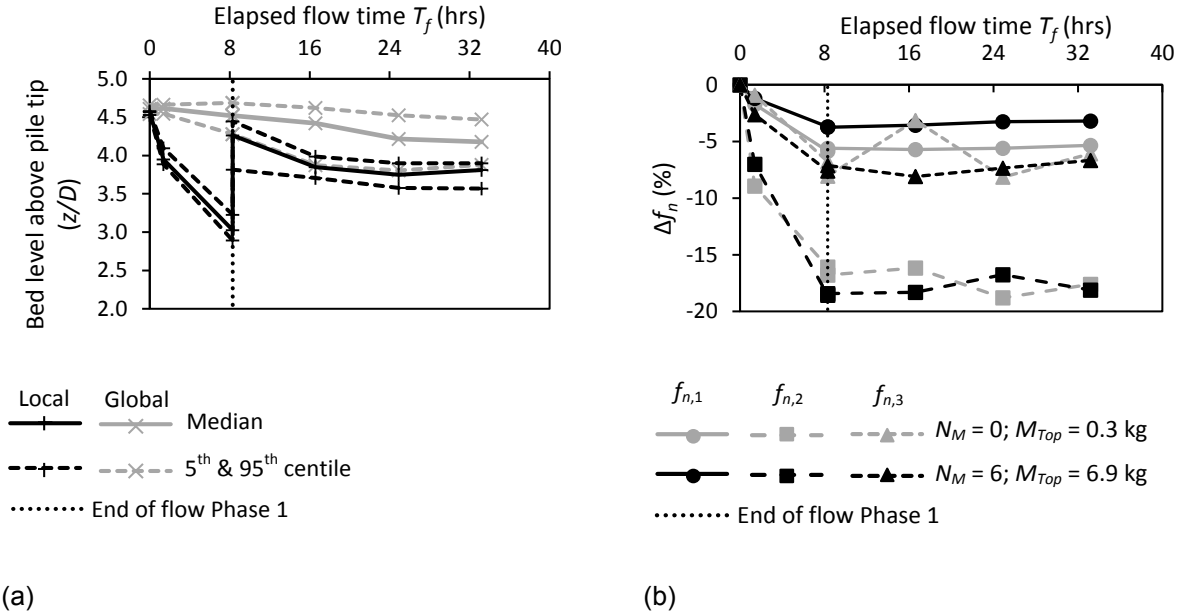

(a) (b)

Fig. 15. Experiment results – Tyre-filled net remedial scour protection (Test 2); (a) Bathymetry outputs; (b) Change in natural frequency

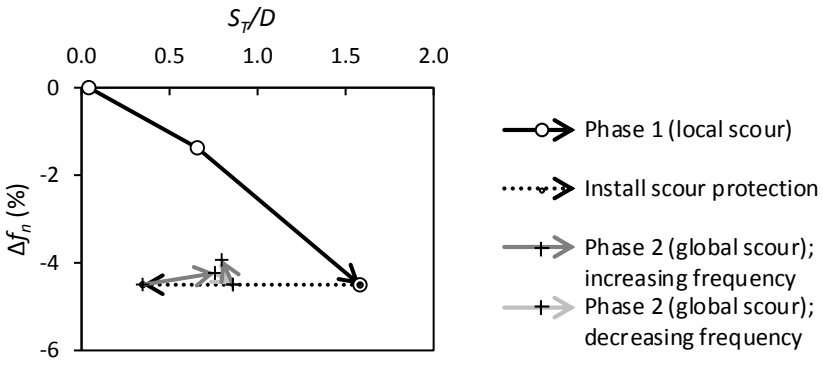

Fig. 16. Mean relative change in mode 1 natural frequency (for N_M = 0, 1, 3, 6) with tyre-filled net remedial scour protection (Test 2)

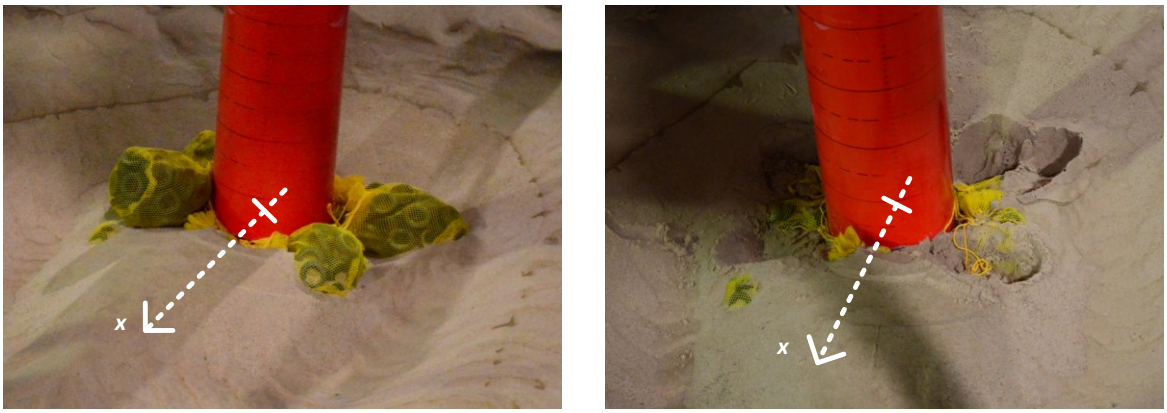

(a) (b)

Fig. 17. Photographs of tyre-filled net remedial scour protection after all flow phases, arrows approximately indicate the flume x-axis direction (see Fig. 2); (a) After draining flume; (b) After removing top layer of tyre-filled nets

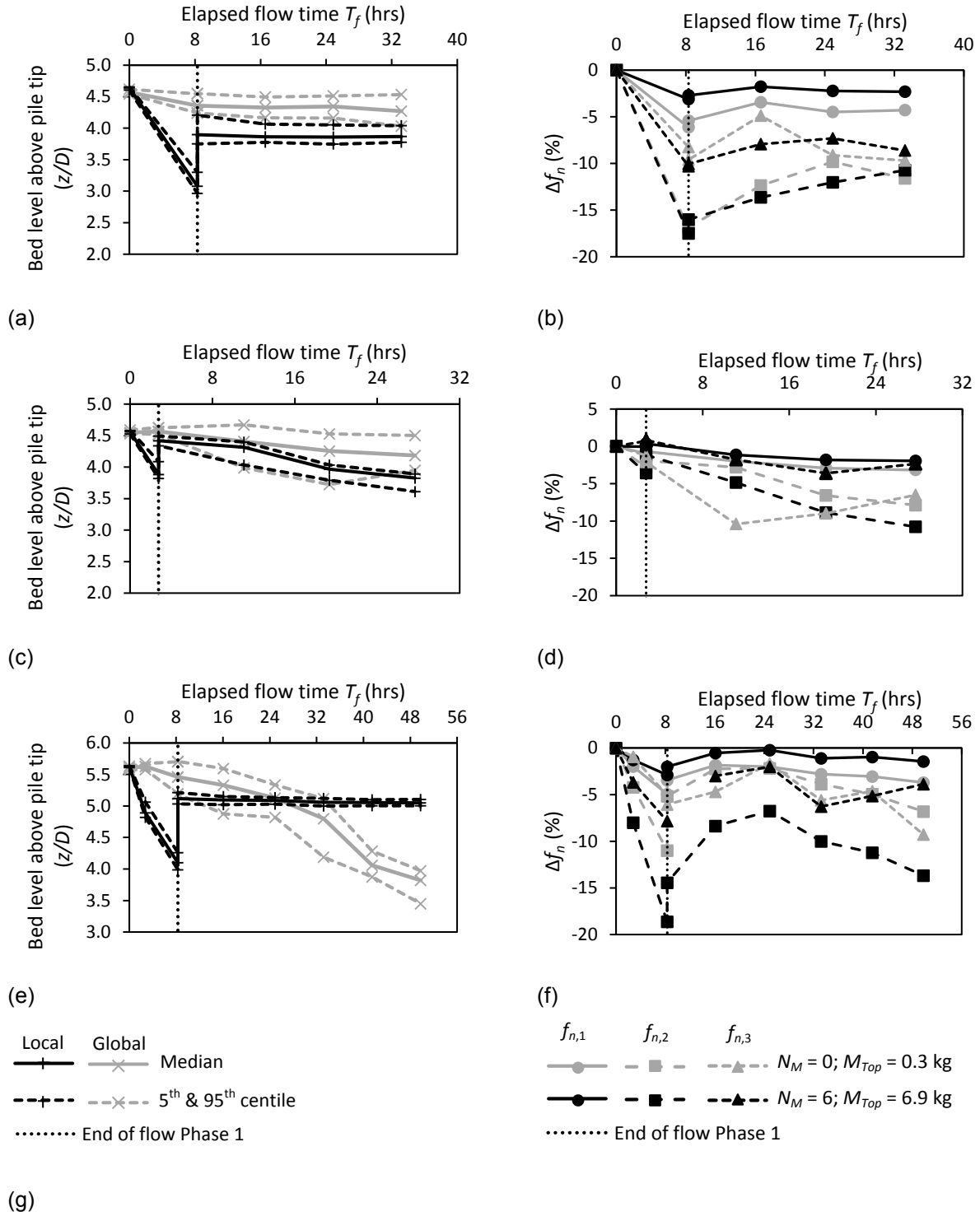

Fig. 18. Experiment results – Rock fill remedial scour protection (Test 3, 4 and 6); (a) Bathymetry outputs (Test 3); (b) Change in natural frequency (Test 3); (c) Bathymetry outputs (Test 4); (d) Change in natural frequency (Test 4); (e) Bathymetry outputs (Test 6); (f) Change in natural frequency (Test 6); (g) Legends

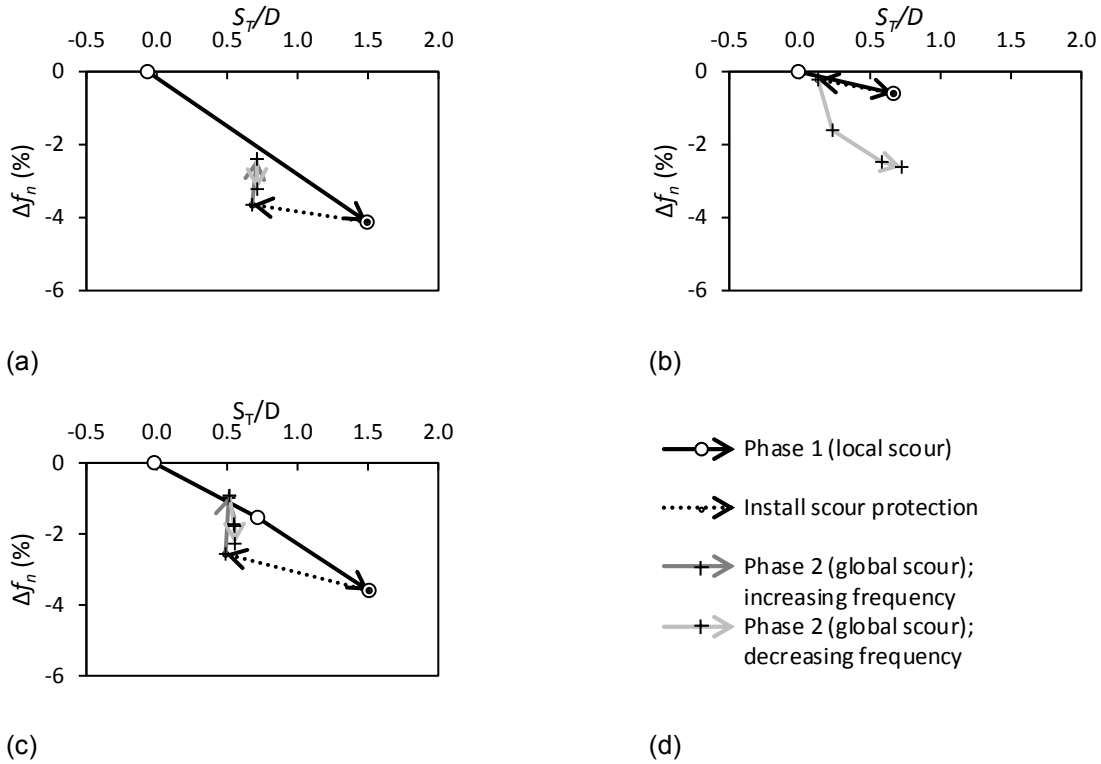

Fig. 19. Mean relative change in mode 1 natural frequency (for N_M = 0, 1, 3, 6) with scour and rock fill remedial scour protection; (a) Test 3; (b) Test 4; (c) Test 6; (d) Legends

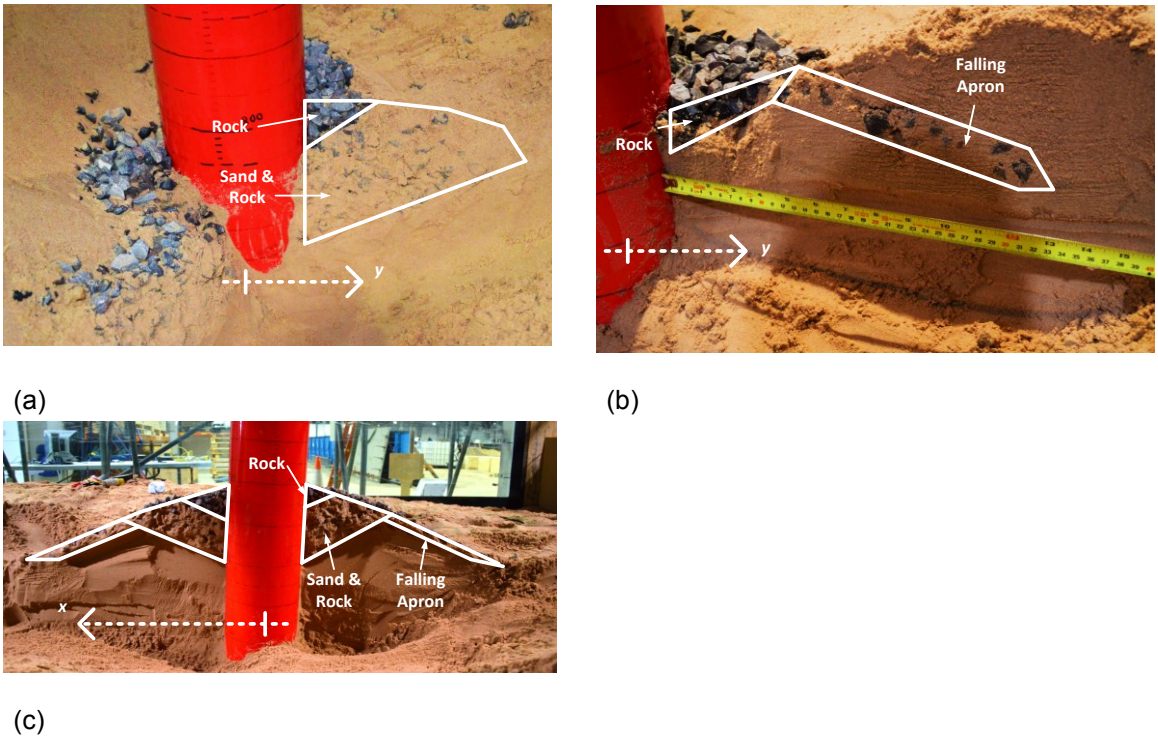

Fig. 20. Photographs of rock scour fill protection cross sections, arrows indicate the flume x and y-axis directions; (a) Test 3 – Rock fill; (b) Test 4 – Rock fill in partial scour hole; (c) Test 6 – Rock fill

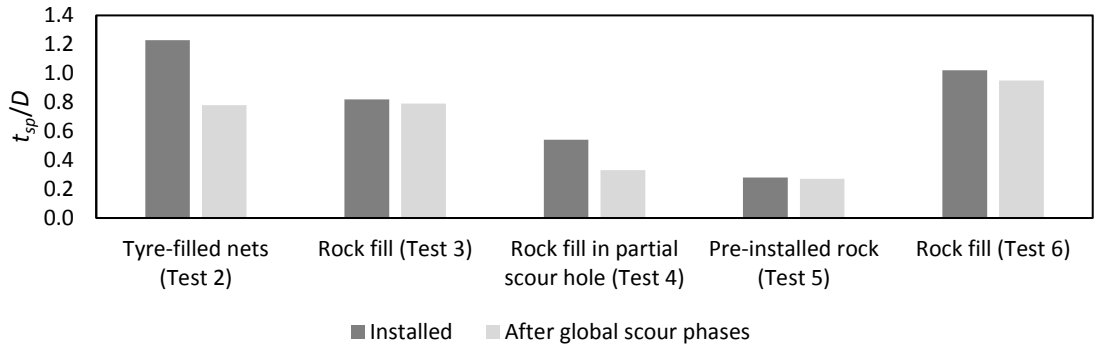

Fig. 21. Change in scour protection thickness adjacent to the pile after global scouring

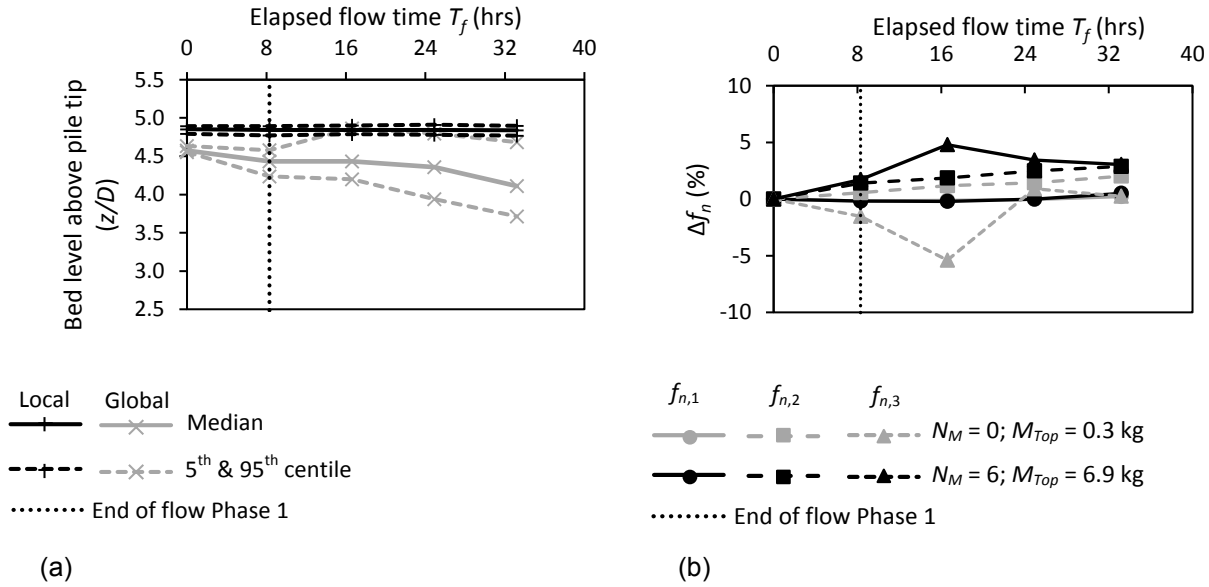

Fig. 22. Experiment results – pre-installed rock armour scour protection (Test 5); (a) Bathymetry outputs; (b) Change in natural frequency

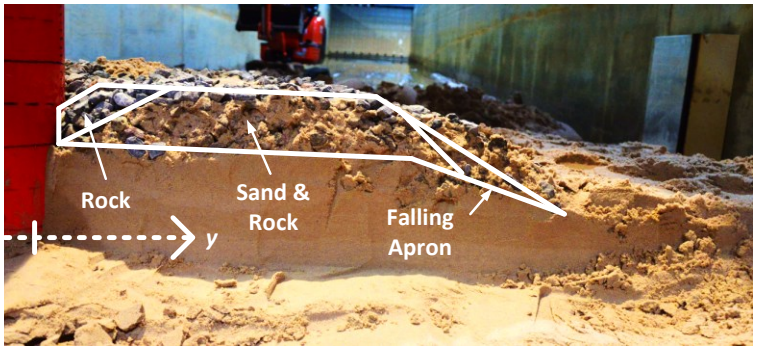

Fig. 23. Photographs of rock scour protection cross sections for Test 5 – pre-installed rock armour, arrow indicates the flume y-axis direction

End of Paper 3

2.3 Bathymetry Data

2.3.1 Bathymetry Data Acquisition

The bathymetry data acquisition and processing was discussed in Paper 3, with an example plan bathymetry plot in Fig. 7 showing the bathymetry of a local scour hole before global scouring. This Section provides further discussion of the bathymetry results and scour development. Appendix C.4 provides additional detail on the bathymetry data analysis and Appendix C.9.1 presents a table of detailed results.

2.3.2 Bathymetry Plots for Unremediated Scour Conditions (Test 1)

Figure 2.1(a) presents the measured bathymetry and at the end of the unremediated scour test (Test 1). The streamwise cross-sections in Figure 2.1(b) show the scour hole before sand backfill, after sand backfill, and at the end of the test.

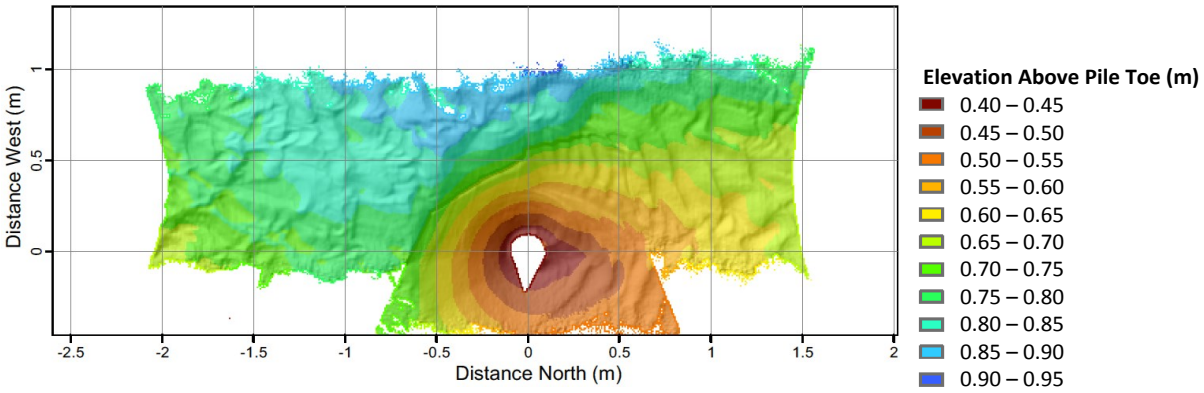

(a) Bathymetry map at end of Test 1

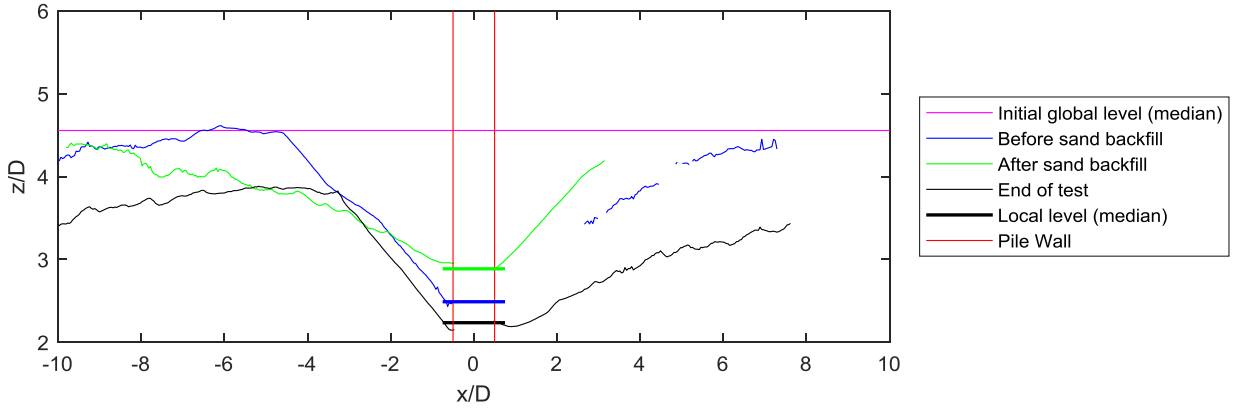

(b) Streamwise cross-section from Test 1

Figure 2.1. Bathymetry plots for unremediated scour conditions (Test 1)

In Figure 2.1 the slope of the scour hole is steeper and the scour depth fractionally deeper on the upstream side of the pile (South, $x < 0$), with a shallower slope and greater extent downstream of the pile. This is a general trend observed across all tests, consistent with the expected greater scouring at the upstream face of the pile than at the downstream face, accompanied by wake effects downstream.

2.3.3 Bathymetry Plots for Tyre-Filled Net Scour Protection (Test 2)

Figure 2.2(a) presents the measured bathymetry at the end of the tyre-filled net test (Test 2), and Figure 2.2(b) presents the streamwise cross-sections for the same test. Secondary scour can be observed around the tyre-filled nets downstream of the pile at the end of the test, at approximately x/D = 3.

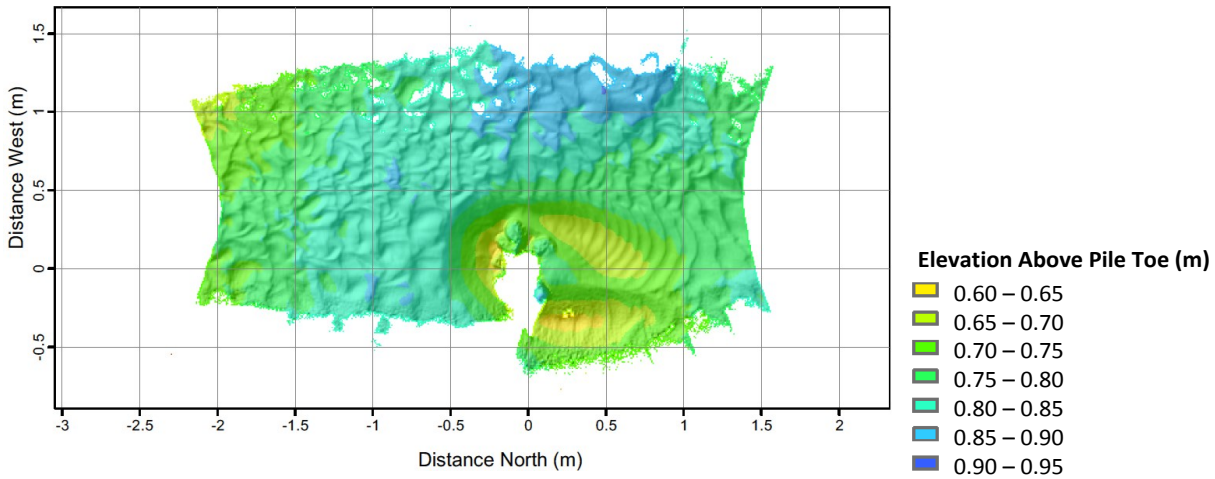

(a) Bathymetry map at end of Test 2

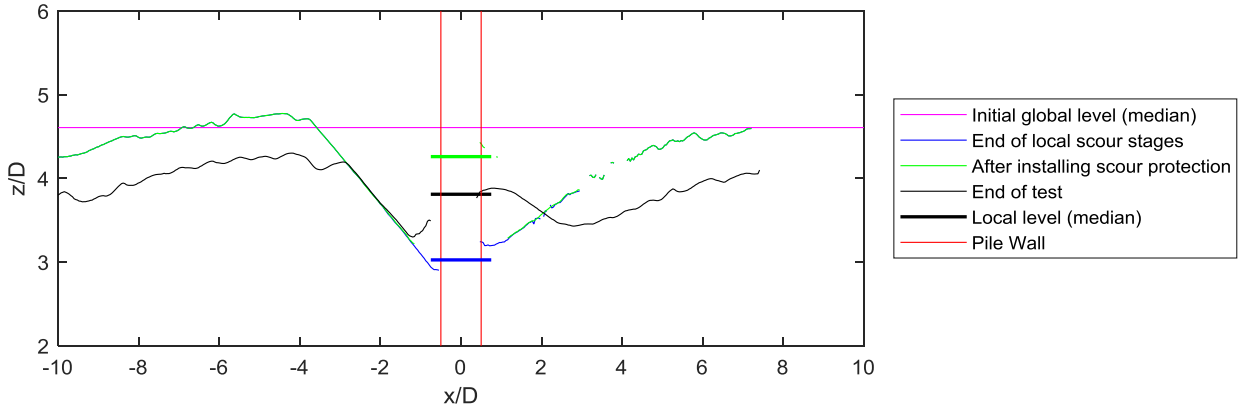

(b) Streamwise cross-section at end of Test 2

Figure 2.2. Bathymetry plots for remedial tyre-filled net scour protection (Test 2)

2.3.4 Bathymetry Plots for Remedial Rock Fill Scour Protection (Test 3, 4 and 6)

Figure 2.3 and Figure 2.4 show the bathymetry results for tests with remedial rock fill scour protection (Tests 3, 4 and 6). The end of test bathymetry plots in Figure 2.3 correspond with the end of test excavations (Fig. 20 in Paper 3), which showed sand accretion in the scour protection material.

In Test 3, the baseline with remedial rock fill in a fully-formed scour hole, the bathymetry (Figure 2.3(a) and Figure 2.4(a)) indicates that there was very little movement of the scour protection at the pile wall, and partial burial by sand at the edge. For Test 4, in which remedial rock fill was installed in a partially-formed scour hole, the bathymetry cross-sections (Figure 2.4(b)) show that the sour protection surface has lowered significantly by the end of the test, to the level of the base of the original scour hole. In Test 6 (Figure 2.3(c) and Figure 2.4(c)) the global bed level had dropped significantly, undermining the outside edge of the scour protection and causing a falling apron of rock to develop, but with the local level adjacent to the pile wall unaffected.

2.3.5 Bathymetry Plots for Pre-installed Rock Armour Scour Protection (Test 5)

Figure 2.5 presents the bathymetry plots for the pre-installed rock armour test (Test 5). The cross-sections (Figure 2.5(b)) and excavations (Fig. 23 in Paper 3) show that the local level close to the pile wall is lower than the overall top surface of the scour protection; this is caused by the removal of a collar around the pile during installation (Paper 3) rather than due to local scour effects. The cross-sections (Figure 2.5(b)) indicate that the pre-installed rock was stable within approximately 3 D of the pile centreline, and that a falling apron had developed at the scour protection edge.

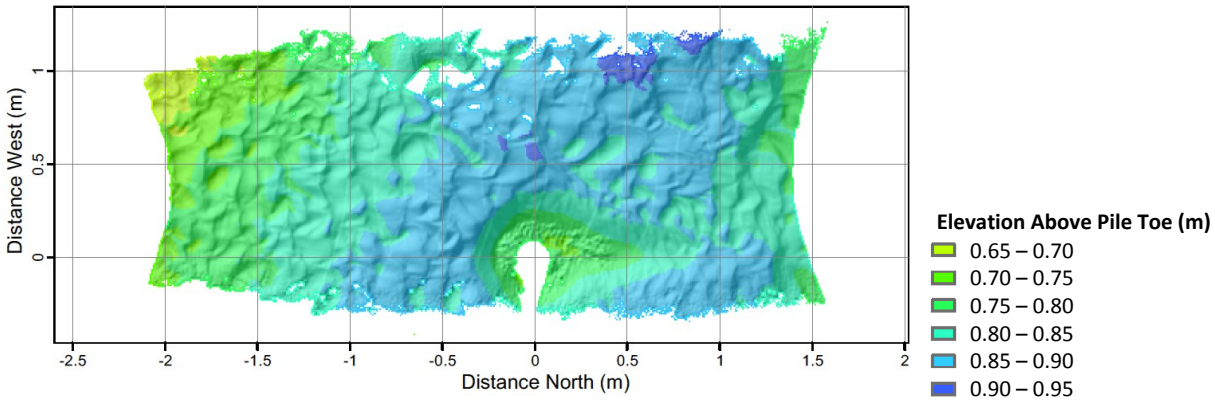

(a) Bathymetry map at end of Test 3 (remedial rock fill scour protection in a fully-formed scour hole)

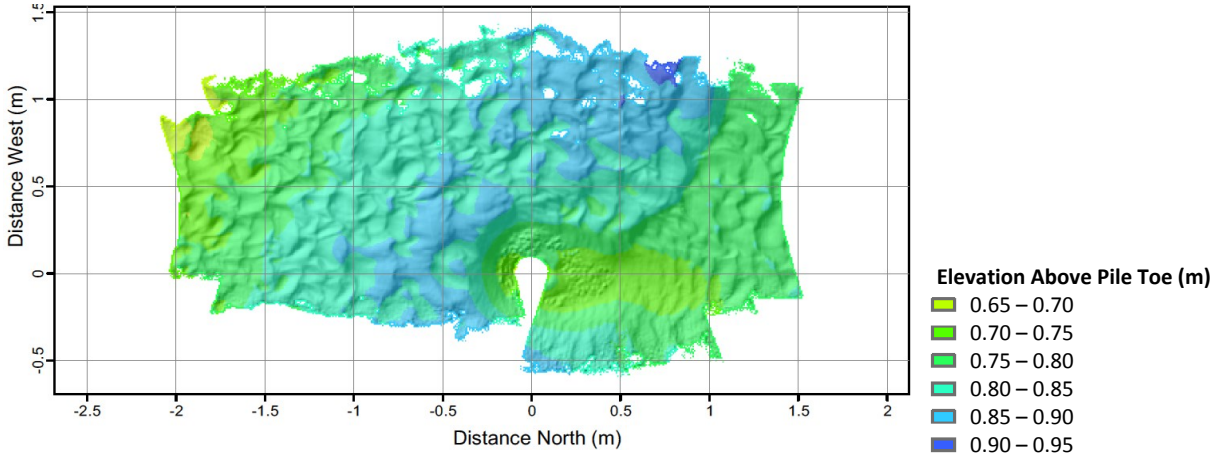

(b) Bathymetry map at end of Test 4 (remedial rock fill scour protection in a partially-formed scour hole)

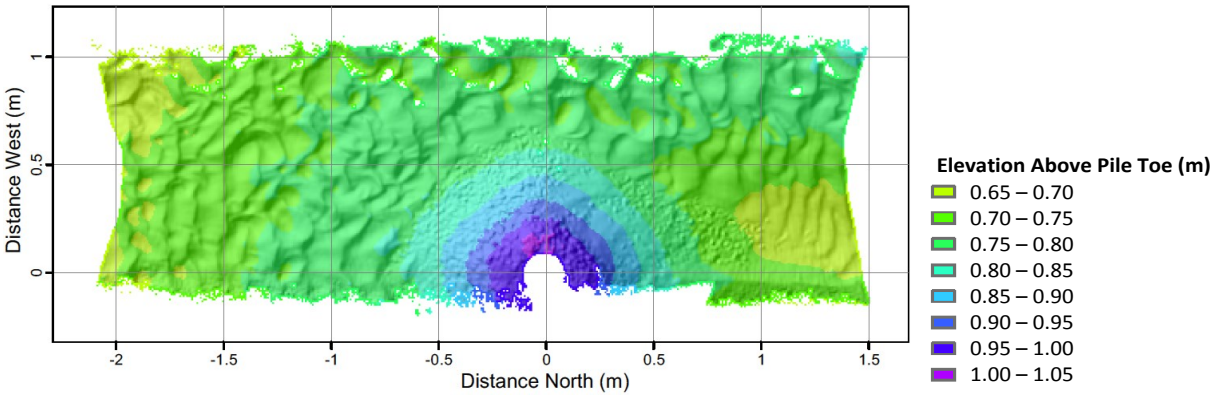

(c) Bathymetry map at end of Test 6 (remedial rock fill scour protection in a fully-formed scour hole with increased global scour)

Figure 2.3. Plan bathymetry plots for remedial rock fill scour protection (Tests 3, 4, and 6)

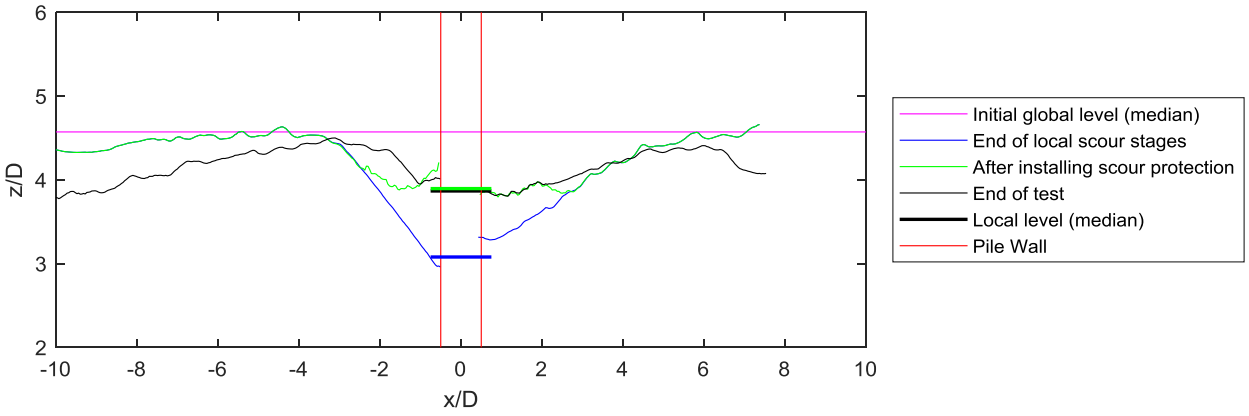

(a) Streamwise cross-section at end of Test 3 (remedial rock fill scour protection in a fully-formed scour hole)

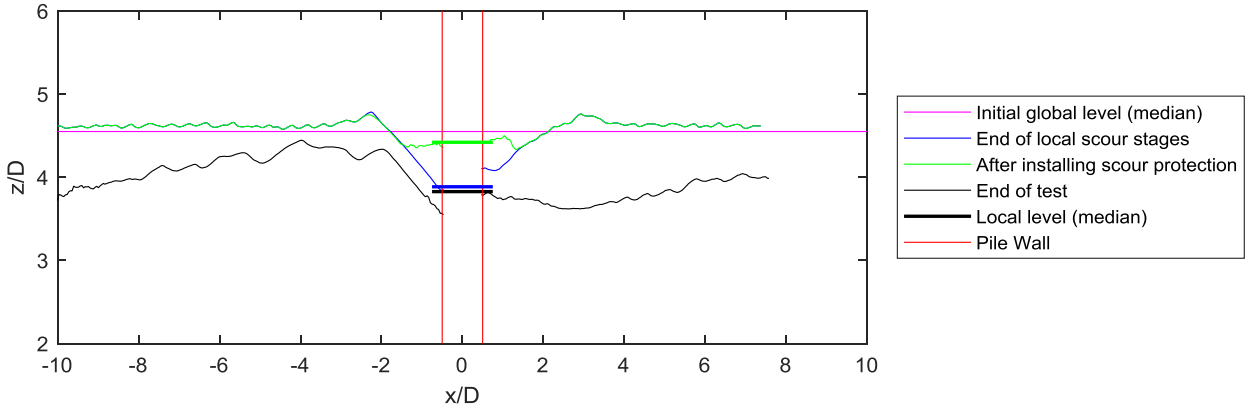

(b) Streamwise cross-section at end of Test 4 (remedial rock fill scour protection in a partially-formed scour hole)

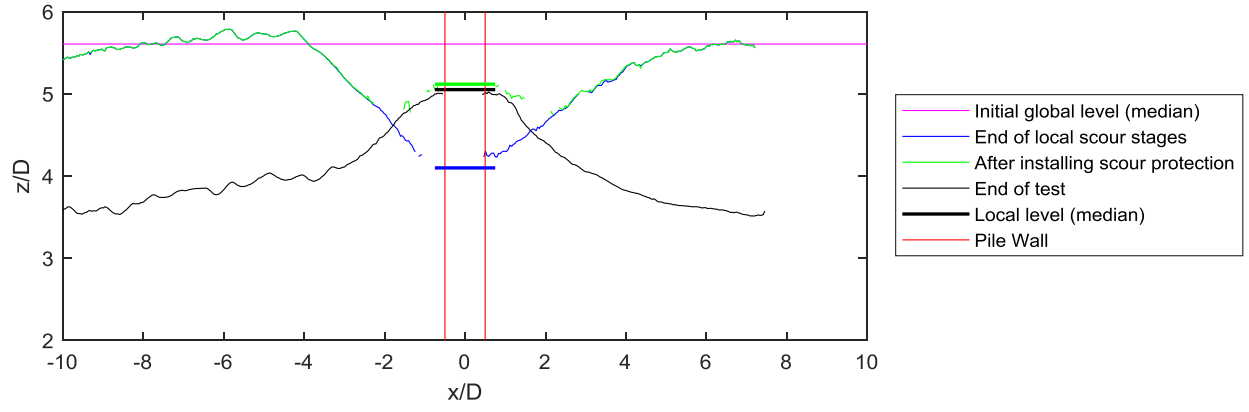

(c) Streamwise cross-section at end of Test 6 (remedial rock fill scour protection in a fully-formed scour hole with increased global scour)

Figure 2.4. Cross-section bathymetry plots for remedial rock fill scour protection (Tests 3, 4, and 6)

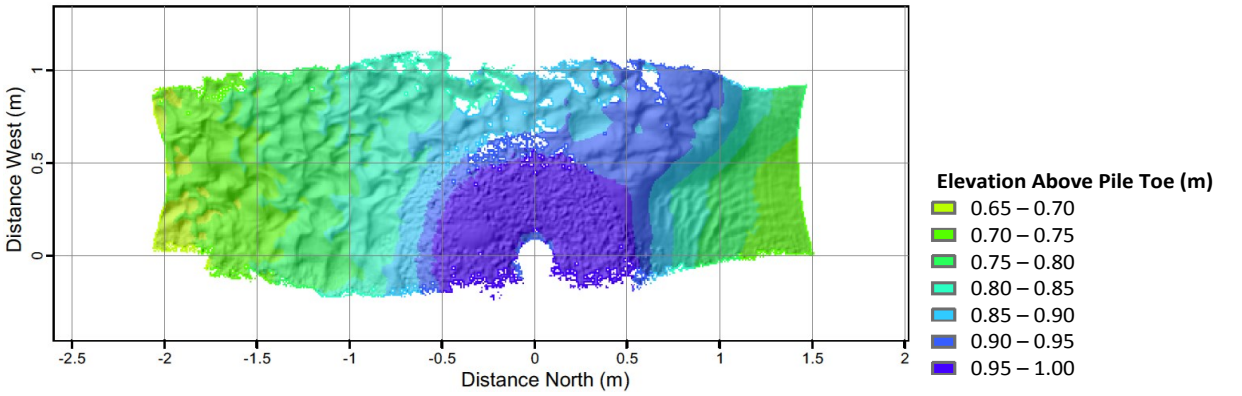

(a) Bathymetry map at end of Test 5

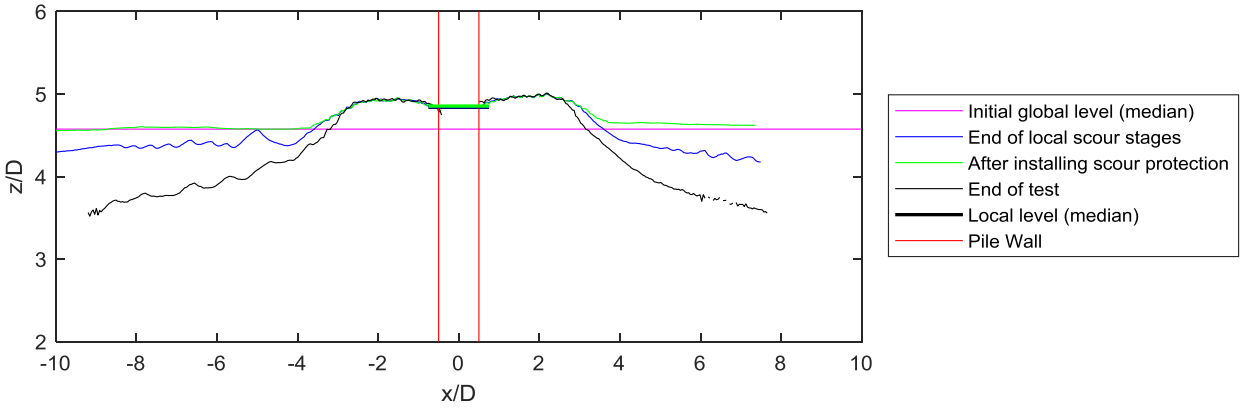

(b) Streamwise cross-section at end of Test 5

Figure 2.5. Bathymetry plots for pre-installed rock armour scour protection (Test 5)

2.3.6 Discussion of Scour Development

The general definitions for global and local scour are given in Figure 1.6. Figure 2.6 presents the total scour development during local scour stages against flow duration for all tests (note that Test 5 had preinstalled scour protection and hence no local scour). Total scour is presented to avoid introducing scatter from the global scour measurements.

Inspection of the intermediate total scour depths plotted in Figure 2.6 indicates that local scour developed more rapidly in Tests 1 and 2 than in Tests 4 and 6. It is noted that Test 1 had slightly higher flow rates during the initial local scour development phase than other tests (Table 8 in Paper 3). The differences in intermediate scour depth suggest that the rate of scour development varied between tests, and may indicate the presence of sand backfill at the time of the bathymetry

measurements in some tests. It is possible for sand backfill to be present due to action of sand falling into the scour hole, competing with the erosion effects due to flume flow.

Figure 2.7 presents the global scour development with elapsed flow for all tests, with global scour defined relative to the global bed level at the start of each test. Global scour development was most successful in Test 6, which used an asymmetric flow regime in the final two stages of global lowering (Table 8 in Paper 3).

Falling aprons of scour protection were observed in Tests 4, 5 and 6 (Fig. 20 and Fig. 23 in Paper 3), and these were partially buried by sand waves. This suggests that the end of test global level is not necessarily the minimum level achieved during the testing. This is not unexpected, due to the moving sand bed under the live bed test conditions.

Figure 2.8 presents the changes in local embedment of the pile after installing scour protection, and Figure 2.9 presents the change in local embedment during flow phases after scour protection installation. The two plots show that the stability of scour protection varied between tests. For all scour protection cases there was concurrent development of global scour.

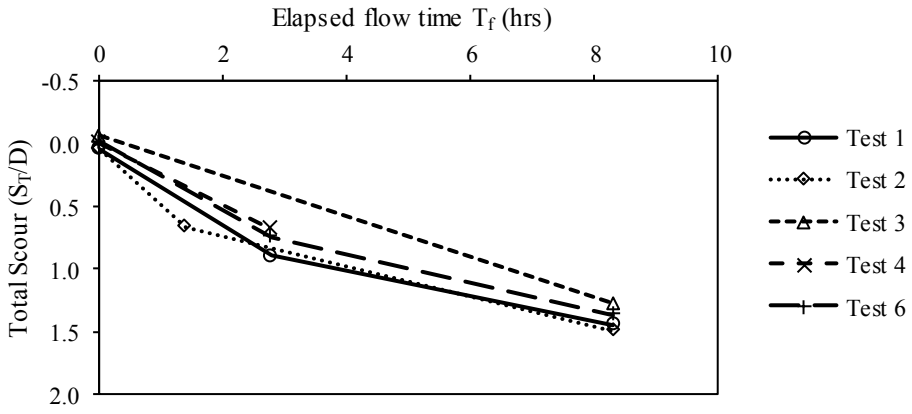

Figure 2.6. Measured total scour depth with elapsed flow time

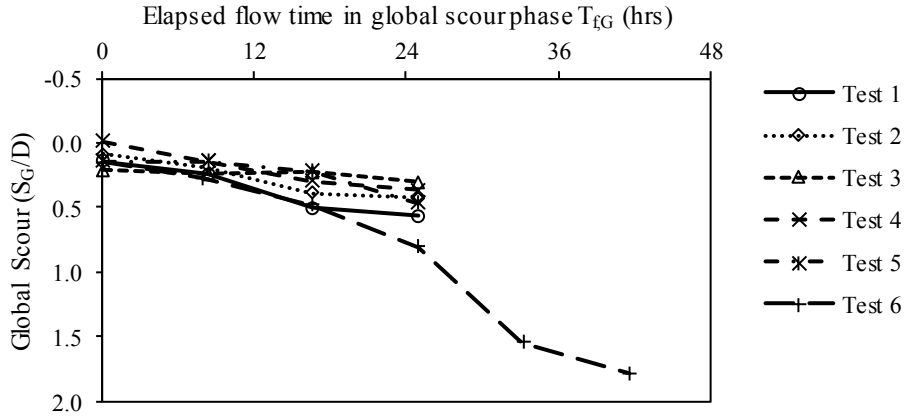

Figure 2.7. Measured global scour depth with elapsed flow time

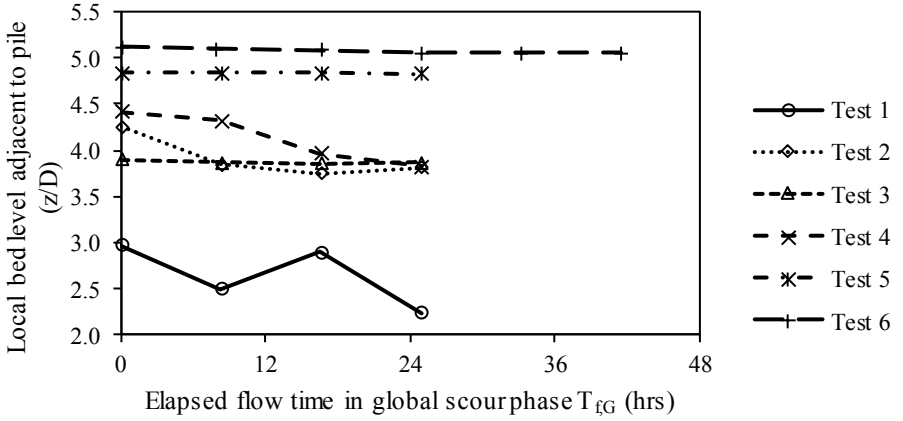

Figure 2.8. Scour protection elevation at the pile wall with elapsed flow time (global scour flow phases defined in Table 8 in Paper 3)

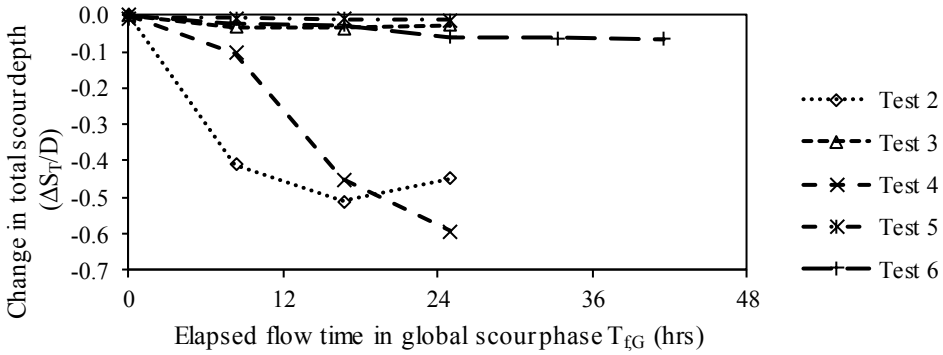

Figure 2.9. Change in scour protection elevation at the pile wall with elapsed flow time (global scour flow phases defined in Table 8 in Paper 3)

2.4 Structural Dynamics Testing

2.4.1 Overview

This Section provides further detail of the structural dynamics testing, expanding on the information provided in Paper 3.

Structural dynamics tests were performed at intervals between flow segments, typically whilst bathymetry measurements were taken by HR Wallingford. Time-varying loads $H(t)$ were applied to a force sensor at the top of the tower, shown in Figure 2.10. Accelerations were measured in the streamwise and spanwise directions down the tower (shown in Figure 2.11), displacement was measured near the pile top, and pile bending moment was measured using strain gauges. The tests included loading both with and without a modal shaker attached to the structure. Figure 2.12 shows the setup of the modal shaker when attached.

2.4.2 Structural Dynamics Testing Methods

A standard test involved the following steps:

i. The response to impulses (finger-taps) was logged, with 3 to 5 impulses applied to each force sensor, for 0, 1, 3 and 6 top masses.

ii. A set of shaker tests were performed for 0, 1, 3 and 6 top masses:

- Test the response to a white noise signal in the streamwise direction.
- Three frequency sweeps in the streamwise direction targeted around the first three natural frequencies (identified from i.).

A *LabVIEW* code was developed to manage the sampling and logging of data for all stages of the testing, including the modal shaker control. The sampling rate for the equipment was 3012 Hz in the structural dynamics tests. The instruments were continuously sampled and stored on a temporary 32 second software buffer, and logged on command from the user interface or internal commands.

The soil response was assumed to remain elastic during the structural dynamics testing, this is discussed in Appendix C.6.7.

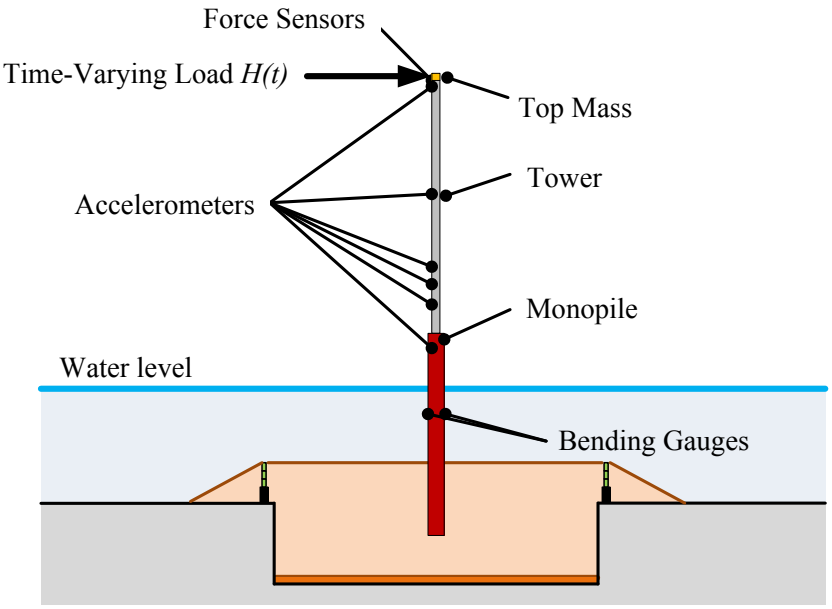

Figure 2.10. Structural dynamics testing layout

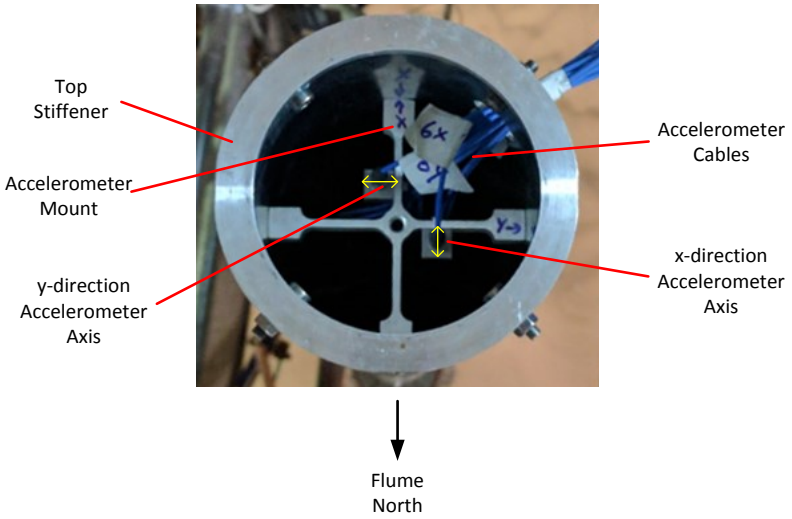

Figure 2.11. Mounted accelerometers viewed from the top of the tower

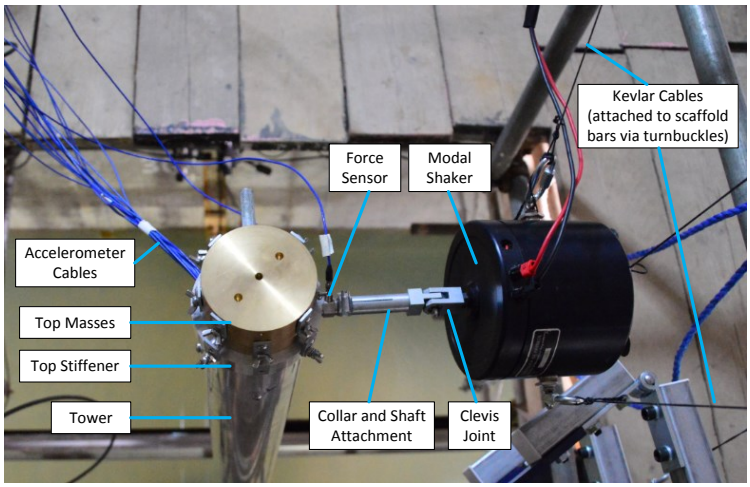

Figure 2.12. Photograph of the modal shaker setup

2.4.2.1 Ambient Measurements

Ambient acceleration measurements were made with no shaker attached and no loads applied to the structure. These ambient measurements were made every 10 minutes during the flume operation, and during the scheduled pauses in flume operation. Data from the ambient measurements collected to provide redundancy in the measured data, but were not analysed in detail.

2.4.2.2 Impulse Tests

During the impulse tests, an impulse was applied to the force sensor by a finger tap, with no shaker attached to the structure. Impulse data were automatically logged by the software after detecting accelerations above a threshold and waiting to fill the temporary buffer. Typically, at least three impulses were applied in each of the streamwise and spanwise directions. The impulse tests are described in Paper 3, and Appendix C.6 presents the details of the method used to analyse the impulse tests.

2.4.2.3 White Noise Tests

Following a series of impulse tests, a cable-suspended modal shaker was attached to a force sensor in the streamwise or spanwise direction, and a white noise signal was sent to the modal shaker. Data from the white noise tests were collected to provide redundancy in the measurements, but were not analysed in detail.

2.4.2.4 Frequency Sweeps

In the frequency sweep tests, a cable-suspended modal shaker was attached to the tower in either the streamwise or spanwise direction, and sinusoidal signals were sent to the modal shaker at discrete frequencies around the estimated natural frequencies of the first three modes. The purpose of the frequency sweep testing was to provide amplitude and phase measurements to identify the modal properties of the structure. Appendix C.7 presents the method used to analyse the frequency sweep tests.

2.4.3 Measurements in Unscoured Conditions

2.4.3.1 Comparison of Frequency Sweeps with Impulse Tests

Figure 2.13 presents a comparison of the natural frequency measured from the frequency sweeps with those measured from impulse tests for the example of Test 3. The mode 1 frequency sweep results in Figure 2.13 are incomplete since some data points were excluded due to low quality. The mode 2 and 3 frequency sweep results in Figure 2.13 show differences in the streamwise and spanwise directions, which is less significant in the impulse tests than in the frequency sweep tests.

Both frequency sweep and impulse test results follow similar trends of reducing natural frequency with increasing top mass. The mode 1 sweep results are close to the impulse tests, but the mode 2 sweep results are significantly below the impulse test results and the mode 3 sweep results show variance. The general trend across all tests completed is that natural frequencies from frequency sweeps are not fully consistent with the impulse tests. It is most likely that the inconsistencies are due to the modal shaker contributing mass, stiffness and damping to the structural response. Considering the difficulty in characterising the dynamic properties of the modal shaker, the impulse tests have been used in the subsequent interpretation of the experiments.

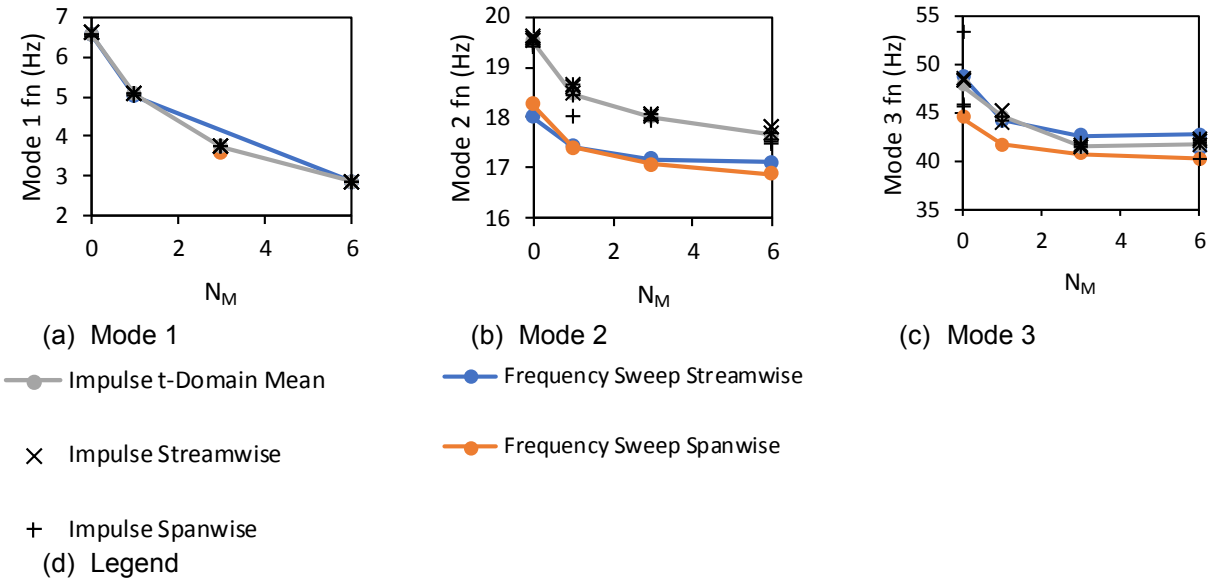

Figure 2.13. Example comparison of natural frequencies from frequency sweep analysis and impulse test time-domain analysis: Test 3, no scour

2.4.3.2 Damping Ratio for Unscoured Conditions

The natural frequencies for unscoured conditions at the start of each test are presented in Fig. 13 in Paper 3, Figure 2.14 presents the associated damping ratios. The damping ratio ζ was generally in the range of 0.5% to 2.0% for all tests, which is broadly similar to values reported from full scale-structures (e.g. discussion in Arany et al., 2016).

The differences in damping ratio between tests (Figure 2.14) do not seem to correspond with changes in the pile embedment, for example Tests 1 to 4 have very similar pile embedment and soil conditions yet different damping ratios. The differences are therefore most likely due to changes in damping within the structure, also reported by Arany et al. (2016) as the second greatest contributor to the overall damping ratio after aerodynamic effects.

2.4.4 Scour Effects on Natural Frequencies

Figure 2.15 presents the plots of frequency versus local embedment (L/D) grouped by mode number and number of top masses, excluding measurements where scour protection was present. Each subplot in Figure 2.15 includes a linear fit through the entire dataset, with Table 2.1 providing the fitting parameters governing the equation,

$$f_m = \alpha_{f,L}\left(\frac{L}{D}\right) + f_{i,L} \tag{2.1}$$

where $\alpha_{f,L}$ is the natural frequency sensitivity to embedment and $f_{i,L}$ is an intercept.

Figure 2.16 presents $\alpha_{f,L}$ values normalised by reference frequencies to provide dimensionless outputs, where reference frequencies were taken as f_m measured at the start of Test 1. From Figure 2.16 it is inferred that for a total scour depth of S_T = 1 D the natural frequency of mode 1 would reduce by approximately 2.6% to 4.8% (mean 3.5%). Similarly, the natural frequency of mode 2 would reduce by approximately 11.7% to 15.6% (mean 14.3%), and the natural frequency of mode 3 would reduce by approximately 6.8% to 8.4% (mean 7.5%).

Taking the mean values, this implies that the natural frequency of mode 2 is 4.13 times more sensitive to pile embedment than mode 1, and that mode 3 is 2.15 times more sensitive than mode 1. These results indicate that there would be merit in monitoring the second and third natural frequencies, rather than only the first mode, to identify scour damage in practice.

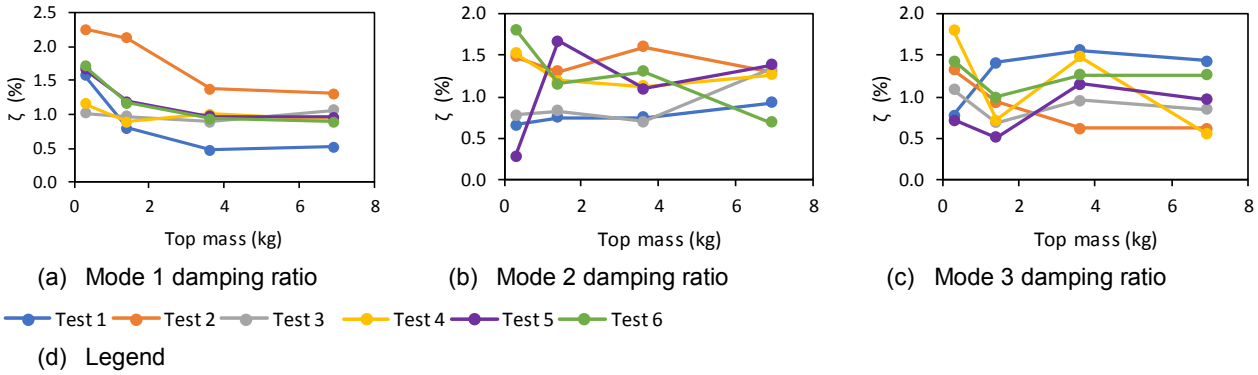

Figure 2.14. Inferred damping ratio at the start of each test

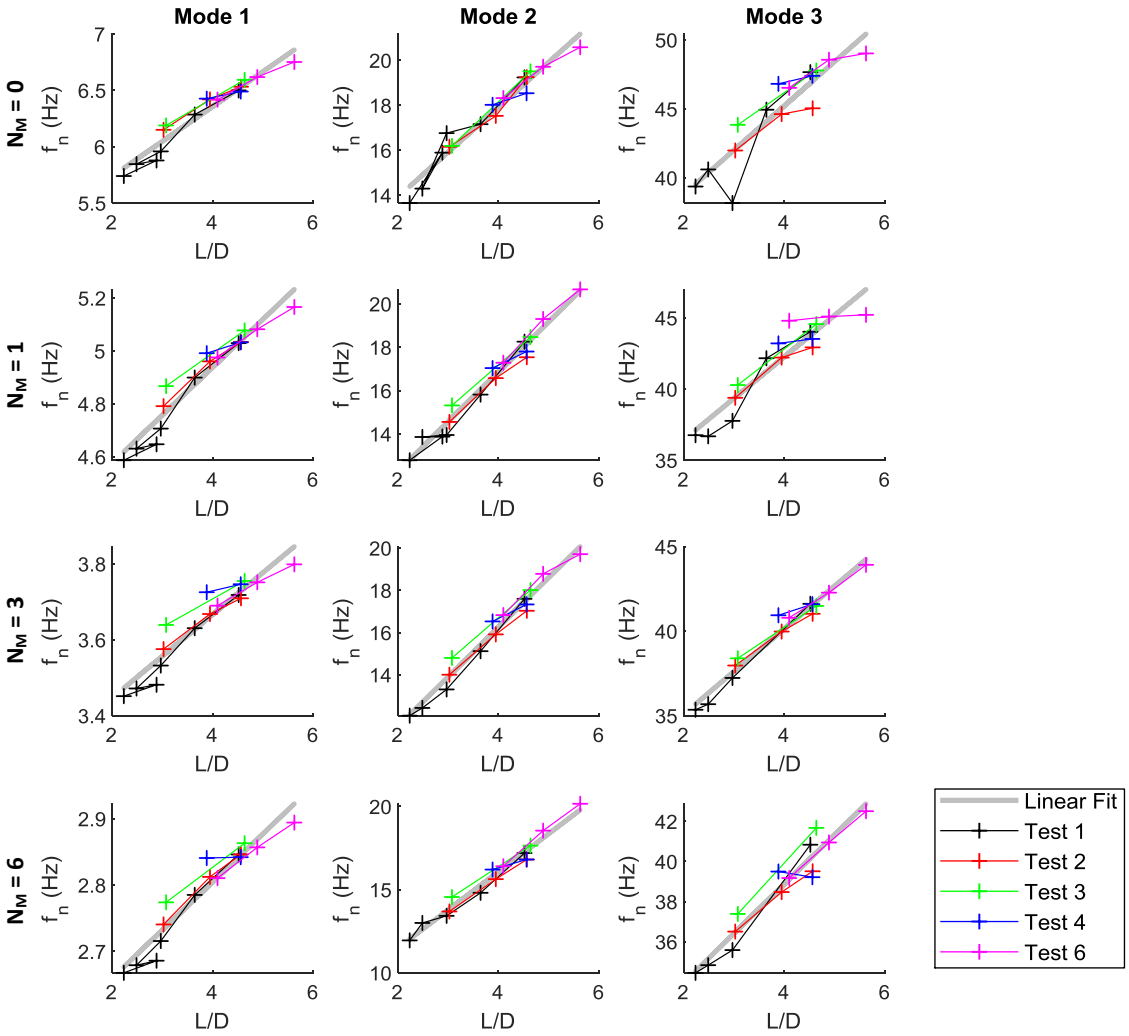

Figure 2.15. Natural frequency for local embedment changes induced by scour

Table 2.1. Natural Frequency versus Local Embedment Fitting Parameters

N_M =	0		1		3		6	
Mode	$\alpha_{f,L}$ [Hz]	$f_{i,L}$ [Hz]	$\alpha_{f,L}$ [Hz]	$f_{i,L}$ [Hz]	$\alpha_{f,L}$ [Hz]	$f_{i,L}$ [Hz]	$\alpha_{f,L}$ [Hz]	$f_{i,L}$ [Hz]
1	0.310	5.117	0.181	4.212	0.110	3.226	0.073	2.514
2	2.004	9.901	2.306	7.643	2.351	6.842	2.291	6.903
3	3.211	32.370	2.917	30.589	2.527	30.031	2.465	29.010

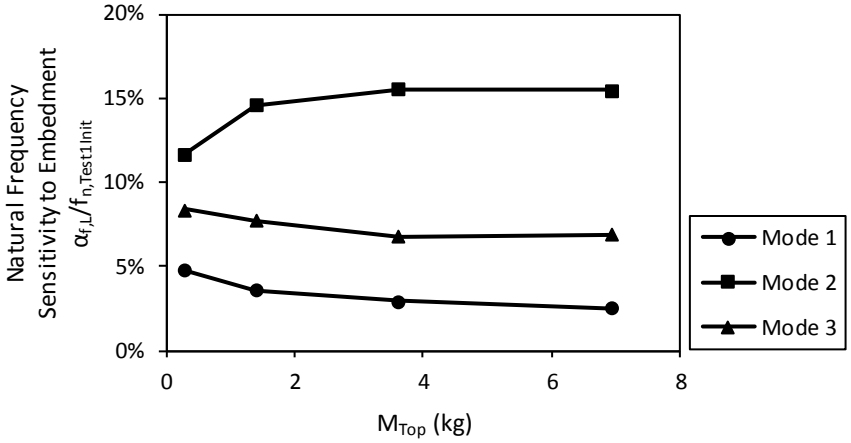

Figure 2.16. Natural frequency sensitivity to local embedment changes induced by scour

2.4.5 Mode Shape Analysis

2.4.5.1 Mode Shape Data

Structural health monitoring (SHM) data can be used to determine the modal parameters of instrumented offshore wind turbine structures, including the mode shapes (e.g. Devriendt et al., 2014), although such instrumentation is not common to all offshore wind farms. The previous section established that the natural frequency of mode 2 is a good indicator of scour development. If scour can be shown to have predictable and measurable effects on the mode shapes of an offshore wind structure, these can further inform recommendations on methods to detect scour development using SHM techniques.

The mode shapes were extracted from vectors of displacement amplitudes, v_0. The magnitude of v_0 is arbitrary, and a normalised version of the mode shape V is a more useful form:

$$\mathrm{V} = v_0 / \max(|v_0|) \tag{2.2}$$

Figure 2.17 presents example mode shapes with and without top mass. The differences in the shape of mode 1 with and without masses is relatively minor; however, in the example with top

masses there is an inflection in the shape of mode 1 near the base of the tower. From a review of the mode shape data output in processing, the inflection is more commonly present with 3 or more top masses attached. It is unclear what has caused the mode 1 inflection, but it may be due to a mass, inertia, or stiffness contribution of the transition piece.

The shape of mode 2 in Figure 2.17 is well captured by the accelerometer positions, with a clear difference in the maxima position with and without top mass. The shape of mode 3 in Figure 2.17 is the least well captured by the accelerometer positions, with the position of maxima being unclear. For mode 2 and 3 there is relatively little movement at the top of the tower with 6 top masses, and a zero-displacement position near the tower top.

2.4.5.2 Mode Shape Metrics

It was assumed that the measured mode shapes in the tower can be approximated by a polynomial curve. For mode 1 a 2nd order polynomial was fitted using *MATLAB* function *polyfit*. For mode 2 a 3rd order polynomial was used, and for mode 3 a 4th order polynomial was used. Figure 2.18 presents examples of the fitted mode shapes.

The fitted polynomials were used to assess the position of certain mode shape features such as maxima and zero-displacement positions, defined in Figure 2.19. For mode 1, since there are no maxima or zero positions captured, it was convenient to examine positions with displacement amplitudes of 25%, 50% and 75% of the maximum. For mode 2 and 3 the position of the maxima and a zero-displacement position near the top of the tower were found. For mode 3 the position of a zero-displacement position near the bottom of the tower is captured in some tests, but in many cases was below the bottom accelerometer.

Figure 2.20 presents the position of these features in unscoured conditions at the start of each test. All mode shape features tend to be closer to the tower top for increasing top mass. Qualitatively, this is consistent with the relative movement at the top of the structure reducing as the top mass increases.

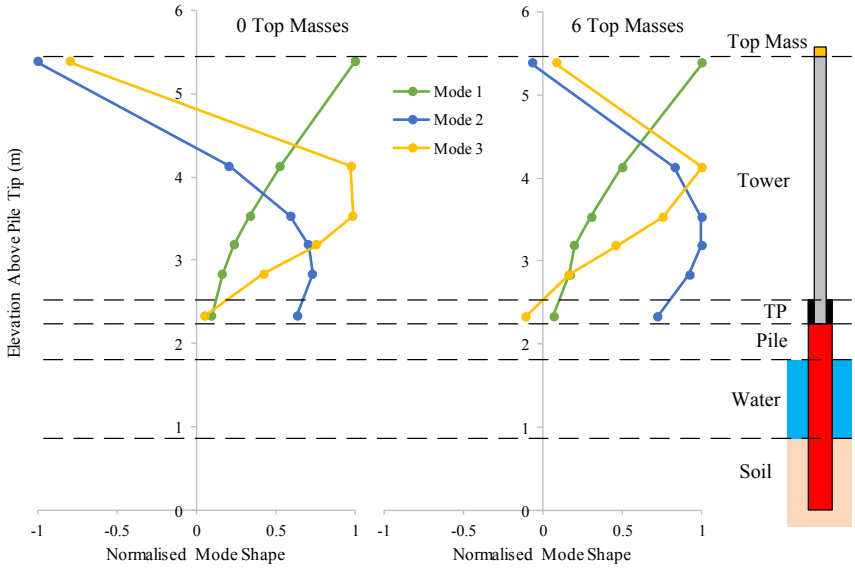

Figure 2.17. Example mode shapes: Test 1, no scour; impulse test results.

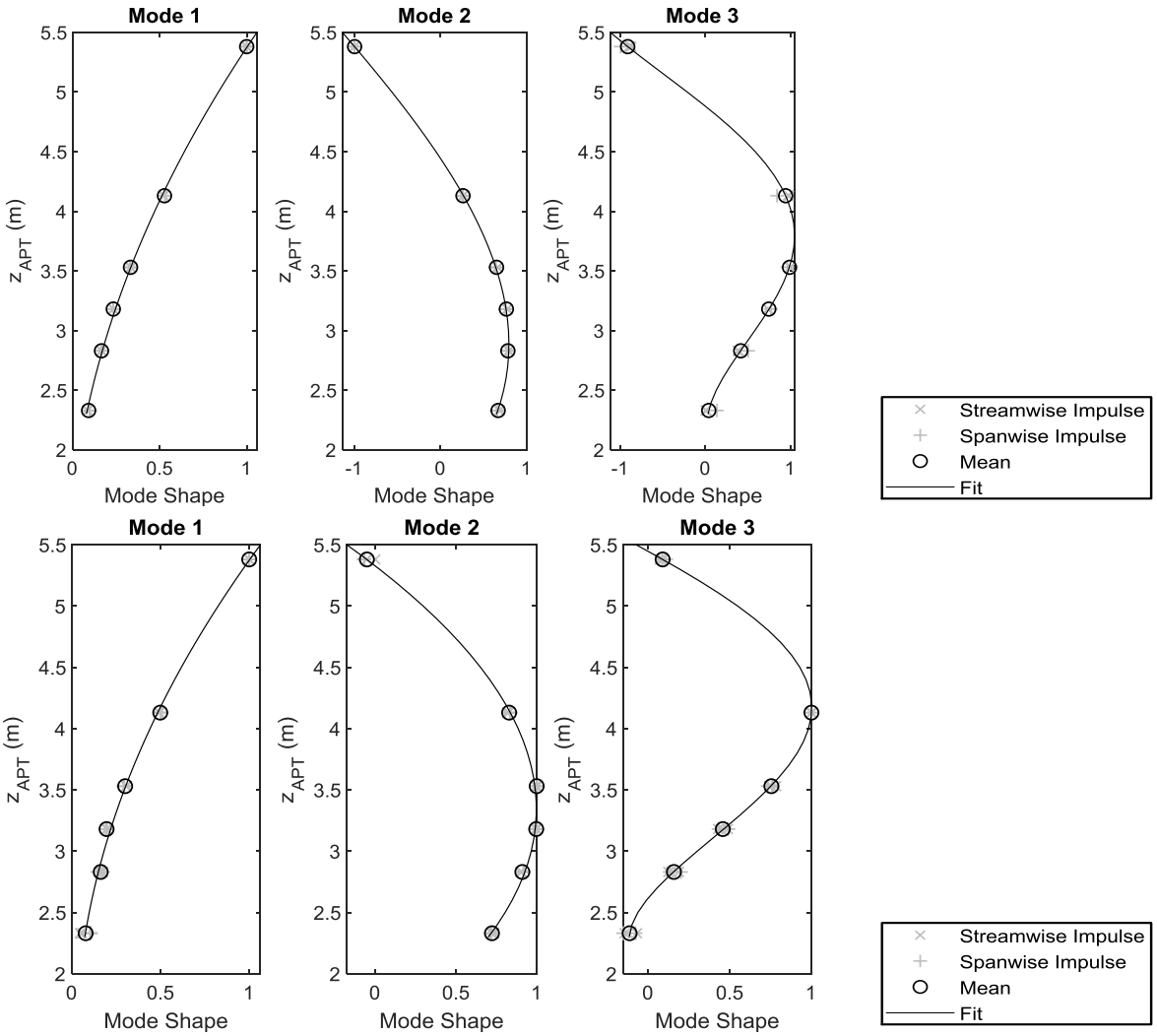

Figure 2.18. Example mode shape fitting with no top mass: Test 2, no scour, impulse test results: (a) 0 masses; (b) 6 masses.

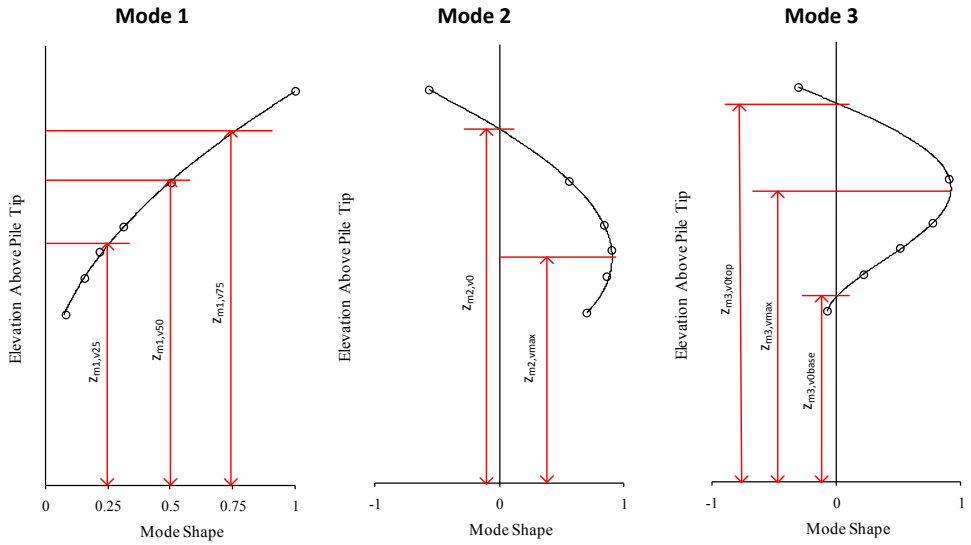

Figure 2.19. Definition of mode shape metrics.

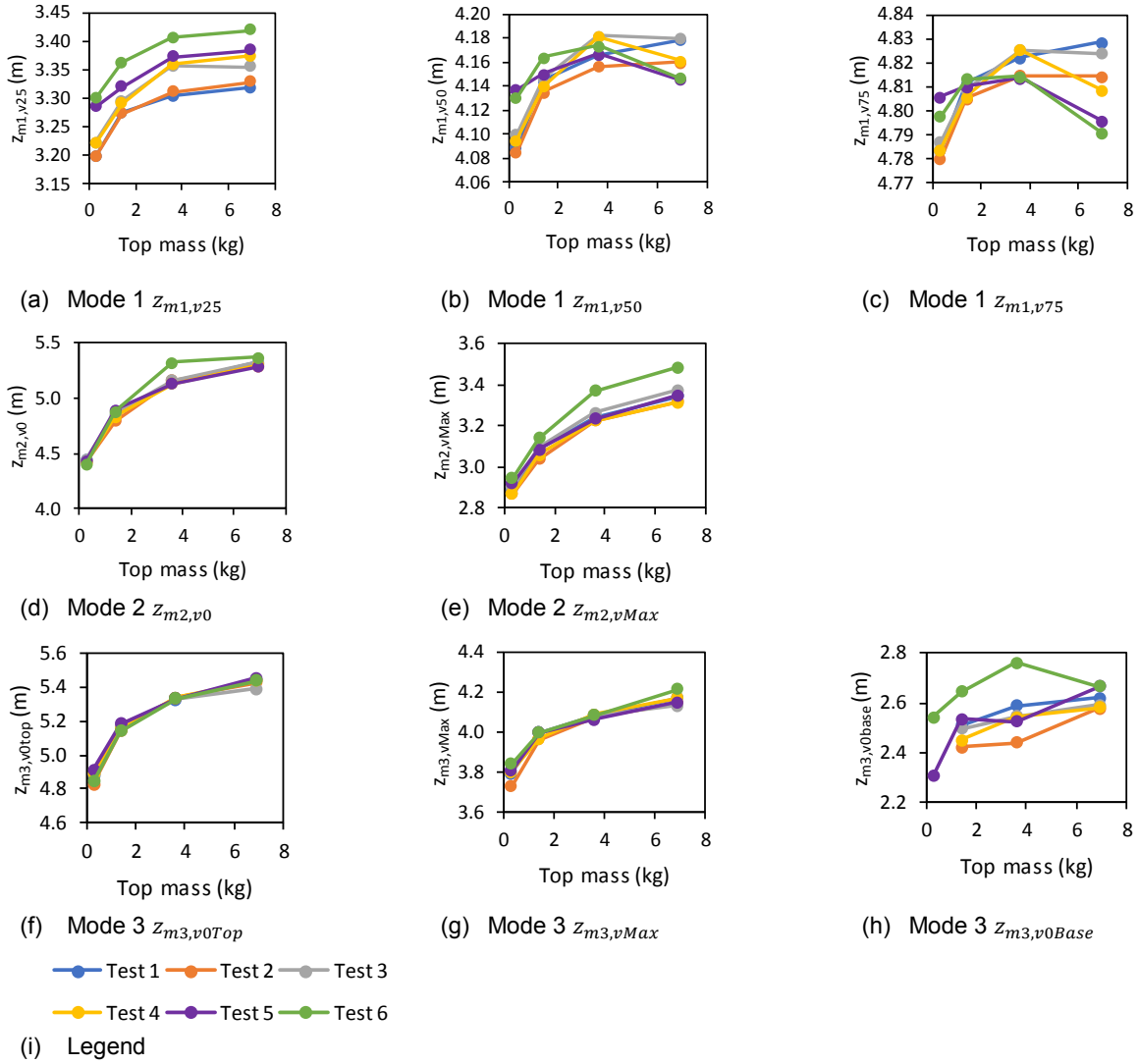

(a) Mode 1 $z_{m1,v25}$ (b) Mode 1 $z_{m1,v50}$ (c) Mode 1 $z_{m1,v75}$

(d) Mode 2 $z_{m2,v0}$ (e) Mode 2 $z_{m2,vMax}$

(f) Mode 3 $z_{m3,v0Top}$ (g) Mode 3 $z_{m3,vMax}$ (h) Mode 3 $z_{m3,v0Base}$

(i) Legend

Figure 2.20. Inferred position of mode shape features at the start of each test (see Figure 2.19 for definition diagram).

2.4.5.3 Scour Effects on Mode Shapes

Figure 2.21 presents the relationship between the elevation of the analysed mode shape features (and the measured natural frequency. The linear fits presented in Figure 2.21 are,

$$z = \alpha_{z,f} f_m + z_{i,f} \tag{2.3}$$

where $\alpha_{z,f}$ is the sensitivity to frequency and $z_{i,f}$ is the intercept; values in Table 2.2. The mode shape feature elevation sensitivity to embedment ($\alpha_{z,L}$) was calculated as:

$$\alpha_{z,L} = \frac{dz}{dL} = \frac{\alpha_{z,f}}{D} \alpha_{f,L} \tag{2.4}$$

Table 2.3 and Figure 2.22 and present the resultant general sensitivity of mode shape feature positions to changes in the pile local embedment ($\alpha_{z,L}$). Figure 2.22 shows that, for modes 1 and 2, the mode shape feature sensitivity clearly varies with top mass; for mode 3 the relationship between mode shape feature sensitivity and top mass is unclear.

The mode 1 features become more sensitive to embedment changes at lower positions on the structure. The mode 2 zero displacement position near the tower top is more sensitive to embedment changes with no top mass than with increasing top mass. In contrast to this, the maxima of mode 2 becomes more sensitive to embedment change with increasing top mass. This could be considered analogous to the top of the tower approaching a pinned condition as the top mass increases.

The mode 3 zero displacement position near the tower top has a low sensitivity to embedment change. The features further down the tower (maxima and zero-displacement near the tower base) are the more sensitive to natural frequency, which is a similar response to mode 1. The mode 3 zero displacement position near the transition piece has a high sensitivity to natural frequency, but also has the most significant scatter, which may have occurred due to the position moving below the lowest accelerometer location in many cases.

These results indicate that SHM campaigns could adopt accelerometers low within the tower to identify the onset of scouring by monitoring changes in the shape of mode 1 (e.g. movement of the 25% point) and movement of the mode 2 maxima.

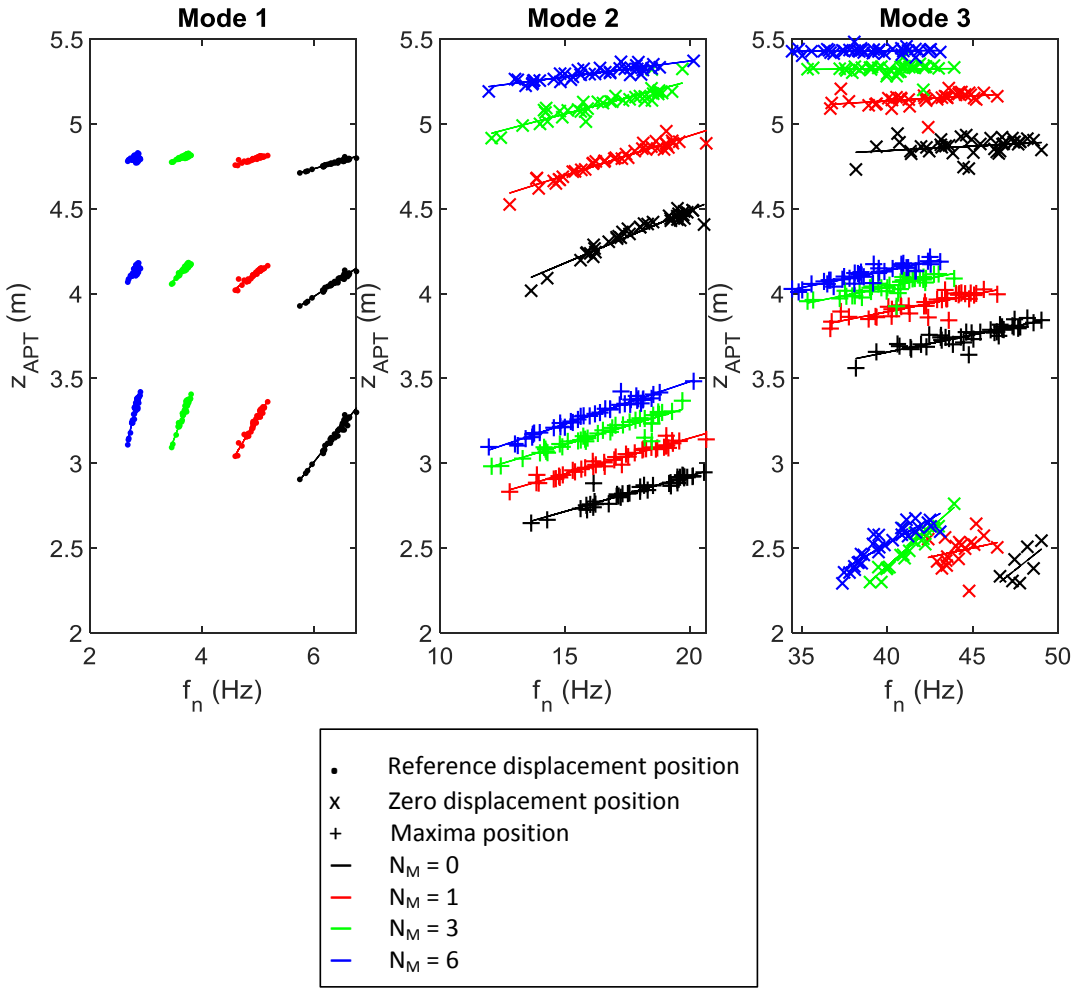

Figure 2.21. Elevation of mode shape metrics plotted against natural frequency (see Figure 2.19 for definition diagram)

Table 2.2. Mode shape metric fitting parameters

N_M =	0		1		3		6	
Mode Shape Feature (see Figure 2.19)	$\alpha_{z,f}$ **[m/Hz]**	$z_{i,f}$ **[m]**	$\alpha_{z,f}$ **[m/Hz]**	$z_{i,f}$ **[m]**	$\alpha_{z,f}$ **[m/Hz]**	$z_{i,f}$ **[m]**	$\alpha_{z,f}$ **[m/Hz]**	$z_{i,f}$ **[m]**
Mode 1 25%	0.420	0.493	0.554	0.508	0.880	0.067	1.311	-0.361
Mode 1 50%	0.220	2.663	0.245	2.904	0.347	2.866	0.365	3.111
Mode 1 75%	0.096	4.162	0.097	4.317	0.126	4.343	0.068	4.607
Mode 2 Zero	0.062	3.251	0.047	3.994	0.039	4.478	0.019	4.996
Mode 2 Max	0.042	2.087	0.042	2.305	0.044	2.448	0.050	2.480
Mode 3 Zero Top	0.005	4.629	0.006	4.897	0.001	5.303	0.000	5.420
Mode 3 Max	0.020	2.834	0.020	3.091	0.020	3.227	0.020	3.327
Mode 3 Zero Base	0.080	-1.429	0.022	1.523	0.089	-1.162	0.058	0.203

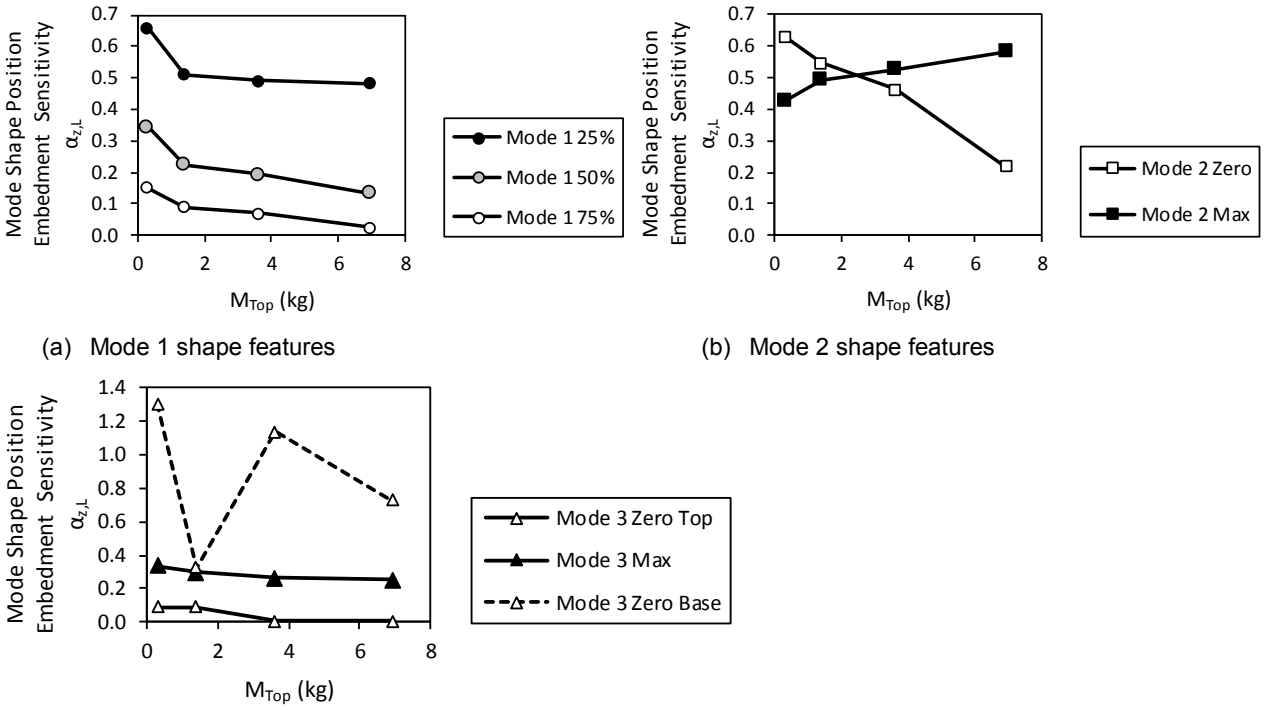

(a) Mode 1 shape features

(b) Mode 2 shape features

(c) Mode 3 shape features

Figure 2.22. Effect of embedment change due to scour on mode shape metrics (see Figure 2.19 for mode shape metric definition diagram)

Table 2.3. Mode shape feature elevation sensitivity to scour depth

Mode Shape Feature (see Figure 2.19)	N_M **= 0**	N_M **= 1**	N_M **= 3**	N_M **= 6**	**Mean**
	$\alpha_{z,L}$	$\alpha_{z,L}$	$\alpha_{z,L}$	$\alpha_{z,L}$	$\alpha_{z,L}$
Mode 1 25%	0.659	0.510	0.492	0.483	0.536
Mode 1 50%	0.346	0.226	0.194	0.134	0.225
Mode 1 75%	0.150	0.089	0.070	0.025	0.084
Mode 2 Zero	0.630	0.547	0.462	0.218	0.464
Mode 2 Max	0.426	0.493	0.526	0.582	0.507
Mode 3 Zero Top	0.087	0.088	0.007	0.003	0.046
Mode 3 Max	0.334	0.297	0.260	0.253	0.286
Mode 3 Zero Base	1.304	0.322	1.140	0.726	0.873

2.4.6 Summary of Scour Effects on Structural Dynamics Measurements

This analysis of the experimental results has explored how a change in embedded length due to scour is anticipated to manifest as changes in the first three bending modes of vibration. The degree of the effects was found to depend on the top mass attached to the structure. As an example (using Figure 2.16 and Table 2.3), the generalised effects per pile diameter of total scour depth (i.e. $S_T/D = 1$) are summarised below:

i. **Mode 1 –** The natural frequency reduces by 2.6% to 4.8%, these values are similar to the results of previous numerical studies (e.g. approximately 4% from Damgaard et al. (2013) in Figure 1.26). Analysis of the mode shape metrics shows that all features move downwards: the 75% displacement position by $\Delta z/S_T =$ -0.02 to -0.15, the 50% position by $\Delta z/S_T =$ -0.13 to -0.35, and the 25% by $\Delta z/S_T =$ -0.48 to -0.66.

ii. **Mode 2 –** The natural frequency reduces by 11.7% to 15.6% these values are slightly higher than the result of previous numerical studies (e.g. approximately 8% from Sørensen and Ibsen (2013) in Figure 1.27). Analysis of the mode shape metrics shows that all features move downwards: the zero-displacement position by $\Delta z/S_T =$ -0.22 to -0.63 and the maxima by $\Delta z/S_T =$ -0.42 to -0.58.

iii. **Mode 3 –** The natural frequency reduces by 6.8% to 8.4%. Analysis of the mode shape metrics shows that all features move downwards: the zero-displacement position near the tower top by $\Delta z/S_T =$ -0.003 to -0.09, the maxima by $\Delta z/S_T =$ -0.25 to -0.33, and the zero-displacement near the TP by $\Delta z/S_T =$ -0.32 to -1.3.

2.5 Monotonic Lateral Loading Tests

2.5.1 Test Configuration

Monotonic lateral loading tests were performed at the end of each of the flume experiment tests using the general layout presented in Figure 2.23. Six lateral loading tests were performed: one with unremediated scour, and five with model scour protection systems installed. The tests were performed to provide insight into the effect of scour and scour protection on the performance of monopile foundations under loading at large displacements.

In the lateral loading tests a horizontal load, H, was applied in the streamwise direction at elevation z = 2.4725 m above pile tip, via an independent reaction frame. Displacements in the streamwise direction were measured using LVDTs at two elevations, z = 1.9 m and z = 2.4 m, with the scaffold as a reference frame. Strain gauges measured bending strains at z = 1.6 m. Appendix C.8 presents supplementary information on the experimental setup and data analysis methods for the monotonic lateral loading tests.

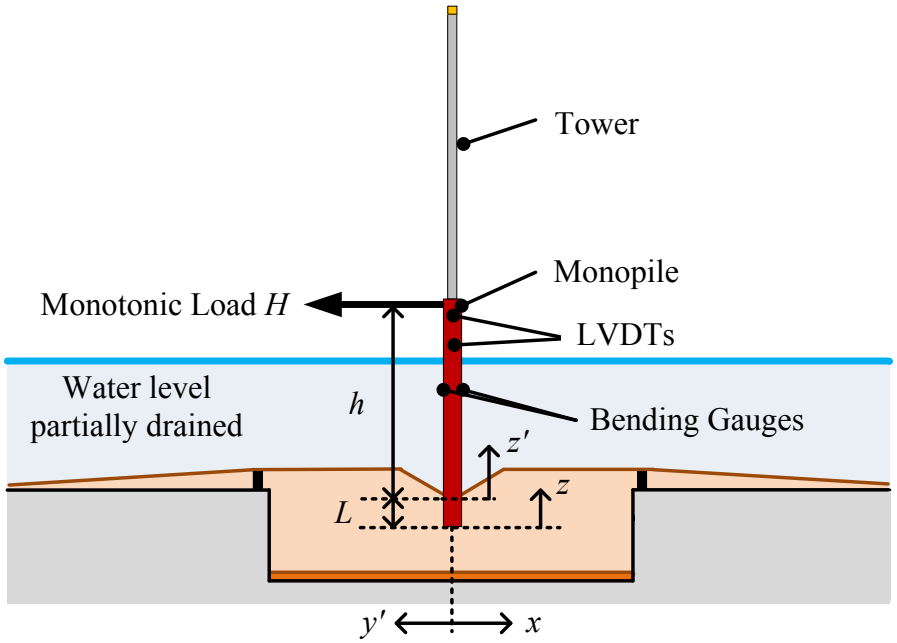

Figure 2.23. Monotonic loading test layout; x and z are flume coordinates (Fig. 2 in Paper 3); y' and z' are coordinates used in the analysis of lateral loading tests, where z' is the height above the median local bed level adjacent to the pile wall.

2.5.2 Lateral Loading Test Results

Figure 2.24 presents the output load-displacement and moment-rotation curves for all tests, in absolute terms and normalised quantities. The normalised load-displacement, H-v_G, and moment-rotation, M_G-θ_G, curves use a reference load, H_R, at a reference ground displacement, $v_G = v_R = 0.1D$, and a reference ground level moment, M_R, at a reference ground level rotation, $\theta_G = \theta_R = 3°$. These reference values nominally represent the condition at the ultimate capacity. Table 2.4 presents the maximum and reference horizontal and moment capacities.

Figure 2.25 presents the test results in two ways: (1) against the pile local embedment, L, and (2) against the pile local embedment in sand, $L - t_{sp}$, representing the embedment excluding the scour protection thickness t_{sp} (t_{sp} from Paper 3). In Figure 2.25, as expected, there is a general trend for the load capacity H_{max} and moment capacity $M_{G,max}$ to increase with pile embedment.

Reference lines are drawn between the local embedment of Test 1 (unremediated scour), and Test 5 (P-RA), which had a relatively thin layer of scour protection. The reference lines pass very close to the local level results for Test 4 (R-RF2), which had a similar scour protection thickness to Test 5. This suggests that the scour protection capacity contribution was similar in Tests 4 and 5.

Test 2 (TFN) and Test 3 (R-RF1) have very similar geometries, but the capacity of Test 3 is higher, sitting above the reference line in Figure 2.25. The capacity of Test 2 is lower and below the reference line. This suggests two things, (1) the lateral capacity contribution of the rock fill in Test 3 was similar to or greater than that of the sand, and (2) the lateral capacity contribution of the tyre-filled nets in Test 2 was negligible or much lower than that of the sand.

Test 6 (R-RF3) has a similar local embedment to Test 5 (P-RA), but a lower capacity relative to the reference line in Figure 2.25. This implies that the scour protection in Test 6 had a smaller capacity contribution than that of the equivalent *in situ* sand. It is likely this reduced capacity is caused by the falling apron of scour protection adjacent to the pile in Test 6 (Fig. 20 in Paper 3). In Test 5 the changes in bathymetry were distant from the pile, and the global scour does not appear to have had a detrimental effect on the lateral capacity.

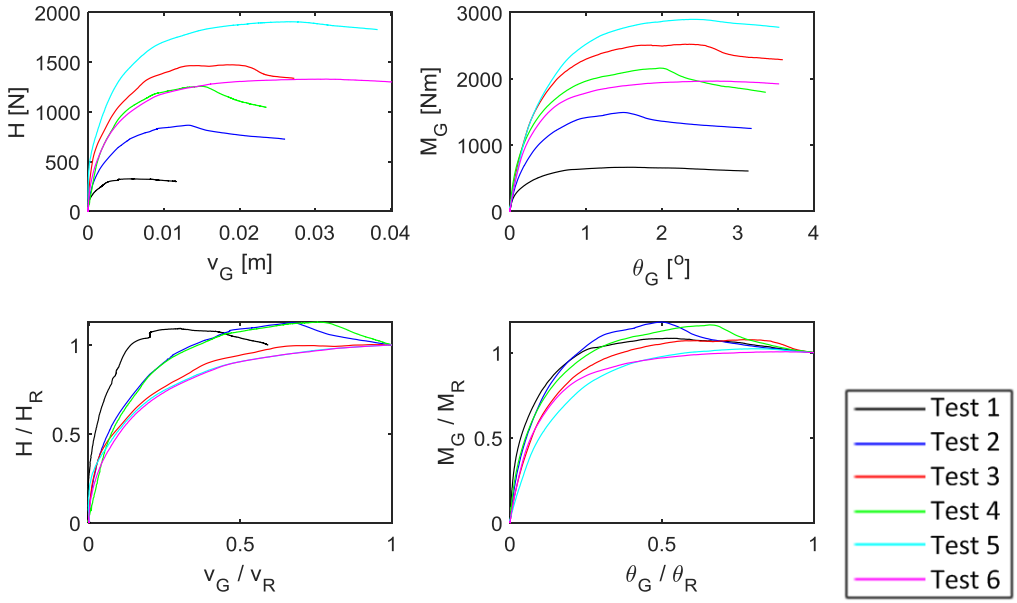

Figure 2.24. Monotonic lateral loading curves: flume experiment results

Table 2.4. Monotonic Lateral Loading Capacity Parameters: Flume Experiment Results

FFF Test (Table 5 in Paper 3)	H_{max} [N]	$M_{G,max}$ [Nm]	v_R [mm]	H_R [N]	θ_R [°]	M_R [Nm]
1[a]	327	665	11.6	300	3.0	613
2 (R-TFN)	866	1491	19.7	770	3.0	1264
3 (R-RF1)	1473	2521	19.7	1471	3.0	2342
4 (R-RF2)	1258	2161	19.7	1115	3.0	1858
5 (P-RA)	1906	2896	19.7	1875	3.0	2831
6 (R-RF3)	1330	1965	19.7	1305	3.0	1954

[a] For Test 1, v_G did not reach $0.1D$, v_R and H_R were measured at the maximum value of v_G

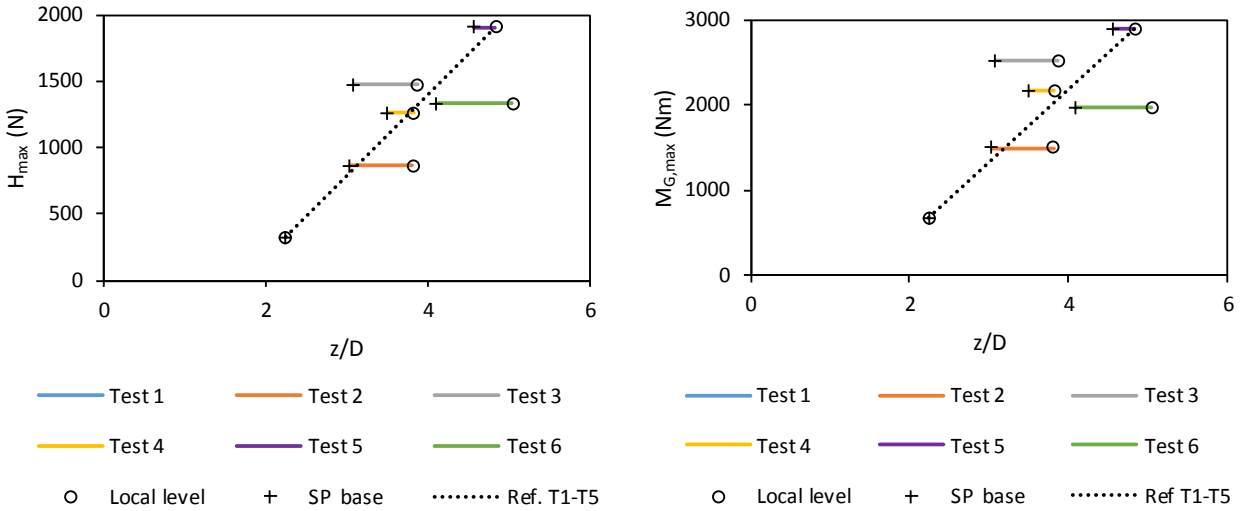

Figure 2.25. Monotonic lateral loading capacity parameters plotted with pile embedment; 'o' indicates local embedment level; '+' indicates embedment in sand excluding scour protection; length of the solid lines is the scour protection thickness; dotted line is a reference line drawn between the Test 1 and Test 5 results and is not intended as a best fit. The global bed level at the end of all tests was located at $z/D = 4.1 \pm 0.2$ (Appendix C.9.1).

2.6 Conclusions

2.6.1 Execution of Flume Experiments

This Section has described the flume experiments, in which a model monopile – tower system was driven into a compacted sand bed, and subsequently exposed to scour in the Fast Flow Facility flume. Six tests were performed, with variations in the initial embedment, target local scour depth, target global scour depth, and scour protection systems.

The experiments were successful in providing measurements of structural dynamics changes with scour development and with scour protection, as well as producing monotonic loading curves. CPT tests showed the bed preparation to be consistent and achieve a dense condition as intended. The scour development and effects of scour were repeatable, and the use of various scour protection models produced differing results as anticipated. Appendix C.10 summarises the practical issues and lessons learned from the flume experiments.

A comparison of the natural frequency measured with two method, frequency sweeps and impulse tests, showed inconsistencies. These inconsistencies are suspected to be due to effects of the modal shaker attached in the frequency sweep tests. The results of the impulse tests were therefore used in subsequent interpretation of the experiments.

2.6.2 Scour Effects on Structural Dynamics

The natural frequency of mode 2 is the most sensitive to scour. The elevation of the maxima in the shape of mode 2 was also shown to be sensitive to scour.

SHM campaigns for scour detection should target the positioning of accelerometers to be around the maxima of mode 2, to provide evidence of scour damage at operating wind farms. The research has not considered other potential damage mechanisms that may influence the dynamics of a wind turbine structure (e.g. damage of the grouted joint in the transition piece). If these other forms of damage occur in the field, they may also induce similar symptoms to those caused by scour damage, such as drops in the natural frequencies and mode shape changes. In these cases, if the source of damage is uncertain, scour development could be eliminated as a potential source of damage if the symptoms are inconsistent with those anticipated for scour based on the experimental results.

2.6.3 Scour Protection Effects

Following the discussion and conclusions in Paper 3, the results have the following implications for full-scale structures with scour protection systems installed:

i. **Pre-installed rock armour** scour protection prevents development of local scour. Changes in the global bed level and secondary scour did not affect the natural frequency of the structure, since the changes were sufficiently distant from the pile.

ii. **Remedial rock fill** scour protection provides an enhancement to the foundation stiffness and strength. The enhancement to stiffness is less than that of the original *in situ* sand, but the enhancement to strength could be greater than the *in situ* sand. These enhancements can be diminished if global scour causes the scour protection to become unstable, and if falling aprons form adjacent to the pile wall.

iii. **Remedial tyre-filled net** scour protection prevents the development of further local scour, but may cause secondary scour. The tyre-filled nets have a negligible effect on the foundation stiffness and capacity.

iv. **Sand accretion** in the scour protection matrix was observed in the tests, caused by the high sediment supply in the live bed test conditions. A similar phenomenon occurred in the work of An et al. (2014). The accretion caused increases in the natural frequencies of up to approximately 2% (Fig. 19 in Paper 3). This supports the hypothesis that the scour protection stiffness was enhanced by particle interlocking effects with sand in the void space. It is unclear if sand accretion occurs in the field, the observed frequency gains for scour protected turbins at Greater Gabbard offshore wind farm were on average 1.34% over 81 months (Hucker et al., 2019) and may be evidence of this effect.

Section 3 – One-dimensional Finite Element Model Development

3.1 Introduction

This Section presents a numerical model to predict the natural frequencies of monopile-supported offshore wind turbine structures. The work adopts a one-dimensional (1D) finite element approach, modelling distributed soil reactions down the pile.

3.2 Model Description

3.2.1 Finite Element Model Configuration

Figure 3.1 presents an overview of the model. The natural frequencies of the structure are determined using an eigenvalue analysis method, described in Section 3.3. Within the model the height above pile tip is used for the vertical coordinate, z, since it is problematic to use a moving seabed with scour as a reference datum.

3.2.2 Soil Stiffness Components

Table 3.1 presents the formulation of the soil stiffness components derived from the PISA 1D model, with the assumption that the stress-strain response is small and remains linear elastic. The non-dimensional stiffness coefficients (k_p,k_m,k_H,k_M) are specified in the general form of the normalised soil reaction curves (Figure 1.14). The dimensioned soil stiffness components (K_p,K_m,K_H,K_M) are defined using the soil reaction normalisations (Table 1.1), these depend on the local small strain shear stiffness G_0. Table 3.2 provides the assumed general forms of G_0 for clay and sand soils. Section 3.5.5 presents further detail on the G_0 expressions implemented in *EigPile*.

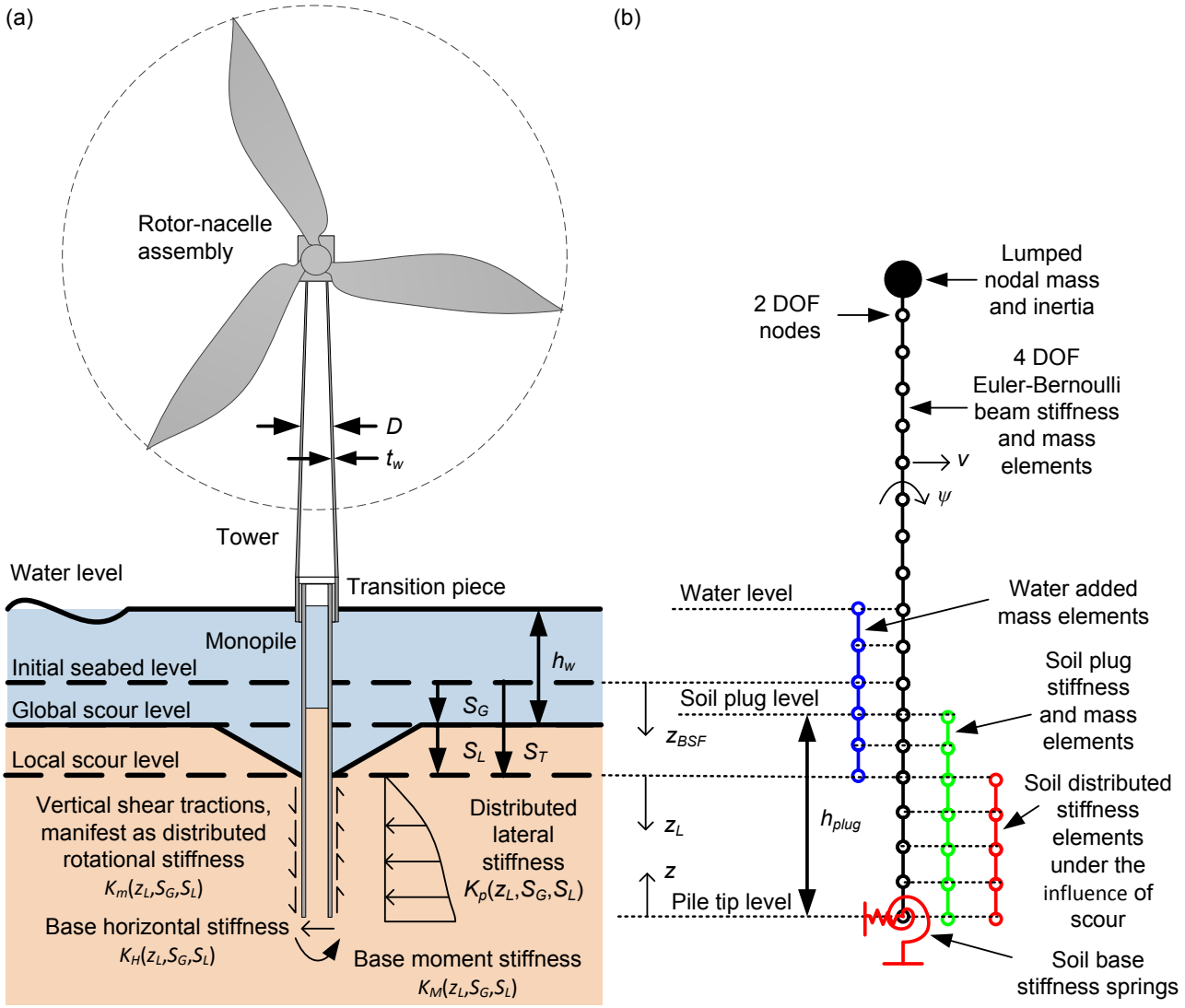

Figure 3.1. *EigPile* finite element model configuration for monopile eigenvalue analysis: (a) Idealised physical configuration; (b) 1D numerical model representation. Coordinate systems: z is used to formulate and define the model; z_{BSF} is used to specify and interpret the soil properties; z_L is used to interpret the influence of scour on the soil properties.

Table 3.1. Soil stiffness coefficients

Stiffness component (Figure 3.1(a))	Non-dimensional	Dimensioned
Distributed lateral stiffness	$k_p = \frac{d\overline{p}}{d\overline{v}}$	$K_p = \frac{dp}{dv} = k_p G_0$
Distributed rotational stiffness	$k_m = \frac{d\overline{m}}{d\overline{\psi}}$	Clay $K_m = \frac{dm}{d\psi} = k_m G_0 D^2$ Sand $K_m = \frac{dm}{d\psi} = k_m G_0 D \left(\frac{p}{\sigma_v'}\right) = 0$
Base horizontal stiffness	$k_H = \frac{d\overline{H}_B}{d\overline{v}_B}$	$K_H = \frac{dH_B}{dv} = k_H G_0 D$
Base moment stiffness	$k_M = \frac{d\overline{M}_B}{d\overline{\psi}_B}$	$K_M = \frac{dM_B}{d\psi} = k_M G_0 D^3$

Table 3.2. General form of small strain shear modulus expressions

Clay (e.g. PISA Final Report, 2016)	Sand (e.g. Hardin and Richart, 1963)
$G_0 = Bp'$	$G_0 = Bf(e)p_{ref}\left(\frac{p'}{p_{ref}}\right)^{0.5}$

3.2.3 Influence of Scour

In the presence of scour, the effective stresses in the soil are reduced, leading to a reduction in the small strain shear stiffness G_0 of the soil, and hence a reduction in the soil stiffness components (K_p,K_m,K_H,K_M). For all soil types it is assumed that excess pore water pressures are fully dissipated and hence that hydrostatic conditions are restored after the scour processes have occurred.

Figure 3.2(a) & (b) presents the bilinear approach suggested by the design standards (e.g. API, 2011) for calculation of the apparent vertical effective stress $\sigma'_{v,A}$ adjacent to the pile under the influence of scour. In API (2011) Δz_O is given as $6D$; the appropriateness of this value is explored in Section 4.

Table 3.3 presents the expressions for $\sigma'_{v,A}$, which is a function of the 'global effective stresses' $\sigma'_{v,G}$, 'local effective stress' $\sigma'_{v,L}$, and the local scour influence factor α_L, where $0 \leq \alpha_L \leq 1$ (Appendix A: Paper 1). Figure 3.2(c) shows an example profile of the local scour influence factor, α_L. The α_L implied by the design standards has a bilinear variation with depth, hence $\sigma'_{v,A}$ will not be bilinear if there is any variation in the soil effective unit weight γ'. Section 3.5.6 presents further detail on the implementation of $\sigma'_{v,A}$ and α_L in *EigPile*.

3.2.4 Influence of Scour Protection

When scour protection is introduced, the soil stiffness components (K_p,K_m,K_H,K_M) are influenced by two effects: (i) changes in the apparent vertical effective stress $\sigma'_{v,A}$ within and below the scour protection, and (ii) the additional stiffness of the scour protection material.

Figure 3.3 presents the proposed bilinear approach to calculate $\sigma'_{v,A}$ under the influence of scour, for cases where the scour protection level adjacent to the pile wall is either (a) recessed or (b) raised relative to the global bed level.

To estimate the additional stiffness introduced by the scour protection, it is reasonable to assume that G_0 for scour protection materials can be estimated from standard correlations for granular materials (i.e. for sand, Table 3.2). The following correlation is proposed,

$$G_0 = B_{SP} p_{ref} \left(\frac{p'}{p_{ref}} \right)^{0.5} \tag{3.1}$$

where B_{SP} is a (non-dimensional) scour protection stiffness coefficient expected to vary between scour protection types.

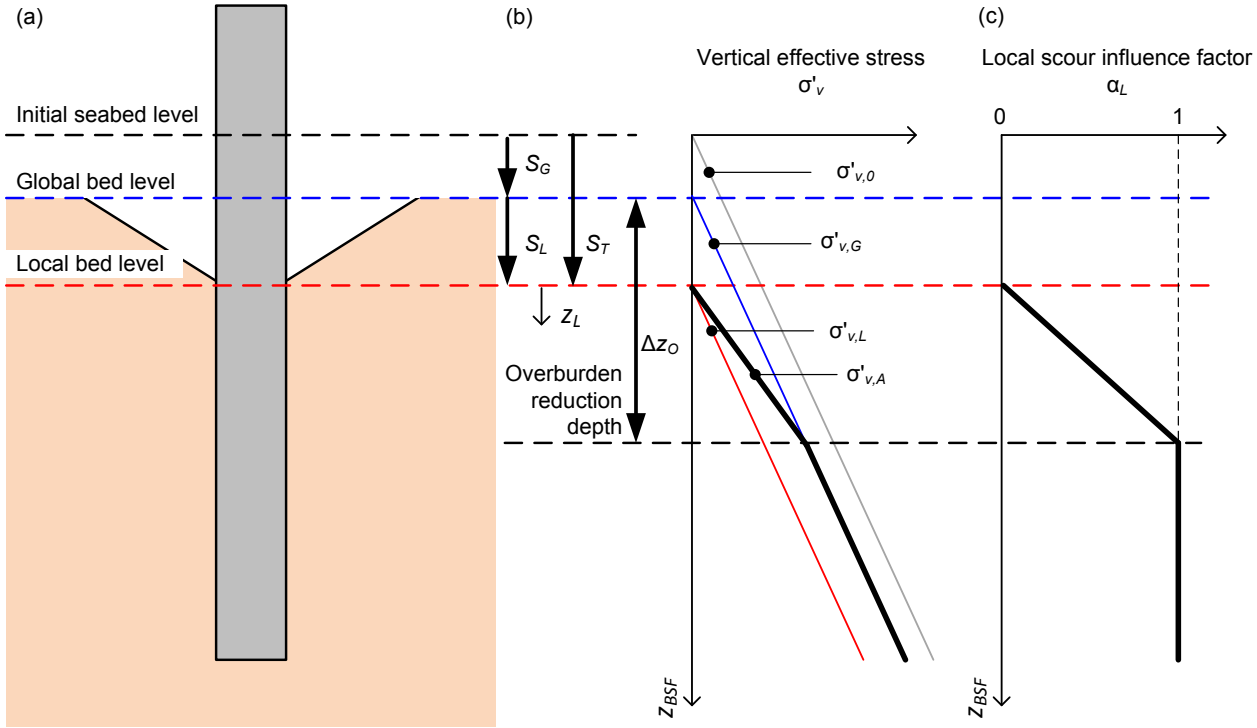

Figure 3.2. Definition of soil vertical effective stress profiles under the influence of scour: (a) Idealised local scour hole geometry; (b) Vertical effective stress profiles; (c) Bilinear profile of local scour influence factor, α_L; z_{BSF} is the depth below seafloor at the time of pile installation.

Table 3.3. Expressions for vertical effective stress under the influence of scour

Description	Vertical effective stress
Unscoured effective stress	$\sigma'_{v,0} = \gamma' z_{BSF}$
Global effective stress	$\sigma'_{v,G} = \gamma'(z_{BSF} - S_G)$
Local effective stress	$\sigma'_{v,L} = \gamma'(z_{BSF} - S_T)$
Apparent effective stress adjacent to the pile wall	$\sigma'_{v,A} = \sigma'_{v,L} + \alpha_L(\sigma'_{v,G} - \sigma'_{v,L})$

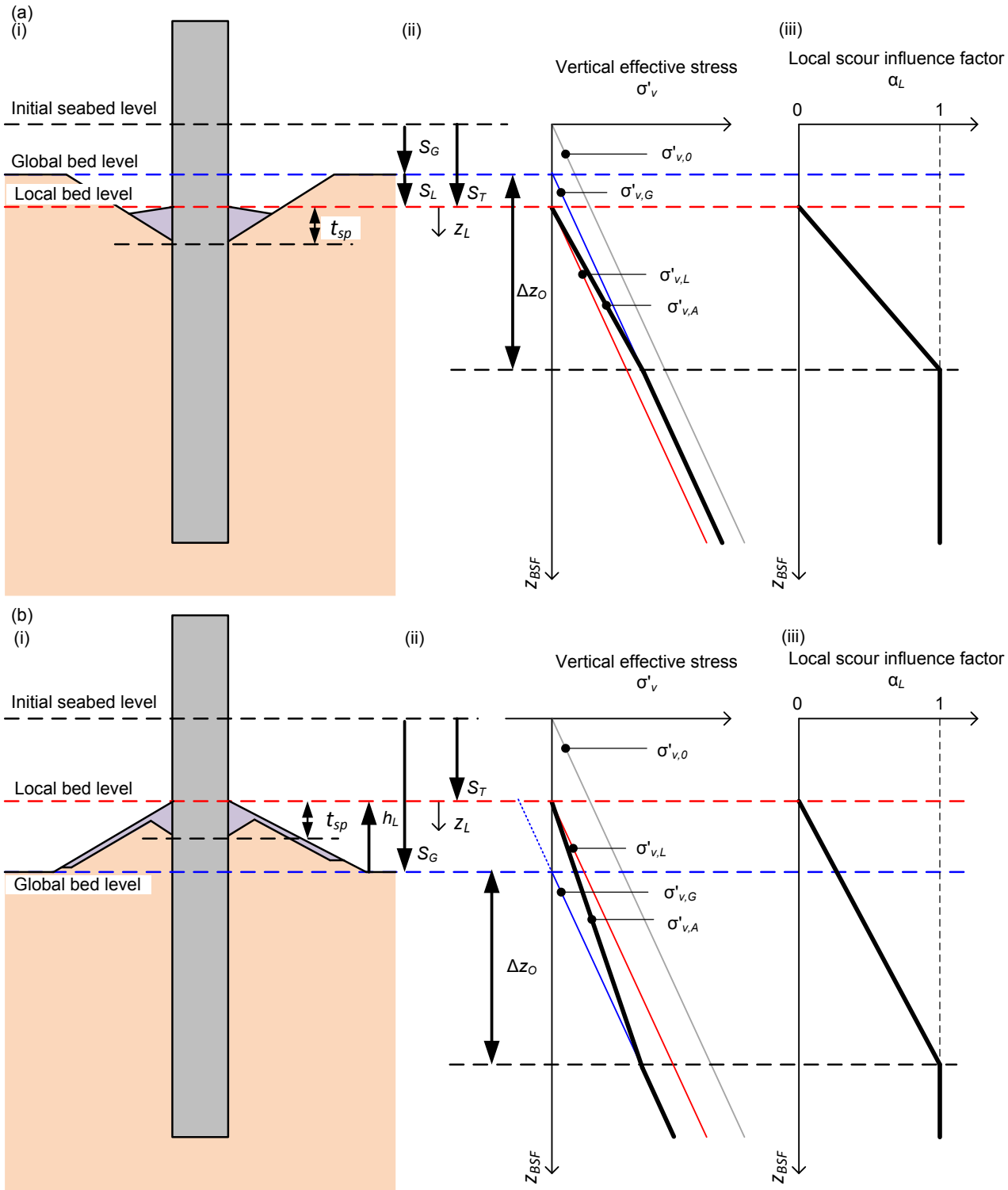

Figure 3.3. Proposed soil vertical effective stress profiles under the influence of scour protection: (a) Scour protection recessed in scour hole, $S_T > S_G$; (b) Scour protection raised above global bed level, $S_T < S_G$. (i) Idealised scour protection geometry; (ii) Vertical effective stress profiles; (iii) Bilinear profile of local scour influence factor.

3.3 Eigenvalue Problem

The equation of motion for a system with mass matrix $\mathbf{M}$, damping matrix $\mathbf{C}$, and stiffness matrix $\mathbf{K}$ subjected to an external force F is (after Williams, 2016),

$$\mathbf{M}\ddot{v} + \mathbf{C}\dot{v} + \mathbf{K}v = \mathrm{F} \tag{3.2}$$

where v is a displacement vector. For an undamped ($\mathbf{C} = 0$) freely vibrating ($\mathrm{F} = 0$) system with an amplitude V and a circular natural frequency $\omega_m = 2\pi f_m$, it can be shown that,

$$(\mathbf{K} - \lambda_m \mathbf{M})\mathrm{V}_m = 0 \tag{3.3}$$

where $\lambda_m = {\omega_m}^2$. For non-trivial solutions, $|\mathbf{K} - \lambda_m \mathbf{M}| = 0$. The natural frequencies can therefore be calculated using an eigenvalue analysis to determine the eigenvalues (λ_m) and the associated mode shape eigenvectors (V_m).

3.4 Finite Element Formulation

3.4.1 Beam Elements

The pile-tower structure is modelled with four degree-of-freedom Euler-Bernoulli beam elements employing the conventions shown in Figure 3.4, based on the notes in Burd (2018, *pers. comm.*).

The element stiffness matrix $\mathbf{K_{e,beam}}$ and element mass matrix $\mathbf{M_{e,beam}}$ contributions are,

$$\mathbf{K_{e,beam}} = \int_{z_1}^{z_2} \mathbf{B_b^T}.EI.\mathbf{B_b}\ dz \tag{3.4}$$

$$\mathbf{M_{e,beam}} = \int_{z_1}^{z_2} \mathbf{B_\psi^T}.j.\mathbf{B_\psi} + \mathbf{B_v^T}.\rho A.\mathbf{B_v}\ dz \tag{3.5}$$

where $\mathbf{B_v}$ is a vector of Hermitian shape functions, and $\mathbf{B_\psi}$ and $\mathbf{B_b}$ contain shape function derivatives. These are matrices defined in terms of the reference coordinate a (Figure 3.4) as,

$$\mathbf{B_v} = [\,1 - 3a^2 + 2a^3 \quad -aL_e(1 - 2a + a^2) \quad 3a^2 - 2a^3 \quad -aL_e(-a + a^2)] \tag{3.6}$$

$$\mathbf{B_\psi} = \frac{d\mathbf{B_v}}{dz} = \frac{1}{L_e}[-6a + 6a^2 \quad L_e(1 - 4a + 3a^2) \quad 6a - 6a^2 \quad L_e(-2a + 3a^2)\,] \tag{3.7}$$

$$\mathbf{B_b} = \frac{d{\mathbf{B_v}}^2}{d^2z} = \frac{1}{L_e^2}[-6 + 12a \quad L_e(-4 + 6a) \quad 6 - 12a \quad L_e(-2 + 6a)] \tag{3.8}$$

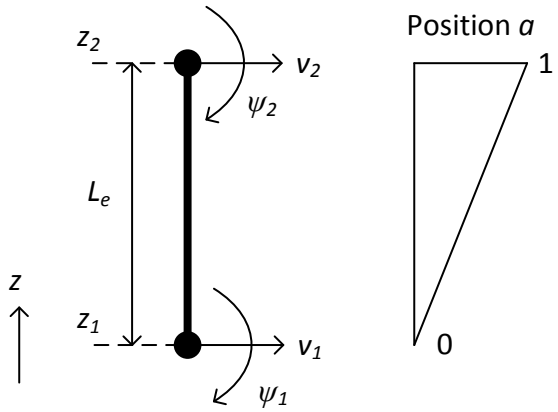

Figure 3.4. Euler-Bernoulli beam element definitions

3.4.2 Lumped Nodal Mass Elements

The turbine rotor and nacelle, and other attachments, are modelled as lumped nodal masses (Figure 3.1), with a mass M and moment of inertia J,

$$J = M.{R_{gyr}}^2 \tag{3.9}$$

where R_{gyr} is radius of gyration.

The lumped nodal masses are effectively single-node elements, with M and J assigned to the relevant degrees of freedom in the nodal mass matrix $\mathbf{M_{nodal}}$.

3.4.3 Water Added Mass Elements

The mass of internal and external water around the pile is represented by water added mass elements with no rotational inertia, consistent with dynamics analyses performed for submerged cylinders in other applications (e.g. riser vortex-induced-vibration, DNV (2010)). Figure 3.5 shows the assumed cross-sectional areas of internal $A_{w,int}$ and external water $A_{w,ext}$ added mass, with an added mass coefficient C_a = 1 assumed (DNV, 2010). The element mass matrix $\mathbf{M_{e,w}}$ for the water added mass elements is,

$$\mathbf{M_{e,w}} = \int_{z_1}^{z_2} \mathbf{B_v}^{\mathrm{T}}.\rho_w\left(A_{w,int} + A_{w,ext}\right).\mathbf{B_v}\ dz \tag{3.10}$$

the density of water was assumed as ρ_w = 1000 kg/m^3.

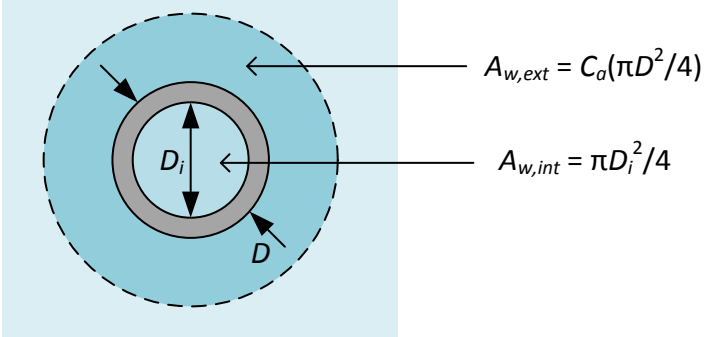

Figure 3.5. Schematic of water added mass

3.4.4 Soil Stiffness Elements

The soil reactions described in Section 3.2.2 are modelled as a series of soil stiffness elements. For the distributed soil reactions, the element stiffness matrix $\mathbf{K_{e,soil,d}}$ including lateral stiffness K_p and rotational stiffness K_m is defined as (after Burd, 2018),

$$\mathbf{K_{e,soil,d}} = \int_{z_1}^{z_2} \mathbf{B_v^T}.K_p.\mathbf{B_v} + \mathbf{B_\psi^T}.K_m.\mathbf{B_\psi}\ dz \tag{3.11}$$

The base soil stiffness $\mathbf{K_{soil,B}}$ is defined by adding the pile base stiffness components (K_H, K_M) at the relevant degrees of freedom.

3.4.5 Soil Plug Elements

The soil plug within the pile is assumed to behave as a beam element, where the element stiffness matrix $\mathbf{K_{e,plug}}$ and element mass matrix $\mathbf{M_{e,plug}}$ are calculated in a consistent manner to the pile stiffness matrix $\mathbf{K_{e,pile}}$ and mass matrix $\mathbf{M_{e,pile}}$ (Section 3.4.1).

The Young's modulus of the soil plug (E_{plug}) is related to the small strain shear modulus by,

$$E_{plug} = 2G_0(1+\nu) \tag{3.12}$$

where G_0 is calculated assuming no scour, and where Poisson's ratio $\nu = 0.5$ was assumed, corresponding to undrained behaviour.

3.4.6 Gaussian Integration

Gaussian integration is used to compute the element mass and stiffness matrices. This involves summation of the weighted values over a discrete number of Gauss points N_g at specific positions along the element. Each Gauss point has a position a_g (Figure 3.4) and weighting w_g. The finite

elements in the numerical model are assessed using $N_g = 4$ Gauss points per element, which allows representation of a quadratic variation across each element.

The positions a_g and weighting w_g are provided below for N_g = 4 (after Burd, 2018).

$$a_g = \frac{1}{2} + \frac{1}{2}\left[-\sqrt{\frac{3}{7}+\frac{2}{7}\sqrt{\frac{6}{5}}} \quad -\sqrt{\frac{3}{7}-\frac{2}{7}\sqrt{\frac{6}{5}}} \quad \sqrt{\frac{3}{7}-\frac{2}{7}\sqrt{\frac{6}{5}}} \quad \sqrt{\frac{3}{7}+\frac{2}{7}\sqrt{\frac{6}{5}}}\right] \tag{3.13}$$

$$w_g = \frac{1}{2}\left[\frac{18}{36}-\frac{\sqrt{30}}{36} \quad \frac{18}{36}+\frac{\sqrt{30}}{36} \quad \frac{18}{36}+\frac{\sqrt{30}}{36} \quad \frac{18}{36}-\frac{\sqrt{30}}{36}\right] \tag{3.14}$$

3.5 Model Implementation

3.5.1 Global Stiffness and Mass Matrix Definitions

The soil-structure system is represented by a global stiffness matrix $\mathbf{K}$ and global mass matrix $\mathbf{M}$, which are assembled as follows,

$$\mathbf{K} = \mathbf{K_{beam}} + \mathbf{K_{soil,d}} + \mathbf{K_{soil,B}} + \mathbf{K_{plug}} \tag{3.15}$$

$$\mathbf{M} = \mathbf{M_{beam}} + \mathbf{M_{nodal}} + \mathbf{M_{plug}} + \mathbf{M_{w,int}} + \mathbf{M_{w,ext}} \tag{3.16}$$

3.5.2 Mesh Generation

EigPile constructs a finite element mesh based on the input data and an input target number of elements ($n_{els,req}$). A maximum element length ($L_{e,max}$) is then specified based on the target number of elements.

$$L_{e,max} = L_{struct}/n_{els,req} \tag{3.17}$$

Firstly, nodes are added at the elevation of structure geometry changes, masses, soil layers, scour depths, water levels, and plug levels. If the spacing between adjacent nodes exceeds $L_{e,max}$ then additional nodes are added with equal spacings less than $L_{e,max}$. This approach typically produces a finite element mesh with one to three elements more than the target $n_{els,req}$. Mesh sensitivity is explored in Section 3.6.1.1.

3.5.3 Calculation of Beam Element Properties

The structure geometry is defined assuming linear variation of D and t_w along each beam element to allow for tapered tower structures to be modelled. The second moment of area (I), cross-sectional area (A) and distributed moment of inertia (j) are calculated as,

$$I = \frac{\pi}{4}\left(\left(\frac{D}{2}\right)^4 - \left(\frac{D}{2} - t_w\right)^4\right) \tag{3.18}$$

$$A = \pi t_w (D - t_w) \tag{3.19}$$

$$j = \rho . I \tag{3.20}$$

3.5.4 Normalised Soil Stiffness Coefficients

Normalised stiffness coefficients (k_p, k_m, k_H, k_M) have been implemented using the generalised Dunkirk sand model (GDSM) determined in the PISA2 project (PISA2 Final Report, 2018), in addition to the clay models for Cowden till, Bothkennar clay, and London clay (see Section 1.4.1.3).

The expressions for normalised stiffness components (k_p, k_m, k_H, k_M) from the PISA2 models are variable with depth and assume a flat seafloor. It is assumed that for a scoured seafloor (e.g. Figure 3.1) the normalised stiffness components vary with the *depth below the local bed level* z_L (as opposed to e.g. the depth below initial seabed level).

3.5.5 Small Strain Shear Modulus

Table 3.4 presents the calculation methods for small strain shear modulus G_0 implemented in *EigPile*. Isotropic stress conditions are assumed ($p' = \sigma'_{v,A}$).

3.5.6 Soil Effective Stress with Scour

On the basis of the discussion in Section 3.2 on effective stresses under the influence of scour and scour protection, Table 3.5 presents the calculation methods for α_L for scoured conditions. The design standard API (2011) suggests a bilinear variation of α_L with depth, whereas Qi et al. (2016) suggests an alternative approach with a hyperbolic tangent variation (see Figure 3 in Paper 1).

Table 3.4. Soil small strain shear modulus models implemented in *EigPile*

G_0 model	G_0 expression	Parameters
Bathgate psf sand (Paper 3)	$G_0 = \frac{Bp_{ref}}{0.3 + 0.7e^2}\left(\frac{p'}{p_{ref}}\right)^{0.5}$	$B = 478$ $p_{ref} = 100\ \text{kPa}$
Dunkirk sand (PISA2 Final Report, 2018)	$G_0 = \frac{Bp_{ref}}{0.3 + 0.7e^2}\left(\frac{p'}{p_{ref}}\right)^{0.5}$	$B = 875$ $p_{ref} = 101.3\ \text{kPa}$
Cowden clay (PISA2 Final Report, 2018)	$G_0 = Bp'$	$B = 1100$
Bothkennar clay (PISA2 Final Report, 2018)	$G_0 = Bp'$	$B = 500$
London clay (PISA2 Final Report, 2018)	$G_0 = Bp'$	$B = 740$
Scour protection	$G_0 = B_{SP}p_{ref}\left(\frac{p'}{p_{ref}}\right)^{0.5}$	$p_{ref} = 100\ \text{kPa}$
Rigid fixity model	$G_0 = 1\text{E}15\ \text{Pa}$	n/a

Table 3.5. Local scour influence factor calculation models (Figure 3.2 shows reference levels)

Scour model	α_L expression	Remarks
Local stress assumption	0	$\sigma'_{v,A} = \sigma'_{v,L}$
Global stress assumption	1	$\sigma'_{v,A} = \sigma'_{v,G}$
Bilinear with $S_T \geq S_G$	$\frac{z_L}{\Delta z_O - S_L} \leq 1$	Note that design standards suggest $\Delta z_O = 6D$ (API, 2011)
Qi et al. (2016)	$\tanh\left(f\frac{z_L}{D}\right)$	Empirical coefficient $f = 1.5$
Bilinear with $S_T < S_G$	$\frac{z_L}{\Delta z_O + h_L} \leq 1$	For scenarios with scour protection raised above global bed level (see Figure 3.3(b))

3.5.7 Eigenvalue Solver

The eigenvalue analysis is solved using the *MATLAB* function *eig*. The eigenvalue analysis produces the same number of modes of vibration as degrees of freedom in the system, however *EigPile* outputs a limited number of frequencies specified by the user, taking the lowest frequencies first. The output mode shapes V are dimensionless with a maximum absolute value $|\mathrm{V}|_{max}$ = 1.

3.6 Model Validation

3.6.1 Analytical Natural Frequency of a Uniform Beam

The analytical solution for natural frequencies of a uniform thin Euler beam – i.e. neglecting the effects of damping, rotary inertia, and shear deformations – are well established (e.g. Williams, 2016) for simple end fixity conditions such as those illustrated in Figure 3.6. For undamped free vibration of a uniform beam the equation of motion is,

$$EI\frac{\partial^4 v}{\partial z^4} + \rho A\frac{\partial^2 v}{\partial t^2} = 0 \tag{3.21}$$

The solution for the natural frequencies of this beam is,

$$\omega_m^2 = \beta_m^4\left(\frac{EI}{\rho AL^4}\right) \tag{3.22}$$

$$f_m = \frac{1}{2\pi}\left(\frac{\beta_m}{L}\right)^2\left(\frac{EI}{\rho A}\right)^{1/2} \tag{3.23}$$

where β_m is a modal coefficient that is dependent on the mode shape. Table 3.6 presents the β_m coefficients for the first four modes for Euler beams with fixed-free and fixed-pinned conditions.

To extend the analytical solution to account for rotary inertia effects, the following approximate expression is proposed (after Nukala, 1999),

$$\omega_m^2 = \Omega_m\beta_m^4\left(\frac{EI}{\rho AL^4}\right) \tag{3.24}$$

$$f_m = \Omega_m^{1/2}\frac{1}{2\pi}\left(\frac{\beta_m}{L}\right)^2\left(\frac{EI}{\rho A}\right)^{1/2} \tag{3.25}$$

where Ω_m is a natural frequency modifying factor for rotary inertia effects, defined as,

$$\Omega_m = \frac{1}{1+\beta_m^2\left(\frac{I}{AL^2}\right)} \tag{3.26}$$

Use of the β_m values from Table 3.6 will give an approximate Ω_m value, since introducing the rotary inertia result in slight differences in the mode shapes from which β_m is derived.

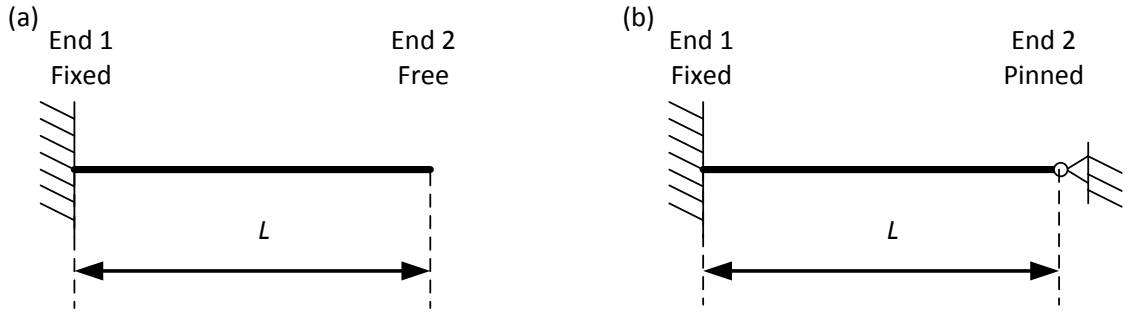

Figure 3.6. Illustration of simply supported beam fixity conditions (a) Fixed-free beam; (b) Fixed-pinned beam.

Table 3.6. Modal coefficients for uniform thin beams (Williams, 2016)

End 1 Fixity	End 2 Fixity	$\boldsymbol{\beta_1}$	$\boldsymbol{\beta_2}$	$\boldsymbol{\beta_3}$	$\boldsymbol{\beta_4}$
Fixed	Free	1.875	4.694	7.855	11.00
Fixed	Pinned	3.940	7.068	10.21	13.35

3.6.1.1 EigPile Model Verification

A simplified wind turbine tower was modelled in *EigPile*, to allow a verification analysis to be performed for a uniform beam with full fixity at the base of the tower. Fixity at the base of the tower was imposed with a large base stiffness (rigid fixity model, Table 3.4). The simplified geometry was based on the tower for the NREL reference wind turbine (Jonkman et al., 2009). Table 3.7 presents the simplified geometry adopted for the *EigPile* model validation, which uses an average of the tower top and base dimensions and assumes steel material properties.

Figure 2.14 presents a comparison of the *EigPile* output natural frequencies with the analytical Euler beam solution for the first four bending modes of a thin beam (3.23), where the rotary inertia j was set to zero. A mesh sensitivity analysis (Figure 2.14(b)) shows that *EigPile* outputs consistent natural frequency results once the number of elements exceeds around 80. The first three frequencies very closely match the analytical solution (error $|\varepsilon_f| < 0.1\%$) for a fixed-free uniform beam (thin beam assumption).

The analysis of the flume experiments (Section 4.2), concerned with the first three modes, used a target number of elements $n_{els,req}$ = 200. The analysis of structures at Robin Rigg offshore wind farm (Section 5), considers only the first mode, and uses a target number of elements $n_{els,req}$ = 50.

3.6.2 Rotational Inertia Effects

Table 3.8 presents a comparison of the natural frequency modifying factor Ω_m determined using the analytical solution (3.25) and the *EigPile* output, where the rotary inertia j was calculated according to Section 3.5.3. The results in Table 3.8 indicate that the influence of rotary inertia effects is similar between the analytical approach and the *EigPile* output, with a difference of less than 1%.

Table 3.7. Simplified tower model parameters

Model	D	t_w	L	E	ρ
	[m]	[mm]	[m]	[GPa]	[kg/m^3]
NREL_M0	4.935	23.5	90	210	7850

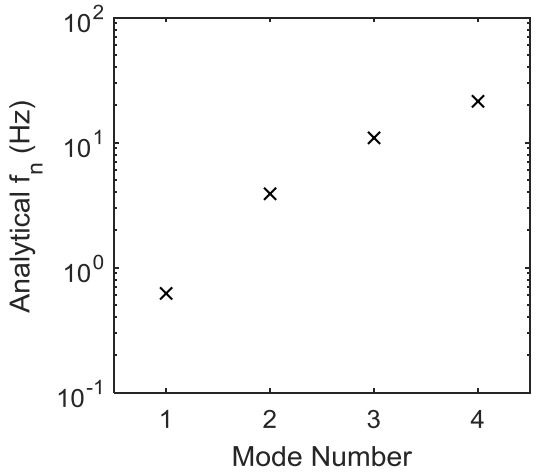

(a) Analytical natural frequencies

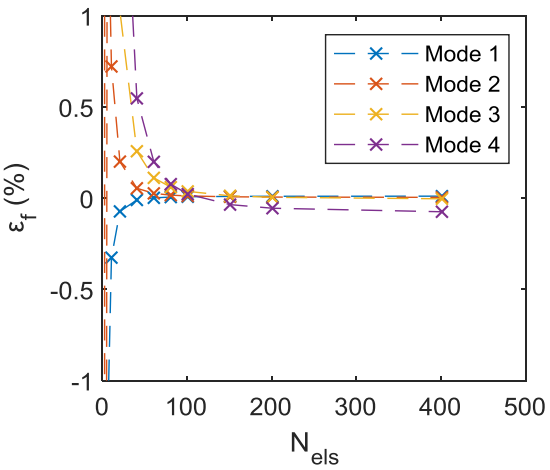

(b) Natural frequency error sensitivity to number of elements

Figure 3.7. Comparison of *EigPile* result to analytical solution: NREL_M0 uniform tower model with fixed-free end conditions and thin beam assumption with no rotary inertia effects and no shear deformation effects

Table 3.8. Natural frequency modifying factor for rotary inertia effects: NREL_M0 uniform tower model with fixed-free end conditions

Model	Ω_1	Ω_2	Ω_3	Ω_4
Analytical solution for rotary inertia	0.9987	0.9919	0.9775	0.9569
EigPile results	0.9985	0.9893	0.9750	0.9546

3.7 Discussion and Limitations

A 1D finite element model *EigPile* was developed to analyse the natural frequencies of monopile-supported offshore wind turbines.

The influence of scour is modelled by incorporating two key mechanisms: (i) increasing the free length of the pile due to loss of soil support, and (ii) reducing the stiffness of the remaining soil due to reduced effective stresses in the soil. To model the influence of scour protection these two mechanisms have parallels of: (i) decreasing the free length of the pile, and (ii) increasing the stiffness of the underlying soil due to the weight of the scour protection; for scour protection there is an additional mechanism of: (iii) introducing the stiffness contribution of the scour protection material in contact with the pile wall. The effects of scour protection on pile foundation behaviour has received limited attention in previous research, and new methods are proposed to model the sour protection stiffness.

The 1D model could be further developed by performance of 3D finite element analysis to produce normalised soil reactions in the presence of scour and with scour protection layers, following a methodology similar to the PISA project. One challenge for such work will be in defining appropriate constitutive models for the scour protection material, which would likely require novel testing methods to be developed to determine the mechanical behaviour of the scour protection matrix. The geometry of seabed bathymetry with scour and scour protection can become complicated, for example by asymmetry and the formation of falling aprons. The models presented in this Section have assumed that the soil stresses vary with the global bed level and local bed level, the validity of these assumptions could be explored through 3D finite element analysis.

The current work adopts a simplifying assumption that the soil stiffness G_0 and the soil reactions vary with vertical effective stress σ_v' under isotropic stress conditions. This model does not consider stress history effects, in that horizontal effective stresses σ_h' may be less influenced by local scour than σ_v' at small distances beneath a scour hole leading to a region of higher K_0. Conversely, there may be a region of lower K_0 in layers of uncompacted scour protection.

Section 4 – Numerical Modelling of the Flume Experiments

4.1 Introduction

This Section presents numerical modelling of the stiffness and stability of the monopile – tower system from the flume experiments. *EigPile* was used to model the natural frequencies for the flume experiments for comparison of results and calibration of the numerical models of scour and scour protection, and *OxPile* was used to model the monotonic lateral loading tests.

The analyses were staged to consider first the unscoured problem, then incrementally explore the scour and scour protection scenarios as follows:

i. Analysis of unscoured structural dynamics tests (Section 4.2.2)
ii. Calibration for scour structural dynamics tests (Section 4.2.3)
iii. Calibration for scour protection structural dynamics tests (Section 4.2.4)
iv. Analysis of the monotonic lateral loading tests (Section 4.3)

4.2 Numerical Modelling of the Structural Dynamics Tests

4.2.1 Numerical Model Specifications

4.2.1.1 Monopile-tower Structure

The geometry of the monopile-tower structure was idealised for input to *EigPile*, as shown in Figure 4.1; Table 4.1 presents the assumed beam element properties and Table 4.2 presents the assumed nodal mass properties. The mass of the cables (for accelerometer, force sensor, and strain gauge instrumentation) has not been modelled.

The top mass was modelled as a beam element with a solid circular cross-section, where the length was scaled depending on the number of masses attached, N_M, and the density, ρ, was back-figured to give the correct top mass, M_{top}. Over the length of the transition piece (h_{TP} region in Figure 4.1), the structure is modelled using tower beam elements. The mass of the pile material above the level of the transition piece bottom bolts was incorporated into the transition piece mass in Table 4.2, which is located at the mid-height of the transition piece.

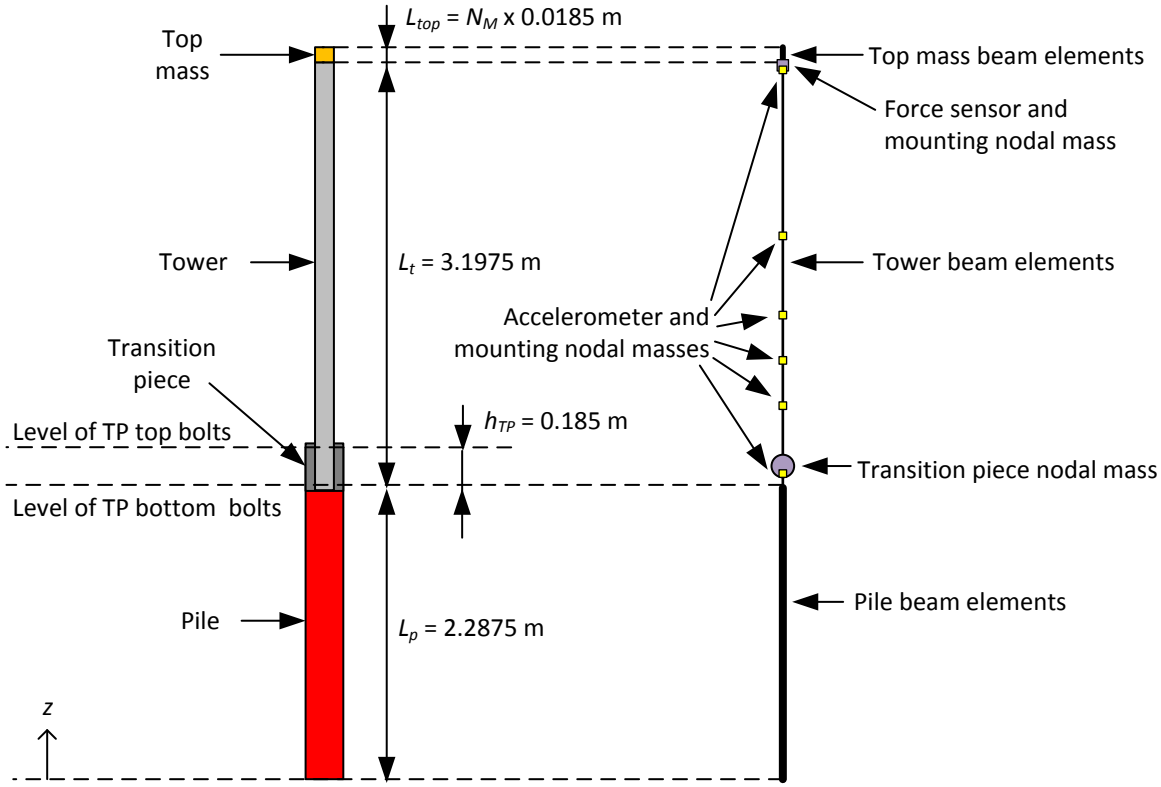

Figure 4.1. Numerical model representation of monopile – tower system

Table 4.1. Beam element properties for numerical models of the monopile – tower system

Beam element type	Material	D	t_w	E	ρ
		[m]	[m]	[GPa]	[kg/m^3]
Top mass	Brass	0.0945	0.04725	407	8529
Tower	Aluminium	0.1016	0.0016	69	2700
Pile	GFRP	0.197	0.0035	31.235	1855

Table 4.2. Nodal mass properties for numerical models of the monopile – tower system

Nodal mass description	z [m]	Mass [kg]	R_{gyr} [m]
Force sensors and mounting	5.47	0.296	0.050
Accelerometers and mounting	5.38, 4.13, 3.53, 3.18, 2.83, 2.33	0.070	0.025
Transition piece plus mass of pile	2.38	3.667	0.075

4.2.1.2 Soil Properties

The soil profiles for the numerical analyses were based on the relative density, D_R, profiles derived from CPTs performed at the pile location for each test. Figure 4.2 presents the interpreted soil parameter profiles for unscoured conditions at the start of each test, excluding Test 5, which had

pre-installed scour protection (Table 3 in Paper 3). The CPT data did not reach the pile tip level for all tests, and D_R below the CPT data was assumed to be constant. The small strain shear stiffness was calculated using the relationship established for Bathgate psf sand (Table 3.4), which is based on bender element test data.

Also shown in Figure 4.2 are the profiles of distributed lateral stiffness (k_p and K_p). The GDSM soil reactions (PISA2 Final Report, 2018) were adopted to model the soil stiffness. Table 4.3 presents a comparison of the non-dimensional geometry of the flume experiments and the GDSM calibration space; key differences are the pile size and range of e_{min} to e_{max} for the Bathgate psf sand. There are also parts of the flume experiment relative density profiles that fall outside of the range of the GDSM calibration ($45\% < D_R < 90\%$). The GDSM normalised soil reaction calculations have been limited to use an input D_R of 45% to 90%, and values are assumed to be constant when extrapolating beyond this range.

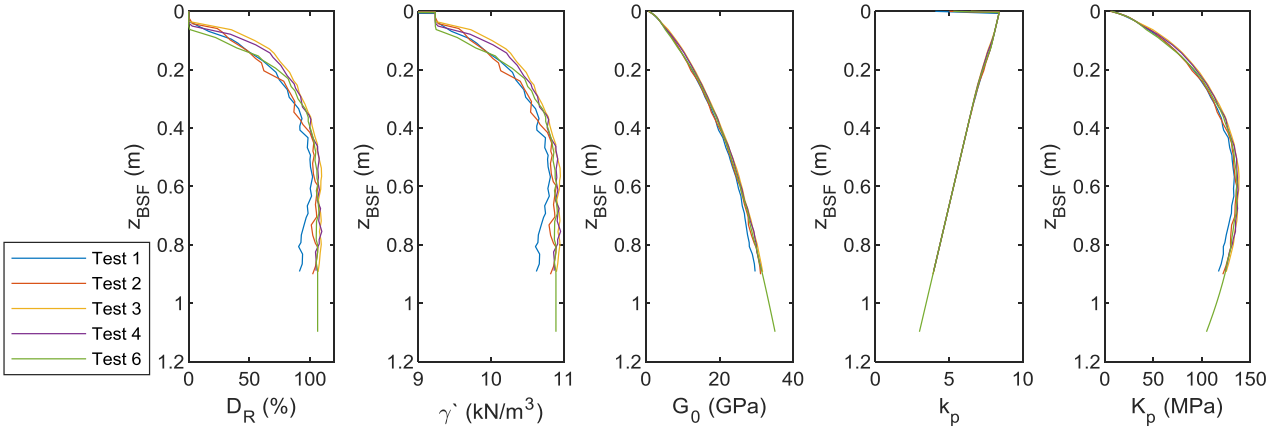

Figure 4.2. Numerical model soil parameter profiles with no scour. Relative density profiles are derived from CPT data (Fig. 3 in Paper 3).

Table 4.3. Comparison of GDSM calibration space with the flume experiments

Soil model	**Pile geometry**				**Soil properties**			
	D **(m)**	L/D	D/t_w	h/D	e_{min}	e_{max}	D_R **(%)**	ϕ'_{cs}
GDSM (Burd et al., 2019)	5 to 10	2 to 6	96 to 110	5 to 15	0.57	0.91	45 to 90	32
Flume Experiments	0.197	2.2 to 5.5	56	n/a	0.5018	0.7528	0 to 100	34

4.2.1.3 Scour Protection Modelling

The scour protection systems installed in the flume experiments included remedial tyre-filled nets (R-TFN), remedial rock fill (R-RF) and pre-installed rock armour (P-RA). Figure 4.3 presents the general configuration of the soil stiffnesses in the 1D model, including those in the scour protection layer. The scour protection stiffness coefficient, B_{SP}, (proposed in Section 3.2.4) is calibrated for the different scour protection systems using data from the flume experiments in Section 4.2.4.

Table 4.4 presents an overview of the scour protection properties and associated scour depths at key times in the flume experiments. For the numerical model, the scour protection was assumed to contain accreted sand throughout the thickness after any post-installation flume flow had occurred. The unit weight of scour protection with accreted sand was calculated using the method described in Appendix D, assuming sand in the rock matrix deposited at D_R = 50%.

A generic value of k_p was selected to model the scour protection; this was taken as the mid-point value determined from the GDSM at the soil surface (i.e. D_R = 67.5%; z/D = 0).

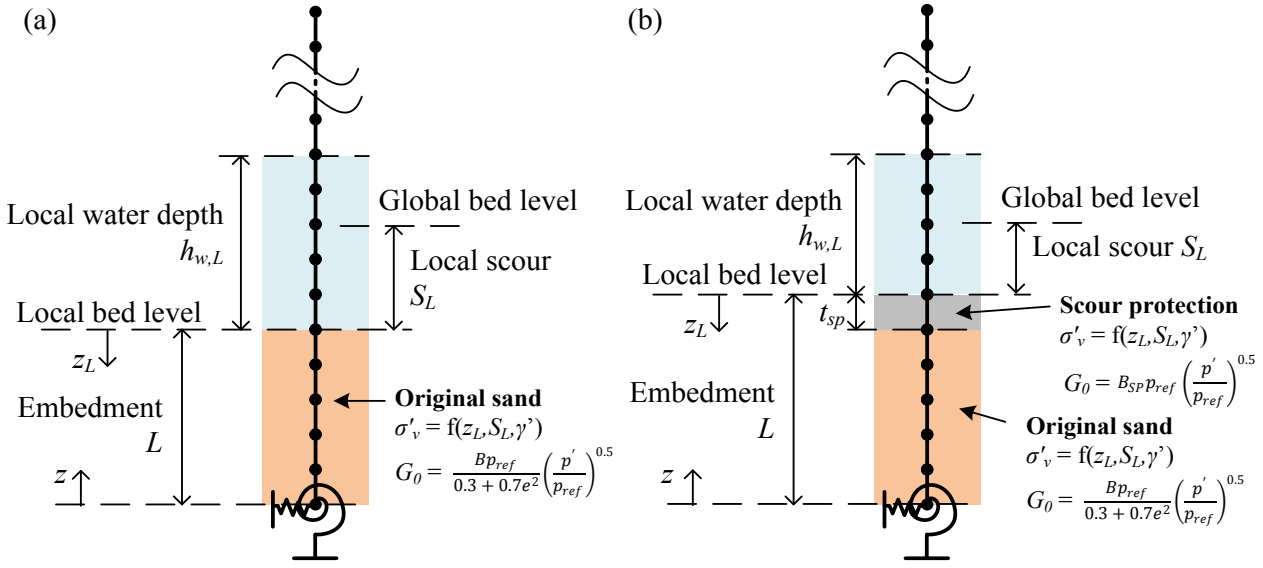

Figure 4.3. Schematic of soil stiffness parameters in the 1D model; (a) before installing scour protection; (b) after installing scour protection (see methods proposed in Section 3.2.4).

Table 4.4. Scour protection properties – flume experiments

FFF Test (Table 5 in Paper 3)	Local scour	Scour protection as-installed condition			Scour protection end of test condition			
	S_L [m]	t_{SP} [m]	γ [kN/m^3]	e	t_{SP} [m]	γ [kN/m^3]	ΔS_T [m]	S_G [m]
2 (R-TFN)	0.311	0.243	10.14	4.960	0.154	18.40	0.089	0.085
3 (R-RF1)	0.294	0.161	18.85	0.953	0.155	23.70	0.006	0.059
4 (R-RF2)	0.025	0.105	18.99	0.923	0.065	23.77	0.117	0.072
5 (P-RA)	0	0.055	18.04	1.146	0.052	23.35	0.003	0.091
6 (R-RF3)	0.297	0.201	18.60	1.008	0.188	23.60	0.013	0.352

4.2.2 Analysis of Unscoured Experiment Test Cases

Natural frequencies were analysed for unscoured conditions (i.e. prior to development of scour and with no scour protection) in five of the flume experiments, with four top mass configurations (N_M = 0, 1, 3, 6).

Figure 4.4 presents an example comparison of *EigPile* output natural frequencies f_m^{Eig} with measured values f_m^{Meas} for one test; included in Figure 4.4 are the *EigPile* natural frequencies for fixity at seabed level and fixity at the pile tip. As expected, the measured frequencies lie between the fixed seabed and fixed pile tip calculations.

Figure 4.5 presents the natural frequency error ($\varepsilon_f = f_m^{Eig}/f_m^{Meas} - 1$) for all unscoured tests. The *EigPile* natural frequencies in Figure 4.5 are generally slightly higher than the measured data for the first three modes. The natural frequencies are overpredicted by up to 3.2% for mode 1, with greater scatter in the errors for modes 2 and 3.

Figure 4.6 presents examples of the mode shapes V_m output from *EigPile*, associated with the natural frequencies in Figure 4.4. The measured mode shapes are compared with the *EigPile* results in Figure 4.6, indicating a close match.

Figure 4.6(c) presents a detailed view of the mode shapes in the pile below ground level, these show that the relative displacements at ground level are highest for mode 2, followed by mode 3 then mode 1; this follows the same sequence of natural frequency sensitivity to scour depth (Section 2.4.4).

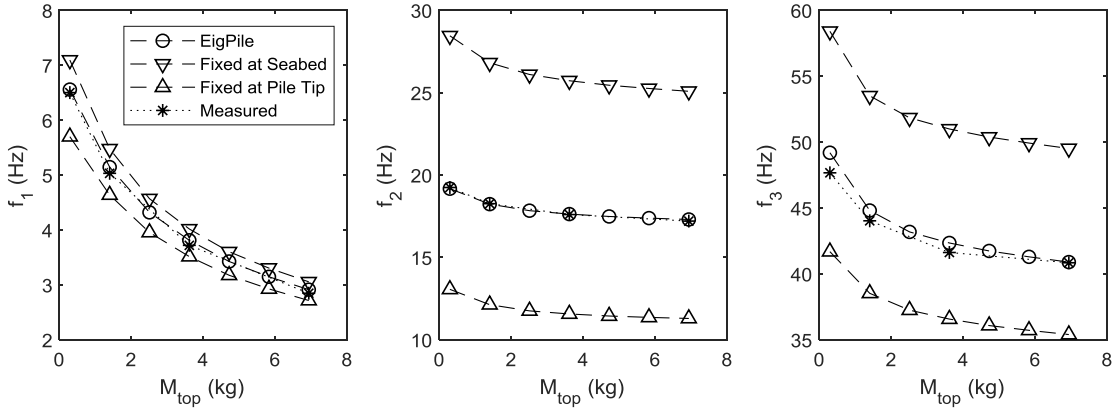

Figure 4.4. Example natural frequency versus top mass *EigPile* calculation and measured: Unscoured, Test 1

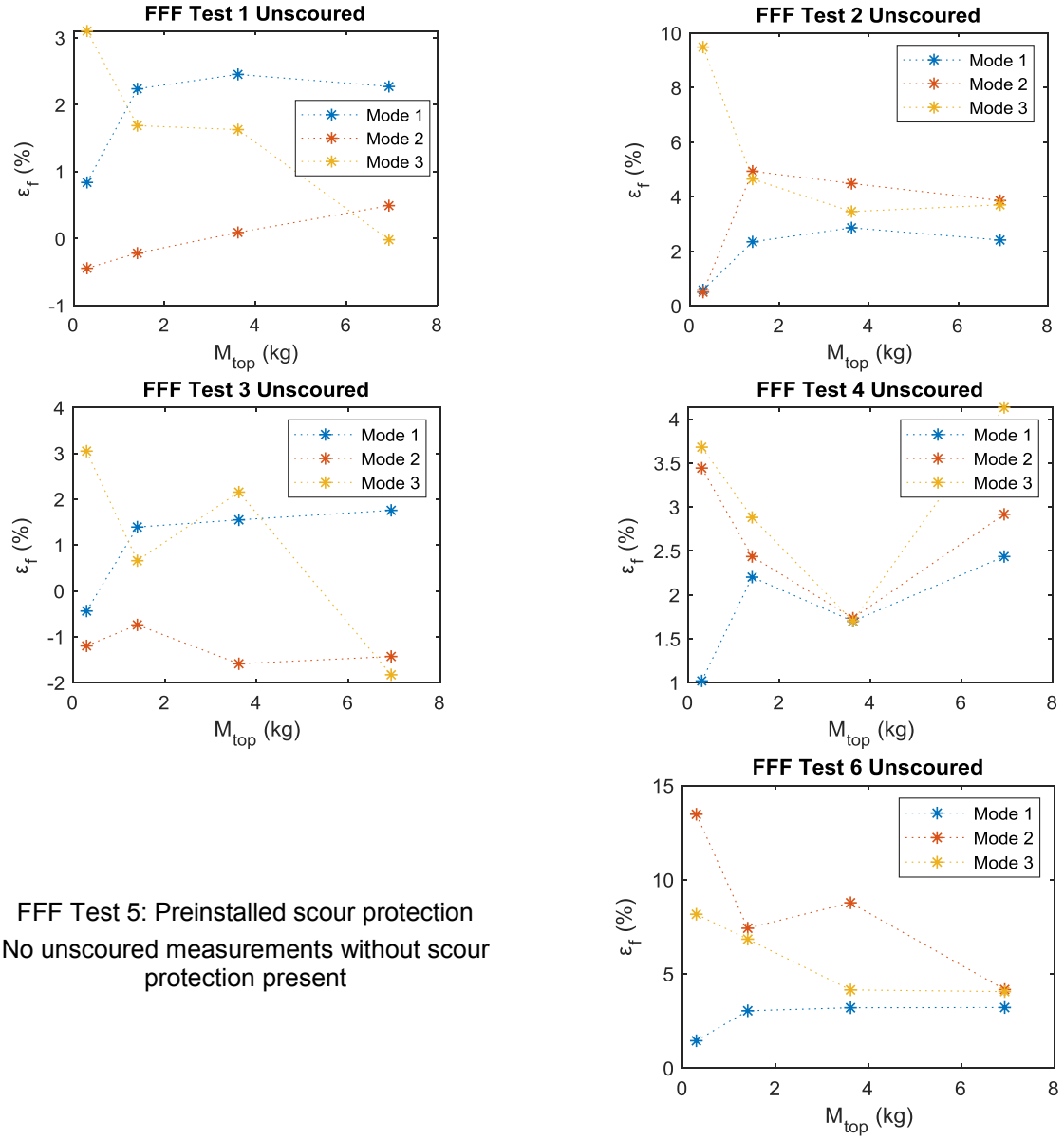

FFF Test 5: Preinstalled scour protection

No unscoured measurements without scour protection present

Figure 4.5. *EigPile* natural frequency error versus top mass: Unscoured conditions

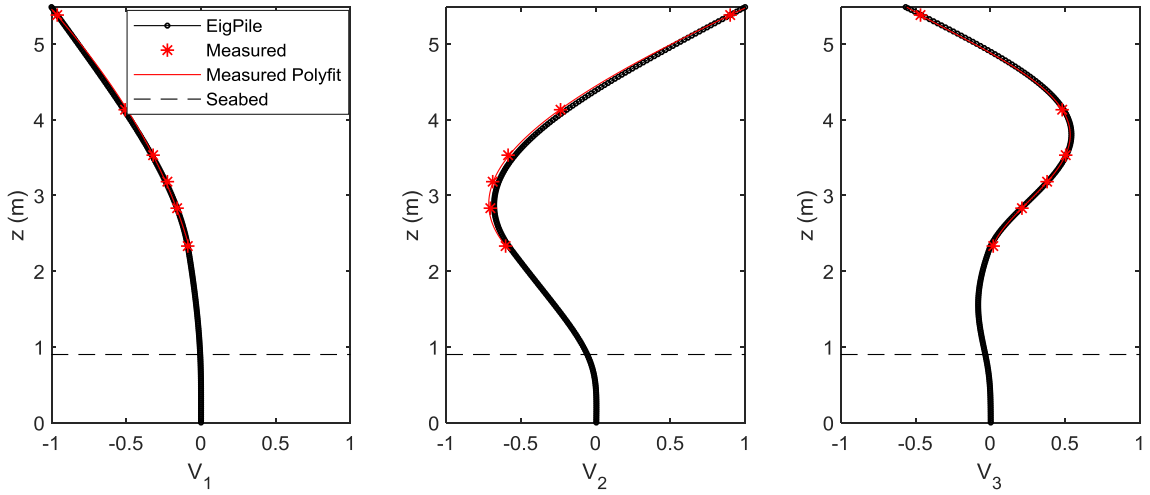

(a) Unscoured, Test 1, $N_M = 0, M_{top} = 0.296$ kg

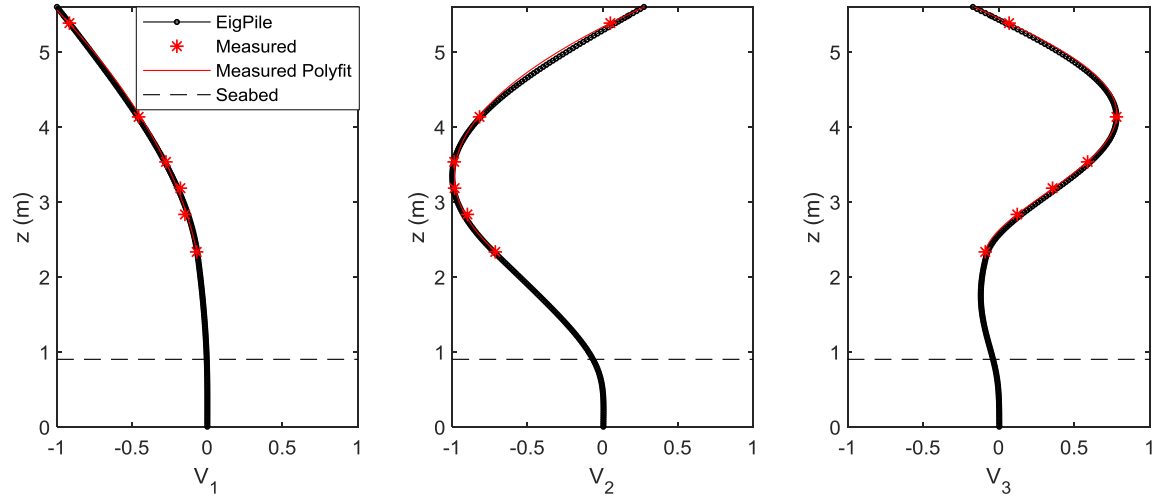

(b) Unscoured, Test 1, $N_M = 6, M_{top} = 6.936$ kg

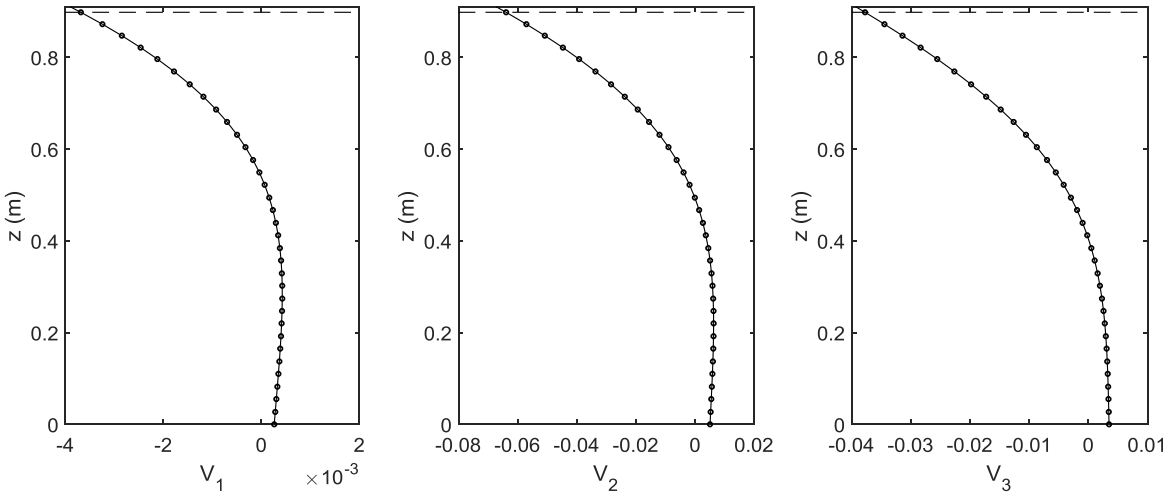

(c) Pile detail: Unscoured, Test 1, $N_M = 6, M_{top} = 6.936$ kg

Figure 4.6. Example mode shapes output from *EigPile* analysis

Overall, the numerical model of the flume experiments for unscoured conditions produces similar results to the dynamic properties inferred from the acceleration measurements. The overprediction of natural frequencies implies that the ratio of stiffness $\mathbf{K}$ to mass $\mathbf{M}$ is too high in the numerical model. These slight errors could have multiple potential sources, for example: exclusion of shear deformations from the beam elements; uncertainty of added mass of water; effects of the accelerometer cable mass; or overestimation of G_0 or k_p.

4.2.3 Analysis of Scour Influence on Natural Frequencies

4.2.3.1 Calibration of Scour Effective Stress Model

An *EigPile* analysis was performed for each measured scour depth (and corresponding natural frequency measurement) from the flume experiments. The bathymetry analysis (Fig. 14 in Paper 3) showed that sand backfilling – deposition of sand in the local scour hole – had occurred during Test 1. The tests with known sand backfilling were excluded from the current analysis, however sand backfilling could be unidentified in other tests if the maximum scour depth was not captured by the measurements. In total, analyses were performed for 44 natural frequency measurement configurations, comprising eleven scour geometries with four top mass configurations (N_M = 0, 1, 3, and 6).

Section 4.2.2 indicates that there is a small apparent offset between the measurements and calculations for the initial unscoured natural frequencies $f_{m,0}$; therefore the comparisons between *EigPile* calculations and measured frequencies presented below consider the proportional change in frequency,

$$\Delta f_m^{Meas} = f_m^{Meas} / f_{m,0}^{Meas} - 1 \tag{4.1}$$

$$\Delta f_m^{Eig} = f_m^{Eig} / f_{m,0}^{Eig} - 1 \tag{4.2}$$

The natural frequencies under the influence of scour were analysed assuming a bilinear local scour influence factor (Figure 3.2 and Figure 3.3; also Section 3.5.6). The analysis of natural frequencies was optimised by variation of the overburden reduction depth Δz_O using the non-dimensional form,

$$\delta_L = \Delta z_O / S_L \tag{4.3}$$

The non-dimensional overburden reduction depth δ_L was analysed in the range of $1 \leq \delta_L \leq 10$; where $\delta_L = 1$ implies that the apparent vertical effective stress $\sigma'_{v,A}$ immediately recovers to the 'global effective stresses' $\sigma'_{v,G}$, and $\delta_L = 10$ implies that $\sigma'_{v,A}$ remains close to the 'local effective stress' $\sigma'_{v,L}$. Note that the API (2011) suggested values of $S_L/D = 1.5$ and $\Delta z_O/D = 6$ have an equivalent $\delta_L = 4$.

The change in the first natural frequency Δf_1 was used to provide independent fitted δ_L values for each scour depth and top mass configuration. The fitted δ_L values were calculated by linear interpolation using the analysed δ_L values. Figure 4.7(a) shows an example of this fitting process for one scour depth in FFF Test 1.

Figure 4.7(b) presents a scatter plot of the fitted δ_L values across all of the analysed natural frequency measurements, and Figure 4.7(c) presents the associated cumulative density function (CDF) of the fitted δ_L values. The value of δ_L at the CDF = 0.5 in Figure 4.7(c) is the 50th percentile i.e. the median fitted value.

Fitted values of δ_L = 10, apparent in Figure 4.7(b)&(c), are likely due to the actual soil stiffness being lower than modelled, one possible cause is the potential for unidentified sand backfill with lower stiffness than the original *in situ* material. The median value (δ_L = 1.49) in Figure 4.7(c) was selected as the best fit value for the bilinear scour effective stress model, which is anticipated to underpredict 50% of the tests and overpredict the remaining 50% of the tests.

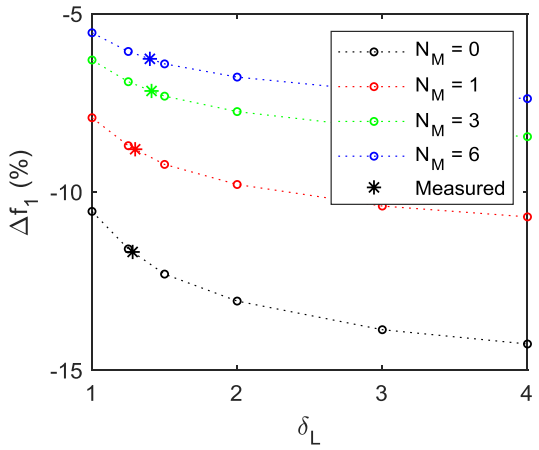

(a) Example fitting of δ_L: Test 1, S_T/D = 2.32

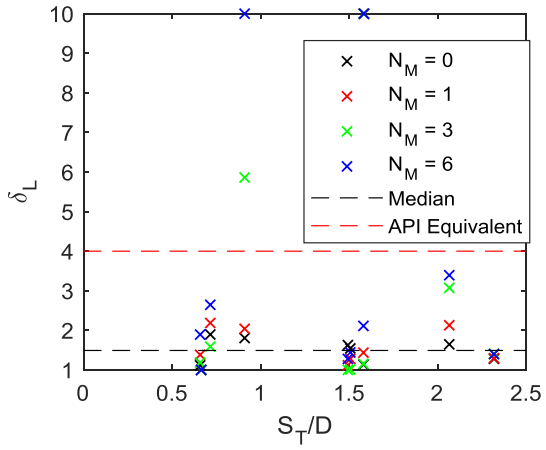

(b) Scatter plot of all fitted δ_L value

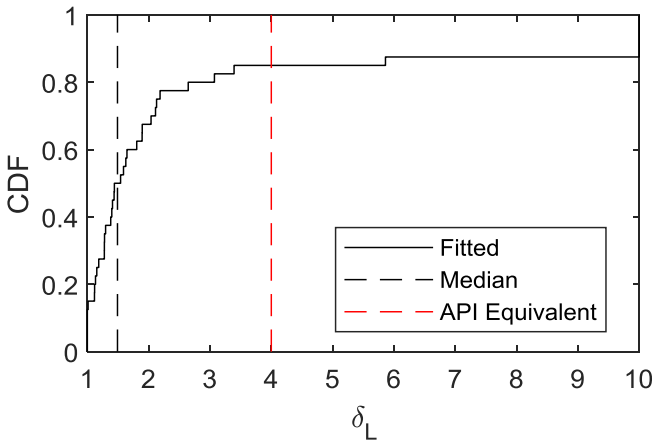

(c) Cumulative density of all fitted δ_L values

Figure 4.7. Calibration of non-dimensional overburden reduction depth δ_L (a) Fitted δ_L values for Test 1 at the end of the test: Hollow circle indicates Δf_1^{Eig}; * indicates linearly interpolated δ_L corresponding to Δf_1^{Meas}. (b) All fitted δ_L values for Tests 1,2,3,4,6 (c) Cumulative density function of all fitted δ_L for Tests 1,2,3,4,6.

4.2.3.2 Scour Effective Stress Models

Several models of scour influence on vertical effective stresses were analysed (see Table 3.5). Figure 4.8 presents a comparison of the calculated stress and stiffness profiles for the analysed scour effective stress models, where G_0 for sands varies with $\sigma_v'^{0.5}$. The calibrated bilinear approach (δ_L = 1.49) produces a quicker recovery of stress with depth than the API (2011) method, and similar stress and stiffness profiles to the Qi et al. (2016) method.

The results are analysed in terms of the error in the calculated change in frequency $\varepsilon_{\Delta f}$,

$$\varepsilon_{\Delta f} = \Delta f_m^{Eig} - \Delta f_m^{Meas} \tag{4.4}$$

For negative values of Δf_m^{Meas}, a positive value of $\varepsilon_{\Delta f}$ would indicate an underprediction of the change Δf_m^{Eig}. Figure 4.9 and Table 4.5 present the error $\varepsilon_{\Delta f}$ for the first three modes for the analysed scour models.

The local stress assumption and global stress assumption are approximate lower and upper bounds for the soil stiffness calculations. The results in Table 4.5 indicate that the natural frequency of mode 1 is relatively insensitive to the effective stress assumption, with a 1.5% difference in the median frequency predictions between the local and global bounds. Mode 2 is the most sensitive to the effective stress assumption (5.7% between bound medians), and mode 3 has an intermediate sensitivity (2.0% between bound medians).

The median and mean values of $\varepsilon_{\Delta f}$ in Table 4.5 are two methods of representing the accuracy of the natural frequency predictions, and the standard deviation represents the precision of these predictions. For mode 1 predictions, the change in natural frequency is most accurately and precisely predicted using the calibrated bilinear effective stress method, with the Qi et al. (2016) method producing similar results (Table 4.5). This is expected, since the model was calibrated using mode 1 alone (Section 4.2.3.1), and Qi et al. (2016) produces similar stiffness profiles (Figure 4.8).

The mode 2 reduction in natural frequency is generally overpredicted for all of the scour stress models (Figure 4.9; Table 4.5), with the most accurate prediction produced using the global stress assumption (approximate upper bound). The mode 2 frequency predictions have a similar precision for all effective stress models. The accuracy of the mode 2 predictions is considered to have been the most heavily influenced by other modelling assumptions (e.g. added mass of water, mass of cables).

The mode 3 reduction in natural frequency (Figure 4.9;Table 4.5) is most accurately predicted using either the calibrated bilinear effective stress method or the Qi et al. (2016) method, both of which have a similar precision.

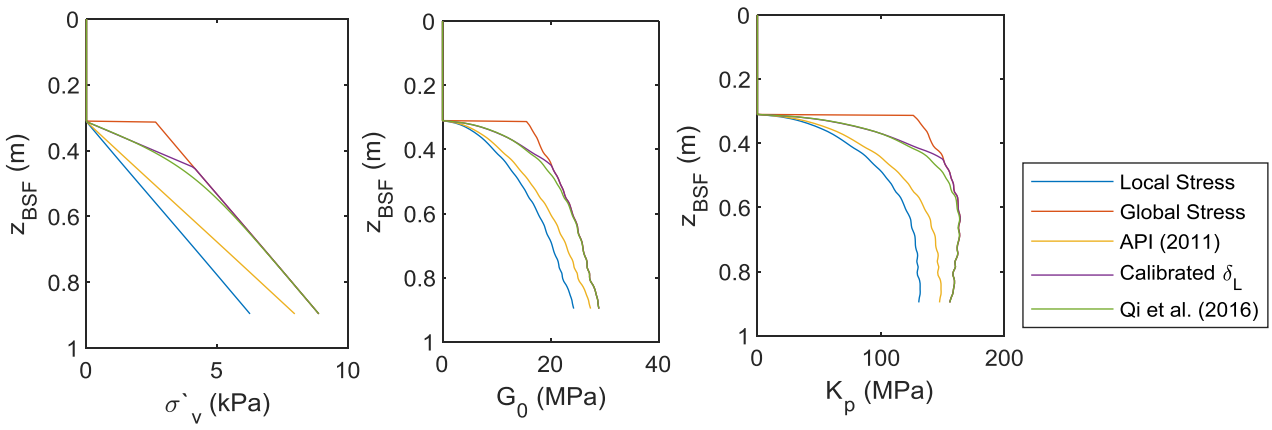

Figure 4.8. Example soil parameter profiles with local scour: Test 1, end of local scour phase

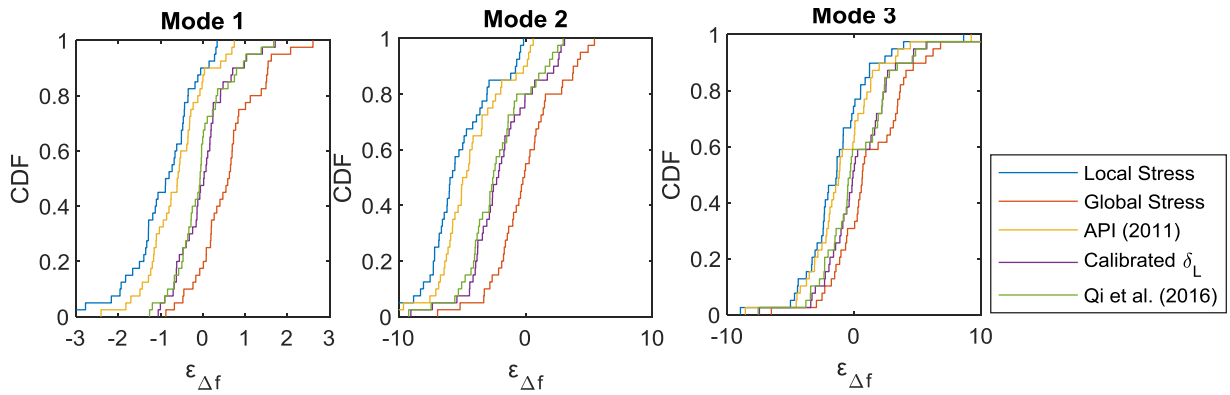

Figure 4.9. Cumulative density of error in natural frequency change for analysed scour stress models: Scoured conditions for Tests 1,2,3,4,6; $\varepsilon_{\Delta f}$ presented as a percentage.

Table 4.5. Statistics for error in natural frequency change

Scour model (Table 3.5)	**Median $\varepsilon_{\Delta f}$ (%)**			**Mean $\varepsilon_{\Delta f}$ (%)**			**Standard Deviation**		
	Mode 1	**Mode 2**	**Mode 3**	**Mode 1**	**Mode 2**	**Mode 3**	**Mode 1**	**Mode 2**	**Mode 3**
Local stress assumption	-0.84	-5.87	-1.37	-0.95	-5.31	-1.28	0.84	2.74	***2.91***
Global stress assumption	0.61	***-0.14***	0.65	0.59	***0.04***	1.37	0.74	2.68	3.27
Bilinear with API Δz_O	-0.60	-4.81	-1.18	-0.64	-4.42	-0.83	0.68	2.66	3.00
Bilinear with calibrated δ_L	***0.02***	-2.21	***-0.09***	***0.02***	-1.96	0.43	***0.62***	2.68	3.06
Tan hyperbolic (Qi et al. 2016)	-0.07	-2.56	-0.32	-0.04	-2.30	***0.28***	0.63	***2.65***	3.16
Bold italic font indicates best value in each column									

4.2.4 Analysis of Scour Protection Influence on Natural Frequencies

4.2.4.1 Calibration for Rock Fill Remedial Scour Protection

EigPile analyses were performed to assess the stress and stiffness of remedial rock fill scour protection, using a total of 56 natural frequency measurements from fourteen scour protection geometries with four top mass configurations (N_M = 0, 1, 3, 6). The scour protection geometries comprise three as-installed conditions plus eleven geometries measured after further flume flow.

The influence of the local versus global scour within the scour protection was accounted for using the calibrated bilinear approach (Figure 3.3), with δ_L = 1.49. In instances where the global scour level dropped below the scour protection level at the pile wall (i.e. $S_T < S_G$, Figure 3.3(b)) the bilinear approach was modified assuming $\Delta z_O / h_L = \delta_L$ = 1.49.

The scour protection stiffness parameter B_{SP} was calibrated using the measured change in mode 1 frequency Δf_1 relative to the initial unscoured condition. Figure 4.10 presents examples of the calculated value of Δf_1 versus B_{SP}, and the associated polynomial fit, for scour protection in Test 3 (a) after installation and (b) at the end of the test. For each top mass configuration, an independent fitted B_{SP} was calculated as the value from the polynomial fit corresponding to the measured frequency change Δf_1.

Figure 4.11(a)-(c) presents the variation of the fitted B_{SP} values throughout Tests 3, 4 and 6. Figure 4.11(d) presents a cumulative density plot of fitted B_{SP} values, where the results are grouped separately the initial 'as-installed' condition (measurement number = 1) and subsequent 'post flow' conditions (measurement number > 1).

The calibrated B_{SP} values are compared with values equivalent to the Bathgate psf sand, calculated by equating the sand expression (Table 3.4) for G_0 with that of scour protection (this gives an equivalent $B_{SP} = B.f(e)$). The equivalent B_{SP} values for Bathgate psf sand in loose ($D_R = 0\%$) and dense ($D_R = 100\%$) conditions are included in Figure 4.11(d) for reference, which indicates that the scour protection stiffness is lower than the equivalent *in situ* sand.

The fitted B_{SP} values in Figure 4.11 vary with time in all tests, and the 'post flow' B_{SP} (measurement number > 1) values have greater scatter than the 'as-installed' (measurement number

= 1) values discussed briefly below. The increase of B_{SP} in Tests 3 and 6 after the initial flow stages is assumed to be due to sand accretion in the RF material causing increased particle interlocking and hence a higher apparent stiffness. The decreases of B_{SP} in Test 4, and in Test 3 and 6 after a peak, are assumed to be due to reductions in the effective stresses caused by global scour. The simplistic scoured effective stress model (Figure 3.3) and scour protection stiffness model (Table 3.4) may be insufficient to capture the full detail of the scour protection stiffness contribution for the more complicated three-dimensional geometries encountered in Tests 4 and 6.

Table 4.6 presents the average B_{SP} values across all tests, and for the 'as-installed' and 'post flow' conditions. The mean B_{SP} values in Table 4.6 are greater than the median values; this is caused by the data points above the 50th percentile are further from the median than those below. Table 4.6 also shows a high standard deviation in the values of B_{SP}, this is caused by the wide range of fitted B_{SP} values (Figure 4.11), and shows that there is uncertainty in the magnitude of B_{SP} for the modelling of scour protection stiffness. The median values from Table 4.6 are proposed to provide a best fit of B_{SP} for the RF scour protection stiffness, with the 'as-installed' value proposed no sand accretion cases and the higher 'post flow' value is proposed when sand accretion is assumed.

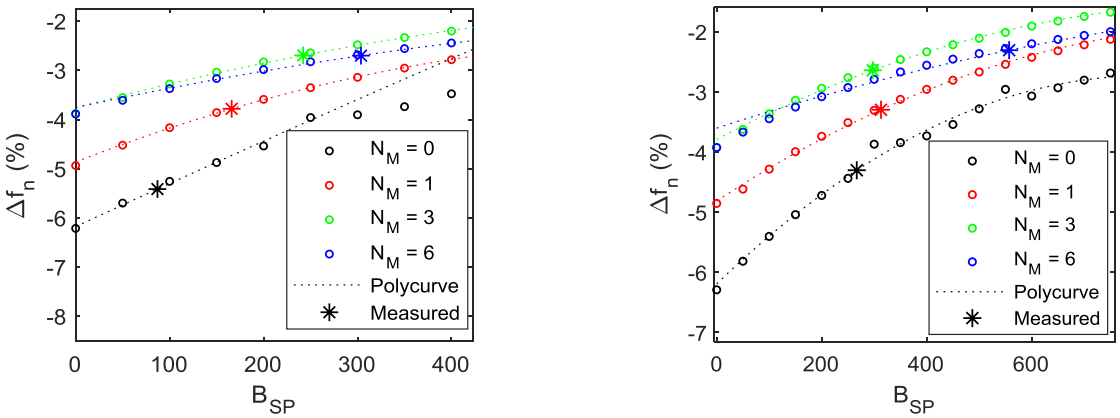

(a) After installation (b) End of test

Figure 4.10. Example (FFF Test 3) B_{SP} fitting for rock fill remedial scour protection using mode 1 change in natural frequency. Hollow circle indicates Δf_1^{Eig}; dotted line indicates polynomial fit for Δf_1^{Eig}; * indicates polynomial fit B_{SP} corresponding to Δf_1^{Meas}.

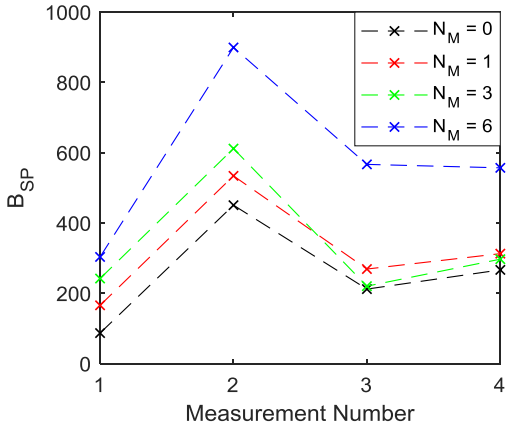

(a) Test 3: rock fill in a full scour hole

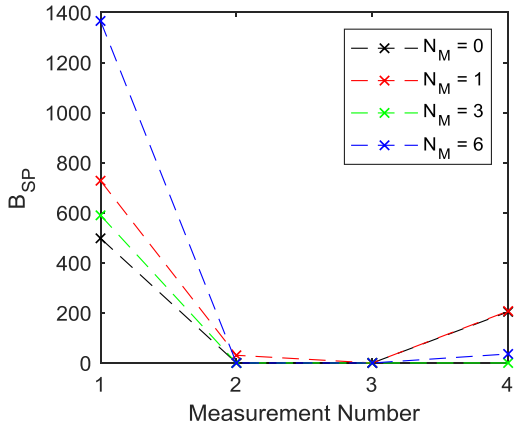

(b) Test 4: rock fill in a partial scour hole

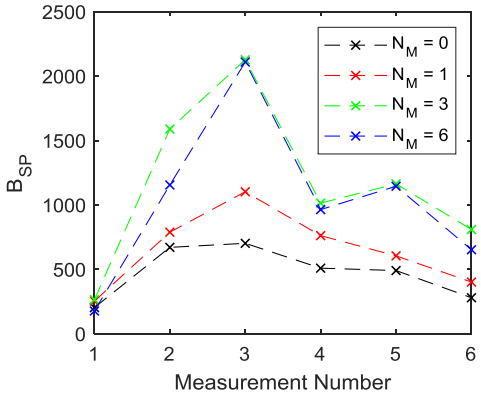

(c) Test 6: rock fill in a full scour hole with falling apron development

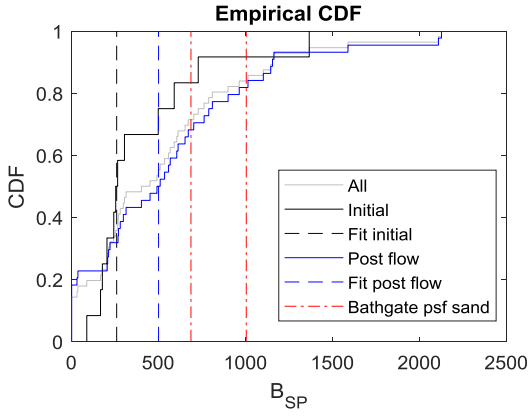

(d) Cumulative density

Figure 4.11. Fitted B_{SP} for rock fill remedial scour protection. (a) to (c) Measurement number 1 corresponds with first scour protection measurement in Appendix C.9, increasing measurement numbers correspond with subsequent rows. (d) Results for all fitted B_{SP} for Tests 3, 4, and 6, red dashed line indicates a range of equivalent B_{SP} for Bathgate psf sand from D_R = 0% to 100%.

Table 4.6. Best fit B_{SP} for rock fill remedial scour protection

Scour protection condition	Median	Mean	Standard deviation
All cases	426.0	528.4	496.4
As-installed	258.9	406.5	357.0
Post flow	499.8	561.7	526.7

4.2.4.2 Calibration for Tyre-Filled Nets Remedial Scour Protection

Tyre-filled nets (TFNs) were used as remedial scour protection in Test 2 of the flume experiments, with a total of 16 natural frequency measurements from 4 scour protection geometries (one as-installed, three after further flow) with four top mass configurations (N_M = 0, 1, 3, 6). The stiffness contribution of the TFNs was analysed in a similar manner to the rock fill, described in Section 4.2.4.1, to determine best fit B_{SP} values. Figure 4.12(a)&(b) present examples of the B_{SP} fit for the 'as-installed' and end of test conditions; Figure 4.12(c) shows the progression of B_{SP} throughout the test; and Figure 4.12(c) presents a cumulative density plot of fitted B_{SP} values.

The results in Figure 4.12 indicate that the stiffness contribution of TFNs is negligible on initial installation (the fitted B_{SP} = 0 for three of four top mass configurations). This is as expected, based on observations of the natural frequency measurements described in Section 2, since limited or no increase was observed on TFN installation. Furthermore, the TFNs have a much higher voids ratio than the *in situ* sand or the rock fill scour protection (Table 4.4), and it is considered that the stiffness of tyre rubber is significantly lower than that of silica sand grains.

In Figure 4.12(c) there is a trend of increasing TFN scour protection stiffness B_{SP} with elapsed flow, which is considered to be caused by increasing sand accretion in the TFNs. As with the RF remediation, the scatter in the fitted B_{SP} values is greater for the 'post flow' condition than for the 'as-installed' condition.

Table 4.7 presents the average values of B_{SP} for the TFN tests. Table 4.7 shows differences between the median and mean values and a high standard deviation, these are similar to Table 4.6 which is discussed in Section 4.2.4.1. A median value is proposed as a best fit. It is interesting to note that the fitted B_{SP} values for the tyre-filled nets with sand accretion are much lower (by a factor of about 10) than those for RF, and lower still (by a factor of about 20) the equivalent stiffness of *in situ* sand.

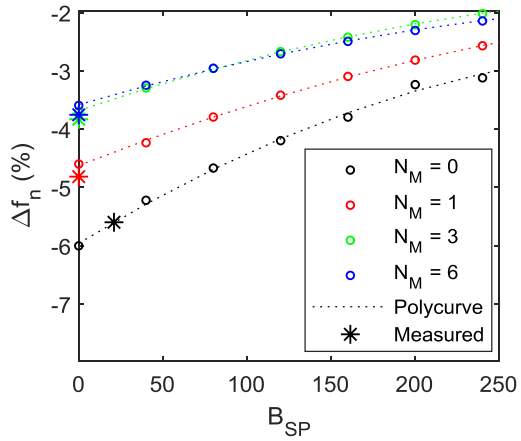

(a) Example fit – as-installed

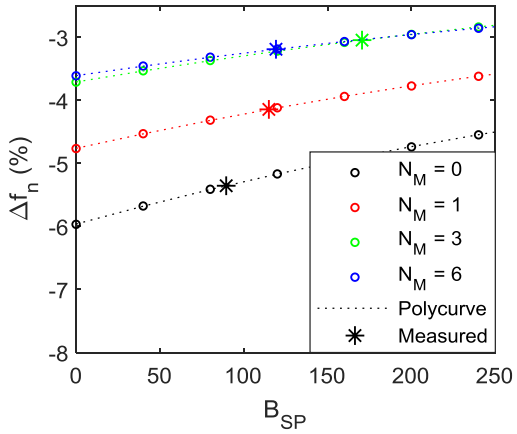

(b) Example fit – end of test

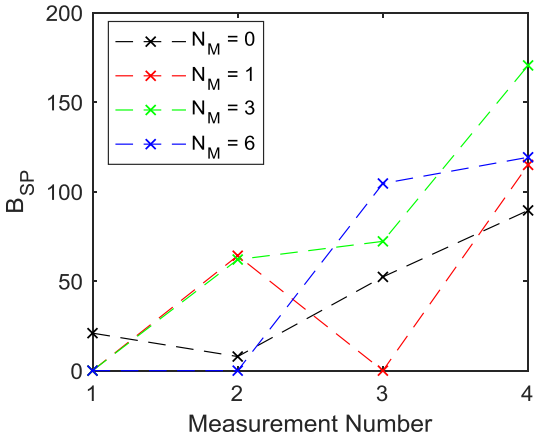

(c) Fitted parameters throughout test

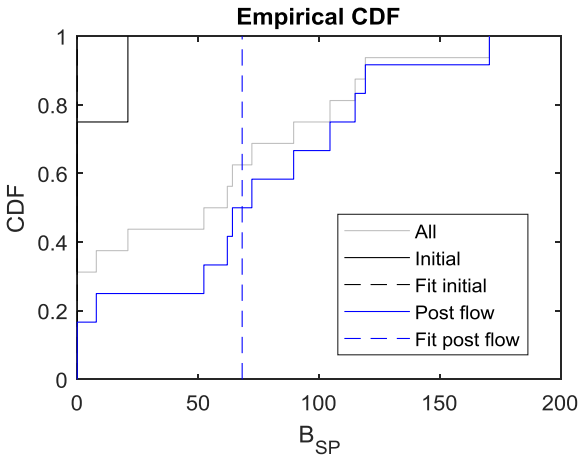

(d) Cumulative density

Figure 4.12. Fitted B_{SP} for tyre-filled net remedial scour protection (a) and (b) Hollow circle indicates Δf_1^{Eig}; dotted line indicates polynomial fit for Δf_1^{Eig} * indicates polynomial fit B_{SP} corresponding to Δf_1^{Meas}. (c) Measurement number correlates with elapsed flow time since installing scour protection (Appendix C.9.1). (d) Cumulative density function of all fitted B_{SP} for Test 2.

Table 4.7. Output B_{SP} for tyre-filled net remedial scour protection

Scour protection condition	Median	Mean	Standard deviation
All cases	57.2	54.9	53.9
As-installed	0	5.2	10.5
Post flow	68.2	71.5	52.4

4.2.5 Comparison with Stiffness Parameters from the Monotonic Lateral Loading Tests

The initial stiffness of the measured H-v_G and M_G-θ_G curves (Figure 2.24) is calculated using a linear regression, where $K_{H,v}^{Meas}$ is the initial stiffness of the H-v_G curve and $K_{M,\theta}^{Meas}$ is the initial stiffness of the M_G-θ_G curve. The linear fit was performed for data over a manually input range of load H and moment M_G for each test. For each structural dynamics test, the *EigPile* analysis produced four calibrated stiffness matrices $\mathbf{K}_{1\mathrm{D}}^{Eig}$, one for each of the four top mass configurations independently calibrated to the mode 1 change in frequency (Section 4.2). This also produces four equivalent uncoupled macro element springs $K_{H,v}^{Eig}$ and $K_{M,\theta}^{Eig}$ per test (method described in Appendix E). The median values of $K_{H,v}^{Eig}$ and $K_{M,\theta}^{Eig}$ are used for comparisons with the lateral loading tests.

Figure 4.13 shows the measured load-displacement and moment-rotation curves at small displacements, with the linear regression fits used to assess the initial lateral and rotational stiffnesses $K_{H,v}^{Meas}$ and $K_{M,\theta}^{Meas}$. Table 4.8 presents the fitted stiffness values $K_{H,v}^{Meas}$ and $K_{M,\theta}^{Meas}$ alongside the computed values of $K_{H,v}^{Eig}$ and $K_{M,\theta}^{Eig}$ (methodology described in Appendix E) based on the structural dynamics calibration.

The results in Table 4.8 show that the stiffness derived from the monotonic loading tests are of similar magnitude to those from the structural dynamics analysis, but there are some inconsistencies. The monotonic loading tests produced a softer response in most cases. This shows that the either the experimental data from the monotonic loading tests is of insufficient quality at small displacements to provide reliable measurements of initial stiffness, or that small strain stiffness is not captured in these tests. This is not unexpected since the experimental setup was specified for large displacements.

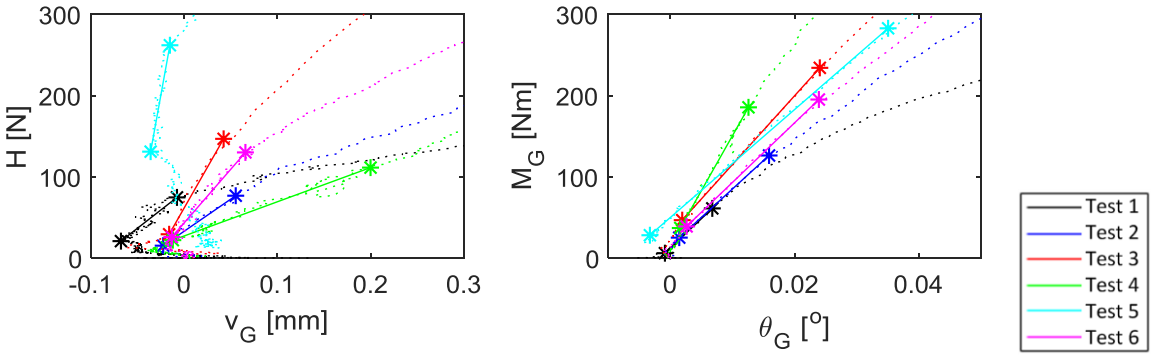

Figure 4.13. Monotonic lateral loading initial stiffness fitting; dotted lines are measured values, solid lines are linear regression fits, * indicates range of loads considered for linear regression

Table 4.8. Monotonic Lateral Loading Initial Stiffness Parameters: Flume Experiment Results

FFF Test (Table 5 in Paper 3)	$K_{H,v}^{Meas}$	$K_{M,\theta}^{Meas}$	$K_{H,v}^{Eig}$	$K_{M,\theta}^{Eig}$
	[kN/m]	**[kNm/°]**	**[kN/m]**	**[kNm/°]**
1	896	7.23	2041	13.0
2 (R-TFN)	790	7.00	1510	11.0
3 (R-RF1)	2010	8.47	1625	11.5
4 (R-RF2)	421	13.5	2129	13.2
5 (P-RA)	6337	6.64	Test 5 not analysed	Test 5 not analysed
6 (R-RF3)	1320	7.34	2004	11.8

4.2.6 Discussion of Natural Frequency Results

Data from the flume experiments were used to calibrate a proposed scoured effective stress model. The stiffness of remedial rock fill and tyre-filled net scour protection systems was inferred using data from the flume experiments. In the experiments the stiffness of the rock fill in the as-installed condition is shown to be lower than that of the undisturbed *in situ* sand. In contrast, the as-installed stiffness of the tyre-filled nets is negligible. There was a general tendency for the inferred scour protection stiffness in the experiments to increase with flume flow time and, for rock fill, to approach that of the original sand. The behaviour is presumed to be due to sediment accretion in the scour protection matrix (see Paper 3). There are exceptions to this behaviour, when stiffness reductions were inferred due to global scour and the formation of a falling apron of scour protection reaching the pile wall.

4.3 Numerical Modelling of the Monotonic Lateral Loading Tests

4.3.1 Numerical Model Specifications

OxPile was used to assess the monotonic lateral loading curves from the flume experiment tests. Figure 4.14 presents a sketch of the 1D numerical model used to represent the lateral loading tests from the flume experiments. The soil reactions for the scour protection and Bathgate psf sand are modelled using the generalised Dunkirk sand model (GDSM) (PISA2 Final Report, 2018). The analysis results are therefore not necessarily expected to be accurate, rather the analysis is used to provide a baseline for comparison of the scour protection contribution to lateral capacity.

The equation from Cowper (1966) was adopted to compute the shear coefficient, κ, for Timoshenko beam theory,

$$\kappa = \frac{2(1+\nu)}{4+3\nu} \tag{4.5}$$

where $\kappa = 0.529$ for the GFRP pile with an assumed Poisson's ratio of $\nu = 0.28$ (e.g. after Sudheer et al., 2015).

An initial study incorporating the distributed moment reactions produced overpredictions of the lateral loads when compared with the experimental data. This may be due to the gloss-painted monopile in the experiments behaving with a smooth interface (friction coefficient likely in the range of 0.1 to 0.2), in contrast to the rough surface condition modelled in the 3D finite element analysis underlying the GDSM (friction coefficient = 1). A smoother interface proportionally reduces the vertical shear tractions and hence the moment reactions, but would also induce slight reduction in the lateral reactions. For the purposes of the current study, the smooth response was modelled by setting the distributed moment reactions to zero and maintaining the distributed lateral reactions.

Table 4.9 presents the modelled pile embedment L used in the lateral loading analysis, which was defined as the median local bed level at the end of the test (from Appendix C.9). Table 4.9 also presents the local scour depth, S_L, or local bed height, h_L, which indicates the difference between the local bed level and global bed level (see Figure 3.2 and Figure 3.3). The scour protection parameters in Table 4.9 are based on the calibrated structural dynamics analysis (Section 4.2.4).

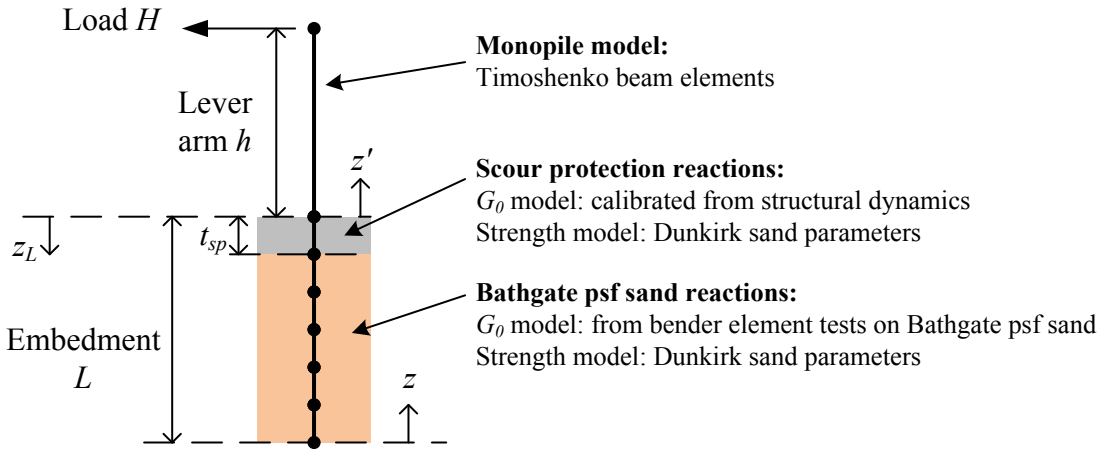

Figure 4.14. 1D numerical model representation of the monotonic lateral loading tests

Table 4.9. Soil model parameters used for analysis of monotonic lateral loading tests

FFF Test (Table 5 in Paper 3)	L [m]	S_L [m]	h_L [m]	t_{SP} [m]	γ_{SP} [kN/m^3]	B_{SP}
1	0.4415	0.344	-	-	-	-
2 (R-TFN)	0.7505	0.073	-	0.154	18.40	68.2
3 (R-RF1)	0.7620	0.079	-	0.155	23.70	500
4 (R-RF2)	0.7545	0.069	-	0.065	23.77	500
5 (P-RA)	0.9535	-	0.144	0.052	23.35	500
6 (R-RF3)	0.9950	-	0.242	0.188	23.60	500

Figure 4.15 presents the profiles of relative density, D_R, used for analysing the lateral loading tests. The relative density, D_R, inferred from CPT measurements (Fig. 3 in Paper 3) has been limited to 45% $\leq D_R \leq$ 90% for compatibility with the GDSM, and the profile has been discretised for input to *OxPile*. For scour protection material the relative density has been specified as D_R = 67.5% for consistency with the calibrated structural dynamics analysis.

OxPile determines the soil reactions using input soil profiles of relative density, D_R, vertical effective stress, σ_v', and small strain shear modulus, G_0. A bilinear profile of the local scour influence factor, α_L (Figure 3.2 & Figure 3.3), was assumed for calculation of the σ_v' profile under the influence of scour and scour protection. This vertical effective stress profile was used to determine the G_0 profile. Table 4.10 presents the four vertical effective stress models analysed for the unremediated scour lateral loading test (Test 1). The global and local effective stress conditions are plausible

theoretical bounds for the *in situ* vertical effective stresses, with the exception of Test 5 (P-RA) where the scour protection material adjacent to the pile is slightly lower than the immediate surrounding area (Figure 2.5).

Table 4.11 presents the combination of vertical effective stress models and scour protection models used for analysis of the scour protection tests. The scour protection soil reactions were modelled as either activated or deactivated (Table 4.11), the vertical effective stress in the underlying soil includes the scour protection effects in both cases. In Tests 5 (P-RA) and 6 (R-RF3) the global bed level was lower than the local level adjacent to the pile wall (i.e. $S_G > S_T$). In the analysis of Tests 5 and 6 it was assumed that: in the 1D FFF Model, $\delta_L = \Delta z_O / h_L$; and in the 1D Global Model, all soil reactions were zero above the global scour level including within the scour protection layer.

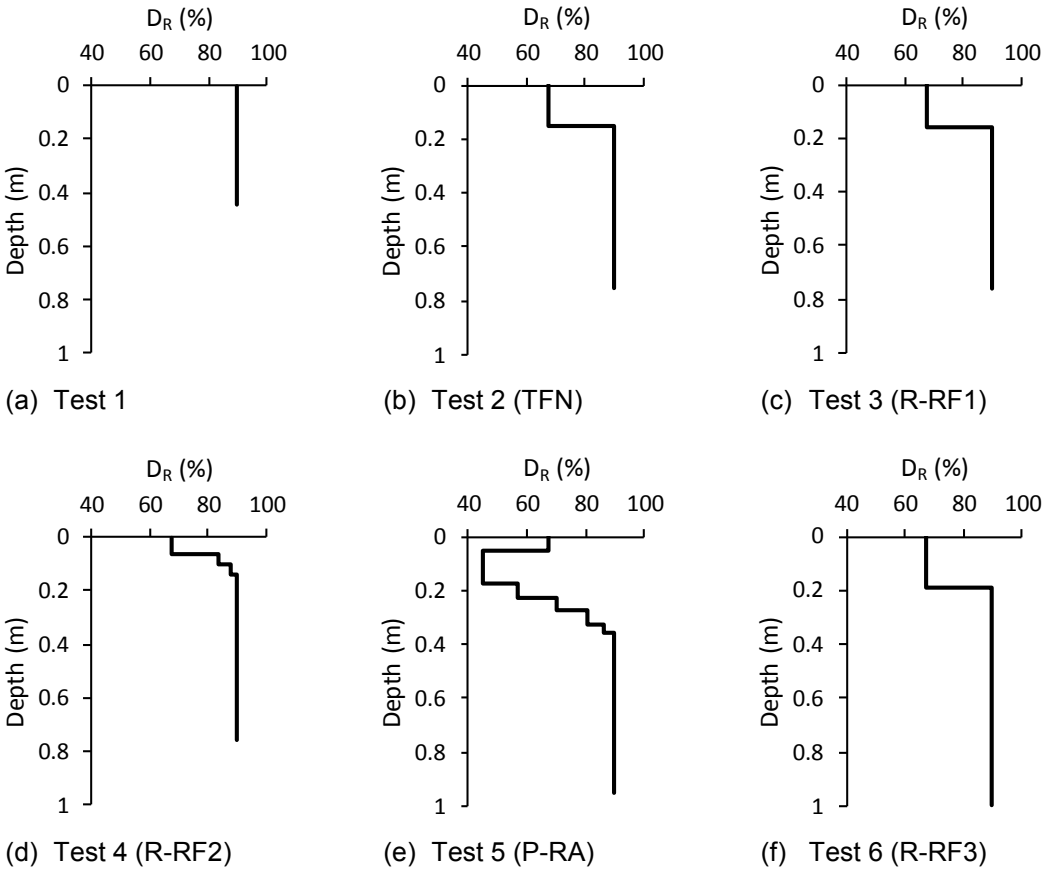

Figure 4.15. Relative density profiles used for analysis of the monotonic lateral loading tests, depths are relative to the local bed level adjacent to the pile wall (i.e. depths correspond to z_L definition in Figure 3.2 & Figure 3.3).

Table 4.10. Analysed scoured vertical effective stress models

Vertical Effective Stress Model	Scour Model (Table 3.5)	$\delta_L = \Delta z_O / S_L$
1D Global Model	Global stress assumption	1
1D FFF Model	Bilinear (calibrated model)	1.49
1D API Model	Bilinear (API equivalent)	4
1D Local Model	Local Stress Assumption	∞

Table 4.11. Analysed scour protection vertical effective stress models

Scour Protection Model	Vertical Effective Stress Model (Table 4.10)	Scour Protection Soil Reactions
1D FFF SP on	1D FFF Model	Activated
1D FFF SP off	1D FFF Model	Deactivated
1D Global SP on	1D Global Model	Activated
1D Local SP on	1D Local Model	Activated

4.3.2 Numerical Modelling Results and Discussion

4.3.2.1 Unremediated Scour; Test 1

Figure 4.16 presents the *OxPile* analysis results for the unremediated scour test (Test 1). Test 1 has the greatest local scour depth S_L from the flume experiments (Table 4.4) and is the monotonic lateral loading test with no scour protection.

The bounds between the global and local vertical effective stress assumptions are quite wide (Figure 4.16(a)); this leads to a wide range of profiles of small strain shear modulus, G_0 (Figure 4.16(b)). The computed lateral load, H, (Figure 4.16(c)) is over 3 times higher at large displacements using the 1D Global Model compared with the 1D Local Model, which show that there is potential for a high degree of uncertainty over the expected capacity.

The 1D FFF Model provides the closest fit to the measured data (Figure 4.16(c)), although the measured response reaches a maximum at a smaller displacement than computed by the 1D model. This shows that the GDSM (excluding distributed moment) is a reasonable representation of the reactions for the experiment monopile in Bathgate psf sand.

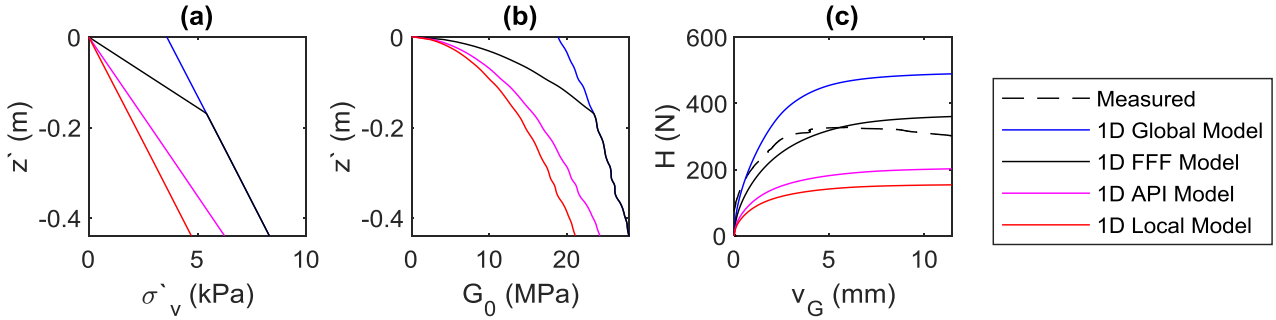

Figure 4.16. Test 1 (unremediated scour) lateral loading analysis results; (a) Vertical effective stress σ_v' profiles; (b) Small strain shear modulus G_0 profiles; (c) Lateral load-displacement curves.

4.3.2.2 Remedial tyre-filled net scour protection; Test 2 (R-TFN)

Figure 4.17 presents the *OxPile* analysis results for the remedial tyre-filled net scour protection test; Test 2 (R-TFN). The 1D Global Model and 1D Local Model bounds for vertical effective stress, σ_v', and small strain shear modulus, G_0, (Figure 4.17(a)&(b)) are much narrower than those in Test 1 (Figure 4.16(a)&(b)); this is because S_L is much lower in Test 2 (see Table 4.4).

The computed lateral load, H, (Figure 4.17(c)) at large displacements is higher using the 1D Global Model compared with the 1D Local Model. This range is much lower than in Test 1 (Figure 4.16(c)), but does show that the computed lateral loads are highly sensitive to the effective stress assumption since the range of σ_v' and G_0 (Figure 4.17(a)&(b)) is quite narrow. The computed lateral loads, H, for the '1D FFF SP on' model are very close to the '1D Global SP on' model.

The measured lateral loads closely match the '1D FFF SP on' model for displacements up to a peak load at around 13 mm. This shows that the peak capacity contribution of the tyre-filled nets, which include accreted sand, is similar to that offered by the GDSM. The post-peak load reduces with increasing displacement to approach the '1D FFF SP off' model; this behaviour may have been caused by movement of the tyre-filled nets induced by the pile displacement.

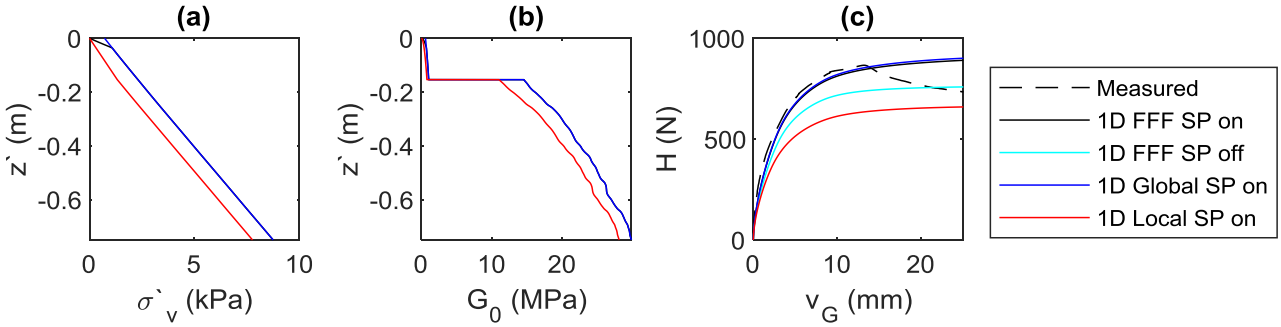

Figure 4.17. Test 2 (remedial tyre-filled net scour protection) lateral loading analysis results; (a) Vertical effective stress σ_v' profiles; (b) Small strain shear modulus G_0 profiles; (c) Lateral load-displacement curves.

4.3.2.3 Remedial rock fill scour protection; Tests 3 (R-RF1), 4 (R-RF2), & 6 (R-RF3)

Figure 4.18 presents the *OxPile* analysis results for the remedial rock fill scour protection tests; Tests 3 (R-RF1), 4 (R-RF2), and 6 (R-RF3). The configuration and geometry of Test 3 (Table 4.4) is a rough baseline from which to draw comparisons. Test 4 has a similar embedment L and local scour depth S_L to Test 3, but with a thinner scour protection layer (Table 4.4). Test 6 has a higher embedment L than Test 3, and a slightly thicker scour protection layer. Test 6 also has much more global scour than Test 3 and a falling apron had developed (Fig. 20 in Paper 3).

In both Tests 3 and 4 the surface of the scour protection is recessed in the scour hole with a low local scour depth S_L modelled, causing a narrow range of vertical effective stress, σ_v', and small strain shear modulus, G_0 (Figure 4.18(1)&(2))). In Test 6 the global scour causes the scour protection to appear raised relative to the global bed level; this has the effect of switching the apparent position of the 1D Global and 1D Local bounds of vertical effective stress, σ_v', and small strain shear modulus, G_0 (Figure 4.18(3)). The σ_v' and G_0 bounds in Test 6 are much wider than Tests 3 and 4.

The computed loads for Tests 3 and 4 (Figure 4.18(1)&(2)) using the '1D Global' stress model is slightly higher than using the '1D Local' stress model. The lateral capacities in Test 6 (Figure 4.18(3)) using the '1D Global' stress much lower than using the '1D Local' stress model. In all cases the lateral loads are reduced using the '1D FFF SP off' model, relative to using the '1D FFF SP on' model.

The computed lateral capacities using the '1D FFF SP on' model in Figure 4.18 are significantly under-predicted for Test 3 and 4 (recessed scour protection), and closely match the measurements for Test 6 (raised scour protection). This has the following potential implications regarding the scour protection effects: (i) where rock fill scour protection is recessed in the scour hole, and hence confined by the scour hole, the contribution of the scour protection to the ultimate lateral capacity is likely to be higher than that of the same thickness of sand; and (ii) where rock fill scour protection is raised relative to the global bed level, and hence is not confined, the contribution to the ultimate lateral capacity is similar to or slightly lower than that of the same thickness of sand.

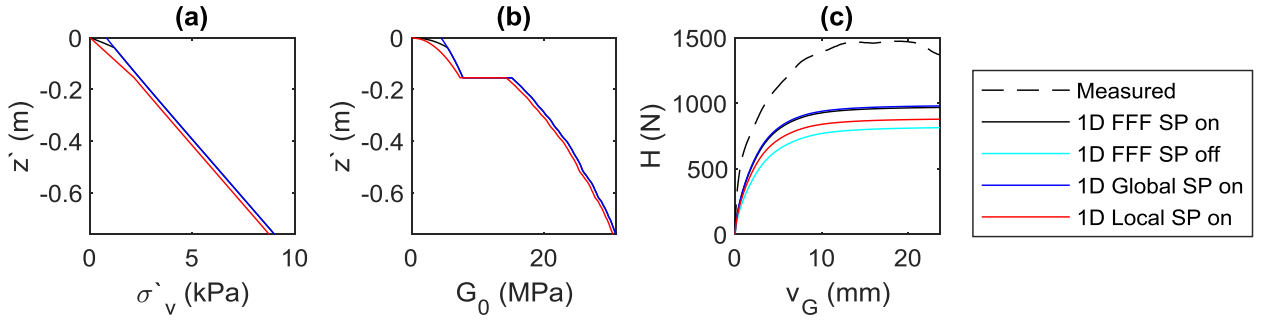

(1) Test 3 (remedial rock fill scour protection in a fully-formed scour hole)

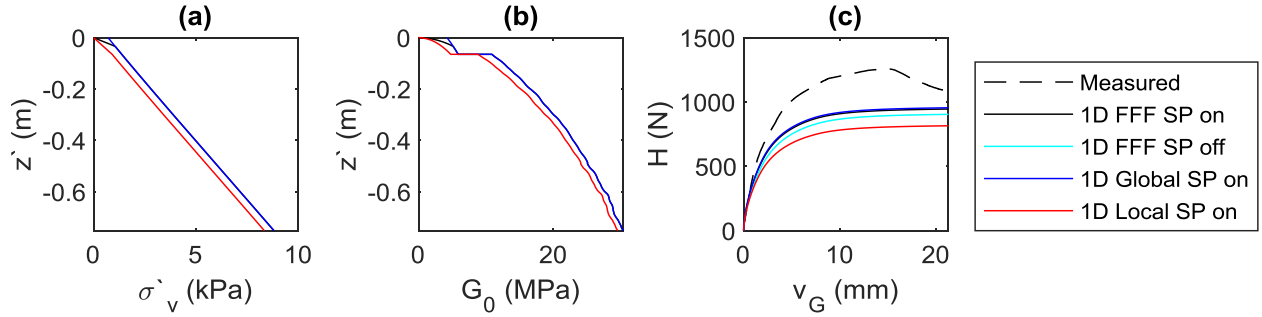

(2) Test 4 (remedial rock fill scour protection in a partially-formed scour hole)

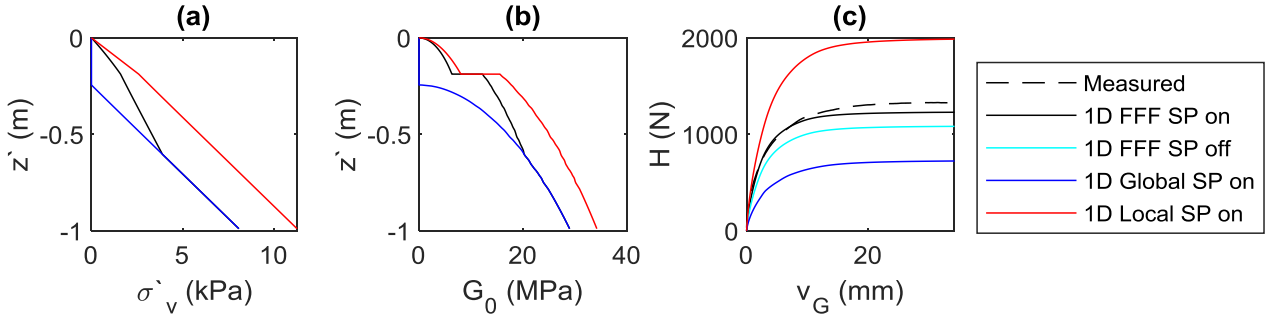

(3) Test 6 (remedial rock fill scour protection in a fully-formed scour hole with a falling apron)

Figure 4.18. Monotonic lateral loading analysis results. (a) Vertical effective stress σ_v' profiles; (b) Small strain shear modulus G_0 profiles; (c) Lateral load-displacement curves.

4.3.2.4 Pre-installed rock armour scour protection; Test 5 (P-RA)

Figure 4.19 presents the *OxPile* analysis results for the pre-installed rock armour scour protection test; Test 5 (P-RA). In Test 5 the scour protection is raised relative to the global bed level, and the scour protection thickness is the smallest of the modelled tests (Table 4.4). As a result of the relatively thin scour protection layer, the difference between the lateral loads computed using the '1D FFF SP on' and '1D FFF SP off' models (Figure 4.19(c)) is very small.

All models produced underpredictions of the measured lateral loads (Figure 4.19(c)). It was previously noted that the scour protection adjacent to the pile wall was slightly lower than the surrounding area (Figure 2.5), this has potential for the soil to have higher effective stresses than are produced using the '1D Local' model and hence reduce the under-prediction.

The results in Figure 4.19 shows that the pre-installed rock has a higher capacity contribution than the equivalent thickness of sand, which is consistent with results from Tests 3 and 4. The results imply that the influence of the global scour could be disregarded for pre-installed rock armour, since the best capacity prediction was made by simply modelling a flat seabed at the level of the top of the scour protection adjacent to the pile wall.

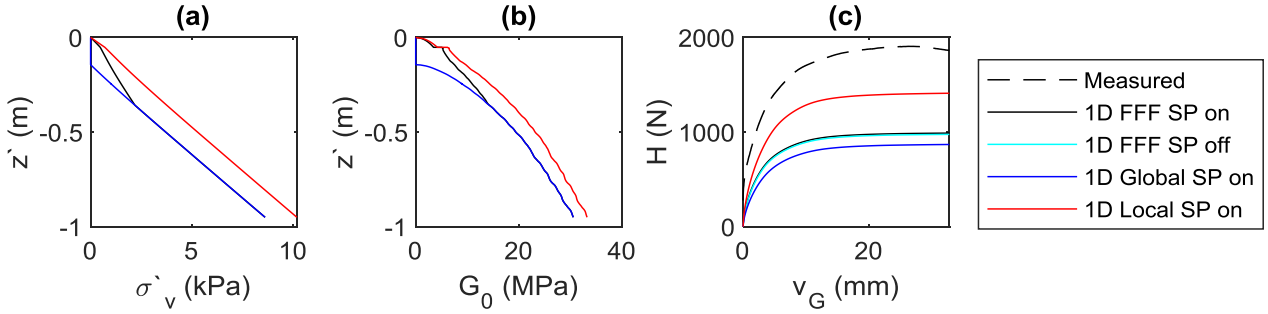

Figure 4.19. Test 5 (pre-installed rock armour) lateral loading analysis results; (a) Vertical effective stress σ_v' profiles; (b) Small strain shear modulus G_0 profiles; (c) Lateral load-displacement curves.

4.4 Conclusions

4.4.1 Numerical Model Calibration

The 1D model *EigPile* is capable of capturing the broad changes in natural frequency due to the effects of scouring and scour protection. For monopiles with scour or scour protection systems installed, the stiffness and capacity is affected by two mechanisms (see Paper 3): (A) the loss of or addition of soil reactions within the scour depth or scour protection layer, and (B) changes in the soil reactions in the underlying soil due to the weight of the scoured material or scour protection material.

Mechanism B was calibrated based on the natural frequency tests in scoured conditions (Section 4.2.3), and is accounted for in the *OxPile* calculations. The stiffness contribution of Mechanism B was calibrated based on the natural frequency tests (Section 4.2.4), but the capacity contribution cannot be modelled without additional data to characterise the scour protection behaviour.

4.4.2 Scour Effects

i. **Vertical effective stresses –** The FFF calibrated results indicate that the effective stresses, and therefore the small strain shear modulus, increases with depth more rapidly than suggested by the design standards (e.g. API, 2011); this finding is consistent with that of Qi et al. (2016).

ii. **Natural frequency –** Table 4.5 shows that the first natural frequency is relatively insensitive to the effective stress assumption within the range of effective stresses relative to the global scour depth and total scour depth, provided the pile embedment is modelled based on the bed level local to the pile wall. This suggests that Mechanism B dominates the natural frequency of mode 1.

iii. **Lateral capacity –** Local scour introduces the potential for a wide range of computed lateral capacities of monopile foundations. These computed lateral capacities are strongly dependent on the assumed effective stress conditions. The calibrated vertical effective stress model produces reasonable calculations of lateral capacity.

4.4.3 Scour Protection Effects

i. **Pre-installed rock armour –** Pre-installed rock armour scour protection enhances the capacity contribution of Mechanisms A and B. Mechanism B is strongly enhanced, since the global seabed level is so distant from the pile that the stresses adjacent to the pile are not affected by global scour developments. For thin layers of scour protection (e.g. $t_{sp}/D < 0.25$) the computed ultimate lateral capacity is insensitive to the magnitude of Mechanism A.

ii. **Remedial rock fill –** The stiffness of rock fill scour protection was lower than that of the original *in situ* material. Remedial rock fill enhances the capacity contribution for both Mechanisms A and B, provided the surface of the scour protection remains lower than the global bed level and is hence constrained by the surrounding soil. The capacity contribution of Mechanism A is higher than that offered by the original in situ material, despite the lower stiffness.

iii. **Sand accretion in scour protection –** Accretion of sand in the rock matrix, due to sediment transport, caused an increase in the stiffness. The capacity enhancements were inferred from the lateral loading tests performed after accretion the enhancement of Mechanism A may have been less significant if sand accretion had not occurred. There is therefore some uncertainty on the Mechanism A for full-scale structures, since it is unclear if such sand accretion occurs in the field.

iv. **Undermining of remedial rock fill –** If remedial rock fill scour protection is significantly undermined by global scour, the capacity contribution of Mechanism A is reduced, even if an enhancement in stiffness remains. Mechanism B becomes more complicated due to the competing effects of the scour protection weight but lowering global bed level.

v. **Remedial tyre-filled nets –** Tyre-filled net scour protection systems have a negligible stiffness contribution in the as-installed condition, with a modest increase over time due to sediment accretion in the tyres. Even with accretion, the stiffness of the tyre-filled nets is likely to remain low relative to the original *in situ* sand. For ultimate lateral capacity, tyre-filled net systems are likely to offer an enhancement to Mechanism B, and Mechanism A is similar to the contribution of the equivalent thickness of *in situ* sand.

Section 5 – Case Study of Robin Rigg Offshore Wind Farm

5.1 Introduction

This case study considers two full-scale wind turbines at Robin Rigg Offshore Wind Farm with remedial rock fill scour protection. Field measurements of scour depth and natural frequencies are presented both during scour development and after installation of scour protection.

The structural details and soil conditions (Section 5.2) are based on the design reports (Ramboll, 2007; MMI, 2013, HR Wallingford, 2015), and the scour protection details are based on the installation report (E.ON, 2016). Bathymetry data (Section 5.3.1) were supplied by HR Wallingford and natural frequency measurements (Section 5.3.2) were provided by E.ON.

The numerical programme *EigPile* is applied to analyse the natural frequencies of two turbine structures, herein referred to as Pile 1 and Pile 2. The numerical programme Ox*Pile* is applied for a lateral loading analysis of Pile 2. Section 5.4 presents the specification of the numerical models. Section 5.5 presents the numerical analysis results, which are discussed in Section 5.6.

5.2 Description of Site

5.2.1 Structure Characterisation

Figure 5.1 presents an overview of the structural arrangements of the wind turbine structures at Robin Rigg; vertical coordinates are generally presented as elevation above the local chart datum (z_{CD}) which corresponds approximately to the lowest astronomical tide (Section 5.2.2). The monopile-tower-nacelle structures comprise a monopile and tower connected by a grouted joint at the transition piece (TP). Figure 5.2 presents the presumed detail of the TP. Figure 5.1 also shows the beam element types used in the finite element model, Section 5.4.2 presents the details of additional masses attached to the structure. Marine fouling has been observed on the monopiles at Robin Rigg, but has not been modelled in this study.

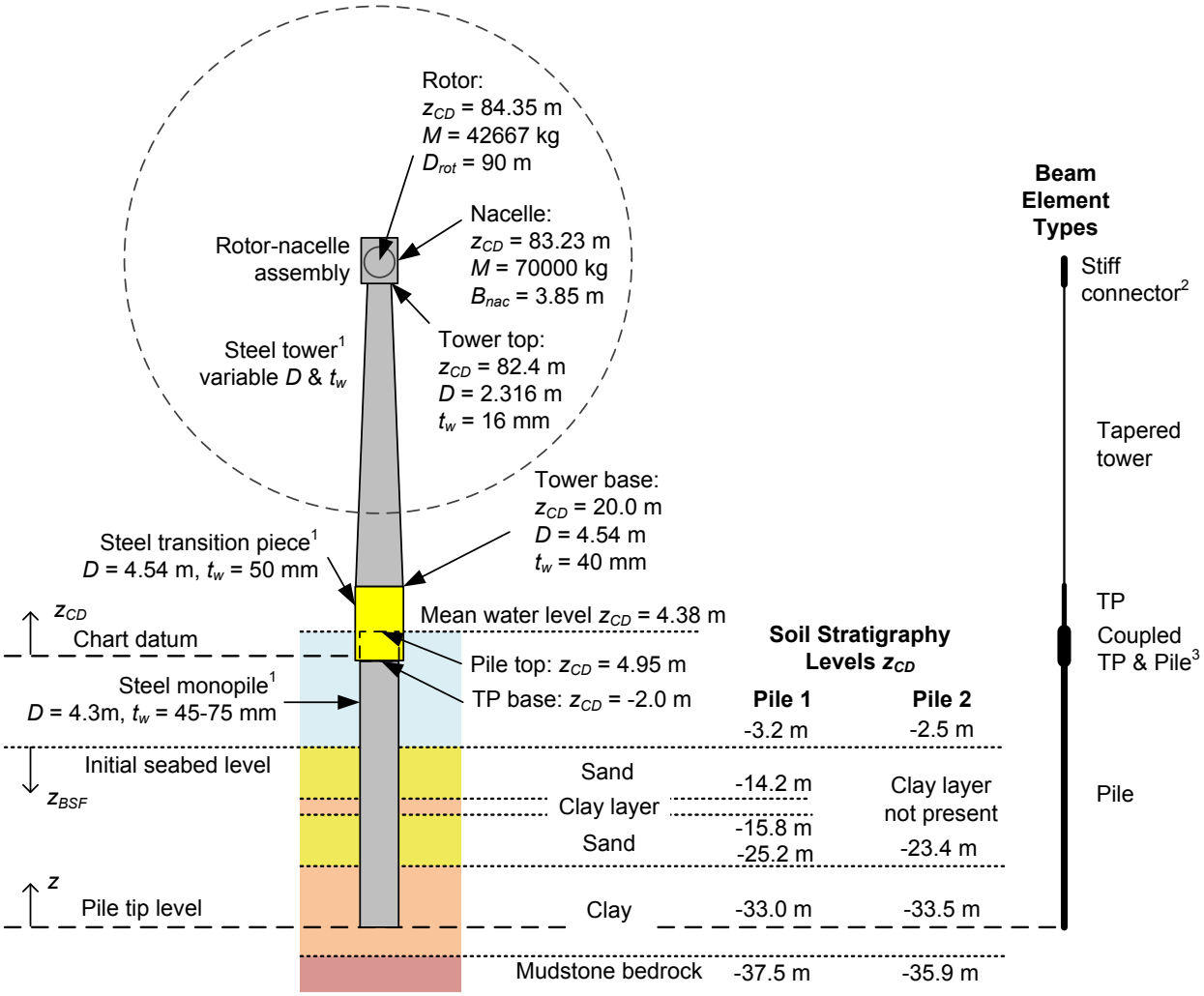

[1]Assumed steel material properties: E = 210 GPa, ρ = 7850 kg/m^3
[2]Stiff connector beam element properties: D = 2.316 m, t_w = 16 mm, E = 1E15 Pa, ρ = 0 kg/m^3
[3]Coupled beam element properties: $EI' = EI_p + EI_{TP}$ & $\rho A' = \rho A_p + \rho A_{TP}$

Figure 5.1. Characterisation of offshore wind turbine structures and soil stratigraphy at Robin Rigg Offshore Wind Farm, Piles 1 and 2

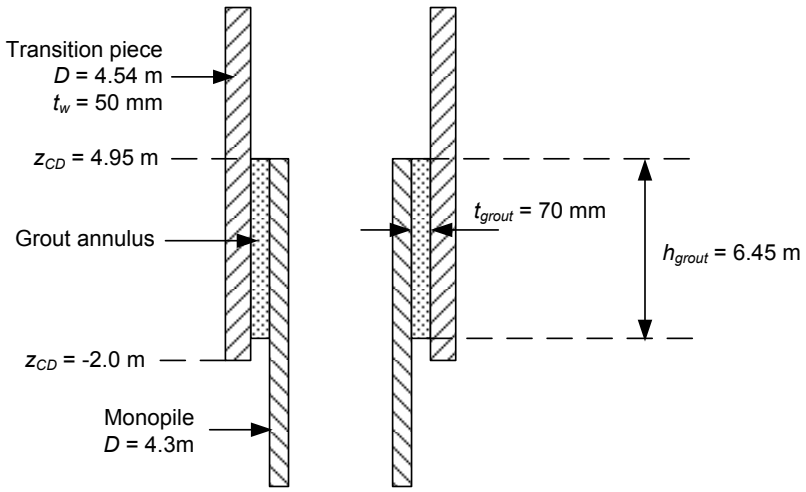

Figure 5.2. Sketch of grouted connection detail

5.2.2 Environmental Conditions

Table 5.1 presents the sea levels at Robin Rigg; the maximum tidal range at the site is 9.21 m.

Table 5.1. Water levels at Robin Rigg Offshore Wind Farm

Water Level	z_{CD} **(m)**
Highest astronomical tide	9.22
Mean high water (spring tide)	8.35
Mean high water (neap tide)	6.54
Mean water level	4.38
Mean low water (neap tide)	2.64
Mean low water (spring tide)	0.92
Lowest astronomical tide	0.01

5.2.3 Soil Conditions

Figure 5.1 shows that the geotechnical conditions at Robin Rigg are layered sand and clay. A mudstone bedrock is present at depth, but this is generally deeper than the pile tip. The site investigation at Robin Rigg did not include measurements of small strain shear modulus G_0, which are a required input for the PISA design method.

The sand layers at Robin Rigg are fine sand. Laboratory test data from the site investigation has informed the selection of e_{min} = 0.5868, e_{max} = 1.0385, and G_s = 2.65 for the Robin Rigg sand.

Clay layers at the Robin Rigg are typically slightly sandy clay. Oedometer tests from the RR OWF site investigation were reanalysed to determine overconsolidation ratio (OCR) for this field case study using the methods of Casagrande (e.g. Craig, 1992) and Pacheco Silva (1970). The results presented in Figure 5.3 reveal that the calculated OCR values are close to 1. This indicates that the clay layers are likely normally consolidated or lightly consolidated.

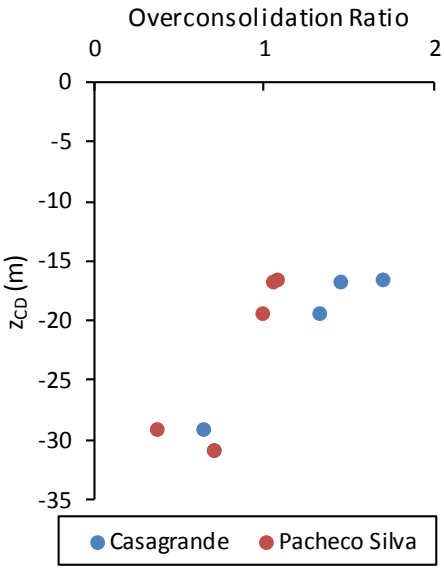

Figure 5.3. Overconsolidation ratio from oedometer tests at Robin Rigg offshore wind farm

5.2.4 Scour Protection

Rock fill remedial scour protection was installed 7.76 years after pile installation at Pile 1 and 7.72 years after pile installation at Pile 2. The rock fill has properties of G_s = 3.15. The median particle mass is 22 kg, which is equivalent to d_{50} = 509 mm for a spherical particle assumption. The total mass of installed scour protection was measured by the installation contractors (3433 tonnes at Pile 1; 3166 tonnes at Pile 2). The *in situ* installed bulk unit weight has not been analysed.

5.3 Field Data

5.3.1 Bathymetry Data

The development of total scour S_T and global scour S_G at Robin Rigg was assessed using the bathymetric surveys. The bathymetry surveys are performed approximately annually, and typically cover the full windfarm extent. Bathymetry data files for Pile 1 and Pile 2 were provided by HR Wallingford. The survey durations are typically in the order of several weeks to several months; the exact date at which the survey vessel is at a given turbine location was estimated as the mid-point of the survey dates. Data cleaning was required for some of the bathymetry data sets to remove rogue points near the pile wall. Figure 5.5 and Figure 5.6 present typical bathymetry maps before and after scour protection installation.

The bathymetry data analysis followed a similar process to that used for the flume experiments (Paper 3) with full 360º radial coverage in the field surveys. Local bed levels were taken as the median value of data points close to the pile wall ($r/D \leq 0.75$) where r is the radial distance from the pile centre; global bed levels were assessed using data points beyond the scour hole extent ($7.5 \leq r/D \leq 15$). Figure 5.6 presents the output scour depth development over time and Table 5.2 presents the maximum recorded scour depths. The maximum local scour depth is 1.85 D, which is in excess of the design guidance of S_L/D = 1.3 (DNVGL, 2016) or S_L/D = 1.5 (API, 2011), but is not unexpected based on other research (e.g. Den Boon et al., 2005).

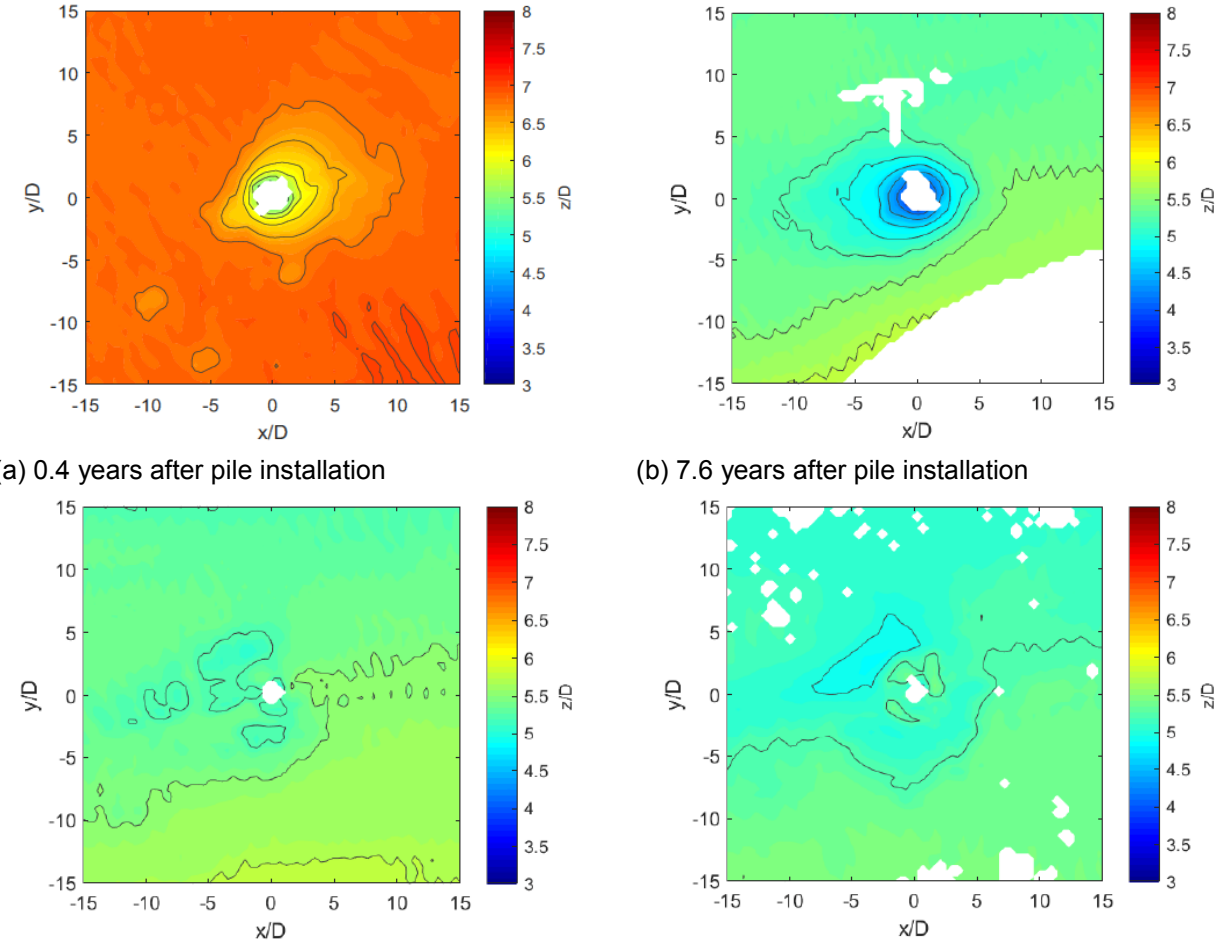

(a) 0.4 years after pile installation

(b) 7.6 years after pile installation

(c) 8.3 years after pile installation (0.6 years after scour protection installation)

(d) 10.2 years after pile installation (2.5 years after scour protection installation)

Figure 5.4. Example bathymetry measurements before and after scour protection installation: Pile 1. Coordinates x and y are distance East and North from pile centreline, respectively; coordinate z is vertical distance above pile tip.

The scour depths in Figure 5.6 show temporary reductions in the total scour depth at approximately 1.2 and 6.4 years, caused by natural backfilling of the scour holes. Since the site bathymetry is only periodically, it is unclear for how long this backfill was present.

The installation of scour protection, indicated in Figure 5.6, manifests as a reduction in measured total scour depth and local scour depth. By coincidence at Pile 1 there was a sudden increase in global scour approximately 7.5 years after pile installation (Figure 5.6(a)), also Figure 5.4), shortly before the scour protection was installed. At Pile 2 (Figure 5.6(b), also Figure 5.5) the global scour has continued after installing scour protection and the global bed level by the end of the data set is lower than the top of the scour protection ($S_G > S_T$).

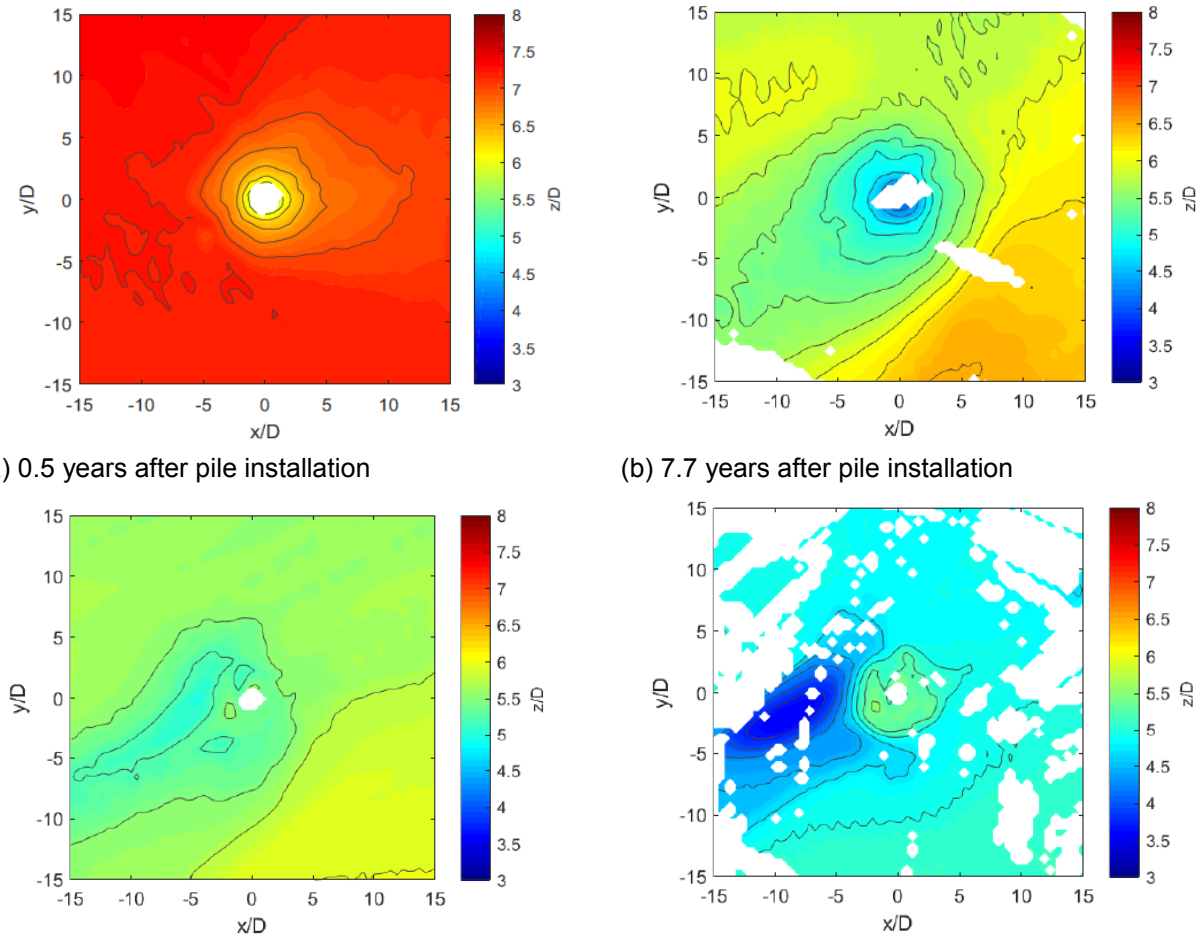

(a) 0.5 years after pile installation

(b) 7.7 years after pile installation

(c) 8.3 years after pile installation (0.6 years after scour protection installation)

(d) 10.2 years after pile installation (2.5 years after scour protection installation)

Figure 5.5. Example bathymetry measurements before and after scour protection installation: Pile 2. Coordinates x and y are distance East and North from pile centreline, respectively; coordinate z is vertical distance above pile tip.

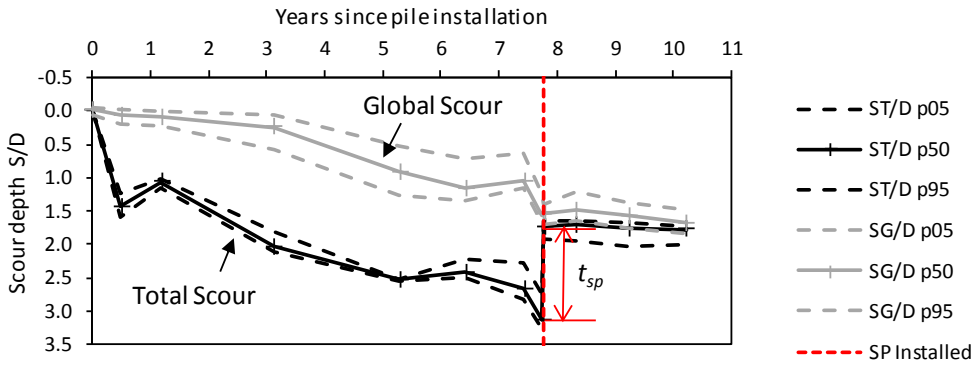

(a) Total and global scour depths at Pile 1. Scour protection installed at 7.76 years (red dashed line).

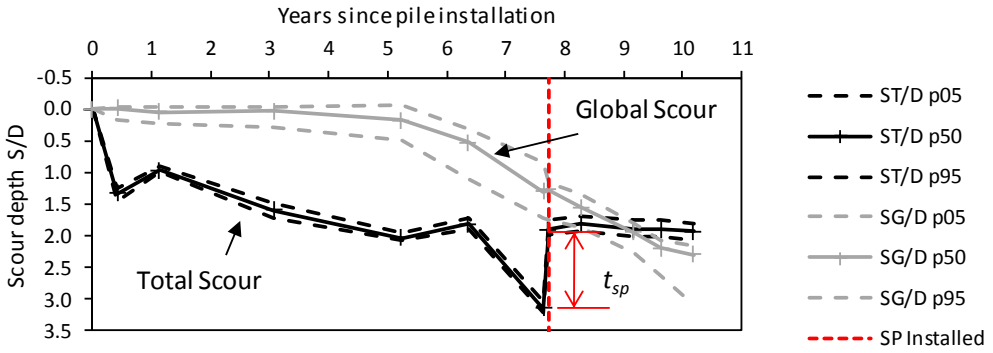

(b) Total and global scour depths at Pile 2. Scour protection installed at 7.72 years (red dashed line).

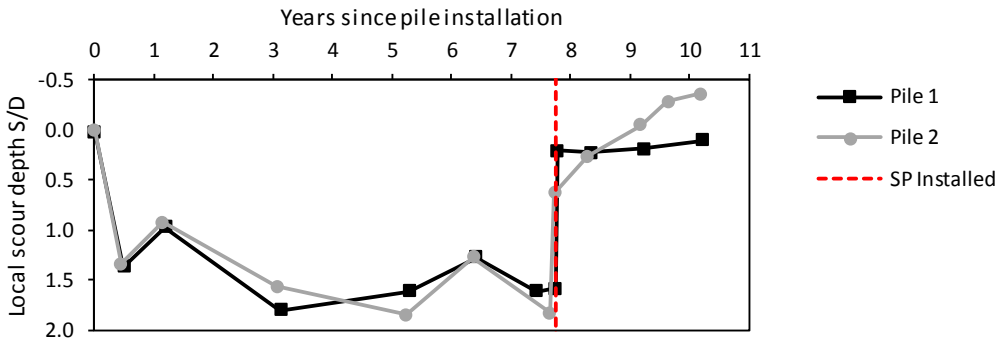

(c) Local scour depths. Calculated from median total and global scour in (a)&(b)

Figure 5.6. Time series of measured scour depths. Notation pXX indicates XXth percentile, i.e. p50 indicates the median value. t_{sp} is the thickness of scour protection adjacent to the pile wall.

Table 5.2. Maximum scour depths in field case study

Location	Installed pile embedment L/D	Maximum global scour S_G/D	Maximum total scour S_T/D	Maximum local scour S_L/D	Installed SP thickness t_{sp}/D
Pile 1 (median)	6.93	1.58	3.14	1.80	1.40
Pile 2 (median)	7.21	2.30	3.14	1.85	1.24

5.3.2 Natural Frequency Data

Natural frequency measurements for Pile 1 and Pile 2 were provided by E.ON. It is understood that the measured natural frequencies were taken as the peak of the power spectral density of acceleration data, where the accelerations are measured in the nacelle during rotor stop tests and standstill periods. The natural frequency field data have the following limitations:

- Only the first natural frequency is calculated.
- The natural frequency data are only available from 4 years after turbine installation (corresponding to the end of the turbine warranty).
- The frequency resolution is approximately 0.012 Hz, roughly 4% of the natural frequency; future monitoring campaigns should aim to produce natural frequencies to a higher precision.
- Measurements are relative to the nacelle orientation, which is a rotating frame of reference, and frequencies are reported in the downwind (DW) and crosswind (CW) directions. Since the orientation of the nacelle was not analysed, it is not possible to identify if the scatter in the measured frequencies are caused by scour asymmetry or rotor inertia effects.

Figure 5.7 presents the natural frequency measurement data; a measurement trend is plotted as the mean of five values centred on each measurement. At pile 1 (Figure 5.7(a)) the natural frequency is stable before scour protection was installed (4 years to 7.76 years), and the scour depths (Figure 5.6(a)) are also relatively stable within the same period. At pile 2 (Figure 5.7(b)) the natural frequency reduces over the monitored period before scour protection was installed (4 years to 7.72 years), and the total scour depth (Figure 5.6(b)) increased leading to a reduction in pile embedment depth over the same period.

The measured natural frequencies tend to be higher after installation of the scour protection at both Pile 1 and 2. The flume experiment results show that the natural frequencies after installing scour protection tend to drift upwards due to sand accretion, or to drift downwards in cases of extreme global scour. It is unclear if either of these effects are present in the measured natural frequency data (Figure 5.7).

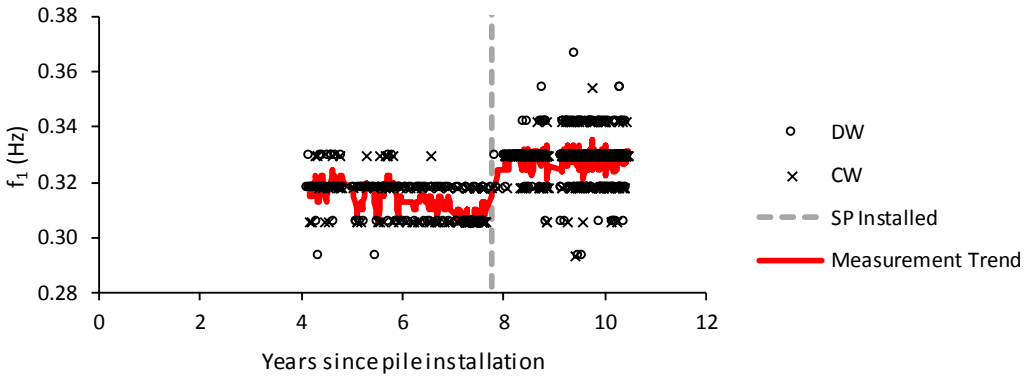

(a) Natural frequency measurements at Pile 1

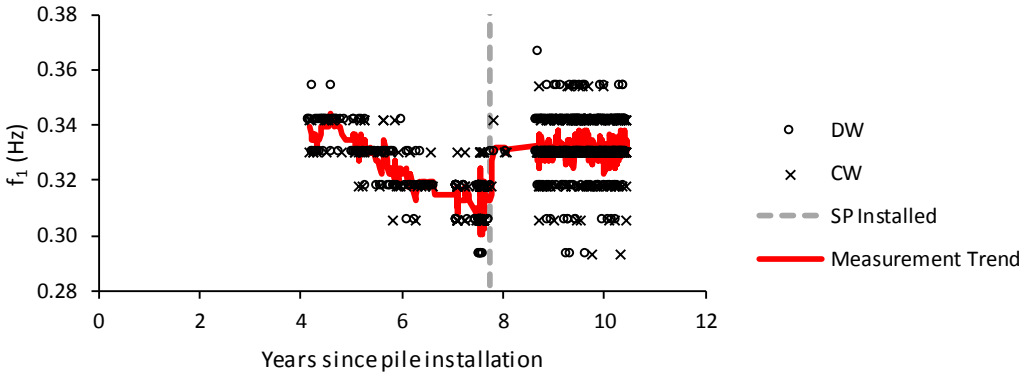

(b) Natural frequency measurements at Pile 2

Figure 5.7. Time series of measured natural frequency at Pile 1 and 2. DW and CW indicate measurement in the downwind and crosswind direction respectively; grey dashed line indicates date of scour protection (SP) installation; measurement trend is the mean value of five data points.

5.4 Numerical Model Specifications

5.4.1 Structure Model

The general configuration of the monopile-tower-nacelle structure (Figure 5.1) includes details of the beam elements used to represent the structure. Figure 5.8 presents the profiles of D and t_w along the structure, as modelled in *EigPile*. Nodes were added at changes in D and t_w (see Section 3.5.2). The lateral loading analysis using *OxPile* adopted a simplified pile geometry with a uniform diameter D = 4.3 m and wall thickness t_w = 55 mm.

5.4.2 Nodal Masses

Items attached to the structure (e.g. rotor, nacelle, ladders, flanges, platforms, etc.) were modelled as lumped nodal masses. These nodal masses are listed in Table 5.3. The radius of gyration R_{gyr} in Table 5.3 was estimated for all items, with the following assumptions:

- For the rotor: $R_{gyr} = D_{rot}/6$, where D_{rot} is the rotor diameter (this presumes that the centre of mass of blades is located at 1/3 of the blade length)
- For the nacelle: $R_{gyr} = B_{nac}/4$, where B_{nac} is the nacelle width (this presumes that nacelle is of uniform density)
- For items attached to the outside of the structure (platforms, external ladders, I-tubes, boat landing bumpers): $R_{gyr} = D/2$
- For items attached circumferentially (flanges, grout): $R_{gyr} = D/4$ (this is a rough approximation of a thin-walled cylinder)
- For items inside the tower (damper, tower ladder): $R_{gyr} = 0$

The sensitivity of the analysis to radius of gyration R_{gyr} assumptions has not been explored.

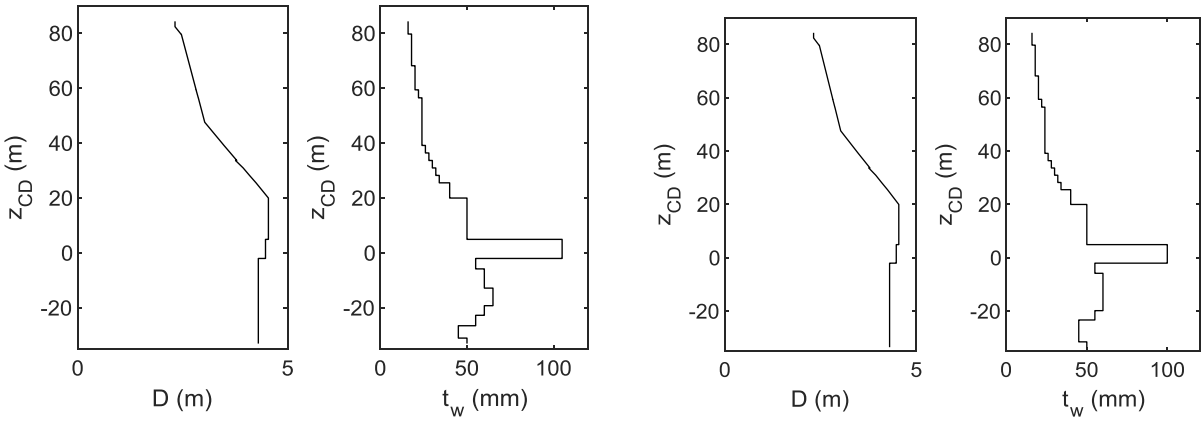

(a) Pile 1 (b) Pile 2

Figure 5.8. Field case study structure geometry

Table 5.3. Field case study structure nodal masses

Item description	z_{CD} (m)	M (kg)	R_{gyr} (m)
Rotor	84.35	42667	15.0
Nacelle	83.23	70000	0.9625
Top flange on tower	82.4	1663	0.579
Damper	82.0	7000	0
Intermediate flanges	47.597	3348	0.756
Tower ladder (100 kg/m over 62.4 m, lumped to 10 locations at 6.24 m spacings)	23.12 to 79.28	624 per location	0
Bottom flange on tower	20.0	2910	1.135
Top flange on TP	20.0	2910	1.135
External platform	20.0	7300	2.27
Upper platform	18.8	2000	2.27
Upper access ladder (100 kg/m over 7 m)	16.5	700	2.27
Rest platform	13.5	1000	2.27
I-tubes (2 x 120 kg/m over 21.5 m)	9.25	5160	2.27
Lower access ladder (10 kg/m over 16.1 m)	6.55	161	2.27
Boat landing bumpers (2 x 166 kg/m over 14.5 m)	5.75	4814	2.27
Platform at pile top	5.0	1000	2.27
Grout (70 mm annulus at 2000 kg/m^3 over 6.45 m)	1.725	12397	1.105

5.4.3 Water Added Mass Assumptions

The water depth was modelled located at the mean water level (Table 5.1) for both the internal and external added mass of water; the sensitivity of the results to water depth has not been explored. The density of water was assumed as ρ_w = 1000 kg/m^3, which is marginally lower than the values expected for seawater but not expected to influence the results.

5.4.4 Soil Models

The soil stratigraphy is described in Figure 5.1 and Section 5.2.3.

The small strain shear modulus, G_0, for sand layers at Robin Rigg were calculated using the relationships for Dunkirk sand (Table 3.4, after PISA2 Final Report, 2018), and soil reactions were modelled using the generalised Dunkirk sand model (GDSM) (PISA2 Final Report, 2018).

The small strain shear modulus, G_0, for clay layers at Robin Rigg were calculated using the relationships for Bothkennar clay (Table 3.4, after PISA2 Final Report, 2018). Bothkennar is a clay site, with OCR ≅ 10 at the soil surface reducing to OCR < 2 at depths greater than 3 m (PISA2 Final Report, 2018); the Cowden till and London clay models from the PISA2 project were developed for soils with higher OCR, therefore the Bothkennar model was considered to be the most appropriate.

The original embedment lengths of some piles at Robin Rigg (e.g. $L/D = 6.93$ at Pile 1) are outside the calibration space of the PISA soil reaction models ($2 \leq L/D \leq 6$). The normalised soil reactions (k_p,k_m,k_H,k_M) were assumed to be constant outside of the calibration space (equal to the value corresponding to $L/D = 6$).

Figure 5.9 and Figure 5.10 present the soil parameter profiles employed in the *EigPile* analysis, which were developed from the original design soil parameter profiles. The *OxPile* analysis adopted a simplified set of soil parameters with sand modelled at a constant relative density, D_R = 90% and clay modelled with a constant undrained shear strength s_u = 100 kPa.

It is noted that the selected soil models and modelling assumptions are not necessarily appropriate for final design calculations. The PISA project recommendation is to calibrate the soil

reactions using 3D finite element analyses using appropriate constitutive soil models based on advanced laboratory soil testing.

5.4.5 Soil Plug Assumption

The soil plug length is unknown and was assumed to be equal to the installed pile embedment length.

5.4.6 Scour Protection Models

It is noted that there is very little design guidance on the specification of the properties of rock fill scour protection. The scour protection unit weight was calculated using an assumed voids ratio representative of the flume experiments (e = 0.95), and the rock fill scour protection stiffness modelled based on the analysis of the flume experiments (Section 4.2.4.1).

Table 5.4 presents the scour protection parameters adopted for the case study. The 'as-installed' scour protection parameters were used to model the initial natural frequency change after installing scour protection. It was assumed that sediment accretion occurs in the field at Robin Rigg, and the parameters 'with accreted sand' (Table 5.4) were used to model the sediment accretion effects. The 'as-installed' parameters were used with the first bathymetry after installing scour protection, and the 'with accreted sand' parameters were used with subsequent bathymetry data.

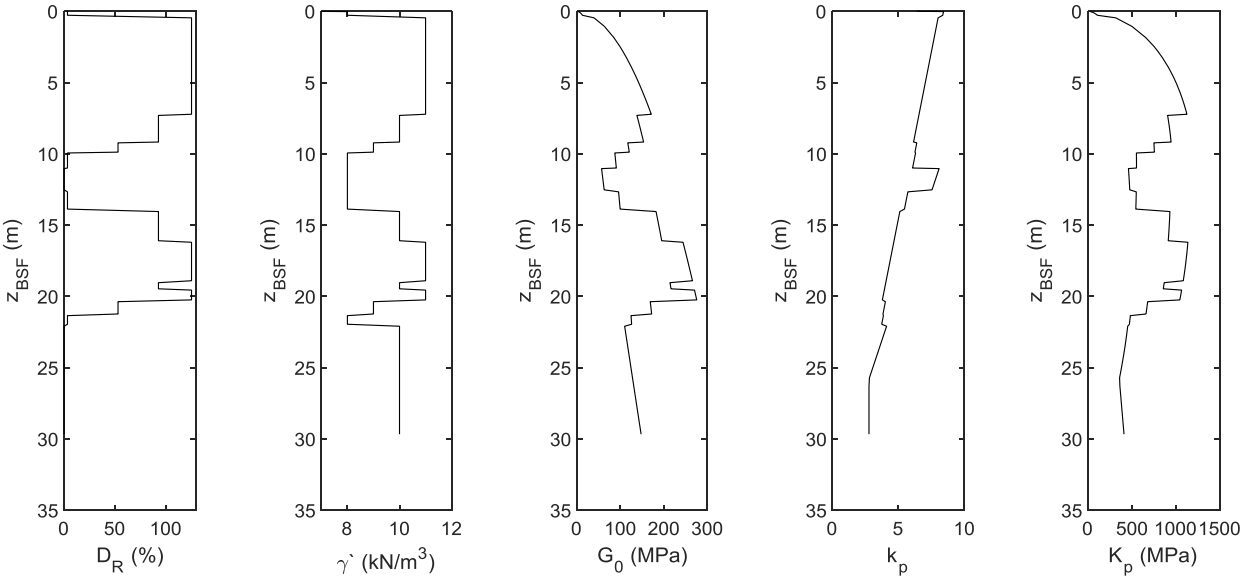

Figure 5.9. Field case study soil parameter profiles at Pile 1; z_{BSF} is the depth below seafloor at the time of pile installation.

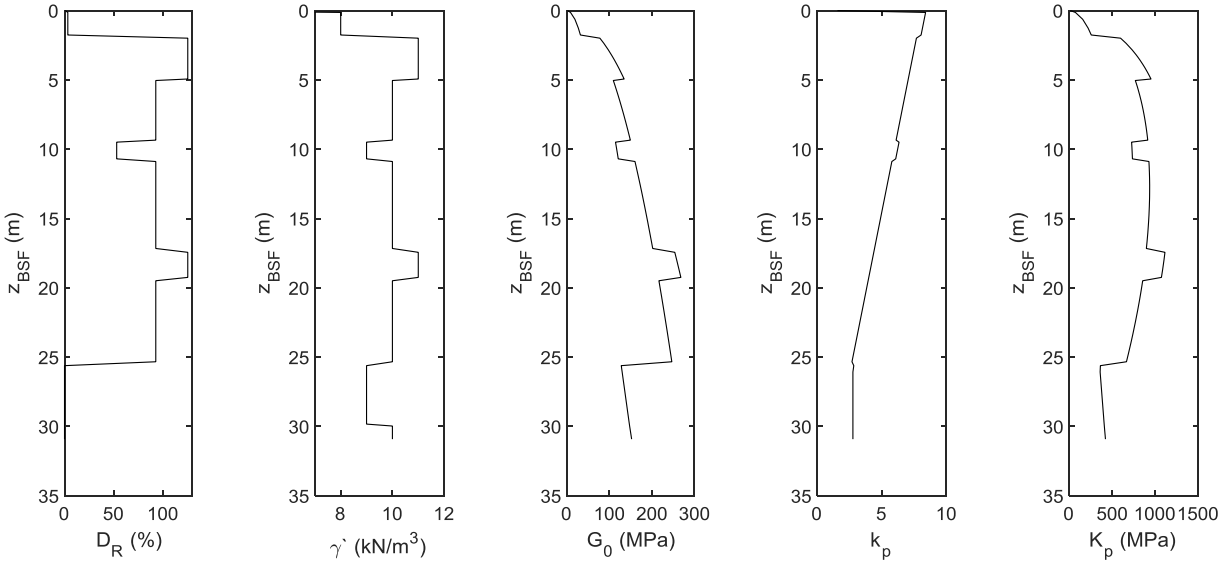

Figure 5.10. Field case study soil parameter profiles at Pile 2; z_{BSF} is the depth below seafloor at the time of pile installation.

Table 5.4. Scour protection model parameters for field case study

Scour protection condition	γ [kN/m^3]	B_{SP}
As-installed	20.63	259
With accreted sand	25.47	500

5.5 Numerical Analysis Results

5.5.1 Natural Frequency Results

The natural frequencies of Pile 1 and 2 were calculated using *EigPile* for each of the measured scour depths (from Figure 5.6) to produce a time series of predicted natural frequencies. Two scour effective stress models were analysed: (1) 'FFF Calibrated' bilinear model from the flume experiments with δ_L = 1.49 (Section 4.2.3); and (2) 'API' (2011) with $\Delta z_O/D$ = 6.

Figure 5.11 presents the output change in natural frequency from the initial unscoured condition. The computed change in natural frequencies in Figure 5.11 are presented alongside the change in natural frequency measurement trends (from Figure 5.7). The computed and measured natural frequencies are normalised by a common initial unscoured natural frequency, inferred from the *EigPile* analysis.

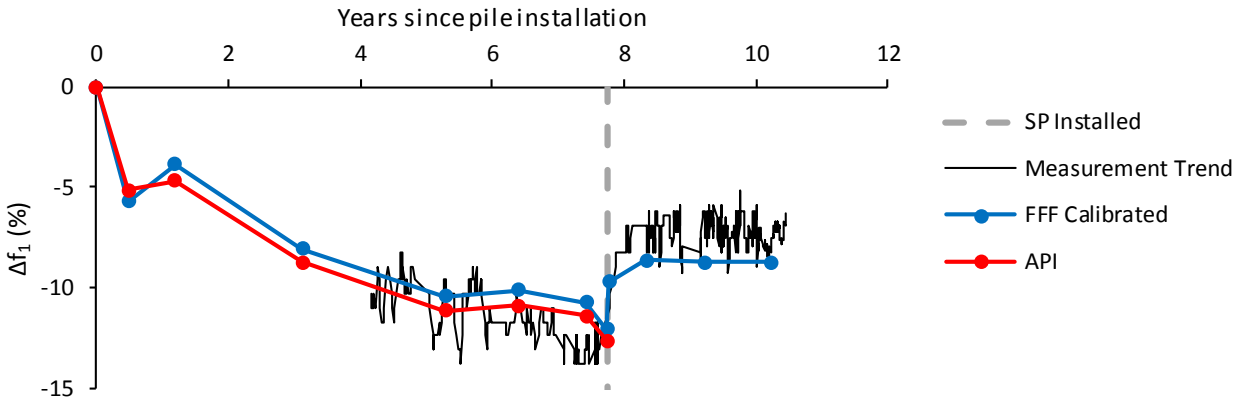

(a) Change in natural frequency at Pile 1

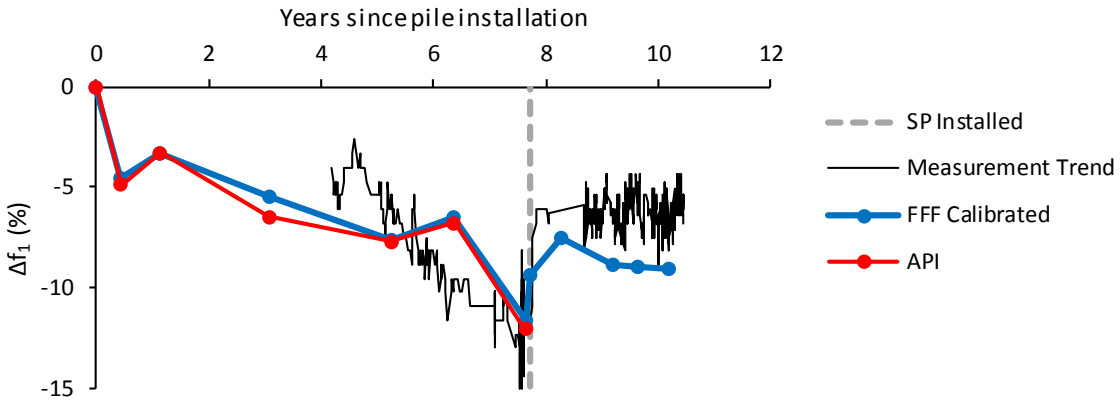

(b) Change in natural frequency at Pile 2

Figure 5.11. Comparison of *EigPile* natural frequency results (measurement trend from Figure 5.7)

5.5.2 Lateral Loading Results

The lateral load-displacement behaviour of Pile 2 was analysed using *OxPile*. Analyses were performed for local scour depth of S_L/D = 0 to 3, and global scour was fixed at zero (S_G/D = 0). Four scour effective stress models were analysed (Table 4.10): (1) '1D Local Model' in which the local scour influence factor α_L = 0; (2) '1D Global Model' in which α_L = 1; (3) '1D API Model' in which the non-dimensional overburden reduction depth δ_L = 4; (4) '1D FFF Model' in which δ_L = 1.49.

Figure 5.12 presents example results for a local scour depth of S_L/D = 2, similar to the bathymetry condition at 5.2 years in Figure 5.6(b). In Figure 5.12(c) the ground level displacements v_G are normalised by a reference value v_R = 0.1D, and lateral loads H are normalised by a reference value H_R at $v_G = v_R$ taken from the '1D Local Model' results. Figure 5.13 presents the computed variation of the normalised reference loads as a function of the local scour depth.

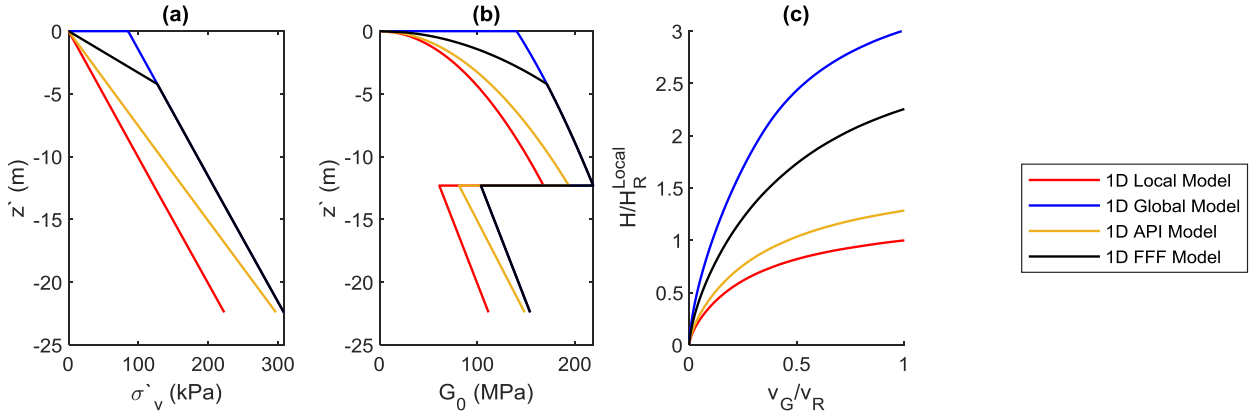

Figure 5.12. Lateral loading analysis results for Robin Rigg Pile 2 with local scour ($S_L/D = 2$) and zero global scour ($S_G/D = 0$); lateral load H applied at mean water level z_{CD} = 4.38; (a) Vertical effective stress σ_v' profiles; (b) Small strain shear modulus G_0 profiles; (c) Normalised lateral load-displacement curves.

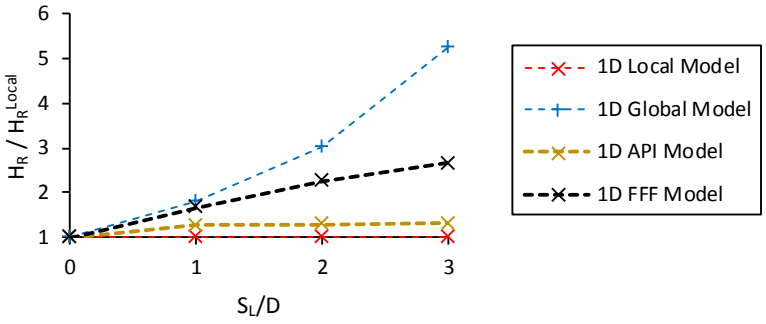

Figure 5.13. Influence of the modelled vertical effective stress on the lateral capacity. Data from the analysis of Robin Rigg Pile 2 with zero global scour ($S_G/D = 0$); lateral load H applied at mean water level z_{CD} = 4.38.

5.6 Discussion

5.6.1 Overview

Comparison of the calculated and measured natural frequencies in Figure 5.11 indicates that the numerical results are plausible for the scoured condition and with scour protection installed. There is uncertainty on the quality of the fit due to the limitations of the measured natural frequencies (Section 5.3.2) and the periodic nature of the known scour depths from the bathymetry surveys (Section 5.3.1).

Overall, the natural frequency results in Figure 5.11 indicate that *EigPile* is capable of producing reasonable predictions of the first natural frequency for field scale offshore wind turbines, where assumptions on the soil stiffness and scour protection stiffness were provisionally calibrated using the flume experiments.

5.6.2 Scour Effects

Both of the scour effective stress models presented in Figure 5.11 give a reasonable match to the measured frequencies before scour protection is installed. This supports the finding that the predicted natural frequencies are rather insensitive to the effective stress assumption, which is consistent with the relatively small differences in mode 1 predictions for the flume experiments (Table 4.5). The results using the Qi et al. (2016) scour effective stress model have not been presented, but is expected to produce very similar to the 'FFF Calibrated' model.

The results of the lateral loading analysis show that there is potential for a wide range of capacity predictions. The capacity prediction is highly dependent on the assumed vertical effective stress profile, with a factor of 3 between the upper and lower predictions in Figure 5.12 (S_L/D = 2). This result is remarkably similar to the same analysis for the flume experiments (Section 4.3.2.1, Figure 4.16). The '1D FFF Model' for vertical effective stresses produces significantly higher capacities than the equivalent API (2011) approach, and therefore presents an opportunity for design optimisation.

5.6.3 Natural Backfill Effects

The predicted natural frequencies in Figure 5.11 show a slight increase at approximately 6.4 years (Figure 5.11), caused by the reduced total scour depth measured at this time (Figure 5.6). This increase is not seen in the natural frequency measurement trends, however the numerical model did not attempt to model sand backfill material as having different properties to the original *in situ* material. These results show that the backfill material should be modelled as having a lower stiffness contribution than the original *in situ* material, this finding is consistent with the flume experiments, where Test 1 showed that backfill material has a lower stiffness contribution than the original *in situ* material (discussion in Paper 3).

5.6.4 Scour Protection Effects

Following installation of scour protection, the predicted increase in natural frequency is slightly less than the measurement trend (Figure 5.11), this shows that the actual stiffness contribution of the scour protection material at Piles 1 and 2 is higher than that modelled. The rock density used at Robin Rigg was higher than in the flume experiments. Since the additional effects of the higher weight are accounted for in the effective stress calculations, the results indicate that B_{SP} for the rock fill scour protection at Piles 1 and 2 is higher than that from the flume experiment calibration.

The lateral capacity of monopiles with scour protection was not explicitly analysed for the Robin Rigg case study. The results of the flume experiment analysis (Section 4.3.2.3) show that the capacity with remedial rock fill is expected to be greater than that predicted with scour protection modelled as a sand layer using the '1D FFF Model' (e.g. Figure 5.13).

5.6.5 Sand Accretion Effects

The natural frequency predictions for both Piles 1 and 2 (Figure 5.11) show an additional increase after installing scour protection due to the assumed higher value of B_{SP} with sand accretion. The natural frequencies are still slightly under-predicted compared with the measurement trend. The effects of sand accretion may be masked in the measurement trend since the frequency resolution of 4% is greater than the expected gain of up to 2% based on the flume experiments (Fig. 19 in Paper 3).

5.6.6 Scour Protection Undermining Effects

The natural frequency prediction for Pile 2 (Figure 5.11(b)) shows a reduction approximately 1 year after scour protection installation (~9 years after pile installation). This is a result of the continued global scour over the same time period (Figure 5.6(b)) causing reduced effective stresses and soil shear modulus values to be modelled. As with the sand accretion effects, the measured frequency resolution may be masking the effects of this scour protection undermining.

Section 6 – Conclusions and Recommendations

6.1 Summary

This portfolio has presented the results of a DEng research project, exploring the effects of scour and scour protection on the natural frequencies and lateral capacities of monopile-supported offshore wind turbines. Section 1 outlined the context of the work, which motivated the novel flume experiments described in Section 2. Three scour protection systems were explored in the flume experiments (pre-installed rock armour, remedial rock fill, remedial tyre-filled nets). Section 3 presented the development of a numerical model for natural frequencies analysis. Numerical modelling of the flume experiments was presented in Section 4, and the findings of the research were applied to a case study of two turbines at Robin Rigg offshore wind farm in Section 5.

This Section presents the conclusions of the research. Section 6.2 outlines the original contributions and main findings of the research, including responses to the research questions posed at the outset. Section 6.3 presents the recommendations arising from the findings, including recommendations for practice and suggested directions for further research.

6.2 Contributions and Findings

6.2.1 Original Contributions

i. **Development and execution of the flume experiments**

A novel programme of flume experiments was developed and executed to explore the behaviour of a driven monopile – tower system with realistic scour and scour protection conditions, using HR Wallingford's Fast Flow Facility flume. The monopile – tower system, developed for the experiments, was specified to model the foundation response and structural dynamics at appropriate scales.

The experiments required a significant logistical and organisational effort to coordinate the activities of the research participants from Oxford University, HR Wallingford, and E.On Energy. The executed test matrix of six tests was devised to explore both scour and scour protection, given the limited number of tests able to be performed in the available flume time.

A compacted and saturated sand bed was prepared for each test, and a CPT was performed for each test to ensure that the achieved sand bed was consistent. Equipment and methods were developed for the pile driving, structural dynamics testing, and monotonic lateral loading testing activities. The scour protection models were developed and specified to be at appropriate geometric scales compared with full scale structures.

Novel aspects of the experiments include measurement of the structural dynamics of a full monopile – tower system, structural dynamic measurements with a variable top mass, and structural dynamic measurements and lateral loading tests in a flume experimental setup. The onset of global scour was initiated during the flume tests by triggering a slope instability at the edge of the test section, as opposed to the typical approach of establishing an instability at the start of the test.

The tests produced measurements of the influence of pre-installed rock armour, remedial rock fill, and tyre-filled net scour protection on the foundation response. Excavations at the end of each test revealed that sand accretion had occurred in the scour protection material, which has not been widely investigated in previous research.

ii. **Analysis of the flume experiment results**

A method was developed for the definition of representative local and global bed levels from bathymetry data as an input to geotechnical analysis. The structural dynamics test data were analysed to produce inferred natural frequencies, damping ratios, and mode shapes. The monotonic loading test data were analysed to produce load-displacement curves and capacity parameters. The results provide new insight into the influence of scour and scour protection on the monopile response, including that sand accretion had significantly influenced the soil-structure interaction.

Soil characterisation activities were carried out to inform subsequent numerical modelling of the tests. This includes determination of relative density profiles from the CPT data, for which a set of calibration tests were performed. The small strain shear modulus G_0 is characterised using bender element test data. A calculation method is proposed to determine the unit weight of scour protection with accreted sand.

iii. **Development of the 1D finite element programme *EigPile***

EigPile was developed for the analysis of natural frequencies, adopting an eigenvalue approach and small strain elastic assumptions, using the soil reaction methodology from the PISA 1D model. This 1D approach offers an improvement in capabilities compared with macro element models, allowing input of layered soil conditions and outputs of results for the higher modes including mode shapes below ground level.

The soil models in *EigPile* account for the influence of scour and scour protection on the vertical effective stresses and small-strain shear modulus. For monopiles with scour protection, simple methods are proposed for calculation of the vertical effective stress profile, small-strain shear modulus G_0, and lateral stiffness component of the soil reactions.

iv. **Numerical modelling of the flume experiments**

The *EigPile* models for scoured vertical effective stress and scour protection stiffness were calibrated using the natural frequency results from the flume experiments. The calibrated models are applied in the numerical analysis of the lateral loading tests, using the PISA 1D model (via the Oxford-developed *MATLAB* programme *OxPile*). The numerical modelling provides new insight into the contributions of scour and scour protection to the stiffness and lateral capacity of monopile foundations.

v. **Numerical modelling of full-scale structures in a case study of field data**

A case study using bathymetry and natural frequency field data from Robin Rigg Offshore Wind Farm was performed to verify the performance of the *EigPile* model. A lateral loading analysis was also performed for the case study using the PISA 1D model (via *OxPile*). The lateral loading analysis for the case study showed similarity to the analysis of the flume experiments. The case study shows that the scour and scour protection stiffness models, calibrated based on the flume experiments, are a reasonable representation of full-scale structures.

6.2.2 Main Findings

i. **Natural frequency modelling –** A sound basis for analysis has been made with *EigPile* through calibration with the scour and scour protection testing in the Fast Flow Facility (FFF) and through demonstration of plausible behaviour through application at two foundations of the Robin Rigg offshore wind farm.

ii. **Mechanisms of scour effects –** The occurrence of scour and scour protection at a piled foundation causes changes in the monopile response due to two mechanisms: (A) the removal or addition of soil reactions due to the change in embedment, and (B) changes in the soil reactions in the underlying soil due to changes in the weight of the overlying material.

iii. **Unremediated local scour –** For unremediated local scour development, the natural frequencies are dominated by the change in embedment (Mechanism A). The natural frequency of the first bending mode is relatively insensitive to the vertical effective stress distribution for Mechanism B, provided it is modelled within plausible bounds (prediction range of 1% to 2%). The lateral capacity is highly sensitive to the vertical effective stress distribution for Mechanism B (e.g. factor of 3 between predictions for S_L/D = 2 in case study), which introduces a level of uncertainty. A bilinear vertical effective stress model was calibrated using the flume experiment natural frequency measurements (calibrated δ_L = 1.49), and also produces a reasonable match to the lateral loading tests. The calibration indicated that the vertical effective stresses are expected to increase with depth more rapidly than suggested in the design standards (equivalent δ_L = 4 from API, 2011). This finding is consistent with other research (Qi et al., 2016; Lin and Jiang, 2019).

iv. **Structural health monitoring for scour detection –** The flume experiments showed that the natural frequency of the second bending mode is a good indicator of scour development (in flume experiments: 11.7% to 15.6% reduction per diameter of total scour S_T, on average 4.13 times more sensitive than mode 1). This finding broadly agrees with previous numerical work (e.g. Sørensen and Ibsen, 2013). The experiments also showed that scour causes measurable changes in the mode shape of the first three bending modes (in flume experiments: mode 2 maxima position moves downwards by $\Delta z/S_T =$ -0.42 to -0.58). Based on these findings, structural health monitoring systems

targeting mode 2 could be adopted to monitor scour development at high risk sites. Structural health monitoring would provide strong evidence of scour development in the field if these changes in mode 2 are observed, concurrent with the expected mode shape changes and lesser frequency drops of mode 1 (in flume experiments: 2.6% to 4.8% per diameter of total scour S_T) and mode 3 (in flume experiments: 6.8% to 8.4% per diameter of total scour S_T). It is recommended to implement structural health monitoring from the outset for offshore wind farm sites in development with a high scour risk, especially if a 'monitor and react' scour design approach is adopted.

v. **Backfill of scour holes –** Natural backfilling of scour holes with sand has a negligible or small positive effect on the natural frequencies, observed in the flume experiments and Robin Rigg field data. This shows that the magnitude of stiffness in Mechanism A is lower in backfill than the original *in situ* sand. When compared with the numerical predictions of Sørensen and Ibsen (2013), this suggests that the sand was deposited at a low relative density. This suggestion contradicts the results of Sørensen et al. (2010), which showed high relative density of backfill – possibly caused by wave compaction. In summary, the natural sand backfilling mechanism provides a temporary enhancement of the foundation stiffness, but the magnitude of the enhancement is not reliable.

vi. **Pre-installed rock armour scour protection –** Pre-installed rock armour of suitable design is likely to remain hydraulically stable. If the crest of the scour protection layer is sufficiently far from the monopile, the monopile response is unaffected by global scour and secondary scour. The magnitude of Mechanism A (the soil-structure interactions in the scour protection layer) has relatively little influence on the lateral capacity if the scour protection layer is thin. The most appropriate method for 1D numerical analysis of monopiles with preinstalled scour protection is to model a rock layer of uniform thickness and to make a flat seabed assumption at the surface of the scour protection layer.

vii. **Remedial rock fill scour protection –** Remedial rock fill enhances the natural frequencies and lateral capacity by a combination of Mechanisms A and B. These enhancements are expected if the scour protection surface is lower than the ambient bed level, i.e. the scour protection material is recessed in the scour hole and constrained by the surrounding soil. The stiffness contribution of

Mechanism A (calibrated B_{SP} = 259) is expected to be lower than that of the original *in situ* material, but the capacity contribution is expected to be higher than the original material.

viii. **Sand accretion in scour protection –** Sand accretion was observed in the rock scour protection matrix in the flume experiments, similarly to An et al. (2014). This accretion can further enhance the stiffness of Mechanism A (calibrated B_{SP} = 500), leading to increases in natural frequencies (measured up to 2%). The stiffness increase is presumably caused by increased particle interlocking in the scour protection matrix with accreted sand in the void space. There is a lack of evidence in the literature exploring whether sand accretion occurs in field conditions, such accretion would likely only occur at sites with live bed conditions and suspended sediment in the flow. It is possible that this accretion mechanism is responsible for the observations of frequency gains for wind turbines with scour protection at Greater Gabbard offshore wind farm (Hucker et al. 2019).

ix. **Undermining of remedial rock fill scour protection –** Remedial rock fill is likely to become unstable if the global scour causes the ambient bed level to drop lower than the surface of the scour protection. In this case the scour protection becomes raised relative to the ambient bed level, hence it is no longer constrained by the surrounding soil. The stiffness contribution of Mechanisms A and B reduce leading to reductions in natural frequencies, and the strength contribution of Mechanism A is expected to become negligible for lateral capacity analysis.

x. **Remedial tyre-filled net scour protection –** Tyre-filled nets provide the potential to limit the development of further local scour. The nets are likely to undergo movement after placement, hence should be tethered. On installation of tyre-filled nets the natural frequencies are expected to be unchanged, and Mechanisms A and B were found to be negligible. There is potential for small increase in natural frequencies over time as the stiffness of Mechanism A becomes enhanced by sand accretion in the tyre-filled nets (calibrated B_{SP} = 68.2 with sand accretion). If accretion occurs, lateral capacities are expected to be greater than the scoured condition due to Mechanism B, the strength contribution of Mechanism A is expected to be similar to the equivalent thickness of sand.

6.2.3 Response to Research Questions

Three research questions were posed at the outset of the research project (Section 1.3.1). The research findings and recommendations support the following responses:

i. What is the effect of scour protection on foundation stiffness and strength?

Foundation stiffness and strength were explored through numerical modelling and flume tank experiments performed at HR Wallingford's Fast Flow Facility. Structural dynamics testing and analysis were used to explore stiffness effects, and monotonic lateral loading testing and analysis were used to explore strength effects.

Scour protection was shown to enhance the stiffness and strength of monopile foundations under lateral loading conditions, with a greater enhancement of the strength than the stiffness. The magnitude of these enhancements depends on the type of scour protection system implemented, with rock having a significant effect and tyre-filled nets having a much smaller effect. Further enhancements were shown to develop due to sediment accretion in the scour protection matrix. These enhancements also have the potential to be diminished if global scour causes the scour protection to become unstable.

ii. What is the effect of global seabed lowering and can stiffness be regained with scour protection?

Global seabed lowering causes the total scour depth to increase for foundations unremediated against scour development, since the flow structures will work to restore the local scour depth to an equilibrium condition for the lower bed level.

Scour protection has the potential to stabilise the seabed level adjacent to the pile wall, which was shown to increase and also stabilise the stiffnesses. The flume experiments indicated that the stiffness is partially but not fully regained with scour protection. A case study of field data from Robin Rigg offshore wind farm indicates a greater stiffness enhancement than in the flume experiments, which may be due to the higher density of rock used in the field.

iii. Does local or global scour dominate foundation response and hence structural natural frequency?

The pile embedment, considering only the soil adjacent to the pile wall, governs the foundation response; in this sense it is the total scour depth, or combined global and local scour depths, which drive changes in the natural frequencies. The local and global scour depths can be used to bound the plausible effective stress profiles in the soil, and hence also bound the soil stiffness profiles. Data from the flume experiments was used to calibrate the effective stress profiles as a function of the global and local scour depths. The calibrated profile is similar to the results from other research (e.g. Qi et al., 2016).

The results indicate that natural frequency of the first structural bending mode is relatively insensitive to the assumed effective stress profile provided it remains within the plausible bounds, with around 1% to 2% difference in predictions. The natural frequency of the second structural bending mode shows greater sensitivity to the assumed effective stress profile.

The research also found that the lateral capacity is sensitive to the assumed effective stress profile. Adopting the calibrated effective stress profile produces a reasonable prediction of the lateral capacity for the flume test with unremediated scour development.

Natural backfill of local scour holes can occur due to sediment deposition. The stiffness contribution of backfill is small compared with the original *in situ* material, and temporary in nature. Hence, natural backfill should not be relied upon in design. There is potential for unidentified backfill at operating sites due to the periodic nature of bathymetry surveys. Locations with unidentified backfill may have natural frequencies lower than would be expected for the equivalent scour depth to the top of the backfill layer.

The knowledge and methods developed in the research project will provide valuable inputs for the fatigue analysis of monopile-supported offshore wind turbines. These fatigue requirements are a key design driver in determining the remaining design life for decommissioning or recommissioning activities.

6.3 Recommendations

6.3.1 Recommendations for Practice

i. **For offshore wind farms in development at sites with a high scour risk**

Pre-installed rock armour scour protection is recommended for offshore wind farms in development. The pre-installed scour protection should have a wide extent to limit the effect of bathymetry changes on the monopile response. This is expected to provide a hydraulically stable solution, with limited change in the foundation stiffness over time. This stability would provide confidence in the design life fatigue analysis for decommissioning or recommissioning activities.

ii. **For offshore wind farms with a 'monitor and react' scour design approach**

It is recommended to deploy supplementary structural health monitoring systems to assist in detecting the onset of scour damage. These monitoring systems should aim to track the frequency of the second structural bending mode and the mode shapes. This would increase the likelihood of identifying excessive scour development. Early identification would allow remediation to be installed in a timely fashion, and therefore limit the potential for fatigue damage.

iii. **For remedial scour protection at monopiles with low natural frequencies**

If the natural frequency is too low there is a risk of fatigue damage and reduced design life, the lateral capacity may also be a concern. It is recommended to use rock fill scour remediation to enhance the stiffness and capacity of the foundation, and reduce the potential for fatigue damage. At locations with potential for global scour to undermine the scour protection, this can be countered by installing a large quantity of rock to allow the scour protection to remain stable. The impact of this rock on secondary scour would need to be evaluated.

iv. **For remedial scour protection at monopiles with acceptable natural frequencies**

If no enhancement of the foundation stiffness is required, the tyre-filled net solution may provide an alternative to rock fill. The flume experiments indicated that the tyre-filled nets limited the development of further local scour, but had a negligible stiffness contribution. The effect of global scour may expose and destabilise the tyre filled nets.

6.3.2 Suggestions for Further Research

There is scope for further research on the influence of scour and scour protection on monopile foundation behaviour. The following list presents some potential areas to be explored:

i. Extension of the PISA framework for local scour conditions, by analysis of normalised soil reactions using appropriate 3D finite element analysis methods and constitutive soil models, perhaps with scope for validation by further experimental testing.

ii. Investigation of the influence of other aspects of the scour hole geometry on monopile responses, such as the base width (e.g. Lin and Jiang, 2019), asymmetry, or secondary scour adjacent to scour protection.

iii. Exploration of the sediment accretion mechanism, and whether it can be relied upon in the field. There may be scope for computational fluid dynamics methods (e.g. Tavouktsoglou et al., 2019) to be used to explore whether sediment accretion occurs in field conditions, perhaps accompanied by large scale field trials or flume tests.

iv. There is a general lack of data on the geotechnical modelling of the mechanical properties of rock-type scour protection materials, future research could reduce uncertainty in this area. Large scale soil element tests could be devised as a method for exploring the mechanical properties of gravel and rock layers, with potential scope to investigate the additional effects of the presence of accreted sand in the scour protection void space.

6.3.3 Concluding Statement

This research confirms, through both laboratory and field scale studies, that scour causes a significant reduction in foundation stiffness and detectable decreases in natural frequencies (the second bending mode is particularly sensitive). The findings demonstrate that a connection exists between monitored natural frequencies and lateral foundation stiffness and strength, and that the foundation response is influenced by scour protection. This provides confidence that rock fill scour remediation is beneficial to foundation stiffness and strength, hence fatigue life and capacity safety margin, with confirmation possible through detectable changes in natural frequencies.

Reference List

The following is a list of all references used in the main body of this portfolio and in Appendices C to E. Papers 1 to 3 in this portfolio contain internal reference lists.

An, H., Cheng, L., Luo, L., Draper, S., White, D. and Jas, E. (2014). Effect of sediment supply on suction scour under a rock berm. in Proceedings of the 7th International Conference on Scour and Erosion, ICSE 2014. vol. 1, Taylor & Francis, London, UK, pp. 265 - 273, 7th International Conference on Scour and Erosion, Perth, Australia, 2/12/14.

API (2011). API RP 2GEO. Recommended Practice for Geotechnical Foundation Design Consideration.

Arany, L., Bhattacharya, S., Macdonald, J.H. and Hogan, S.J. (2016). Closed form solution of Eigen frequency of monopile supported offshore wind turbines in deeper waters incorporating stiffness of substructure and SSI. Soil Dynamics and Earthquake Engineering, 83, pp.18-32.

AWG (2016). PISA Final Report. Report Number 2595138, PISA AWG.

AWG (2018). PISA2 Final Report. Report Number 3107410, PISA2 AWG.

Baldi, G., Bellotti, R., Ghionna, V., Jamiolkowski, M. and Pasqualini, E. (1986). Interpretation of CPTs and CPTUs; 2nd part: drained penetration of sands. Proceedings of Fourth International Geotechnical Seminar, Singapore, 143-156.

Breusers, H.N.C., Nicollet, G. and Shen, H.W. (1977). Local scour around cylindrical piers. Journal of Hydraulic Research, 15(3), pp.211-252.

British Standards Institution (1996). BS 1377-2:1990. Methods of test for soils for civil engineering purposes. Classification tests. London, UK.

Brown D.A. and Castelli R.J. (2010). Drilled shafts: construction procedures and LRFD design methods, FHWA NHI-0-016. Washington, D.C.: Federal Highway Administration, U.S. Department of transportation.

Bui, M.T. (2009). Influence of some particle characteristics on the small strain response of granular materials (Doctoral dissertation, University of Southampton).

Burd, H.J., Byrne, B.W., McAdam, R.A., Houlsby, G.T., Martin, C.M., Beuckelaers, W.J.A.P., Zdravković, L., Taborda, D. M. G., Potts, D.M., Jardine, R.J., Gavin, K., Doherty, P., Igoe, D., Gretlund, J.S., Andrade, M.P. and Muir Wood, A. (2017). Design aspects for monopile foundations. Proceedings of TC 209 Workshop – 19th ICSMGE, Seoul 20 September 2017.

Burd, H.J. (2018). Formulation of 1D soil structure interaction models. May 7, 2018.

Burd, H.J., Beuckelaers, W.J.A.P., Byrne, B.W., Gavin, K.G, Houlsby, G.T., Igoe, D.J.P., Jardine, R.J., Martin, C.M., McAdam, R.A., Muir Wood, A., Potts, D.M., Skov Gretlund, J., Taborda, D.M.G. and Zdravković, L. (2019). New data analysis methods for instrumented medium scale monopile field tests. Géotechnique, https://doi.org/10.1680/jgeot.18.pisa.002.

Byrne, B.W., McAdam, R., Burd, H., Houlsby, G., Martin, C., Zdravkovi, L., Taborda, D., Potts, D., Jardine, R. and Sideri, M. (2015). New design methods for large diameter piles under lateral loading for offshore wind applications. In 3rd International Symposium on Frontiers in Offshore Geotechnics (ISFOG 2015), Oslo, Norway, June (pp. 10-12).

Byrne, B.W., McAdam, R.A., Burd, H.J., Beuckelaers, W.J.A.P., Gavin, K.G, Houlsby, G.T., Igoe, D.J.P., Jardine, R.J., Martin, C.M., Muir Wood, A., Potts, D.M., Skov Gretlund, J., Taborda, D.M.G. and Zdravković, L. (2019). Monotonic laterally loaded pile testing in a stiff glacial clay till at Cowden. Géotechnique, https://doi.org/10.1680/jgeot.18.pisa.003.

Clayton, C.R.I. (2011). Stiffness at small strain: research and practice. Géotechnique, 61(1), pp.5-37.

Cowper, G.R. (1966). The shear coefficient in Timoshenko's beam theory. Journal of Applied Mechanics 33(2): 335-340.

Craig, R.F. (1992). Craig's Soil Mechanics. London, Spon Press.

Darendeli, M.B. (2001). Development of a new family of normalized modulus reduction and material damping curves. Ph.D. thesis, Univ. of Texas at Austin, Austin, TX.

Devriendt, C., Magalhães, F., Weijtjens, W., De Sitter, G., Cunha, Á. and Guillame, P. (2014). Structural health monitoring of offshore wind turbines using automated operational modal analysis. Structural Health Monitoring 2014, Col 13(6) 644-659.

Damgaard, M., Ibsen, L.B., Andersen, L.V. and Andersen, J.K. (2013). Cross-wind modal properties of offshore wind turbines identified by full scale testing. Journal of Wind Engineering and Industrial Aerodynamics, 116, pp.94-108.

De Vos, L., De Rouck, J., Troch, P. and Frigaard, P. (2011). Empirical design of scour protections around monopile foundations Part 1: Static approach. Coastal Engineering 58 540-553.

Den Boon, J.H., Sutherland, J., Whitehouse, R., Soulsby, R., Stam, C.J.M., Verhoven K., Høgedal, M. and Hald, T. (2005). Scour Behaviour and Scour Protection for Monopile Foundations of Offshore Windfarms. Proceedings of the European Wind Energy Conference, 2004, London, UK. UWEA. pp14.

Dingam, S. (2009). Fluvial Hydraulics. New York: Oxford University Press.

DNV (2010). Det Norske Veritas Recommended Practice DNV-RP-C205 Environmental conditions and environmental loads.

DNVGL (2016). Standard DNVGL-ST-0126, Support structures for wind turbines, Edition April 2016.

Energy Numbers (2016). UK offshore wind capacity factors. In: energynumbers.info web page ⟨http://energynumbers.info/uk-offshore-wind-capacity-factors⟩ [accessed 05.08.2016].

E.ON, (2016). Robin Rigg Scour Protection – Completion Report – Report Number 06097/16/0 (21/12/16)

Ewins, D.J. (2000). Modal Testing: Theory, Practice and Application. Second Edition. Research Studies Press Ltd. Baldock, Hertfordshire, England.

Hannigan P.J., Gobe G.G., Likins G.E. and Rausche F. (2006). Design and construction of driven pile foundation, vol. I. FHWA-NHI-05-042. Washington, DC: Federal Highway Administration, U.S. Department of Transportation.

Hanssen, S.B. (2015). Small strain overlay to the API p-y curves for sand. In 3rd International Symposium on Frontiers in Offshore Geotechnics (ISFOG 2015), Oslo, Norway, June (pp. 557-562).

Hardin, B.O. and Black, W.L. (1968). "Vibration modulus of normally consolidated clay." Journal of the Soil Mechanics and Foundations Division, 92, 27-42.

Hardin, B.O. and Drnevich, V.P. (1972). Shear modulus and damping in soils: measurement and parameter effects. Journal of Soil Mechanics & Foundations Div, 98(sm6).

Hardin, B.O. and Richart Jr, F.E. (1963). Elastic wave velocities in granular soils. Journal of Soil Mechanics & Foundations Div, 89 (Proc. Paper 3407).

Head, K.H. (2006). Manual of Soil Laboratory Testing. Volume 1: Soil Classification and Compaction Tests. 3rd Edition. Whittles Publishing, Caithness, Scotland, UK.

Hoffmans, G.J. and Verheij, H.J. (1997). Scour manual (Vol. 96). CRC Press.

Høgedal, M. and Hald, T. (2005). Scour assessment and design for scour for monopile foundations for offshore wind turbines. In: Proceedings of the Copenhagen Offshore Wind. Copenhagen, Denmark.

Houlsby, G.T. and Hitchman, R. (1988). Calibration chamber tests of a cone penetrometer in sand. Géotechnique, 38(1), pp.39-44.

HR Wallingford (2015). Robin Rigg Offshore Windfarm – Seabed Erosion Study. Report Number DDR5393-RT001-R01-00.

HR Wallingford (2018). Foundation response to scour protection. Summary of large-scale laboratory modelling tests. RT001-R02-00, March 2018. Report produced for E.ON Climate & Renewables. HR Wallingford: Wallingford, UK.

Hucker, N., Ward, I. and Manceau, S. (2019). Measured changes in the natural frequency of offshore wind turbines with monopile foundations. SECED Conference 2019, London.

International Organization for Standardization (ISO) (2004). ISO 19901-4 Petroleum and natural gas industries – Specific requirements for offshore structures – Part 4: Geotechnical and foundation design considerations. Geneva: ISO.

International Organization for Standardization (ISO) (2007). ISO 19902 Petroleum and natural gas industries – Fixed steel offshore structures. Geneva: ISO.

Jamiolkowski, M., Ladd, C.C., Germaine, J.T. and Lancelotta, R. (1985). New developments in field and laboratory testing of soils. State-of-the-art report. Proceedings of the 11th International Conference on Soil Mechanics and Foundation Engineering, San Francisco, 1, 57-153, Balkema Pub., Rotterdam.

Jamiolkowski, M., Lo Presti, D.C.F. and Manassero, M. (2003), Evaluation of relative density and shear strength of sands from CPT and DMT, Germaine, J.T., Sheahan, T.C. and Whitman, R.V. (Eds.), Soil behavior and soft ground construction: proceedings of the symposium, October 5-6, 2001, Cambridge, Massachusetts, Geotechnical Special Publication, No. 119, American Society of Civil Engineers, Reston, pp. 201-238.

Jonkman, J., Butterfield, S., Musial, W. and Scott, G. (2009). Definition of a 5-MW Reference Wind Turbine for Offshore System Development. Colorado.

Kallehave, D., Byrne, B.W., LeBlanc Thilsted, C. and Mikkelsen, K.K. (2015). Optimization of monopiles for offshore wind turbines. Phil.Trans.R.Soc.A 373: 20140100. http://dx.doi.org/10.1098/rsta.2014.0100.

Larsen, S.M., Roulund, A., Brooks, A.J. and Chaffey, A., (2016). Sandwaves and megaripples at Race Bank (UK) offshore windfarm. ICSE 2016.

Lesny, K. (2010). Foundations for offshore wind turbines: tools for planning and design. VGE-Verlag.

Li, H., Ong, M.C., Leira, B.J. and Myrhaug, D. (2018). Effects of Soil Profile Variation and Scour on Structural Response of an Offshore Monopile Wind Turbine. J. Offshore Mech. Arct. Eng. Aug 2018, 140(4): 042001. Paper No: OMAE-16-1099 https://doi.org/10.1115/1.4039297.

Lin, C., Bennett, C., Han, J. and Parsons, R.L. (2010). Scour effects on the response of laterally loaded piles considering stress history of sand. Computers and Geotechnics 37 (2010) 1008-1014.

Lin C., Han J., Bennett C. and Parsons R.L., (2014). Analysis of laterally loaded piles in sand considering scour hole dimensions. J Geotech Geoenviron Eng 140(6):04014024.

Lin, C. (2017). The loss of pile axial capacities due to scour: vertical stress distribution. In: 2017 International Conference on Transportation Infrastructure and Materials (ICTIM 2017). Qingdao, China.

Lin, C. and Jiang, W. (2019). Evaluation of vertical effective stress and pile tension capacity in sands considering scour-hole dimensions, Computers and Geotechnics, Volume 105, pp 94-98, ISSN 0266-352X, https://doi.org/10.1016/j.compgeo.2018.09.013.

Mayall, R.O., (2018). Foundation response to scour and scour protection. D3: Fast Flow experiment factual report. Issue 02, 15/02/2018, Final. University of Oxford: Oxford, UK.

Mayall, R.O., (2019). Foundation response to scour and scour protection. D4: Fast Flow experiment data analysis report. Issue 02, 05/04/2019. University of Oxford: Oxford, UK.

Mayall, R.O., McAdam, R.A., Byrne, B.W., Burd, H.J., Sheil, B.B., Cassie, P. and Whitehouse, R.J.S. (2018). Experimental modelling of the effects of scour on offshore wind turbine monopile foundations. In: *9th* International Conference Physical Modelling in Geotechnics (ICPMG 2018). London, UK, July. (c109 pp. 725-730).

Mayall, R.O., Byrne, B.W., Burd, H.J., McAdam, R.A., Cassie, P. and Whitehouse, R.J.S. (2019). Modelling of foundation response to scour and scour protection for offshore wind turbine structures. Scour and Erosion IX - Proceedings of the 9th International Conference on Scour and Erosion, ICSE 2018, pp. 405.

Mayall, R.O., McAdam, R.A., Whitehouse, R.J.S., Burd, H.J., Byrne, B.W., Heald, S.G., Sheil, B.B., and Slater, P.L. [Forthcoming]. Flume tank testing of offshore wind turbine dynamics with foundation scour and scour protection. Journal of Waterway, Port, Coastal, and Ocean Engineering. DOI: 10.1061/(ASCE)WW.1943-5460.0000587.

McAdam, R.A., Byrne, B.W., Houlsby, G.T., Beuckelaers, W.J.A.P., Burd, H.J., Gavin, K.G., Igoe, D.J.P., Jardine, R.J., Martin, C.M., Muir Wood, A., Potts, D.M., Skov Gretlund, J., Taborda, D.M.G. and Zdravković, L. (2019). Monotonic lateral loaded pile testing in a dense marine sand at Dunkirk. Géotechnique, https://doi.org/10.1680/jgeot.18.pisa.004.

MMI, (2013). Robin Rigg Study to investigate the Sensitivity of Monopile Response to Scour and Grout Damage. Report Number MMU330-P01-R01 Issue 2.

Mostafa, Y.E., 2012. Effect of Local and Global Scour on Lateral Response of Single Piles in Different Soil Conditions. Engineering, 2012, 4, 297-306.

Nukala, P.K. (1999). Implementation of Rotary Inertia Effect on the Free Vibration Response of Beams. Lawrence Livermore National Laboratory.

Pacheco Silva, F. (1970). A new graphical construction for determination of the preconsolidation stress of a soil sample. Proceedings of the 4th Brazilian Conference on Soil Mechanics and Foundation Engineering, Rio de Janeiro, Brazil. Vol. 2. No. 1. 1970.

Petersen, T.U., Sumer, B.M., Meyer, K.E., Fredøe, J. and Christensen, E.D. (2012). Edge scour in current adjacent to stone covers. ICSE6 Paris – August 27-31, 2012.

Petersen, T.U., Sumer, B.M., Fredsøe, J., Raaijmakers, T. and Schouten, J. (2015). "Edge scour at scour protection around piles in the marine environment – Laboratory and field Investigation". Coastal Engineering (106), December (2015) 42-72.

Petersen, T.U., Nielsen, A.W., Hansen, D.A., Pedersen, A.V., Christensen, E.D. and Fredsøe, J. (2019). "Stability of single-graded scour protection around a monopile in current". Scour and Erosion IX - Proceedings of the 9th International Conference on Scour and Erosion, ICSE 2018, pp. 405.

Prendergast, L.J., Hester, D., Gavin, K. and O'Sullivan, J.J. (2013). An investigation of the changes in the natural frequency of a pile affected by scour. Journal of Sound and Vibration, vol. 332, no. 25, pp. 6685-6702.

Prendergast, L.J., Gavin., K. and Doherty, P., (2015). An investigation into the effect of scour on the natural frequency of an offshore wind turbine. Ocean Engineering 101 1-11.

Prendergast, L.J., Reale, C. and Gavin, K., (2018). Probabilistic examination of the change in eigenfrequencies of an offshore wind turbine under progressive scour incorporating soil spatial variability, Marine Structures, Volume 57, Pages 87-104, ISSN 0951-8339, https://doi.org/10.1016/j.marstruc.2017.09.009.

Qi, W.G., Gao, F.P., Randolph, M.F. and Lehane, B.M. (2016). Scour effects on p–y curves for shallowly embedded piles in sand. Géotechnique.

Raaijmakers, T. (2019). DEL070 - JIP HaSPro: Joint-Industry-Project Handbook Scour and cable Protection methods. ⟨https://publicwiki.deltares.nl/display/TKIP/DEL070+-+JIP+HaSPro%3A+Joint-Industry-Project+Handbook+Scour+and+cable+Protection+methods⟩ [accessed 10.09.2019].

Ram Babu, M., Sundar, V. and Narasimha Rao, S., (2003). Measurement of scour in cohesive soils around a vertical pile-simplified instrumentation and regression analysis. IEEE Journal of Ocean Engineering, Vol. 28, No. 1, pp. 106-117.

Ramboll (2007). Robin Rigg Offshore Wind Farms - Design Report Summary. Document no.: 221186 – 4.2.1 Revision: 1

Richards, I.A., Byrne, B.W. and Houlsby, G.T. (2018). Physical modelling of monopile foundations under variable cyclic lateral loading. In: 9th International Conference Physical Modelling in Geotechnics (ICPMG 2018). London, UK, July. (c111 pp. 737-742).

Richards, I.A., Byrne, B.W. and Houlsby, G.T. (2019). Monopile rotation under complex cyclic lateral loading in sand. Géotechnique, https://doi.org/10.1680/jgeot.18.p.302.

Richards, I.A. (2019). Monopile foundations under complex cyclic lateral loading. DPhil Thesis, University of Oxford.

Riezebos, H., Raaijmakers, T., Tönnies-Lohmann, A.,Waßmuth, S. and Van Steijn, P. (2016). Scour protection design in highly morphodynamic environments. In: ICSE 2016 (8th International Conference on Scour and Erosion), 12-15 September 2016, Oxford, UK. (2016).

Rix, G.J. and Stokoe, K.H. (1992). Correlation of initial tangent modulus and cone resistance. Proceedings of the International Symposium on Calibration Chamber Testing, Postdam, New York, 1991, 351-362, Elsevier.

Schmertmann, J.H. (1976). An Updated Correlation between Relative Density DR and Fugro-Type Electric Cone Bearing, qc. Contract Report DACW 39-76 M 6646 WES, Vicksburg, Miss., 1976.

Sørensen, S.P.H., Ibsen, L.B. and Frigaard, P. (2010). Experimental evaluation of backfill in scour holes around offshore monopiles. In: Proceedings of the Second International Symposium on Frontiers in Offshore Geotechnics, Perth, Western Australia, Australia, pp. 617–622.

Sørensen, S.P.H. and Ibsen, L.B. (2013). Assessment of foundation design for offshore monopiles unprotected against scour. Ocean Engineering 63 17-25.

Sudheer, M., Pradyoth K. R. and Shashiraj Somayaji (2015) Analytical and Numerical Validation of Epoxy/Glass Structural Composites for Elastic Models. American Journal of Materials Science 2015, 5(3C): 162-168. DOI: 10.5923/c.materials.201502.32.

Sumer, B.M., Fredsøe, J. and Christiansen, N. (1992a). Scour around vertical pile in waves. J. Waterw. Port Coastal Ocean Eng. 118, 15–31.

Sumer, B.M, Christiansen, N. and Fredsøe, J. (1992b). Time scale of scour around a vertical pile. Proc. 2nd Int. Offshore and Polar Eng. Conf., ISOPE, San Francisco, USA, Vol. 3, pp. 308 – 315.

Taborda, D.M.G., Zdravković, L., Potts, D.M., Burd, H.J., Byrne, B.W., Gavin, K.G, Houlsby, G.T., Jardine, R.J., Liu, T., Martin, C.M. & McAdam, R.A. (2019). Finite element modelling of laterally loaded piles in a dense marine sand at Dunkirk. Géotechnique, https://doi.org/10.1680/jgeot.18.pisa.006.

Tami, D. and Jaapar, A.R. (2015). Comparison of shear modulus from SCPT, PS logging & laboratory tests of offshore Myanmar. ISFOG 2015. In 3rd International Symposium on Frontiers in Offshore Geotechnics (ISFOG 2015), Oslo, Norway, June.

Tavouktsoglou, N.S., Harris, J.M., Whitehouse, R.J.S. and Simons, R.R. (2019). CFD simulation of clearwater scour at complex foundations. Scour and Erosion IX - Proceedings of the 9th International Conference on Scour and Erosion, ICSE 2018, pp. 183.

Tempel, J., Zaaijer, M.B. and Subroto, H. (2004). The effects of Scour on the design of Offshore Wind Turbines.

Van Rijn, L.C. (1984). Sediment transport, part I: bed load transport. Journal of hydraulic engineering, 110(10), pp.1431-1456.

Vardanega, P.J. and Bolton, M.D. (2013). Stiffness of clays and silts: Normalizing shear modulus and shear strain. Journal of Geotechnical and Geoenvironmental Engineering, 139(9), pp.1575-1589.

Viggiani, G. and Atkinson, J.H. (1995). Stiffness of fine-grained soil at very small strains. Géotechnique, 45(2), pp.249-265.

Williams, M. (2016). Structural Dynamics. CRC Press.

Whitehouse, R.J.S., Harris, J.M., Sutherland, J. and Rees, J. (2011). The nature of scour development and scour protection at offshore windfarm foundation. Marine Pollution Bulletin 62 73-88.

WindEurope (2019). Offshore Wind in Europe Key trends and statistics 2018. Published in February 2019. windeurope.org.

Yang, X., Zeng, X., Wang, X. and Li, X. (2019). Assessment of Monopile-Gravel Wheel Foundations under Lateral-Moment Loading for Offshore Wind Turbines. J. Waterway, Port, Coastal, Ocean Eng., 2019, 145(1): 04018034. DOI: 10.1061/(ASCE)WW.1943-5460.0000493.

Zaaijer, M.B. and Tempel, J. (2004). Scour Protection: A Necessity or a Waste of Money?. Proceedings of the 43 IEA Topixal Expert Meeting, Stockholm, pp. 43-51.

Zdravković, L., Taborda, D.M.G., Potts, D.M., Jardine, R.J., Sideri, M., Schroeder, F.C., Byrne, B.W., McAdam, R., Burd, H.J., Houlsby, G.T. and Martin, C.M. (2015). Numerical modelling of large diameter piles under lateral loading for offshore wind applications. In Proc 3rd International Symposium on Frontiers in Offshore Geotechnics (ISFOG 2015). Oslo, Norway.

Zdravković, L., Jardine, R.J., Taborda, D.M.G., Abadias, D., Burd, H.J., Byrne, B.W., Gavin, K.G, Houlsby, G.T., Igoe, D.J.P., Liu, T., Martin, C.M., McAdam, R.A., Muir Wood, A., Potts, D.M., Skov Gretlund, J. and Ushev, E. (2019a). Ground characterisation for PISA pile testing and analysis. Géotechnique, https://doi.org/10.1680/jgeot.18.pisa.001.

Zdravković, L., Taborda, D.M.G., Potts, D.M., Abadias, D., Burd, H.J., Byrne, B.W., Gavin, K.G, Houlsby, G.T., Jardine, R.J., Martin, C.M., McAdam, R.A. and Ushev, E. (2019b). Finite element modelling of laterally loaded piles in a stiff glacial clay till at Cowden. Géotechnique, https://doi.org/10.1680/jgeot.18.pisa.005.

Zhang, J., Andrus, R.D. and Juang, C.H. (2005). Normalized shear modulus and material damping ratio relationships. J. Geotech. Geoenviron. Eng., 131(4), 453–464.

Zuccarino, L., Morandi, D.A. and Sottile, M. (2015). Shear wave velocity and shear modulus in offshore clays. ISFOG (2015). In Proc 3rd International Symposium on Frontiers in Offshore Geotechnics (ISFOG 2015). Oslo, Norway.

Appendix A Paper 1

Monopile Response to Scour and Scour Protection

Paper 1

Modelling of foundation response to scour and scour protection for offshore wind turbine structures

Mayall, R.O., Byrne, B.W., Burd, H.J.,

McAdam, R.A., Cassie, P. and Whitehouse, R.J.S.

2019

Scour and Erosion IX – Keh-Chia (Ed.)

Modelling of foundation response to scour and scour protection for offshore wind turbine structures

R.O. Mayall, B.W. Byrne, H.J. Burd & R.A. McAdam
Department of Engineering Science, University of Oxford, Oxford, UK

P. Cassie
E.ON Climate & Renewables, Coventry, UK

R.J.S. Whitehouse
HR Wallingford, Wallingford, UK

ABSTRACT: Local and global scour around offshore monopile wind turbine structures can cause a reduction in foundation strength and stiffness, and a consequential reduction in the structure's natural frequency. To devise optimal scour remediation schemes, it is necessary to develop an understanding of the interactions between scour development, soil-foundation stiffness, and the dynamic response of the structure. This paper describes a research project that develops a framework to assess the influence of scour and scour remediation systems on the dynamic characteristics of offshore wind turbine structures. The research project includes one-dimensional (1D) finite element modelling, calibrated using three-dimensional (3D) finite element analysis, experimental measurements, and monitored field data. The paper outlines the development of the 1D and 3D finite element models, as well as a novel experimental programme carried out on a 1:20 scale offshore wind structure in the Fast Flow Facility at HR Wallingford, UK.

1 INTRODUCTION

Loss of soil support around offshore wind turbine monopile structures, due to scour, can cause a drop in the structure's natural frequency due to the loss of foundation stiffness. Local scour around piles, and the effect of moving bed-forms such as sand waves, can be onerous at sites with high currents (e.g. Høgedal & Hald, 2005; Larsen et al., 2016; Tseng et al., 2017). At such sites it is important to incorporate scour processes and/or scour protection into the wind farm design.

E.ON Climate & Renewables and HR Wallingford are jointly funding an ongoing research project at the University of Oxford that investigates the effect of scour and scour protection on wind turbine structures. The focus of the research is on assessing the influence of scour and scour remediation systems on the dynamic characteristics (frequencies and mode shapes) of monopile-supported offshore wind turbine structures. Fig. 1 presents the framework of the research project, which includes one-dimensional (1D) and three-dimensional (3D) finite element analysis (FEA) validated using experimental work, supported by field data. It is anticipated that this framework can be applied to the design of future offshore wind farms, the selection of scour protection systems for future or operating wind farms, and for the lifetime assessment of existing scour-affected assets.

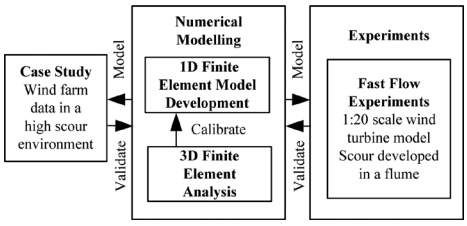

Figure 1. Research project framework.

2 BACKGROUND

2.1 *Scour at offshore foundations*

Scour around offshore foundations can take the form of global seabed scour or local scour, and both types of scour can be present. Table 1 and Fig. 2 present a summary of the adopted definitions of global and local scour. The development of scour is influenced by the site wave and current environment, the character of the seabed sediments, the local geology, and the properties of the structures and infrastructure placed on the seabed.

Table 1. Summary of scour definitions adopted in this research for offshore foundations.

Scour type	Description	Remarks
Global Scour	Overall seabed movement, for example: – Migrating sandwaves and sandbanks – Migrating channel features	Some references use the terminology general scour (e.g. API, 2011; DNVGL, 2016), rather than global scour (e.g. ISO, 2007). An alternative definition of global scour is dishpan scour around jacket structures.
Local Scour	A scour pit around a foundation caused by the formation of horseshoe vortices around the pile in a flow. Local scour pits may be asymmetric, with deposition downstream.	Recommended design local scour depths are based on empirical data (e.g. Breusers et al., 1977). Some design standards (API, 2011; ISO, 2007) recommend a design local scour depth of 1.5 D; DNVGL (2016) recommends a design local scour depth of 1.3 D. More recent emprical methods are available (e.g. Tavouktsoglou et al., 2017).

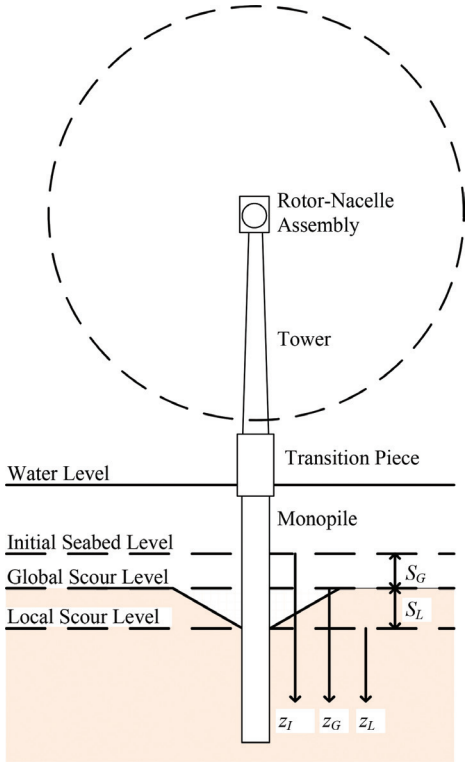

Figure 2. Scour around a monopile offshore wind turbine (adapted from Mayall et al., 2018).

2.2 *Natural frequency of wind turbine structures*

Monopile wind turbines are typically designed for the resonant frequency (first natural frequency) to be above the rotor frequency band (1P) and below the blade passing frequency band (3P) (Kallehave et al., 2015).

Removal of soil by scour causes a loss of foundation stiffness, so that the natural frequency moves closer to 1P. This leads to increased dynamic amplification of the rotor frequency loads and consequently increased fatigue damage within the structure. For accurate predictions of natural frequencies it is important to suitably model the stiffness of the foundation itself, including the effect that any scour and scour protection has on the foundation response.

2.3 *Pile foundation analysis*

Design standards for offshore structures (e.g. DNVGL, 2016; API, 2011; ISO, 2007) recommend that the lateral load-displacement behaviour of piles should be predicted using a nonlinear Winkler spring method within a 1D model, with the soil represented by discrete *p-y* curves. The PISA project (Byrne et al., 2015; Zdravković et al., 2015) proposes a more comprehensive model of the soil resistance for monopile design incorporating the distributed lateral reaction, distributed moment due to the rotation of the pile cross-section, plus moment and shear reaction at the base of the pile. The PISA approach recommends calibrating the soil resistance curves using 3D FEA of the load-displacement behaviour, where the initial pile response is defined as a function of small strain shear stiffness (G_0) of the soil.

2.4 *Effects of scour on monopile behaviour*

2.4.1 *Global scour*

For global scour it is generally accepted that soil stresses can be calculated assuming that the removed layers have no residual effects on the stresses (e.g. DNVGL, 2016; Qi et al., 2016). Vertical effective stresses under global scour (σ'_{VG}) can be calculated using the depth below the lowered seabed level (z_G).

2.4.2 *Local scour*

Under local scour, the design standards (e.g. API, 2011) recommend using reduced effective stresses,

which return linearly to the globally-scoured background condition over a defined overburden reduction depth. An alternative hyperbolic return is proposed by Qi et al. (2016). Note that both methods are intended for capacity predictions, rather than for small displacement problems.

The calculation of vertical effective stress adjacent to the pile for local scour conditions (σ'_{VL}) can be expressed using an effective soil depth (z_e):

$$\sigma'_{VL} = ze\gamma'_{av} \quad (1)$$

The effective soil depth can be calculated using a local scour influence factor (α_L) between 0 and 1; as presented in Fig. 3 for the API (2011) and Qi et al. (2016) methods.

2.4.3 *Effect of scour on structural dynamics*

There are a number of influences of scour on the foundation behaviour. Firstly, the stiffness of the soil response may reduce, secondly as there is less embedment the combined response is more flexible, and thirdly a larger free length of tower is more flexible. Several numerical studies in the literature make use of 1D models to predict the effect of scour on the natural frequency of monopile wind turbines; a selection are collated in Table 2. The predicted sensitivity of natural frequency to scour varies significantly between these studies; it is unclear if this is due to differences in the modelling approaches or simply due to the differences in the modelled structures and foundations.

Previous experimental tests (Prendergast et al., 2015) provide data on the change in natural frequency with scour for a uniform pile in dry conditions. The current research project includes models of a wind turbine tower and rotor-nacelle assembly (Mayall et al., 2018), which are felt influential on the overall dynamic behaviour of the structure.

2.5 *Scour protection*

Scour protection can be installed before or after the foundation installation, and can be applied as a remedial measure where necessary. The primary function of scour protection is to prevent the development of scour at a foundation, but the presence

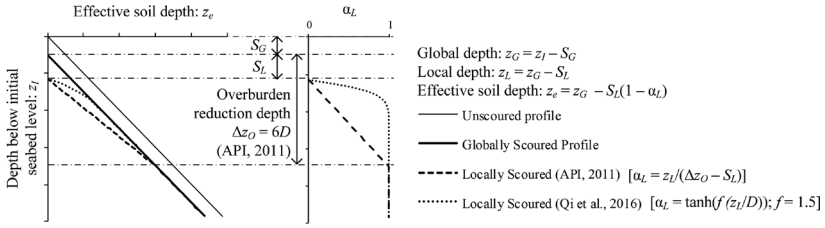

Figure 3. Effective soil depth for calculation of stresses beneath local scour (after API, 2011 and Qi et al., 2016).

Table 2. Selected numerical studies on the effects of scour on monopile offshore wind turbine natural frequency.

Reference	Description	Soil description	Pile model	Scour model
Tempel et al. (2004)	Preliminary design at a test site, analysis methods not stated	Not stated	D = 4.7 m	Local scour, analysis methods not stated
Damgaard et al. (2013)	First eigenfrequency calculated using *p-y* initial stiffness; also includes analysis of backfill	Dense sand over firm clay	D = 4.3 m Embedment = 29.5 m	Local scour, vertical effective stresses reduce linearly to 3 D below the scour hole base
Sørensen and Ibsen (2013)	Eigenfrequency mode 1 and 2 calculated using *p-y* initial stiffness; also includes analysis of backfill (varying fill density)	Sand	D = 4.0 m Embedment = 21.9 m	For local scour, only the ultimate resistance of *p-y* curves is modified and not the initial slope
Prendergast et al. (2018)	Stochastic analysis, soil stiffness from modulus of subgrade reaction, model includes added mass of external water	Predominantly medium dense sand	D = 6.0 m Embedment = 30 m	Sequential removal of soil springs

of the placed material may also affect the overall foundation response.

Scour protection can take the form of rock fill, filled bags or nets, or mattresses. Rock armour or fill (also termed riprap) is the most common solution and usually consists of a rock or gravel fill. Scour protection bag and net solutions include filter units (rock-filled nets), grout bags, geobags (sand-filled bags), and tyre-filled nets. Mattress solutions include mudmats or collars, hinged plates, composite rubber mats, grout-filled mattresses, articulating concrete block systems, and fronded mats.

Other mitigation strategies include monitoring, structural modifications, and ground improvement. Each mitigation strategy has differing cost and risk implications, which can be significant when applied across an entire wind farm site.

3 NUMERICAL MODELLING

3.1 *One-dimensional finite element analysis*

A 1D FEA model has been developed to provide a method of predicting changes to the dynamic response of a monopile structure for varying scour and scour protection conditions. Fig. 4 presents the model configuration, which uses Euler-Bernoulli beam elements. Natural frequencies and mode shapes of the structure are calculated by performing an eigenvalue analysis, using the model's stiffness and mass matrices. The eigenvalue analysis outputs the same number of vibration modes as degrees of freedom in the system. These can be sorted in order of increasing frequency to identify the first few modes of vibration, as these are of interest.

The stiffness matrix includes contributions from beam elements to model the structure itself, and the initial stiffness of the pile-soil reaction curves from a PISA-type approach. The shear modulus of the soil at small displacements (G_0) is used to define the initial pile-soil stiffness, where G_0 can be defined as a function of vertical effective stress (Clayton, 2011). To account for scour, σ'_{VL} can be calculated along the pile length and input to the G_0 calculation.

The mass matrix includes contributions from the pile-tower structure, rotor-nacelle assembly, soil plug, and internal and external water.

3.2 *Three-dimensional finite element analysis*

A 3D FEA model was developed using a configuration based on field-scale offshore wind turbines. Fig. 5 presents the model configuration, which includes a conical region to allow formation of a scour pit; the elements can be deactivated to simulate local scour. Alternatively the material proper-

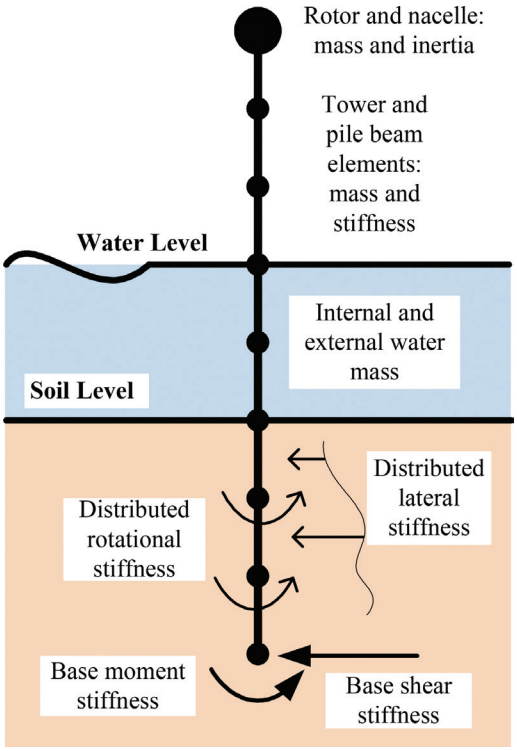

Figure 4. 1D finite element model configuration (number and length of elements not to scale).

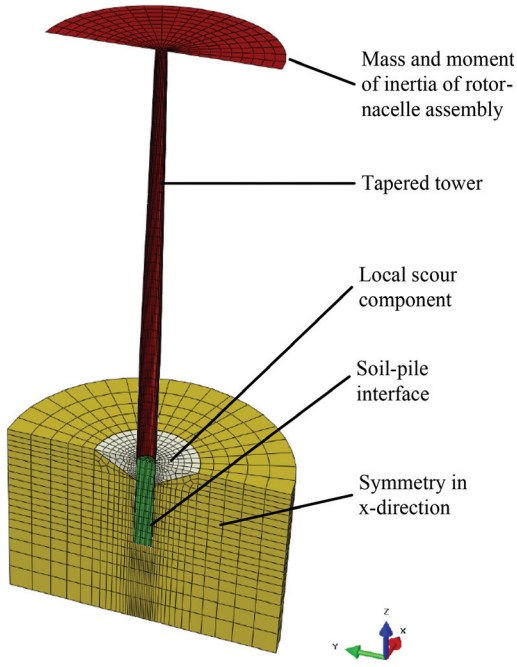

Figure 5. 3D finite element model configuration.

ties of the cone can be varied to simulate scour protection. Global scour can be simulated by reducing the embedded pile length in the model. The mass and inertia of the rotor-nacelle assembly is modelled as a high stiffness disc.

A linear perturbation frequency analysis can be performed, which requires linear elastic assumptions and outputs vibration frequencies and mode shapes for the model from an eigenvalue analysis. The output includes the results for vibration modes that are not necessarily of interest, such as standing waves in the soil body or ovalising of the structure. The number of these modes increases with the number of degrees of freedom in the system.

In a preliminary model, the soil was modelled with a uniform stiffness, and the results were compared with the 1D model for the same structure and soil at field scale. For the unscoured case, the frequency predictions of the first three modes were within 1%. For the scoured case, the frequency predictions of the first two modes were within 1% of each other, with a more significant (5%) difference for the third mode of vibration.

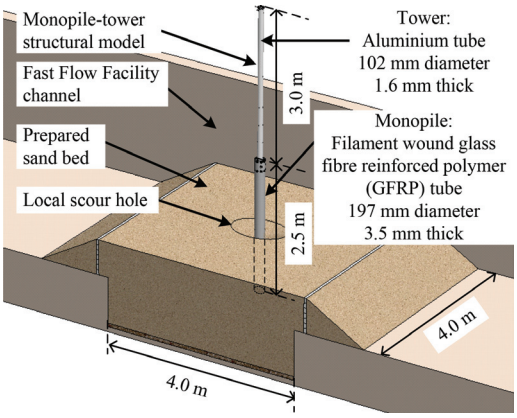

Figure 6. Fast Flow Facility experiment layout (from Mayall et al., 2018).

4 EXPERIMENTAL MODELLING

4.1 *Scope of experiments*

An experimental programme was carried out in the Fast Flow Facility at HR Wallingford, UK. This experimental programme explored measurement of the dynamic and static response of a 1:20 scale offshore wind structure with flow-developed scour. Mayall et al. (2018) provide a detailed description of the experimental setup and procedures.

The model structure comprised a monopile-tower structure (Fig. 6) with a top mass to mimic the rotor-nacelle assembly. The structure was instrumented with accelerometers, force sensors, strain gauges and displacement sensors.

Six tests were performed in the Fast Flow Facility, incorporating variations in scour protection (Table 3). For each test, after flooding the flume to the required water depth, the pile was installed into a prepared sand bed. Reversing (tidal) flow was applied to produce local scour around the pile in live-bed conditions. Once the target local scour was achieved the scour protection (if any) was installed. Global scour was simulated by removal of temporary retaining bars upstream and downstream of the main test section and continued tidal flow.

Additional elements of the testing programme not described in this paper included cone penetration testing of the sand bed and monotonic lateral loading of the pile at the end of each test.

4.2 *Scour protection models*

4.2.1 *Rock armour*

Rock armour scour remediation was installed in three tests; in each case the rock armour was placed to fill approximately 2/3 of the scour hole depth. The rock scour protection comprised an angular gravel with density of 2670 kg/m^3 and median grain size of 14.1 mm.

In Tests 3 and 6 the remediation was installed in a fully-formed scour hole, and in Test 4 the remediation was installed in a partially formed scour hole. The rock remediation was installed underwater using an inclined fall pipe (Fig. 7).

Table 3. Summary of Fast Flow Facility experiments.

Test number	Initial global bed level above Pile Tip	Scour depth prior to remediation	Scour protection model
1	4.56 *D*	1.58 *D*	None
2	4.61 *D*	1.58 *D*	Tyre-filled nets
3	4.57 *D*	1.49 *D*	Rock armour remediation (76 kg)
4	4.55 *D*	0.66 *D*	Rock armour remediation (22 kg)
5	4.57 *D*	None	Pre-installed rock armour (145 kg)
6	5.61 *D*	1.51 *D*	Rock armour remediation (76 kg)

Rock armour scour protection was pre-installed in Test 5. For this test the scour protection was placed after the bed preparation but before filling the flume or installing the pile. The scour protection was installed using a template (Fig. 7), with a distance of 400 mm from the pile wall to the crest, edge slope of 1V:3H, and a protection thickness of 75 mm.

Figure 7. Rock armour scour protection at model scale. (Left: rock detail; Top right: Installation of remediation by fall pipe; Bottom right: Pre-installation of protection using templates).

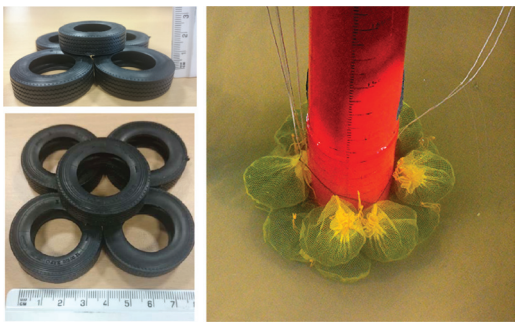

Figure 8. Tyre-filled net scour protection at model scale (Left: tyre detail; Right: Installation of tyre-filled nets).

4.2.2 *Tyre-Filled Nets*

Tyre-filled net (TFN) scour protection systems have been installed at a small number of offshore sites. They are designed to trap sediment and hence prevent further scour developing.

During Test 2 a set of generic tyre-filled nets was installed as scour remediation in a fully-formed scour hole. Rubber model truck tyres (approximate dimensions: 26 mm inside diameter, 42 mm outside diameter, 11 mm wide, 1 mm wall thickness) were placed in nylon mesh bags, with a mesh size of approximately 2–3 mm. The TFNs were installed by lowering into place as two rings of six nets (Fig. 8). 50 tyres were placed in each net, making 600 tyres in total.

5 EXPERIMENT RESULTS

5.1 *Bathymetry measurements*

During the Fast Flow Facility experiments, bed levels were measured using an underwater laser scanner at scheduled pauses in the flume operation, and also at the end of each test using a terrestrial laser scanner. Fig. 9 presents an example of the typical data acquired from the underwater laser scanner. Whilst coverage was limited, by the water clarity and by line of sight obstructions such as the pile, good data for scour evolution were obtained.

The bathymetry data were analysed to extract local embedment levels and global bed levels by statistical analysis of data in the areas of interest (Fig. 9). The global bed levels have a greater range of measurements due to transient bed-forms moving through the test section.

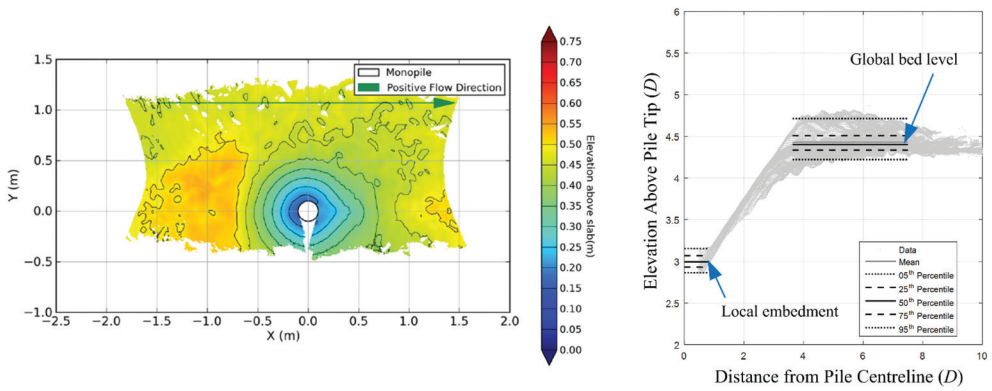

Figure 9. Underwater laser scanner bathymetry example from Test 1, end of local scour stage (Left: Mapped elevation of bed relative to slab datum, note that pile tip depth is 400 mm below slab datum; Right: Statistical analysis of local embedment and global bed level).

5.2 *Natural frequency measurements*

The tower-structure model included a variable top mass, which enabled the structural response to be systematically varied. Fig. 10 presents an example of the top mass versus measured frequency. Table 4 presents a subset of the natural frequency measurements at the start of each test, with 3.616 kg top mass attached. These natural frequencies were calculated using time-domain fitting of decaying acceleration signals following an impulse load.

5.3 *Effect of scour on natural frequencies*

One of the central aims of the Fast Flow Facility experiments performed at HR Wallingford was to provide natural frequency and scour measurements for validation and calibration of the proposed numerical models.

Fig. 11 presents the change in frequency for the first three modes of vibration during the local scour stage of the Fast Flow Facility experiments for the subset of top mass = 3.616 kg. From these plots it can be observed that mode 2 is the most sensitive to scour. These data indicate that the natural frequency of mode 2 reduces approximately four times more rapidly than mode 1, and mode 3 reduces approximately two times more rapidly than mode 1. Differences in sensitivity between tests are most likely caused by variations in the achieved soil conditions and experimental scatter.

Fig. 12 presents an example comparison of measured natural frequencies with Class C predictions

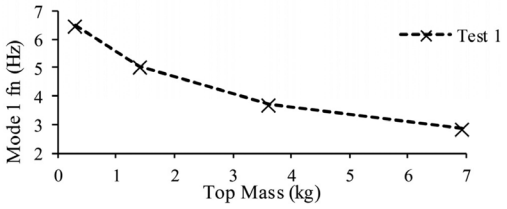

Figure 10. Example of measured natural frequency versus top mass (Mode 1, start of Test 1).

Table 4. Initial Natural Frequency Measurements from Fast Flow Facility Experiments (top mass = 3.616 kg).

Test number	Initial mode 1 f_n (Hz)	Initial mode 2 f_n (Hz)	Initial mode 3 f_n (Hz)
1	3.72	17.6	41.6
2	3.72	17.1	40.9
3	3.76	18.0	41.5
4	3.75	17.3	41.4
5	3.73	18.4	42.0
6	3.80	19.7	43.9

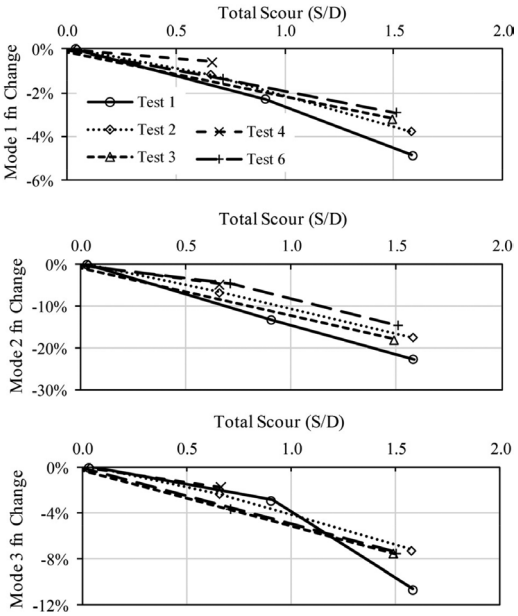

Figure 11. Measured change in natural frequencies with developing local scour (top mass = 3.616 kg).

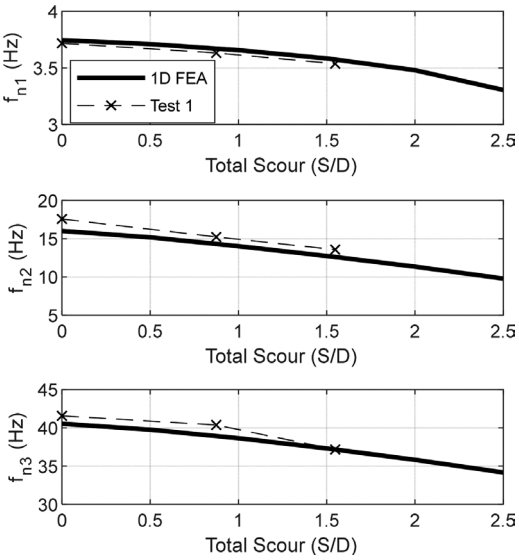

Figure 12. Comparison of 1D numerical model output with experimental data (Test 1, top mass = 3.616 kg, α_L = 1).

from the 1D FEA at model scale. [Class C predictions are made with sight of the results.] In the example shown the trends of natural frequency with scour are very similar between the prediction and the experiments; the frequency of mode 1 is overpredicted by roughly 1%, mode 2 is underpredicted

Table 5. Summary of scour protection performance in fast flow facility experiments.

Test number	End of test bed level above Pile Tip (Median)		Observations of scour protection condition at end of test	% Change in natural frequency (from unscoured case with top mass = 3.616 kg)			
				After scour protection end of test			
	Global level	Local level at Pile Wall		Mode 1	Mode 2	Mode 1	Mode 2
1	3.99 *D*	2.24 *D*	–	–	–	–7.2	–31.2
2	4.18 *D*	3.81 *D*	Trapped sediment, nets partially buried	–3.9	–16.5	–3.3	–16.0
3	4.27 *D*	3.87 *D*	Trapped sediment, rock partially buried	–2.8	–17.3	–2.7	–12.0
4	4.18 *D*	3.83 *D*	Trapped sediment, falling apron of rock falling apron partially buried	–0.4	–2.5	–2.8	–10.4
5	4.11 *D*	4.84 *D*	Trapped sediment, falling apron of rock, surface rocks undisturbed	–	–	+0.3	+1.5
6	3.82 *D*	5.05 *D*	Trapped sediment, falling apron of rock	–2.3	–8.1	–1.6	–9.5

by less than 10% and mode 3 is underpredicted by less than 5%.

5.4 *Scour protection performance*

In all tests involving scour protection, the condition of the scour protection was identified at the end of the test through an excavation process. Key observations are noted in Table 5, which includes notes on the natural frequency measurements immediately after installing scour protection and at the end of each test following the global scouring stage.

In all tests, trapped sediment accumulated in the scour protection material, with the edges of the scour protection being partially buried by sand waves. In most tests scour protection caused the natural frequency to increase; the clearest exception is Test 4 where the scour protection material was not sufficient to maintain the local embedment, resulting in a drop in measured natural frequency.

6 CONCLUSIONS

The effect of scour and scour protection on monopile supported wind turbine structures is an important area of offshore design. This paper describes an ongoing research project exploring this topic at the University of Oxford including:

– 1D and 3D finite element models for predicting changes in the dynamic response of an offshore wind structure for varying scour conditions
– An experimental programme exploring the dynamic response of a 1:20 scale offshore wind structure with scour and with scour protection

The experimental programme has produced a significant data set, including bathymetry measurements and natural frequency measurements for a range of modelled rotor-nacelle masses. Key findings from the experimental programme thus far are:

– The frequency of second and third vibration modes are more sensitive to scour than the frequency of the first vibration mode
– The testing method achieved global scouring of the test bed, with significant bed-forms causing spatial variation in the global levels
– In tests with scour protection, sediment was deposited within the scour protection material
– The natural frequency of structures with scour protection increased or remained stable after further flow in cases where the scour protection level at the pile wall did not reduce significantly

The experimental data will be used for calibration and validation of the numerical models, including the following elements of the analysis:

– Soil stress and stiffness profiles for small displacement problems with local scour
– Modelling the stiffness contribution of scour protection material with global and local scour

ACKNOWLEDGEMENTS

This research project is supported through funding from E.ON Climate & Renewables and HR Wallingford, and by grant EP/L016303/1 for Cranfield University and the University of Oxford, Centre for Doctoral Training in Renewable Energy Marine Structures—REMS (http://www.rems-cdt.ac.uk/) from the UK Engineering and Physical Sciences Research Council (EPSRC).

REFERENCES

API, 2011. RP 2GEO. *Recommended Practice for Geotechnical Foundation Design Consideration.*

Breusers, H.N.C., Nicollet, G. & Shen, H.W., 1977. Local scour around cylindrical piers. *Journal of Hydraulic Research*, 15(3), pp.211–252.

Byrne, B.W., McAdam, R.A., Burd, H.J., Houlsby, G.T., Martin, C.M., Zdravkovic, L., Taborda, D.M.G., Potts, D.M., Jardine, R.J., Sideri, M., Schroeder, F.C., Gavin, K., Doherty, P., Igoe, D., Muir Wood, A., Kallehave, D. & Skov Gretlund, J., 2015. New design methods for large diameter piles under lateral loading for offshore wind applications. In: *3rd International Symposium on Frontiers in Offshore Geotechnics (ISFOG 2015)*. Oslo, Norway, June (pp. 10–12).

Clayton, C.R.I., 2011. Stiffness at small strain: research and practice. *Géotechnique*, 61(1), pp.5–37.

Damgaard, M., Ibsen, L.B., Andersen, L.V. & Andersen, J.K., 2013. Cross-wind modal properties of offshore wind turbines identified by full scale testing. *Journal of Wind Engineering and Industrial Aerodynamics*, 116, pp.94–108.

DNVGL, 2016. *Standard DNVGL-ST-0126, Support structures for wind turbines*, Edition April 2016.

Høgedal, M. & Hald, T., 2005. Scour assessment and design for scour for monopile foundations for offshore wind turbines. In: *Proceedings of the Copenhagen Offshore Wind*. Copenhagen, Denmark.

International Organization for Standardization (ISO), 2007. *ISO 19902 Petroleum and natural gas industries—Fixed steel offshore structures*. Geneva: ISO.

Kallehave, D., Byrne, B.W., LeBlanc Thilsted, C. & Mikkelsen, K.K., 2015. *Optimization of monopiles for offshore wind turbines*. Phil.Trans.R.Soc.A 373: 20140100. http://dx.doi.org/10.1098/rsta.2014.0100

Larsen, S.M., Roulund, A., Brooks, A.J. and Chaffey, A., 2016. Sandwaves and megaripples at Race Bank (UK) offshore windfarm. In: *8th International Conference on Scour and Erosion (ICSE 2016)*. Oxford, UK.

Mayall, R.O., McAdam, R.A., Byrne, B.W., Burd, H.J., Sheil, B.B., Cassie, P., & Whitehouse, R.J.S., 2018. Experimental modelling of the effects of scour on offshore wind turbine structures. In: *9th International Conference Physical Modelling in Geotechnics (ICPMG 2018)*. London, UK, July.

Prendergast, L.J., Gavin., K. & Doherty, P., 2015. An investigation into the effect of scour on the natural frequency of an offshore wind turbine. *Ocean Engineering* 101 1–11.

Prendergast, L.J., Reale, C. & Gavin, K., 2018. Probabilistic examination of the change in eigenfrequencies of an offshore wind turbine under progressive scour incorporating soil spatial variability. *Marine Structures* 57 87–104

Qi, W.G., Gao, F.P., Randolph, M.F. & Lehane, B.M., 2016. Scour effects on p–y curves for shallowly embedded piles in sand. *Géotechnique*, 66(8), pp.648–660.

Sørensen, S.P.H. & Ibsen, L.B., 2013. Assessment of foundation design for offshore monopiles unprotected against scour. *Ocean Engineering* 63, 17–25.

Tavouktsoglou, N.S., Harris, J.M., Simons, R.R. & Whitehouse, R.J.S., 2017. Equilibrium Scour-Depth Prediction around Cylindrical Structures. *J. Waterway, Port, Coastal, Ocean Eng.*, 143(5): 04017017.

Tempel, J., Zaaijer, M.B. & Subroto, H., 2004. *The effects of Scour on the design of Offshore Wind Turbines.*

Tseng, W., Kuo, Y., Chen, J., 2017. An Investigation into the Effect of Scour on the Loading and Deformation Responses of Monopile Foundations. In: *Energies 2017, 10, 1190.*

Zdravković, L., Taborda, D.M.G., Potts, D.M., Jardine, R.J., Sideri, M., Schroeder, F.C., Byrne, B.W., McAdam, R., Burd, H.J., Houlsby, G.T. & Martin, C.M., 2015. Numerical modelling of large diameter piles under lateral loading for offshore wind applications. In: *3rd International Symposium on Frontiers in Offshore Geotechnics (ISFOG 2015)*. Oslo, Norway.

Appendix B Paper 2

Monopile Response to Scour and Scour Protection

Paper 2

Experimental modelling of the effects of scour on offshore wind turbine monopile foundations

Mayall, R.O., McAdam, R.A., Byrne, B.W., Burd, H.J.,

Sheil, B.B., Cassie, P. and Whitehouse, R.J.S.

2018

Physical Modelling in Geotechnics – McNamara et al. (Eds)

Experimental modelling of the effects of scour on offshore wind turbine monopile foundations

R.O. Mayall, R.A. McAdam, B.W. Byrne, H.J. Burd & B.B. Sheil
Department of Engineering Science, University of Oxford, Oxford, UK

P. Cassie
E.ON Climate & Renewables, Coventry, UK

R.J.S. Whitehouse
HR Wallingford, Wallingford, UK

ABSTRACT: Local and global scour around offshore wind turbine monopile foundations can lead to a reduction in system stiffness, and a consequential drop in the natural frequency of the combined monopile-tower-nacelle structure. If unchecked this could lead to operational problems such as accelerated fatigue damage and de-rating or decommissioning of the turbine. Research exploring the interaction between scour, foundation stiffness, and structural dynamic behaviour is therefore critical if scour formation is to be properly accounted for in predictions of structural performance, and to guide the implementation of scour remediation strategies. This paper describes experimental work that explores these interactions, conducted on a 1:20 scale driven monopile foundation and tower-nacelle superstructure in a prepared sand test-bed at HR Wallingford's Fast Flow Facility. The flume allowed realistic scour geometries to be developed, providing a means to explore the effectiveness of different remediation strategies. Measured acceleration and strain caused by harmonic lateral loading are interpreted to deduce changes in structural performance as scour develops.

1 INTRODUCTION

1.1 *Background*

Scour of seabed sediments can occur around offshore structures due to the interaction between the structure and the water flow around it. The resulting reduction in strength and stiffness of the structure's foundation can present operational and structural problems. For monopile wind turbine structures this can be of particular concern due to the consequential reduction in natural frequency, and potential for increased fatigue damage.

Ongoing research at the University of Oxford involves development of a numerical modelling framework for analysis of the effects of scour and scour protection on monopile offshore wind turbines. The numerical framework involves structural dynamic analysis using a 1-dimensional (1D) finite element model of the monopile-tower system, calibrated using three-dimensional (3D) finite element analyses and scale model testing, and further validated using experimental and field data.

This paper describes a programme of experiments conducted using the Fast Flow Facility (FFF) at HR Wallingford. The experiments were designed to provide validation cases for the numerical framework and to inform predictions of the effects of scour and scour protection on the structural dynamic response of field scale monopile offshore wind turbines.

1.2 *Scour around offshore piles*

Scour around offshore foundations can take the form of a combination of global scour (S_G) and local scour (S_L), as illustrated in Figure 1.

Global scour, also termed general scour, is a global lowering of the seabed, caused by overall seabed movement, migrating sand waves and sandbanks, or migrating channel features.

Local scour is the formation of a scour pit around a foundation due to the effects of horseshoe vortices that develop around the pile in a flow (Sumer & Fredsøe, 2002). The scour pit will typically reach an equilibrium depth for a particular set of current and wave conditions and no global scour.

Empirical calculation methods for predicting the local scour depth have been developed by several authors (e.g. Breusers et al., 1977; Høgedal & Hald, 2005), and are typically normalized by pile diameter, D. Commonly cited is the experimental data of Breusers et al. (1977), with a mean equilibrium local scour depth of $S_L/D = 1.5$ (or 2 to be on the safe side

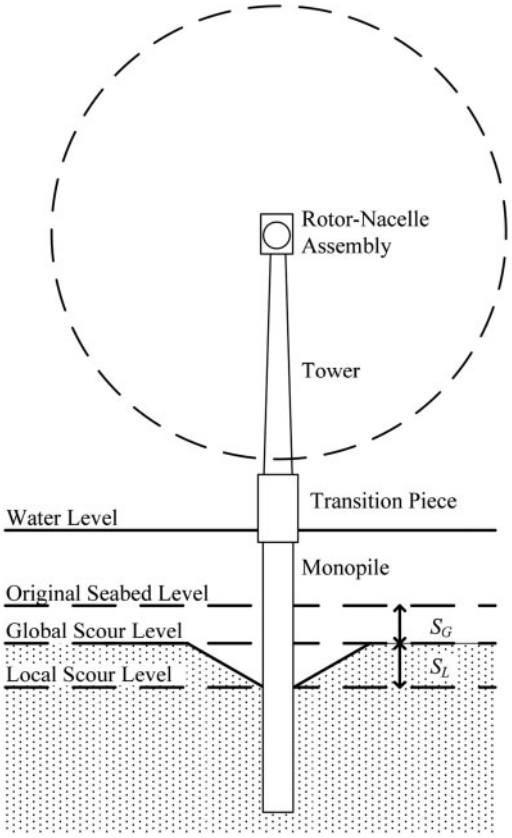

Figure 1. Scour around a monopile offshore wind turbine.

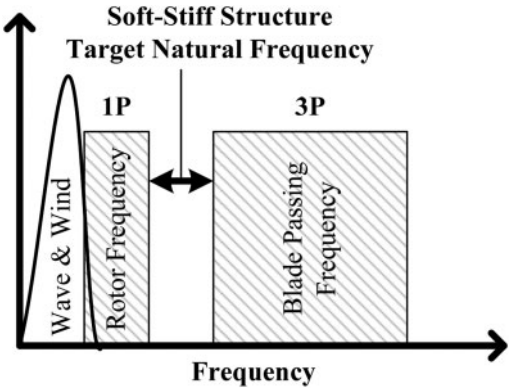

Figure 2. Offshore wind turbine loading frequencies.

for design) or $S_L/D = 1.3$ with a standard deviation of 0.7 (Sumer & Fredsøe, 2002). Design standards from the petroleum industry (API, 2011; ISO, 2007) recommend a design $S_L/D = 1.5$ whilst DNVGL (2016) recommends $S_L/D = 1.3$.

1.3 *Natural frequencies of offshore wind turbines*

Wind turbine structures are designed such that their fundamental natural frequency avoids the loading

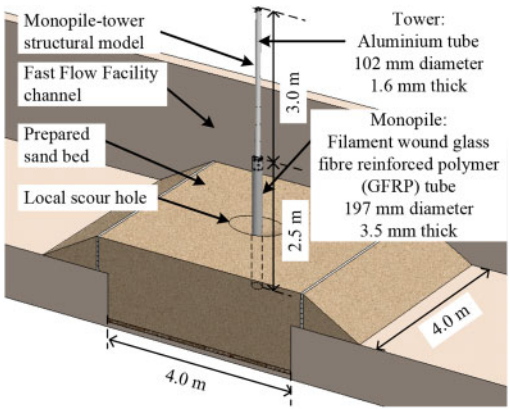

Figure 3. Fast Flow Facility experiment layout.

frequencies of the rotor (1P), blade passing (3P) and wind and wave frequencies, to minimise the dynamic amplification of loads (Kallehave et al., 2015). Monopile wind turbines are soft-stiff structures with the design natural frequency placed between the 1P and 3P loading bands (Fig. 2), and typically above the wind and wave frequencies.

With the development of scour the embedded pile length, L, is reduced, and the foundation stiffness and natural frequency drifts downwards. A turbine may fall out of warranty or have to be decommissioned if the natural frequency of the structure becomes too close to the 1P frequency; this leads to a loss of revenue unless the natural frequency can be restored by remediation.

2 EXPERIMENTAL SETUP

2.1 *Scope of experiments*

An experimental programme was conducted to investigate the influence of scour and scour protection on the natural frequencies of an instrumented model monopile-tower system. The tests were conducted at 1:20 scale in the Fast Flow Facility (FFF) at HR Wallingford. The experiment elements include a prepared sand test bed, the monopile-tower model, and development of scour using the flume (Fig. 3).

Six separate tests were conducted, each of which included the following sequence of activities:

1. Soil bed preparation and saturation
2. Filling the flume to the required water level
3. Pile driving to target initial embedment L/D
4. Initial structural dynamics testing
5. Developing local scour
6. Installing scour protection (if any)
7. Developing global scour
8. Draining the flume
9. Excavating pile and disturbed areas of soil

Table 1 presents the variations in the initial embedment, target local scour before installing scour protection, scour protection type, and target global scour

Table 1. Summary of target scour conditions for the Fast Flow Facility experiments.

Test Number	Initial Pile Embedment L/D	Local Scour S_L/D	Scour Protection	Global Scour S_G/D
1	4.5	1.5	None	1.5
2	4.5	1.5	Tyre-filled nets	1.5
3	4.5	1.5	Rock armour	1.5
4	4.5	0.75	Rock armour	1.5
5	4.5	0.0	Rock armour	1.5
6	5.5	1.5	Rock armour	2.5

Figure 4. Pit section of the Fast Flow Facility prior to installation of the experiments.

depth for the tests. The details of the scour protection models falls outside the scope of this paper.

2.2 *Fast Flow Facility (FFF)*

The FFF is a research flume capable of producing flows up to 4.9 m^3/s and generating wave heights of up to 1 m. The FFF channel has a cross section 4.0 m wide × 2.5 m deep and length of 57 m between sediment traps. The experiments described in this paper were prepared in a deeper 4.0 m long × 3.5 m deep pit section of the FFF (Fig. 4).

Scour development in the FFF tests comprised local and global scouring stages (Fig. 5). Scour was developed using currents, including cycling of direction; wave generation was not used.

The scour development was scaled using conventional approaches to produce a live bed scour regime. To ensure that all sediment was mobile the ratio of current speed to threshold current speed for sand motion was selected to be greater than 1.0 (Whitehouse, 1998). This regime generates realistic local scour depths scaled on the pile diameter, in line with empirical predictions.

The extent of scour is controlled by the sand properties and by vortex shedding downstream of the pile. Cycling the flow direction simulates a tidal situation and enables the scour extent to grow in both directions.

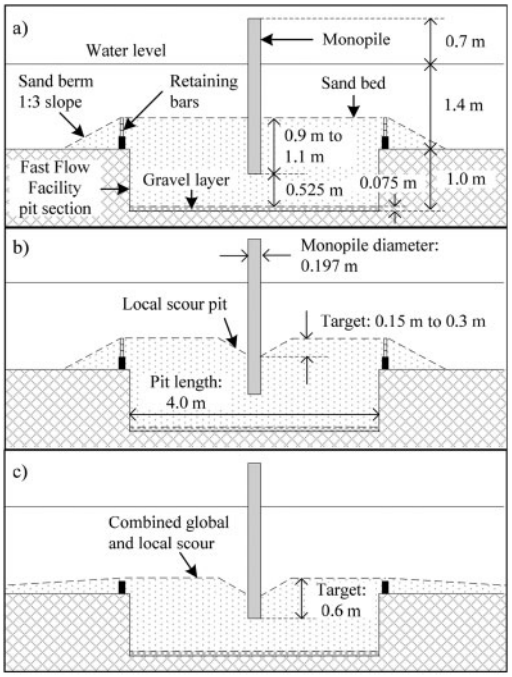

Figure 5. Schematic of scouring process, tower not shown. a) Condition at end of bed preparation and pile driving. b) Condition after development of local scour. c) Condition after removing retaining bars and flow segments for global scour.

Typically 8.25 hours of flow was used to develop local scour.

Global scour was developed by incrementally removing temporary retaining bars, and running further flow at higher velocity. After each 0.1 m deep bar was removed the flow was again run for 8.25 hours before the next bar was removed.

The same water level (1.8 m above pile toe) was used throughout the testing, as a result the water depth varied as global scour developed. The soil bed bathymetry was measured using an underwater laser scanner between flow cycles, and with a terrestrial laser scanner at test completion.

2.3 *Soil bed preparation*

Scour phenomena are particularly prevalent at wind farm sites where superficial sand layers exist. A fine-grained silica sand with a mean particle size of 0.16 mm was therefore used for the experiments.

After initial filling of the pit with sand, the central area of the pit was re-prepared for each test. The preparation consisted of excavating a hole of at least 1.5 m width to a depth of 50 mm to 100 mm below the target pile toe depth. Sand was then added in 50 mm thick compacted layers (using a 240 V plate compactor, Fig. 6) up to the target bed level.

Following compaction of the final soil layer the soil bed was saturated, prior to filling the FFF to the required water level. To aid the saturation process a

Figure 6. Compaction of sand layers using plate compactor.

Figure 7. Perforated pipes installed in the pit section of the Fast Flow Facility.

set of perforated pipes (Fig. 7) were installed in the base of the pit within a 75 mm thick gravel bed, and overlain by a geotextile membrane. This allowed saturation of the sand using an upwards hydraulic gradient by connection to a header tank.

2.4 *Monopile-tower structural model*

The model monopile-tower structure consisted of a pile, transition piece, tower, top masses, and top stiffener. The model structure dimensions and materials (Fig. 3) were specified to achieve geometry and stiffness that scale appropriately to a full-sized structure, within practical limitations. The relative lengths and diameters of the pile and tower are similar to field scale structures.

The monopile geometry and material was selected such that the non-dimensional group E_pI_p/E_sL^4 (Poulos & Davis, 1980) was similar to field scale, where E_pI_p is the flexural stiffness of the pile and E_s is an estimate of the soil stiffness. The tower geometry and material was selected using the non-dimensional group E_tI_t/E_pI_p (Arany et al., 2016) where E_tI_t is the flexural stiffness of the tower. For practical reasons the moment of inertia of the rotor-nacelle was

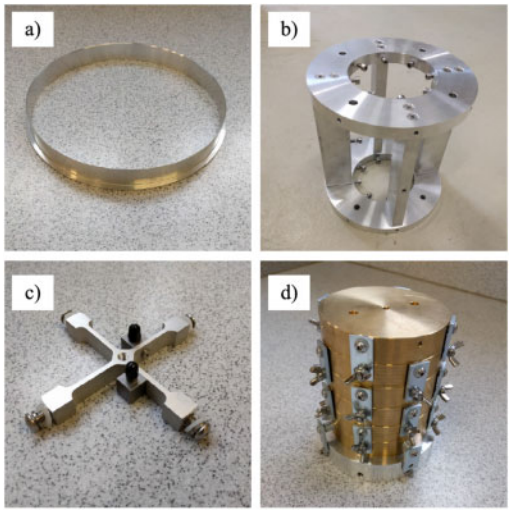

Figure 8. Structure model components. a) Pile shoe. b) Transition piece. c) Mounted accelerometer pair. d) Variable top mass.

not replicated; this is anticipated to have a negligible influence and does not restrict the use of the results in validating the numerical framework.

An annular aluminium driving shoe was bonded to the pile toe to reduce risk of damage during installation (Fig. 8a). The pile and tower were attached by bolted connections using an aluminium transition piece (Fig. 8b). The model also included accelerometers mounted within the tower (Fig. 8c), and a variable top mass to mimic a rotor-nacelle assembly (Fig. 8d).

2.5 *Pile driving*

The monopile-tower model was installed by pile driving. Fig. 9 presents the set-up of the pile driving equipment used in the experiments. Driving took place with the structure fully assembled, with the tower attached to the pile. A pair of pulleys were used to manually raise the driving hammer to a set elevation, with the tower acting as a guide for the hammer. A polyethylene driving cushion was used, underlain by a rubber layer on top of the pile annulus to reduce the risk of damaging the pile. The hammer had a mass of 7.75 kg and the maximum stroke used in any test was 1 m.

A set of guides with inwards-facing rubber wheels were used to ensure pile verticality during driving. These guides were fixed to a portal-layout scaffold frame constructed over the FFF.

2.6 *Structural dynamics testing*

2.6.1 *Structural dynamics testing overview*

Structural dynamics measurements were repeated at each scour depth, to track changes of response with scour condition. Tests were conducted with different amounts of mass attached to the top of the tower

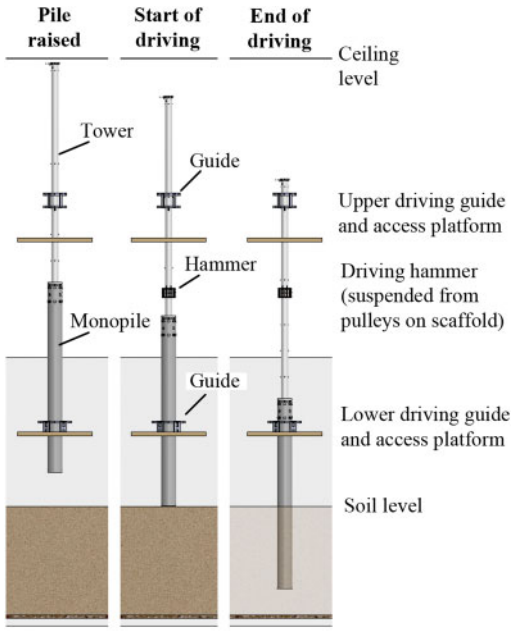

Figure 9. Illustration of pile driving process.

(Fig. 8d). Increasing the top mass reduces the natural frequency and also changes the shape of the higher order bending modes. Changing the top mass therefore provides valuable additional information on the foundation response for validating and/or calibrating the numerical models.

The structural natural frequencies and mode shapes were measured using accelerometer pairs mounted within the tower structure (Fig. 8c) at 2.33 m, 2.83 m, 3.18 m, 3.53 m, 4.13 m and 5.38 m above pile tip (APT). This instrumentation was mounted before pile driving; accelerometers were therefore required with a high shock rating to withstand pile driving. The accelerometer axes were aligned to measure the response in the streamwise and spanwise directions.

Additional instrumentation included: bending gauges on the pile in the streamwise direction at 1.61 m APT, a temposonics displacement sensor mounted to the pile in the streamwise direction at 1.95 m APT, and force sensors attached to the top of the tower in the streamwise and spanwise directions. All instruments were sampled and logged at 3 kHz.

Measurements of natural frequencies were made using impulse loading, and also by measuring the response with a modal shaker attached, as described below.

2.6.2 *Impulse loading*

The impulse loading tests were used to measure the natural frequencies for the first three bending modes. The impulses were applied as a light impact to the force sensor attached at the top of the tower; the magnitude of the impulse could therefore be recorded. The natural frequencies were identified from the power spectral density (PSD) of the measured accelerations.

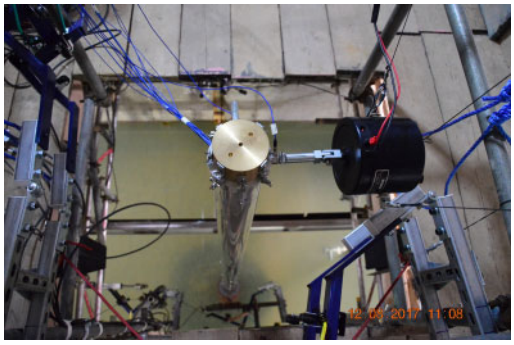

Figure 10. Modal shaker attached to the top of the tower.

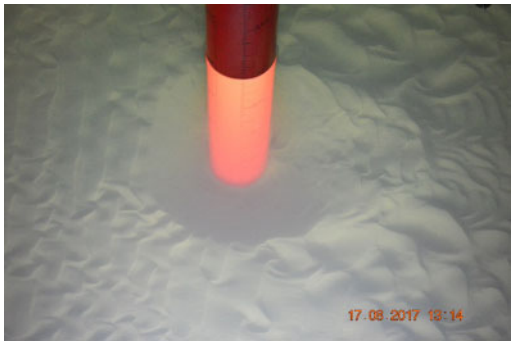

Figure 11. Local scour pit formed around the model monopile. From Test 6 in the Fast Flow Facility.

2.6.3 *Modal shaker tests*

Measurements of natural frequencies were also made using a modal shaker (Fig. 10). The modal shaker was suspended via lightweight cables, and attached to the required force sensor in the streamwise or spanwise direction. Two types of test were performed using the modal shaker:

1. Frequency sweeps, generating sinusoidal signals at a series of discrete frequencies around a target frequency.
2. White noise tests, in which white noise vibrations were sent to the modal shaker.

In the frequency sweeps the magnitude of accelerations and force provide information on the structural dynamics. The natural frequencies are determined as the frequencies at which the phase difference between the measured input force signal and acceleration signal is 90°.

3 EXAMPLE RESULTS

An example of the scour pit developing during the FFF experiments is shown in Figure 11, from Test 6 (see Table 1). The image in Figure 11 was taken part-way through the full duration of flow for local scour, with an approximate depth of $S_L/D = 0.75$. This test continued until the target $S_L/D = 1.5$ was achieved.

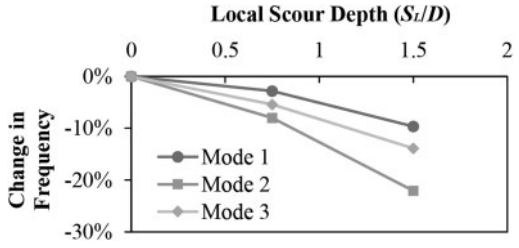

Figure 12. Measured change in natural frequency of model wind turbine with local scour (Test 1, no top mass).

In Test 1 (see Table 1) structural dynamics testing was performed at approximate local scour depths $S_L/D = 0.75$ and 1.5. With no top mass, the natural frequencies (interpreted from peaks of the PSD) were 6.5 Hz, 18.4 Hz and 47.6 Hz for the first three modes. Figure 12 presents the changes in the natural frequency of the first three modes for Test 1 as the local scour develops. These example results show natural frequencies reducing as local scour develops, consistent with the loss of foundation stiffness caused by the scouring process. All three frequencies show increasing sensitivity to scour as the scour depth increases. An interesting observation is the mode 2 and mode 3 frequencies are more strongly affected by local scour than mode 1.

4 CONCLUSIONS

This paper has described experiments to measure the response of a monopile wind turbine structure to scour developed in a flume. The experiments were successful in providing a measurable change in natural frequency as the scour developed.

The observation that mode 2 and 3 natural frequencies are more strongly affected by scour than mode 1 may provide useful insight for structural health monitoring of offshore wind turbine structures to inform detection of scour without bathymetry surveys.

Further results to be extracted from the experiments include: measured damping, mode shapes, effects of global scour on the structural dynamics, and a comparison of the natural frequency measurement methods employed in the tests. The trends in the natural frequency measurements will be used to validate numerical models of scour on monopile wind turbine structures.

ACKNOWLEDGEMENTS

This research project is supported through funding from E.ON and HR Wallingford, and by grant EP/L016303/1 for Cranfield University and the University of Oxford, Centre for Doctoral Training in Renewable Energy Marine Structures – REMS (http://www.rems-cdt.ac.uk/) from the UK Engineering and Physical Sciences Research Council (EPSRC).

The authors would like to thank the individuals that assisted during the experimental campaign; from E.ON: Ben Holland, Patrick Rainey, and Steve Heald; from HR Wallingford: David Todd, Esther Gomes, Joe Mitchell, Amelia Astley, James Sutherland, John Harris, Andrew Huckstep, plus the electronics lab, build team, and workshop staff; and from the University of Oxford: Iona Richards, Toby Balaam, and Teodor Totev.

REFERENCES

API 2011. RP 2GEO. *Recommended Practice for Geotechnical Foundation Design Consideration*.

Arany, L., Bhattacharya, S., Macdonald, J.H. & Hogan, S.J. 2016. Closed form solution of Eigen frequency of monopile supported offshore wind turbines in deeper waters incorporating stiffness of substructure and SSI. *Soil Dynamics and Earthquake Engineering*, 83, pp. 18–32.

Breusers, H.N.C., Nicollet, G. & Shen, H.W. 1977. Local scour around cylindrical piers. *Journal of Hydraulic Research*, 15(3), pp. 211–252.

DNVGL 2016. *Standard DNVGL-ST-0126, Support structures for wind turbines*, Edition April 2016.

Høgedal, M. & Hald, T. 2005. Scour assessment and design for scour for monopile foundations for offshore wind turbines. In: *Proceedings of the Copenhagen Offshore Wind*. Copenhagen, Denmark.

International Organization for Standardization (ISO) 2007. *ISO 19902 Petroleum and natural gas industries – Fixed steel offshore structures*. Geneva: ISO.

Kallehave, D., Byrne, B.W., LeBlanc Thilsted, C. & Mikkelsen, K.K. 2015. *Optimization of monopiles for offshore wind turbines*. Phil.Trans.R.Soc.A 373: 20140100. http://dx.doi.org/10.1098/rsta.2014.0100

Poulos, H. G. & Davis, E. H., 1980. *Pile foundation analysis and design*, John Wiley & Sons, New York.

Sumer, B.M. & Fredsøe, J. 2002. *The mechanics of scour in the marine environment*. World Scientific, Singapore.

Whitehouse, R., 1998. *Scour at Marine Structures*. Thomas Telford, London.

Appendix C Flume Experiment Supplementary Material

This Appendix presents supplementary information relating to the flume experiments described in Section 2.

Appendix C.1 presents detail of the equipment specifications.

Appendix C.2 presents soil characterisation data.

Appendix C.3 presents the further detail on the CPT testing, including detail of the equipment, and presentation of the relative density calibration tests.

Appendix C.4 presents an assessment of the flume hydraulics during flow phases for scour development.

Appendix C.5 presents further detail on the bathymetry data analysis methods.

Appendix C.6 presents the methods used to analyse the structural dynamics impulse tests.

Appendix C.7 presents the methods used to analyse the structural dynamics frequency sweep tests.

Appendix C.8 presents further detail on the monotonic lateral loading tests, including detail of the equipment and data analysis methods.

Appendix C.9 presents results tables of the output bathymetry data and structural dynamics natural frequencies and mode shapes.

Appendix C.10 presents a summary of lessons from experimental programme and analysis.

C.1 Equipment Specifications

C.1.1 Model Monopile – Tower System

Figure C.1.1 presents the general arrangement of the model monopile – tower system, which consisted of a pile, transition piece, tower, top masses, and top stiffener. Table C.1.1 defines the material, mass and geometry of the components in the model.

Circumferential lines, marking distance above the pile tip, were added to the pile for reference in photographs of the experiments (single marks at 10 mm vertical spacing, dashed rings at 50 mm spacing, and solid rings at 100 mm spacing).

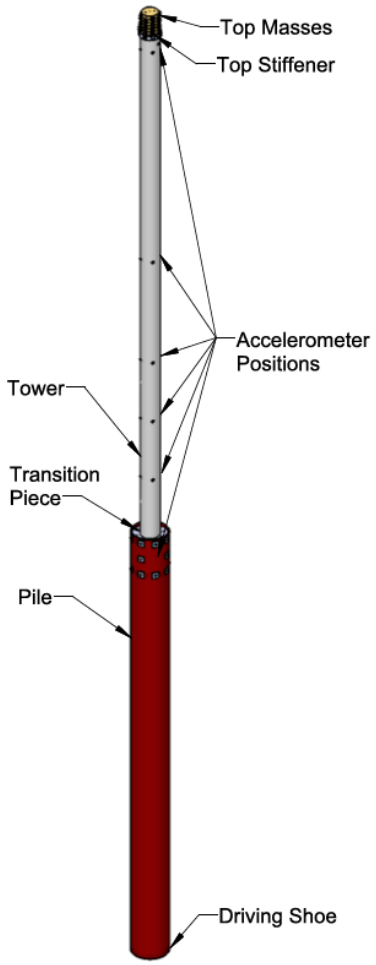

Figure C.1.1. The model monopile - tower system employed in the flume experiments

Table C.1.1. Model Monopile – Tower System Components

Item	Material	Mass	Geometry	Photograph
Pile	GFRP	7.725 kg (with hole stiffeners, driving shoe & bending gauges plus cables)	Length = 2500 mm Diameter = 197 mm Wall thickness = 3.5 mm	
Tower	Aluminium	7.19 kg (with TP & top stiffener) 8.46 kg (with TP, top stiffener & accelerometers plus cables)	Length = 3200 mm Diameter = 101.6 mm Wall thickness = 1.6 mm Pile overlap = 220 mm	
Driving shoe	Aluminium	Not measured	Height = 22 mm Wall thickness = 1 mm Annulus outer diameter = 197.5 mm Annulus radial thickness = 4.25 mm Annulus vertical thickness = 2 mm	
Transition piece	Aluminium	2.83 kg (with bolts)	Height = 200 mm Distance between top and bottom horizontal bolts = 185 mm Plate thickness = 15 mm	
Accelerometer mount	Aluminium	0.07 kg per mount (with accelerometers)	Height = 12 mm Arm thickness = 3 mm	
Top stiffener	Aluminium	0.18 kg (with bolts)	Height = 25 mm Outer diameter = 114 mm Wall thickness = 6.1 mm Tower overlap = 20 mm	
Top masses	Brass masses, steel fixings	6.64 kg (six masses with fixings)	Brass disc height = 18.5 mm per mass Brass disc diameter = 94.5 mm	

C.1.2 Scaffold Access Frame

Figure C.1.2 shows the arrangement of the scaffold frame installed for the flume experiments, which was required to provide access to the monopile – tower system.

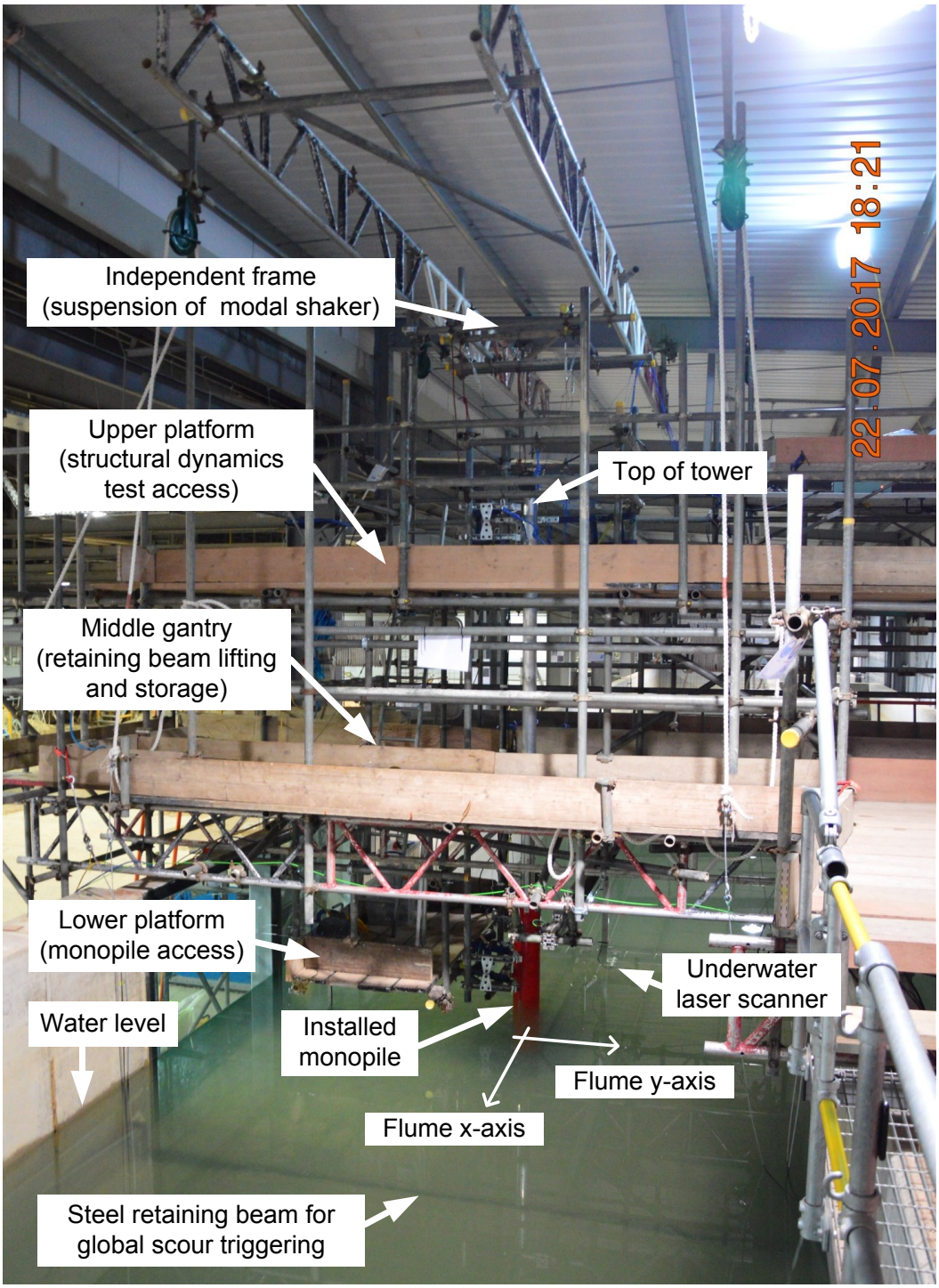

Figure C.1.2. Annotated photograph of scaffold frame configuration for the flume experiments (photograph taken during Test 3 after installing remedial rock fill scour protection)

C.1.3 Pile Driving Equipment

The pile driving process adopted in the flume experiments is described in Paper 2. Table C.1.2 presents an overview of the equipment temporarily attached to the structure during pile driving. Figure C.1.3 shows the assembled pile driving equipment.

Table C.1.2. Pile Driving System Components

Item	Description	Photograph
Driving hammer	A weight that can be split into two sections to be attached to the pile for pile driving. Two rows of bearings to ensure the hammer remains vertical during driving. Assembled mass = 7.75 kg.	
Driving cushion	Cushion to avoid damaging pile or transition piece during pile driving. Polyethylene split ring bolted together around tower. Cushion diameter slightly larger than the pile, such that impact loads were directly transferred to the pile wall.	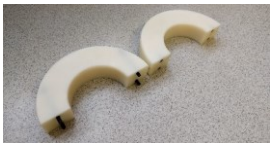
Upper driving guide	Steel frame with inward-facing rubber caster wheels to ensure pile verticality during driving. Attached to vertical scaffold bars near upper platform.	
Lower driving guide	Steel frame with inward-facing rubber caster wheels to ensure pile verticality during driving. Also used to fix pile in a raised position between FFF tests. Attached to vertical scaffold bars near lower platform.	
Plumb line	The soil plug length was measured using a plumb line lowered through a hole in the transition piece.	-

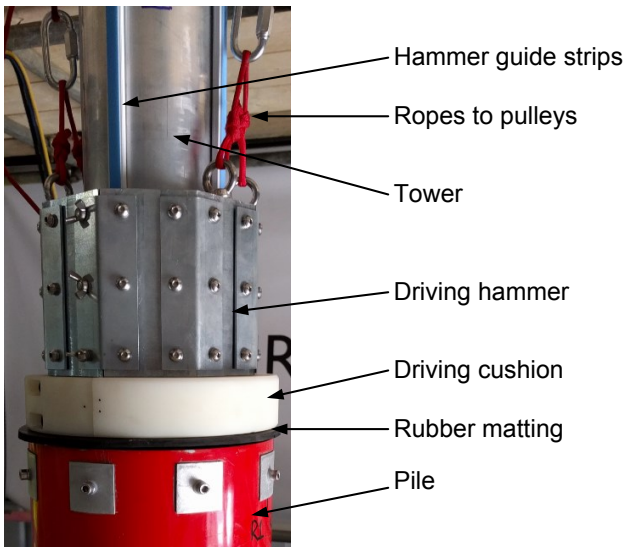

Figure C.1.3. Photograph of the assembled pile driving equipment

C.1.4 Electronic Equipment and Instruments

Various electronic equipment and instruments, listed in Table C.1.3, were used for sampling, logging and control during the experiments. Table C.1.4 presents a summary of the location and labelling of the sensors attached to the monopile – tower system. The sensors were mounted before pile driving, which informed the selection of accelerometers with a high shock rating to survive the pile driving. The force sensors were only attached to the structure after pile driving, and the LVDTs and load cell were only attached during monotonic lateral loading. Figure C.1.4 shows the displacement sensors attached to the structure.

Table C.1.3. Instrumentation in Structural Dynamics Tests

Item	Testing Type*	Brand	Model
USB Multifunction I/O	All	National Instruments	NI USB-6211
DAQ chassis	All	National Instruments	cDAQ-9188
Analogue input DAQ module	All	National Instruments	NI 9205
Bridge DAQ module	All	National Instruments	NI 9237
Power supply for position sensors	All	University of Oxford	-
Analogue output DAQ module	SD	National Instruments	NI 9263
Digital I/O DAQ module	SD	National Instruments	NI 9402
IEPE DAQ module	SD	National Instruments	NI 9234
IEPE Accelerometer	SD	PCB Piezotronics	333B50
IEPE Force sensor	SD	PCB Piezotronics	208C01
Modal shaker	SD	Bruel & Kjaer	Type 4809
Amplifier	SD	Bruel & Kjaer	Type 2712
Voltage-controlled amplifier	SD	RDL	ST-VCA3 Stick-on
Bending strain gauges on GFRP pile	SD, MLL	University of Oxford	-
Temposonics position sensor	SD, MLL	RDP	EP20100MD341V01
USB to RS-232	CPT, MLL	National Instruments	RS-232
Power supply for motor	CPT, MLL	McLennan Servo Supplies	48VDC
LVDT	MLL	RDP	DCV150C
Load cell	MLL	Applied Measurements Limited	DBBE-100kg
Motor	MLL	Applied Motion Products	23Q-3AN
Positronics position sensor	CPT	Measurement Specialists	SP2-50
Load cell	CPT	Omegadyne Inc	LCM105-500
Motor	CPT	Applied Motion Products	23Q-3AE
Strain gauges in CPT rod	CPT	University of Oxford	-
* CPT = cone penetrometer, SD = Structural Dynamics, MLL = Monotonic Lateral Loading			

Table C.1.4. Model Structure Sensor Positions

Sensor Description	**Height above pile tip *z* [mm] (see Fig. 2 in Paper 3)**	**Sensor Label**	
		Streamwise Direction	**Spanwise Direction**
Pile bending gauges mounted to pile	1605	BX	-
Temposonics position sensor on pile	1950	DX	-
LVDT (for monotonic lateral loading)	1900	LVDT1	-
	2400	LVDT2	-
Load cell (for monotonic lateral loading)	2472.5	H	-
Accelerometer mounted in tower	2330	1X	1Y
	2830	2X	2Y
	3180	3X	3Y
	3530	4X	4Y
	4130	5X	5Y
	5380	6X	6Y
Force sensor at top of tower	5468	FX	FY
Amplifier signal driving modal shaker	-	AI	

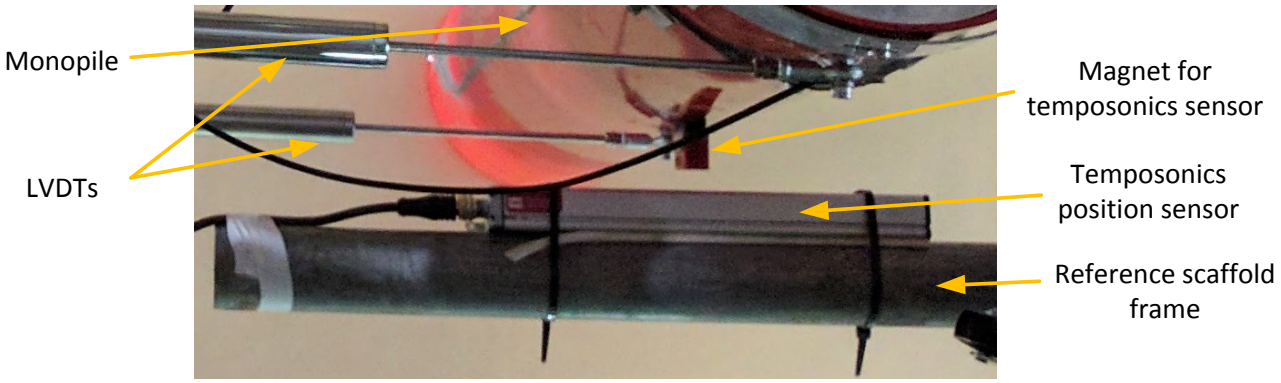

Figure C.1.4. Photograph of displacement sensors (photograph taken during monotonic lateral loading tests)

C.2 Soil Characterisation

C.2.1 Soil Characteristics

Soil characterisation tests were performed on samples of Bathgate psf sand taken from the experiments at the end of the testing programme. Table C.2.1 summarises the measured parameters and testing methods. Figure C.2.1 presents the particle size distribution for Bathgate psf sand, alongside that of the scour protection rock.

C.2.2 Critical State Friction Angle

Table C.2.2 presents the critical state friction angle determined from the shearing stages of triaxial compression tests performed, following bender element testing (Table C.2.2, see also Table 6 in Paper 3). The internal angle of friction was calculated as follows (Craig, 1992):

$$\phi' = \sin^{-1}\left(\frac{\sigma_1' - \sigma_3'}{\sigma_1' + \sigma_3'}\right) \quad \text{(C.2.1)}$$

Figure C.2.2(a) to (c) shows the strains and principal stresses during shearing. Some noise is present in the results for BE2_Medium, which may be due to the control system that maintains the back pressure to achieve zero excess pore water pressure. This noise does not appear to have significantly influenced the results. A critical state value of ϕ'_{cs} = 34° was selected based on the results in Table C.2.2.

Table C.2.1. Soil Parameters – Bathgate psf Sand

Parameter	Units	Value	Test Method
G_s	-	2.65	Assumed for silica sand
e_{min}	-	0.5018	Vibrating hammer (in: Head, 2006)
e_{max}	-	0.7528	2000 cm^3 measuring cylinder (in: Head, 2006)
d_{10}	mm	0.0765	Dry sieving using British Standard sieve sizes (BS 1377-2, 1996)
d_{50}	mm	0.1612	
d_{90}	mm	0.2818	

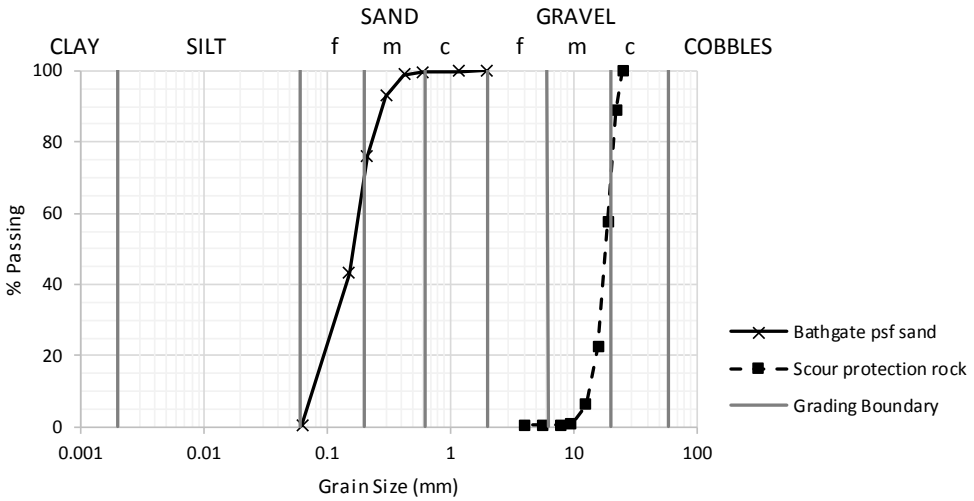

Figure C.2.1. Particle size distribution curves for Bathgate psf sand and scour protection rock (data for scour protection rock provided by HR Wallingford)

Table C.2.2. Soil Shearing Test Results – Bathgate psf Sand

Test ID	Shearing Type	e_0	D_R	Initial σ_3'	ϕ'_{peak}	ϕ'_{end}
		[-]	[%]	[kPa]	[°]	[°]
BE1_Loose	Undrained Compression	0.665	35.0	11.4	37.4	34.3
BE2_Medium	Drained Compression	0.600	60.9	10.3	44.5	33.7

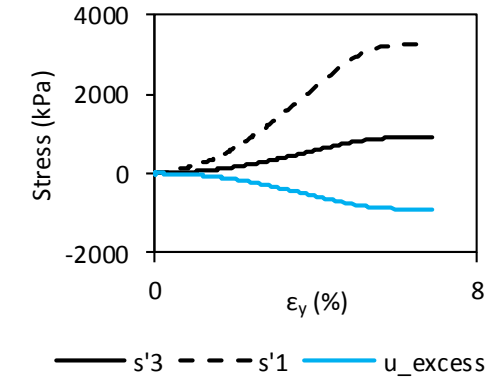

(a) BE1_Loose stress-strain curves

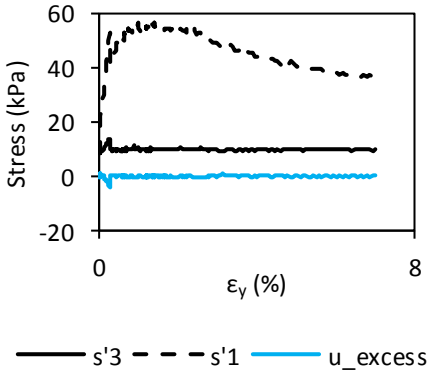

(b) BE2_Medium stress-strain curves

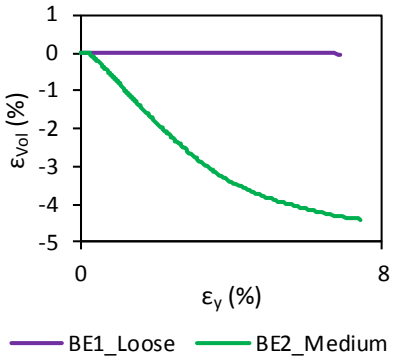

(c) Volumetric strain

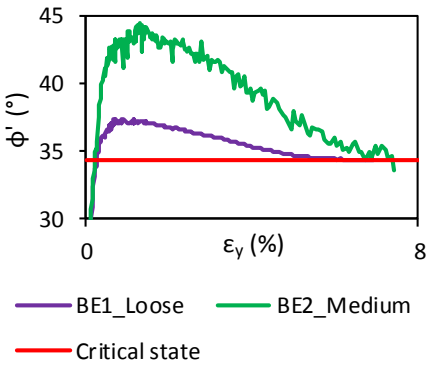

(d) Friction angle

Figure C.2.2. Results of triaxial shearing tests on Bathgate psf sand (data provided by Fugro)

C.3 Cone Penetrometer Testing and Calibration

C.3.1 Overview

A cone penetrometer was developed for the flume experiments to allow cone penetrometer tests (CPTs) to be performed following completion of the sand bed compaction process for each test. Calibration CPTs were performed to provide an empirical method for determining *in situ* soil parameters, such as relative density, from CPT data. The calibration CPTs focused on two sand types: Bathgate psf sand (fine silica sand, from flume experiments) in dry and saturated conditions, and Leighton Buzzard 14/25 sand (coarse silica sand, reference sand) in dry conditions.

C.3.2 CPT Equipment

The rod is 8 mm diameter with a 60° cone. Loads on the cone tip were measured directly using strain gauge instrumentation within the rod close to the cone. Side friction was inferred by subtracting the cone tip load from measurements of the total load at the top of the rod. A positronic position sensor was used to measure the vertical cone displacement. Data were logged at 1613 Hz. Figure C.3.1 shows the CPT equipment positioned on the prepared sand bed. The CPT equipment and *LabVIEW* data acquisition code were developed by Ross McAdam and Brian Sheil.

The CPTs followed the activity sequence below:

i. After bed compaction (Paper 2), a set of walking boards were placed on the soil bed in positions to support the CPT rig (see Figure C.3.1)

ii. The CPT rig was moved into position, including reaction weights

iii. The soil bed was saturated

iv. A CPT push and recovery was performed. All tests used a target depth of 950 mm, with a forward speed of 4 mm/s during the push

v. The soil bed was partially desaturated before removal of the CPT rig and walking boards

vi. The soil bed was re-saturated

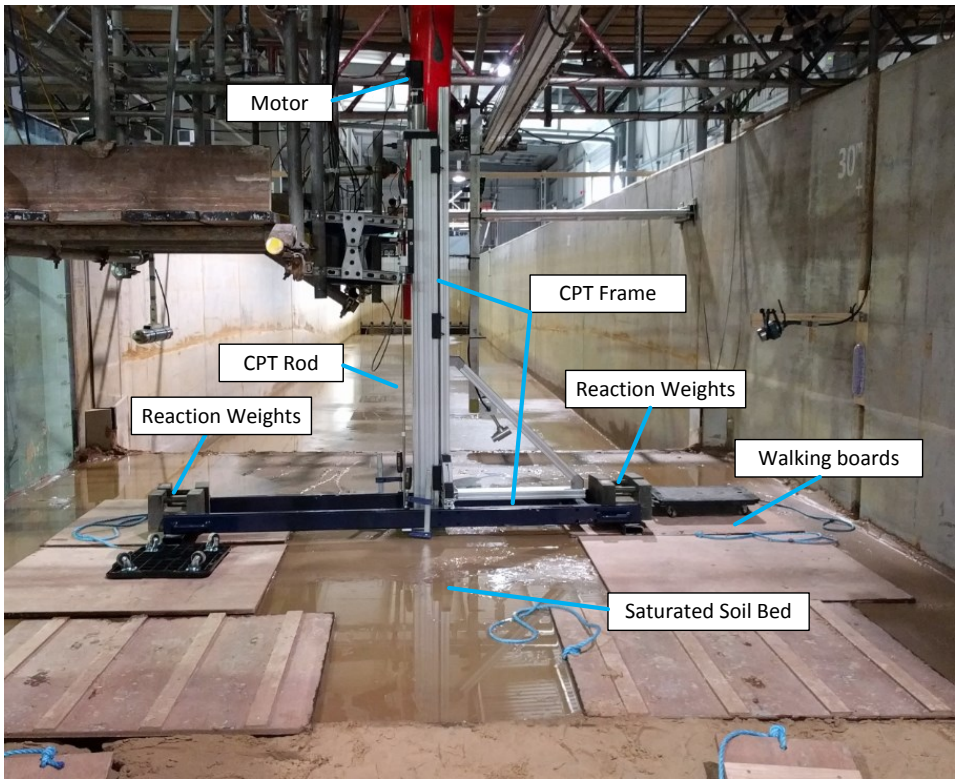

Figure C.3.1. Photograph of the CPT rig on a prepared sand bed

C.3.3 Relative Density Calibration Methods

Relationships between relative density (D_R) and CPT cone tip resistance (q_c) are proposed by numerous authors in the literature (e.g. Schmertmann, 1976; Jamiolkowski et al., 1985; Baldi et al., 1986), usually based on tests performed in dry sand. These methods can be generalised as having to:

$$D_R = \alpha_1 + \alpha_2 \log_{\alpha_3} \frac{q_c}{(\sigma')^{\alpha_4}} \tag{C.3.1}$$

where α_1 to α_4 are fitting parameters. Houlsby and Hitchman (1988) showed that q_c is generally dependant on the horizontal stresses, σ'_h, rather than the vertical stresses, σ'_v. For the current study the earth pressure coefficient, $K_h = \sigma'_h/\sigma'_v$, is unknown so a relationship based on σ'_v is used. A simplified form of (C.3.1) is adopted:

$$D_R = \alpha_1 + \alpha_2 \chi_c \qquad \chi_c = \ln \frac{q_c/p_{ref}}{\left(\sigma'_v/p_{ref}\right)^{0.5}} \tag{C.3.2}$$

where χ_c is a normalised cone resistance, α_1 and α_2 are expressed in the same units as D_R, and the reference stress is taken as p_{ref} = 100 kPa.

Jamiolkowski et al. (2003) noted that empirical fits based on dry calibration chamber CPTs would underpredict the density using CPTs in saturated calibration chamber tests by 7% to 10%, and proposed the following empirical correction:

$$\frac{D_{R,sat} - D_{R,dry}}{D_{R,dry}} 100 = -1.87 + 2.32 \ln \frac{q_c}{\left(\sigma'_v p_{ref}\right)^{0.5}} \qquad \text{for:} \quad \ln \frac{q_c}{\left(\sigma'_v p_{ref}\right)^{0.5}} > 2.24 \qquad \text{(C.3.3)}$$

This can also be rearranged as a function of χ_c:

$$D_{R,sat} = D_{R,dry}[0.9813 + 0.0232\chi_c] \qquad \text{(C.3.4)}$$

The Jamiolkowski et al. (2003) relationship is used for analysis of CPT measurements of saturated Bathgate psf sand (Appendix C.3.6).

C.3.4 Leighton Buzzard Sand CPT Calibration Tests

An initial set of calibration CPTs were performed using dry Leighton Buzzard 14/25 sand, in collaboration with Iona Richards (DPhil candidate in REMS CDT). Table C.3.1 presents the index soil properties of Leighton Buzzard sand. A specific gravity of G_s = 2.65 was assumed for silica sand.

Dry sand samples were prepared to a range of relative densities, summarised in Table C.3.2. The samples were prepared in a 800 mm internal diameter testing tank (described in Richards et al., 2018; 2019). Samples with relative density close to 0% were prepared by loose placement, samples with higher densities were prepared using a sand raining method. The sand raining method achieves different densities by releasing sand from a hopper and varying the rate of flow using a diffuser sieve (Richards, 2019). The limitation of the sand rainer volume required samples to be prepared in two layers, and the approximate position of the transition is included in Table C.3.2.

Figure C.3.2 presents the acquired CPT q_c profiles. The peaks in the CPT q_c profiles correspond to layers in the preparation of samples.

Table C.3.1. Soil Parameters – Leighton Buzzard 14/25 Sand (from Richards et al., 2018)

Parameter	Units	Value
γ_{min}	kN/m^3	14.43
γ_{max}	kN/m^3	17.64
d_{50}	mm	0.81

Table C.3.2. List of Calibration CPTs Performed on Dry Leighton Buzzard 14/25 Sand

Test ID	Date	γ	D_R	Penetration	Approx. layer level below top of sample	Remarks
		[kN/m^3]	[%]	[m]	[m]	
DryLB_RD68	28/03/18	16.46	67.75	0.26	Not recorded	Test aborted early due to high cone resistance*
DryLB_RD00	03/04/18	14.42	-0.37	0.60	Not applicable	-
DryLB_RD50	04/04/18	15.86	49.43	0.60	Not recorded	-
DryLB_RD51	05/04/18	15.89	50.62	0.60	0.39	-
DryLB_RD18	06/04/18	14.91	17.59	0.60	0.40	-
DryLB_RD18b				0.60		Additional test 230 mm off-centre*
DryLB_RD18c				0.60		Additional test 180 mm off-centre*
DryLB_RD60_T1	10/04/18	16.36	60	0.60	0.40	-
DryLB_RD60_T2	18/04/18	16.35	59.8	0.60	0.40	-

Notes:
Sample preparation carried out by Iona Richards
* = Not used in calibrations

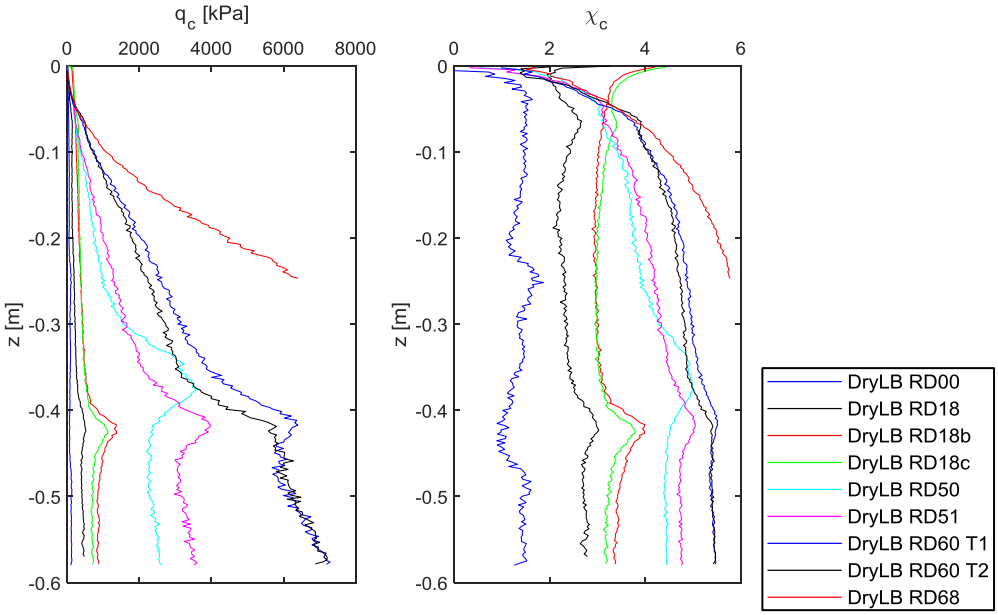

Figure C.3.2. Profiles of CPT cone tip resistance q_c and normalised cone resistance χ_c: Dry Leighton Buzzard 14/25 sand calibration tests

C.3.5 Bathgate psf Sand CPT Calibration Tests

Calibration CPTs were performed on Bathgate psf sand in dry and saturated conditions, with relative densities D_R ranging 7% to 66%. The tests were performed in a 450 mm internal diameter tank, which also allowed saturated sand tests to be performed.

For the loose tests the sand was prepared by either loose placement or by raining using a simple funnel. For the denser tests the sand was prepared by sequentially placing layers approximately 50 mm thick, then loading with a surcharge and applying vibration to densify the sample. Saturation was achieved by a siphon from a static head of water attached to the drainage channels incorporated in the base of the test tank, allowing the sand to saturate slowly with a low head difference (during saturation a rigid disc was clamped to the top of the tank to prevent volume changes).

The full list of tests performed is provided in Table C.3.3; Figure C.3.3 presents the q_c and χ_c profiles for the dry tests, and Figure C.3.4 presents the profiles for the saturated tests.

Table C.3.3. List of Calibration CPTs Performed on Bathgate psf Sand

Test ID	Date	Dry / Wet	ρ_{dry} [kg/m^3]	D_R [%]	Sand Preparation	Remarks
BG1-1D Loose	15/10/2018	Dry	-	-	Loose placement	Density not measured accurately
BG2-1D RD7	31/10/2018	Dry	1527	7.2	Loose placement	-
BG3-1D RD17	20/02/2019	Dry	1551	17.5	Funnel raining, from 0.5 m drop	-
BG4-1D RD66	21/02/2019	Dry	1670	66.2	Vibration, surcharge 4.6 kPa	-
BG5-1D RD62	22/02/2019	Dry	1658	61.6	Vibration, surcharge 2.5 kPa	-
BG6-1W RD62	04/03/2019	Wet	1660	62.4	Vibration, surcharge 9.9 kPa	-
BG6-2W RD62	04/03/2019	Wet				Repeat test off-centre
BG7-1D RD15	11/03/2019	Dry	1545	15.1	Funnel raining, from 0.5 m drop	Initial dry off-centre test
BG7-2D RD15	11/03/2019	Dry				Repeat test off-centre
BG7-3W RD15	12/03/2019	Wet				Test at centre
BG7-3Wr RD15	12/03/2019	Wet				Repeat test at exact location of previous
BG8-1D RD26	18/03/2019	Dry	1571	26.2	Funnel raining, from 1.0 m drop	Initial dry off-centre test
BG8-1Wr RD26	19/03/2019	Wet				Repeat test at exact location of previous
BG8-2W RD26	19/03/2019	Wet				Test at centre
BG8-2Wr RD26	19/03/2019	Wet				Repeat test at exact location of previous

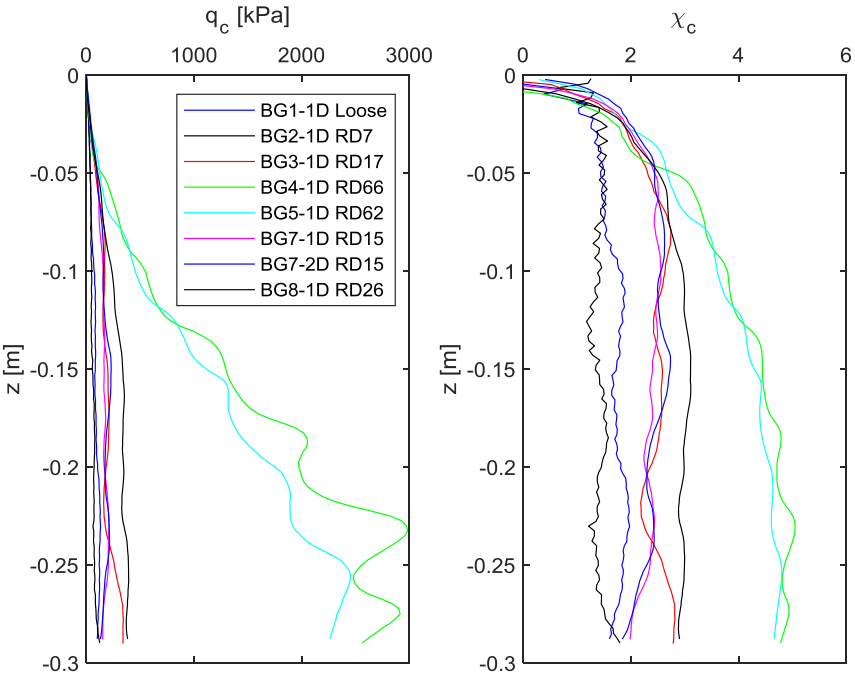

Figure C.3.3. Profiles of CPT cone tip resistance q_c and normalised cone resistance χ_c: Dry Bathgate psf sand calibration tests

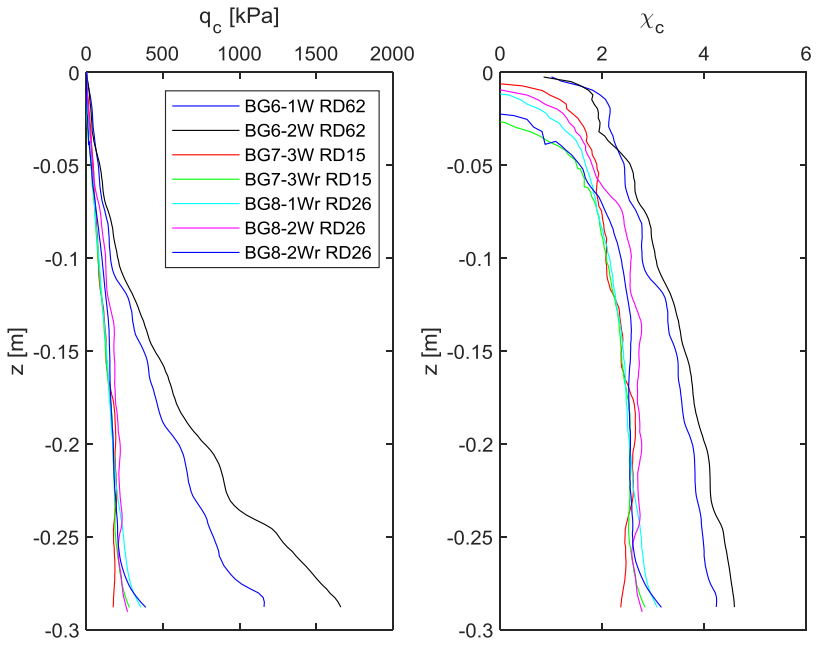

Figure C.3.4. Profiles of CPT cone tip resistance q_c and normalised cone resistance χ_c: Saturated Bathgate psf sand calibration tests

C.3.6 Relative Density Calibration Parameters

The proposed CPT relative density calibration method (Appendix C.3.3) assumes a linear relationship between D_R and the normalised cone resistance χ_c.

A representative value of the normalised cone resistance, $\bar{\chi}_c$, was taken as the mean value from the push for each CPT. Data from less than 0.12 m penetration was excluded to avoid the influence of alternative failure mechanisms at shallow depths, as well as the influence of noise on relatively low q_c measurements. Figure C.3.5 presents the resulting plot of D_R versus representative $\bar{\chi}_c$ for all CPT calibration tests. The results indicate that for the same relative density Leighton Buzzard 14/25 gives a higher cone resistance than Bathgate psf.

A least squares linear regression was performed on the dry Leighton Buzzard 14/25 and Bathgate psf tests to find the relative density fitting parameters in Table C.3.4, excluding off-centre and repeat tests from the analysis. Due to the limited number of saturated tests, the fitting parameters for saturated Bathgate psf were defined using the parameters for dry conditions with a correction for saturated conditions as described by Jamiolkowski et al. (2003).

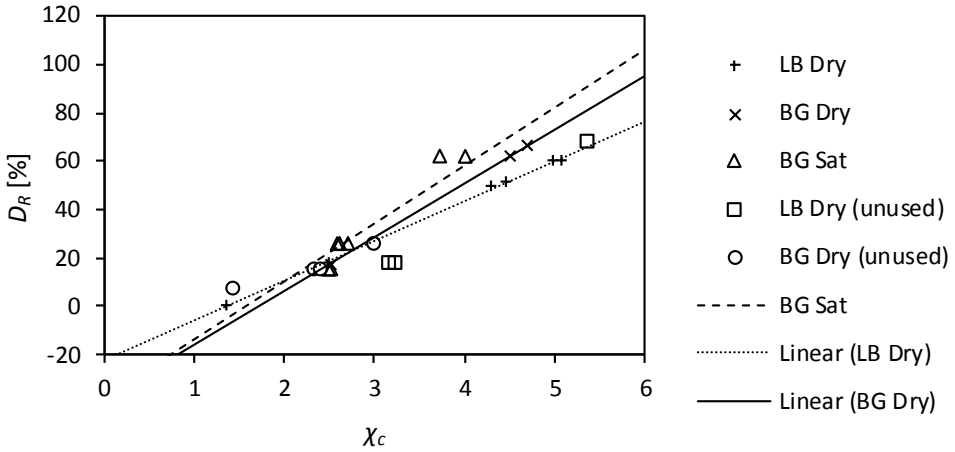

Figure C.3.5. CPT relative density values versus representative χ_c. LB indicates Leighton Buzzard 14/25 sand, BG indicates Bathgate psf sand; 'Dry' indicates dry sand, 'Sat' indicates saturated sand; hollow markers are not used in the calibration; 'linear' indicates linear regression results; 'BG Sat' line calculated as BG Dry fit with correction after Jamiolkowski et al. (2003).

Table C.3.4. Relative Density CPT Fitting Parameters

Soil Type	**Dry / Saturated**	α_1	α_2
		[%]	**[%]**
Leighton Buzzard 14/25 (coarse silica sand)	Dry	-22.39	16.48
Bathgate psf (fine silica sand)	Dry	-38.25	22.18
	Saturated	-37.53	23.97

C.3.7 Representative Soil Densities

Table C.3.5 presents a set of representative inferred soil densities for the flume experiments, using a representative value of measured normalised cone resistance χ_c and the calibration parameters for saturated Bathgate psf sand. The results show that for all tests the sand was consistently compacted to a very dense condition, as intended for the work.

Table C.3.5. Representative Soil Density Parameters – Flume Experiments

Test	$\overline{\chi}_c$	D_R	e	γ_{bulk}
	[-]	[%]	[-]	[kN/m^3]
1	5.296	89.4	0.5284	20.40
2	5.458	93.3	0.5186	20.47
3	5.755	100.4	0.5008	20.60
4	5.682	98.7	0.5051	20.56
5	5.596	96.6	0.5103	20.53
6	5.588	96.4	0.5108	20.52

C.4 Hydraulics During Scour Development

The scour development in the flume was generated using depth-averaged flow velocities, $\overline{U}$, between 0.35 m/s and 0.7 m/s (Table 8 in Paper 2), producing turbulent flow conditions (Reynolds Number = 5.6×10^4 to 1.1×10^5). Steady bow waves with heights of around 50 mm were observed at the upstream face of the monopile, and vortex shedding was observed downstream.

The frequency of vortex shedding was not directly measured during the tests, but was consistent with the expected range of 0.32 Hz to 0.64 Hz. This is a significant margin below the natural frequencies of the structure (> 2.6 Hz), and did not cause measurable vortex-induced-vibration effects. Turbulence associated by the vortex shedding is thought to have caused additional erosion downstream of the pile (e.g. Figure 2.1(a))

During the flow Phase 1a of Test 1 ($\overline{U}$ = 0.4 m/s) the vortex shedding frequency coincided with the frequency of a lateral seiche wave in the test section (section width = 4.0 m, water depth = 0.9 m). This caused a lateral wave to accumulate after around 20 minutes of flume flow with 50 mm height and frequency ≅ 0.38 Hz (described in the report by HR Wallingford, 2018). The loading of the monopile due to the seiche was negligible, however a small peak could be seen in the power spectral density during this flow phase. This was not accounted for in the test design, and the Phase 1a flow velocity was adjusted to $\overline{U}$ = 0.35 m/s for subsequent tests, which removed the phenomenon.

The drag force acting on the monopile during the flow phases is estimated to be in the range of 10 N to 50 N for the range of flow velocities and water depths in the flume experiments (assuming a drag coefficient of 1.0). During the flow the maximum displacements at the temposonics position sensor (located on the transition piece, see Table C.1.4) were approximately 100 μm, and the associated ground level displacements are estimated as less than 50 μm and rotations less than 0.005° (assuming limited bending of the monopile). These loads and displacements are small in comparison to the initial stage of the lateral loading tests (Figure 4.13), and are similar in magnitude to displacements in the structural dynamics testing (discussed in Appendix C.6.7). The effect on the soil response is expected to be negligible.

C.5 Bathymetry Data Analysis

C.5.1 Bathymetry Data Acquisition

The laser scanner bathymetry data were collected and processed by HR Wallingford (2018). This processing involved averaging the individual laser scan data points within 8 mm square bins, producing maps with 8 mm resolution. The general procedure and results of the bathymetry data analysis are discussed in Paper 3, further detail is provided here.

C.5.2 Bathymetry Asymmetry Analysis Method

To investigate asymmetry, the bed levels were calculated within selected subsets zones, illustrated in Figure C.5.1. The subset zones were defined based on the position clockwise from pile North, with subsets for East (45° to 135°), South (180° to 225°), West (225° to 315°), and North (315° to 360°). For the North and South subsets, the data East of the centreline were excluded, which is consistent with the analysis in Fig. 7 in Paper 3. The output bathymetry levels are presented in Appendix C.9.1.

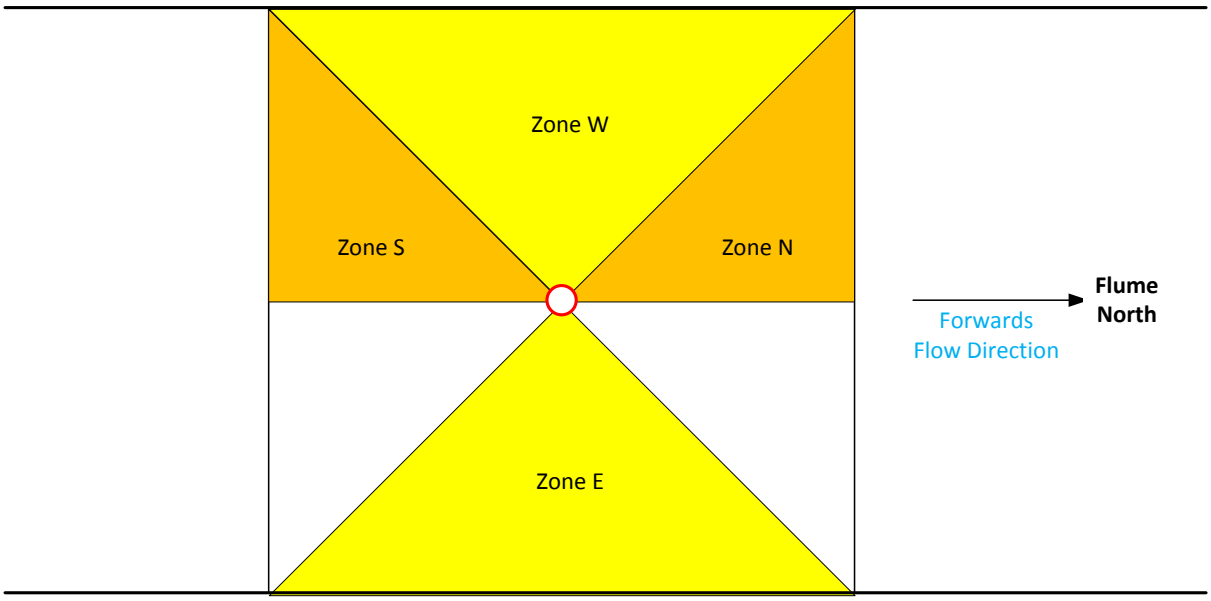

Figure C.5.1. Bathymetry data subset zones in the Fast Flow Facility

C.6 Impulse Test Analysis Method

C.6.1 Overview

The natural frequencies of the structure were determined using a time-domain method of interpreting the response to an impulse load, following structural dynamics principles of free vibration (e.g. Williams, 2016).

Figure C.6.1 presents an example of the acquired impulse data. In this example there is a permanent displacement in the order of 50 μm, which was believed to be caused by small movements of the reference scaffold frame for the temposonics position sensor, rather than a true displacement of the pile.

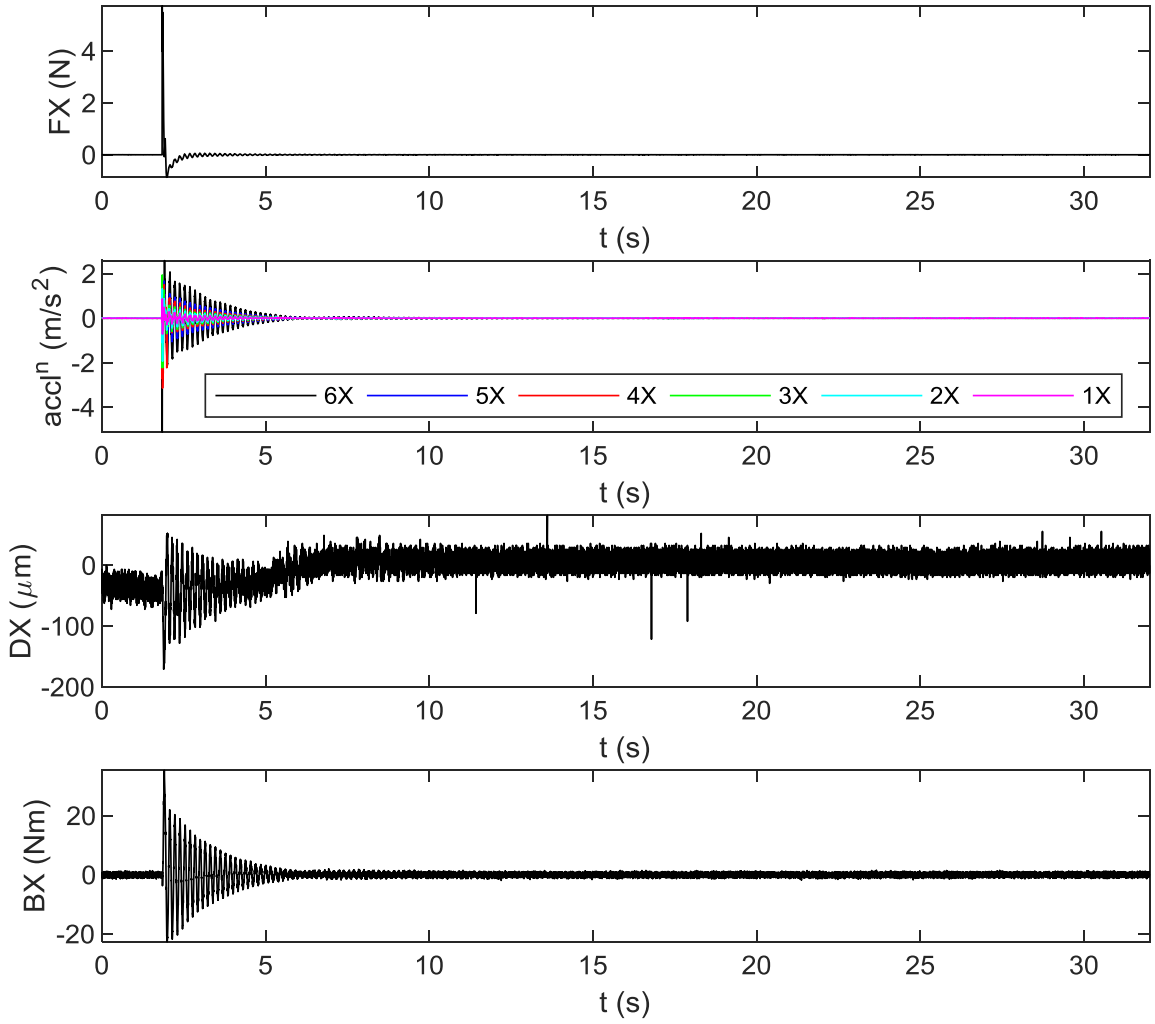

Figure C.6.1. Example impulse data – streamwise direction loading: Test 3 unscoured condition, no top masses (see Table C.1.4 for instrument label key; X indicates measurement in the streamwise direction, F indicates force sensor at the tower top, 6X is the uppermost accelerometer, 1X is the lowermost accelerometer, D indicates displacement, B indicates bending moment)

C.6.2 Damped Free Vibration Signals

Time-domain fitting of the impulse response measurements was performed using timeseries of load, acceleration and displacement starting after the impulse but before the signal had fully decayed. By excluding the impulse from the analysed signal the theoretical response for damped free vibration can be assessed, using SDOF and viscous damping assumptions (Williams, 2016). The response is governed by the equation of motion:

$$M\ddot{v}(t) + C\dot{v}(t) + Kv(t) = F(t) \tag{C.6.1}$$

For free vibration, $F(t) = 0$, with viscous damping, $C = 2\zeta\sqrt{K/M}$, the displacement v is,

$$v(t) = v_0 e^{-\zeta\omega_m t}\sin(\omega_m\sqrt{1-\zeta_m^2}t + \phi) \tag{C.6.2}$$

where v_0 is the initial displacement amplitude, ζ_m is the damping ratio, ω_m is the circular natural frequency, and ϕ is the phase. Acceleration $\ddot{v}$ is calculated as:

$$\ddot{v}(t) = -(\omega_m^2 v(t) + 2\zeta_m\omega_m\dot{v}(t)) \tag{C.6.3}$$

C.6.3 Signal Fitting Procedure

For a measured displacement or acceleration time-series signal s_{Meas} the parameters for defining the response (ω_m, ζ, v_0, ϕ) were fitted by minimising the error function ε_s,

$$\varepsilon_s = s_{fit} - s_{Meas} \tag{C.6.4}$$

where s_{fit} is approximated using the displacement or acceleration expressions (Appendix C.6.2). A least squares fitting method (*MATLAB* function *lsqnonlin*) was used to minimise ε_s.

The six acceleration signals in the direction of loading were analysed simultaneously, where the fitted parameters of ω_m, ζ_m, ϕ were common for all accelerometers, and v_0 was fitted individually to each accelerometer and the temposonics position sensor. Note that the direction of movement is captured in the sign of v_0 by forcing the phase ϕ to be consistent down the structure.

To allow analysis of the second and third mode of vibration, it is assumed that the signal comprises the superimposed response from several vibration modes, m (Williams, 2016),

$$s_{fit,\Sigma} = \sum_{m=1}^{N_m} s_{fit(m)} \tag{C.6.5}$$

To analyse the second mode (m = 2), the residual measured signal $s_{Meas}(m)$ after removal of the first mode was computed as follows:

$$s_{Meas}(m) = s_{Meas}(m-1) - s_{fit}(m-1) \quad \text{(C.6.6)}$$

The approach of calculating residuals and fitting was repeated for vibration modes 2 and 3, using data for approximately 20 cycles of signal at ω_m for each mode.

C.6.4 Example Impulse Signal Fitting Results

Figure C.6.2 presents an example time-domain fit of an impulse signal, using the method described (grey = s_m, black = $s_{fit(m)}$, green = $s_{fit,\Sigma}$). There is recurring high frequency noise in the mode 3 residual signals, as well as a residual signal at the frequency of modes 1 and 2. This noise is likely to be due to the free-hanging wires in the tower impacting on the inside of the tower or on the accelerometer mounts.

Figure C.6.3 presents an example time-domain fit using a smoothed version of the data from Figure C.6.2. The measured signals s were smoothed (using *MATLAB* function *smoothdata*, moving mean with window length of 30) to remove high frequency noise, with linear trends removed from displacement signals to eliminate drift for the analysis of mode 1. Linear trends were applied to remove drift from the residual acceleration and displacement signals for the analysis of modes 2 and 3. The fitted frequencies were almost identical using the unsmoothed (Figure C.6.2) and smoothed (Figure C.6.3) data.

Figure C.6.4 presents an example of the fitted mode 1 to 3 natural frequencies and damping ratio plotted against the number of top masses (N_M), using the smoothed signal fitting approach. The amount of scatter increases with the mode number, and there are apparent anomalous data points in mode 2 and 3 for the case of 3 and 6 top masses. The residual signals for these outliers (not shown) have a particularly large magnitude of the recurring high frequency noise in modes 2 and 3.

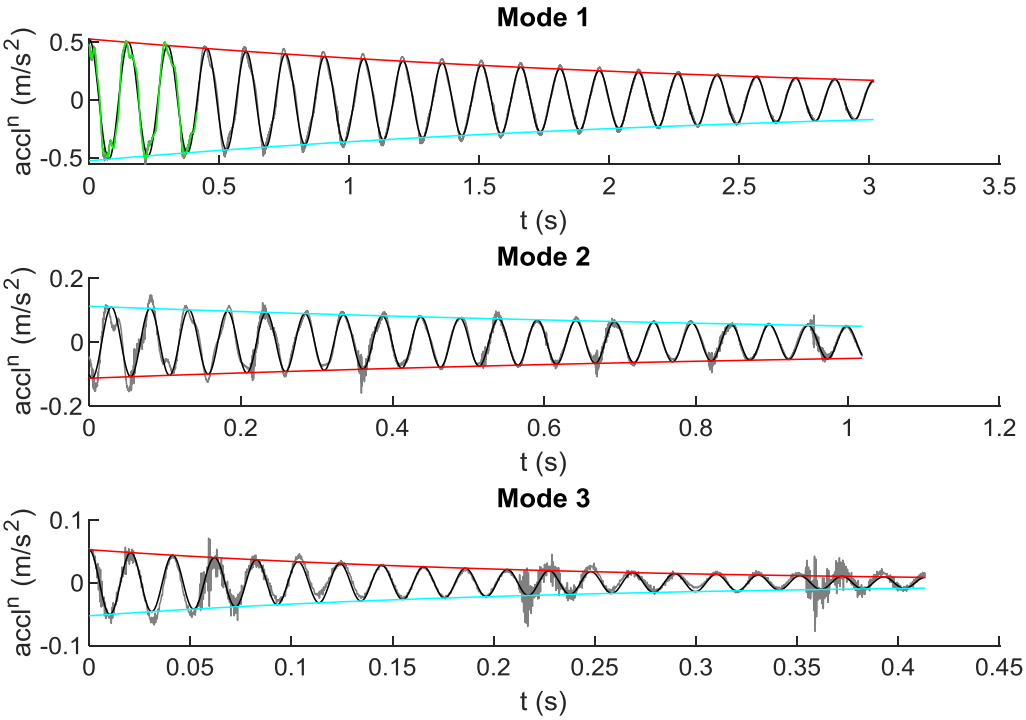

Figure C.6.2. Example impulse signal analysis with no signal smoothing: Test 3, no scour, no top masses, streamwise direction loading, top accelerometer; grey data is measured (residual for modes 2 and 3), black data is fitted, green data is cumulative fit for all modes, red and cyan are bound of the fitted logarithmic decay

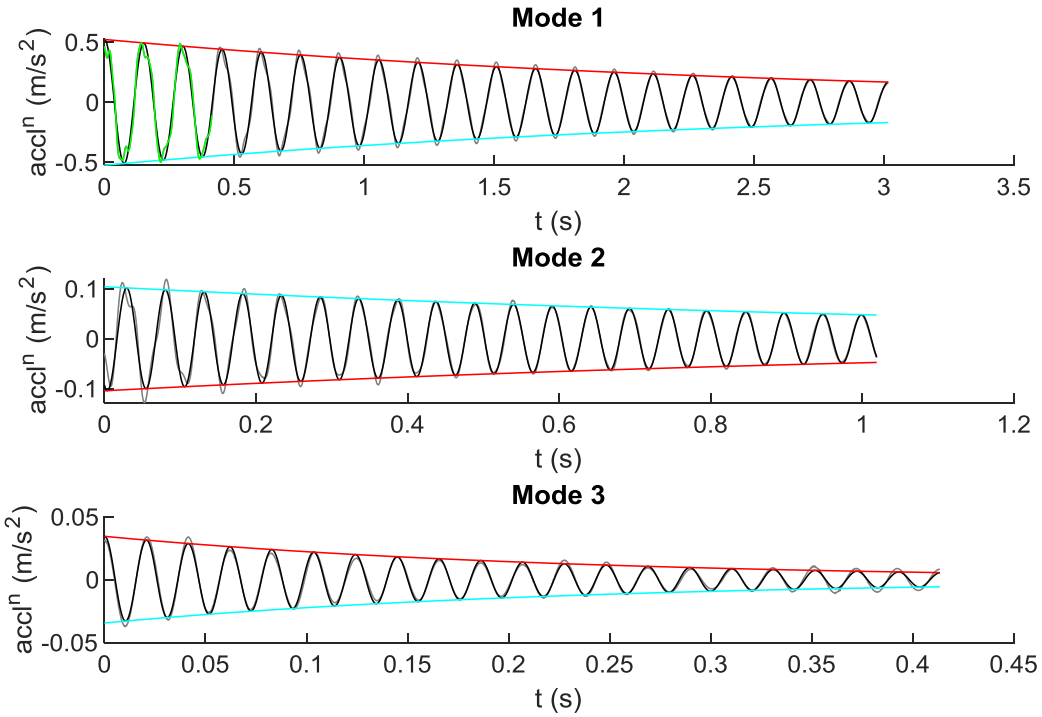

Figure C.6.3. Example impulse signal analysis with signal smoothing: Test 3, no scour, no top masses, streamwise direction loading, top accelerometer; grey data is measured (residual for modes 2 and 3), black data is fitted, green data is cumulative fit for all modes, red and cyan are bound of the fitted logarithmic decay

C.6.5 Quality of Fit

The quality of the fit for each mode was calculated following an R^2 approach using the acceleration signals,

$$R^2(m) = 1 - \frac{\sum\left(s_{Meas}(m) - s_{fit}(m)\right)^2}{\sum(s_{Meas}(m) - \overline{s_{Meas}}(m))^2} \quad \text{(C.6.7)}$$

where $\overline{s_{Meas}}$ is the mean measured signal.

An example of R^2 quality of fit data is presented in Figure C.6.5 (associated with the data in Figure C.6.4). Mode 1 consistently has a high quality of fit (R^2 close to 1). Ffor mode 2 the quality is lower (R^2 around 0.6 to 1, with outliers), and mode 3 has the lowest quality (R^2 around 0.2 to 0.9, with outliers). The lowest quality points in Figure C.6.5 (R^2 less than 0.2) are associated with mode 2 and 3 outliers in Figure C.6.4.

C.6.6 Selection of Mean Values

Finally a mean value of the fitted structural dynamics parameters (f_m, ζ_m) was calculated for each mode, for each top mass and bathymetry condition. Following an inspection of the results, data were excluded from the averaging if it fell outside of specified quality thresholds. The quality thresholds were defined to exclude low quality data where $R^2 < 0.2$, or if the damping ratio was outside of the typical range (specified as $\zeta < 0.11\%$ or $\zeta > 4\%$). Data were also excluded for repeat impulse tests taken after modal shaker tests, and impulses during partial draining of the FFF flume during Test 1.

C.6.7 Estimated Ground Level Displacements

The lateral displacements along the monopile – tower structure during the impulse tests were not explicitly analysed from the test data, however the data in Figure C.6.1 were typical and can be considered for a brief assessment of the soil strain levels. In this dataset the peak acceleration amplitude is at the top of the tower (6X in Figure C.6.1) is approximately 2 m/s^2 (displacement amplitude 1.2 mm for the inferred frequency f_1 = 6.6 Hz), and the peak displacement amplitude at the temposonics position sensor (DX in Figure C.6.1) is approximately 0.1 mm.

The displacements at and below ground level can be estimated using the mode shape results output from the *EigPile* numerical analysis (e.g. Figure 4.6), giving peak ground level displacements of less than 10 μm. The ground level displacements produce strains in the soil with an order of magnitude around 10^{-5} to 10^{-4}, with the greatest strain levels occurring close to ground level and diminishing with depth. Similar estimates can be made for mode 2 ground level displacements as less than 1 μm and for mode 3 ground level displacements as less than 0.1 μm, with lower strain levels accordingly. These strain levels are at or close to the region where the soil response can be assumed as elastic, for example by considering the degradation of G_0 with strain illustrated in Figure 1.15.

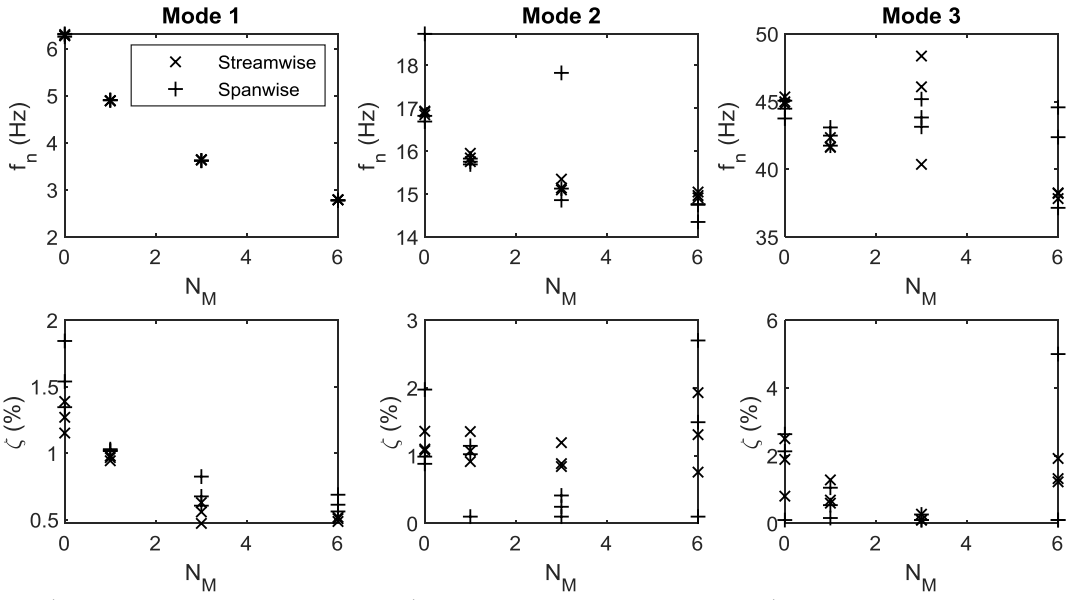

Figure C.6.4. Example natural frequency and damping ratio for modes 1 to 3 plotted against top mass: Test 1, partial scour

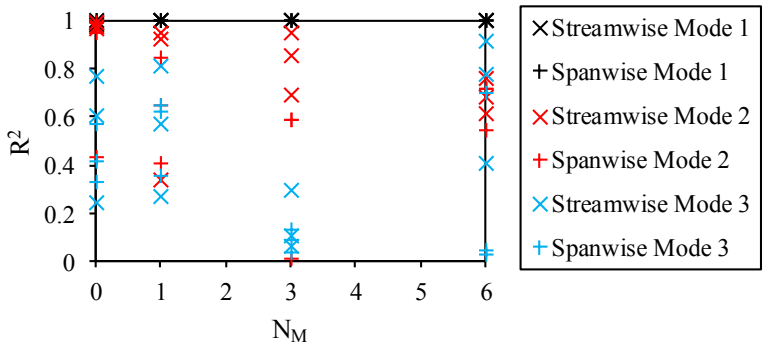

Figure C.6.5. Example R^2 quality of fit plotted against top mass: Test 1, partial scour

C.7 Frequency Sweep Analysis Method

C.7.1 Frequency Sweep Testing Method

In the frequency sweep tests, sinusoidal loads were applied to the structure at frequencies ω_F close to the estimated natural frequency from impulse tests. The testing procedure involved the following steps, controlled through the *LabVIEW* code:

i. User input of the estimated natural frequency of modes 1, 2 and 3 (based on the power spectral density peaks of the previous impulses)

ii. Select evenly spaced loading frequencies ω_F below and above the estimated natural frequency (from i.), where the frequency range took typical values of +/- 7.5% for mode 1, and +/- 15% for mode 2 and 3 (typically 11 loading frequencies were used)

iii. Generate a sinusoidal signal at the first loading frequency (ω_F), with a low amplitude

iv. Ramp the amplitude until the measured peak force reaches a target value

v. Hold the amplitude for 50 cycles of loading, log the data and stop generating the signal

vi. Repeat iii. to v. for all the selected loading frequencies from step ii.

C.7.2 Background – Frequency Response Function

The analysis of the frequency sweep data requires two stages: (1) fitting to the measured sinusoidal signals, and (2) a modal analysis of the complex frequency response function (FRF). Figure C.7.1 illustrates the real and imaginary components of the FRF for single and multiple degree of freedom systems. The theoretical FRF, H, for a SDOF system with viscous damping is (Ewins, 2000),

$$H = Ae^{i\phi} = A(\sin\phi + i\cos\phi) \tag{C.7.1}$$

where A is the accelerance and ϕ is the phase difference between force and displacement;

$$A = -v_0 DAF \omega_F^2 \tag{C.7.2}$$

$$DAF = \frac{1}{\sqrt{(1-\Omega^2)^2 + (2\zeta\Omega)^2}} \tag{C.7.3}$$

$$\tan\phi = \frac{2\zeta_m\Omega}{1-\Omega^2} \quad \text{and} \quad \Omega = \frac{\omega_F}{\omega_m} \tag{C.7.4}$$

where v_0 is the displacement amplitude, DAF is the dynamic amplification factor, and Ω is the harmonic frequency ratio.

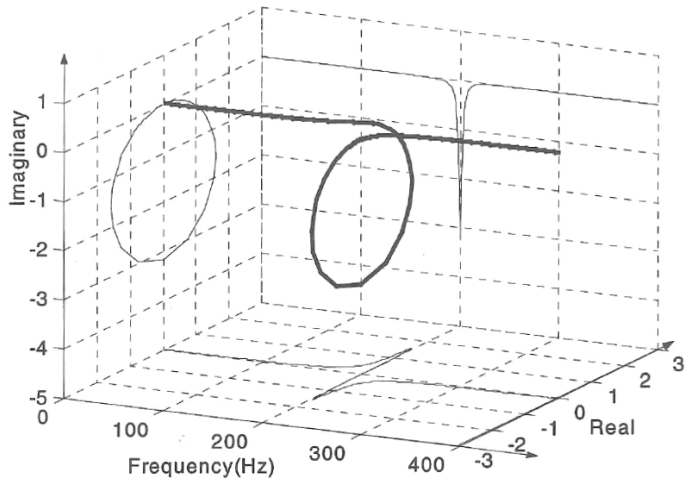

(a)

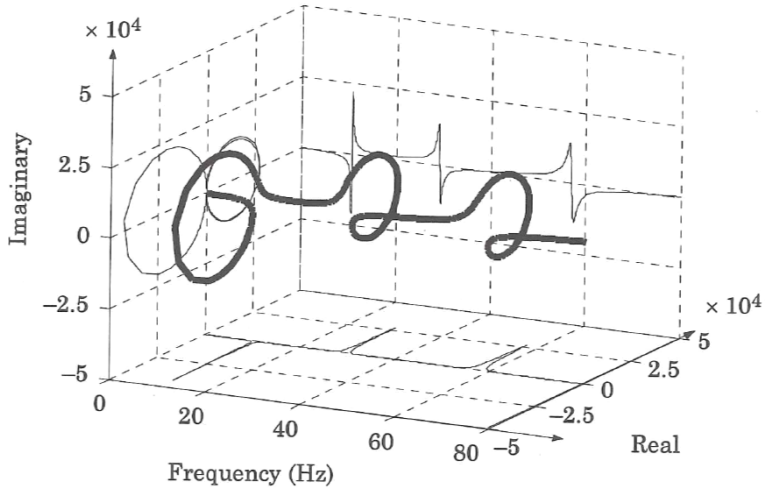

(b)

Figure C.7.1. Three-dimensional frequency response functions (from Ewins, 2000). (a) Single degree of freedom system; (b) Multiple degree of freedom system.

C.7.3 Harmonic Signal Fitting

The measured signals $s_{Meas}(t)$ were analysed over 50 cycles at loading frequency ω_F to identify the amplitude (s_0) phase (ϕ_s) and offset (s_{off}) for each signal:

$$s_{fit}(t) = s_0(\omega_F)\sin\big(\omega_F t + \phi_s(\omega_F)\big) - s_{off}(\omega_F) \tag{C.7.5}$$

The signals were fitted using a least squares method by minimising the following expression (using *MATLAB* function *fminsearch* for each signal):

$$SS = \frac{\sum\left(s_{Meas}(t) - s_{fit}(t)\right)^2}{\sum(s_{Meas}(t) - \overline{s_{Meas}})^2} \tag{C.7.6}$$

Figure C.7.2 and Figure C.7.3 present examples of the harmonic sine signal fitting for loading frequencies near mode 1 and 2 respectively; acceleration is plotted in the logged units of g (1g = 9.81 m/s^2).

The signals for mode 1 (Figure C.7.2) generally have more noise, that is neglected during the fitting process. The measured accelerations for mode 1 are sinusoidal, but the measured force includes components at higher frequencies; it is expected that this is due to loading the structure at the point of maximum displacement (i.e. lowest stiffness) for mode 1.

For mode 2 (Figure C.7.3) the measured displacement is the only signal with significant noise not represented by the fit.

C.7.4 Fitted Frequency Response Function

The measured FRF was calculated for each of the frequency sweeps, and fitted using the theoretical FRF for an equivalent single degree of freedom system. Only signals from the accelerometers in the direction of loading were used. For each loading frequency (ω_F) the measured accelerance (A_{Meas}) was calculated from the acceleration amplitude ($\ddot{v}_0$) and force amplitude (F_0) from the harmonic signal fitting (Ewins, 2000),

$$A_{Meas}(\omega_F) = \ddot{v}_0(\omega_F)/F_0(\omega_F) \tag{C.7.7}$$

The measured FRF (H_{Meas}) was then calculated,

$$H_{Meas} = A_{Meas}e^{i\phi_{Meas}} \tag{C.7.8}$$

where ϕ_{Meas} is the phase difference.

The theoretical single degree of freedom response H requires a complex offset to be applied in order to achieve a good fit of H_{Meas}; this is to account for residual parts of the response to modes of vibration other than that being tested (e.g. Figure C.7.1(b)). These residual FRF components were assumed to be constant within the testing range and to cause no distortion of the FRF. The complex offset was applied using real and imaginary components (α_1 and α_2),

$$H_{fit} = H' + (\alpha_1 + \alpha_2 i) \tag{C.7.9}$$

A prime has been used in the notation to indicate the equivalent SDOF values of the FRF (H'). For the analysis of each frequency sweep there are 5 fitting parameters (ω_m, ζ_m, v_0, α_1, α_2), with ω_m and ζ_m assumed constant for all accelerometers. The parameters were fitted using a least squares method (*MATLAB* function *lsqnonlin*) to minimise the error εH,

$$\varepsilon H = H_{fit} - H_{Meas} \tag{C.7.10}$$

(Note: εH is complex; to avoid complex solutions from *lsqnonlin*, εH was stored as an array with two columns to handle the real and imaginary components)

In the fitting, data were excluded if the force amplitude $F_0(\omega_F)$ was below a threshold (selected as 0.01 N). The signals of all accelerometers in a data set were analysed using consistent values of ω_m and ζ_m, selected based on fitting the signal with the greatest amplitude for the mode of vibration and top mass configuration:

i. Mode 1 used accelerometer 6 (top most)
ii. Mode 2 used accelerometer 6 for no top mass or accelerometer 3 with top mass
iii. Mode 3 used accelerometer 6 for no top mass or accelerometer 5 with top mass

C.7.5 Quality of Fit

The quality of the fitted FRF H_{fit} was quantified using the expression,

$$\varepsilon H_{norm} = \frac{\frac{1}{N_F}\sum\left|Re\left(\varepsilon H(\omega_F)\right).Im\left(\varepsilon H(\omega_F)\right)\right|}{H_{ref}} \tag{C.7.11}$$

where N_F is the number of loading frequencies and H_{ref} is a reference value,

$$H_{ref} = \frac{1}{N_F}\left(\sum[\mathrm{Re}(H_{Meas}) + \mathrm{Im}(H_{Meas})i]\right) - H_{Meas} \tag{C.7.12}$$

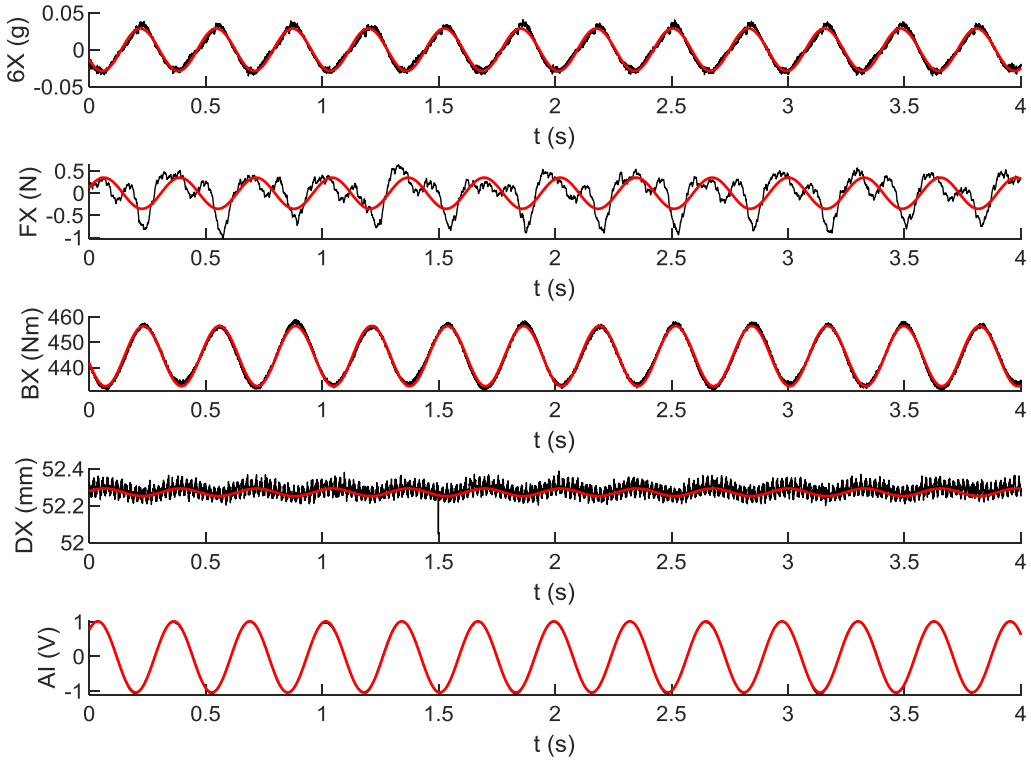

Figure C.7.2. Example mode 1 harmonic signals: Test 3, no scour, 6 masses, loading frequency = 3.063 Hz, streamwise loading; black indicates measured signals, red indicates sinusoidal fit (see Table C.1.3 for instrument labels relating to vertical axes)

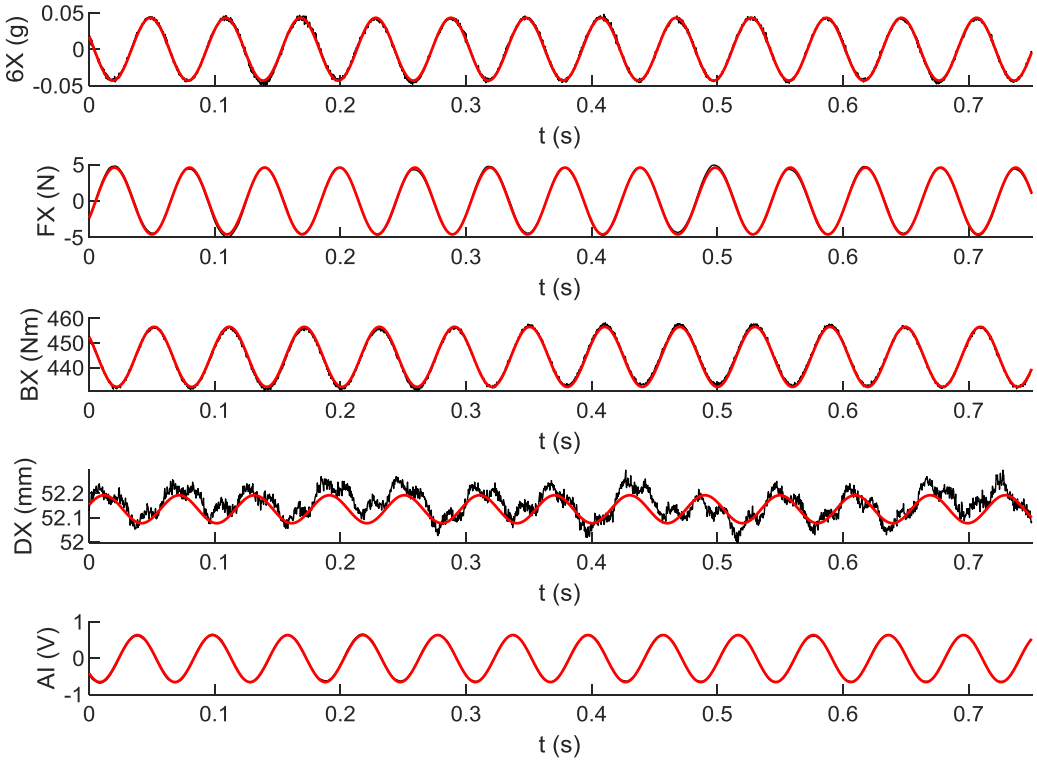

Figure C.7.3. Example mode 2 harmonic signals: Test 3, no scour, 6 masses, loading frequency = 16.73 Hz, streamwise loading; black indicates measured signals, red indicates sinusoidal fit (see Table C.1.3 for instrument labels relating to vertical axes)

C.7.6 Example Results

The measured FRF H_{Meas} for each accelerometer was converted to an equivalent SDOF H'_{Meas}, for comparison of results between accelerometers,

$$H'_{Meas} = H_{Meas} - (\alpha_1 + \alpha_2 i) \tag{C.7.13}$$

For this equivalent SDOF system the measured accelerance A'_{Meas} and phase difference ϕ'_{Meas},

$$A'_{Meas}(\omega_F) = \sqrt{\mathrm{Re}(H'_{Meas}(\omega_F))^2 + \mathrm{Im}(H'_{Meas}(\omega_F))^2} \tag{C.7.14}$$

$$\phi'_{Meas}(\omega_F) = \tan^{-1}\left(\frac{\mathrm{Im}\left(H'_{Meas}(\omega_F)\right)}{\mathrm{Re}\left(H'_{Meas}(\omega_F)\right)}\right) \tag{C.7.15}$$

A final stage of processing produced a normalised version of the equivalent SDOF FRF $H'_{Meas,norm}$,

$$H'_{Meas,norm} = H'_{Meas}/A'_{max} \tag{C.7.16}$$

where A'_{max} is the maximum accelerance of the equivalent SDOF system,

$$A'_{max} = v_0\left(\frac{\omega_m^2}{2\zeta_m\sqrt{1-\zeta_m^2}}\right) \tag{C.7.17}$$

Figure C.7.5 and Figure C.7.6 present examples of the FRF fitting for mode 1 and 2 respectively. Figure C.7.4 presents the layout of these FRF results figures.

The ground level displacements, and associated strain in the soil, are estimated to be of a similar order of magnitude to the impulse tests discussed in Appendix C.6.7.

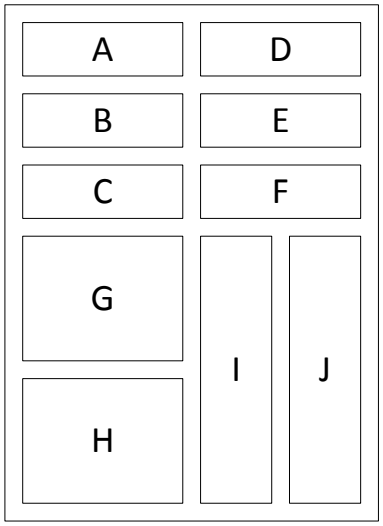

A. Acceleration amplitudes A'_{Meas} vs. loading frequency f_F
B. Phase difference ϕ'_{Meas} vs. f_F
C. Fit error εH vs. f_F
D. Load amplitude F_0 vs. f_F
E. Bending and displacement amplitude vs. f_F
F. Signal to noise ratio vs. f_F
G. Measured modal circle H_{Meas} real vs. imaginary
H. Normalised modal circle $H'_{Meas,norm}$ real vs. imaginary
I. Mode shape z vs. v_0/F_0
J. Fit error z vs. εH_{norm}

See Table C.1.3 for instrument label key

Figure C.7.4. Layout of frequency sweep results subfigures in Figure C.7.5 and Figure C.7.6

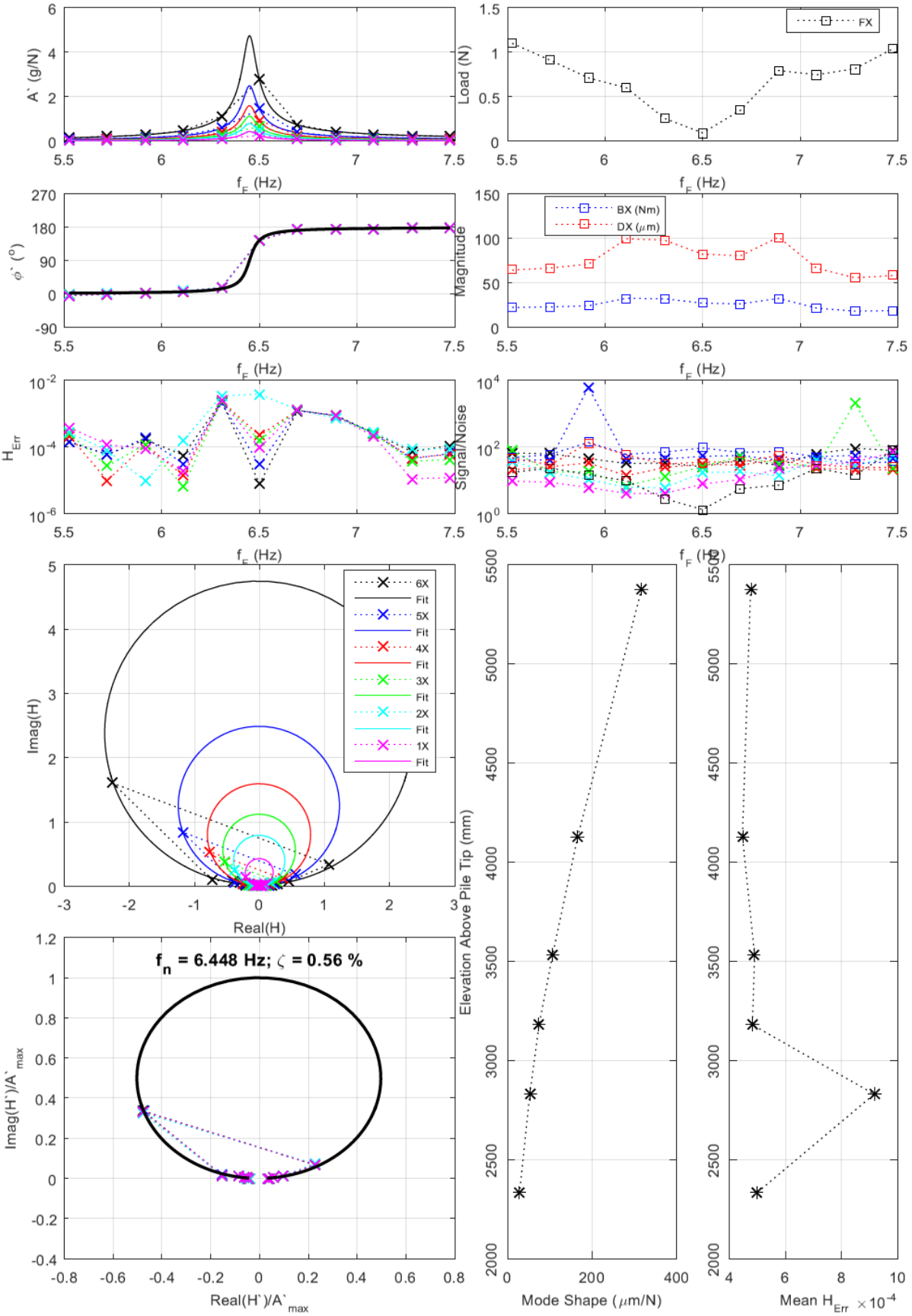

Figure C.7.5. Example mode 1 response function fitting: Test 1, no scour, 0 masses, streamwise loading (see Figure C.7.4 for description of subfigures)

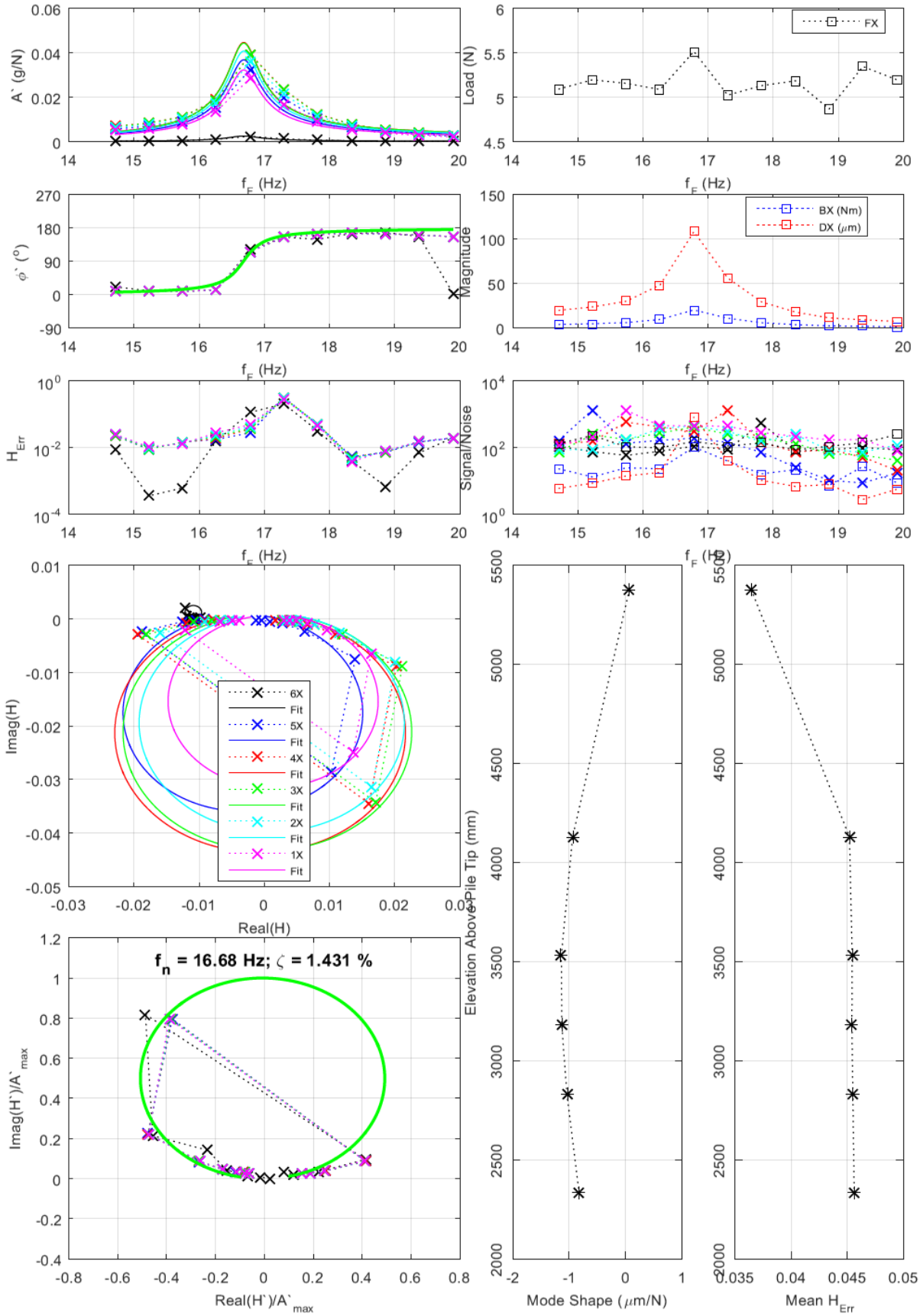

Figure C.7.6. Example mode 2 response function fitting: Test 1, no scour, 6 masses, streamwise loading (see Figure C.7.4 for description of subfigures)

C.8 Monotonic Lateral Loading Testing and Analysis

C.8.1 Equipment

Figure C.8.1 presents the setup of the monotonic loading equipment attached to the pile. For the monotonic loading tests a collar was attached around the top set of bolts of the pile transition piece, such that the load was carried by the pile without loading the tower (which had a lower strength).

An actuator powered by a motor was used to pull the pile at a constant rate of displacement of 8 mm/min at the height of load application. This rate of displacement was intended to provide an approximate rate of displacement at ground level of D/100 (i.e. 2 mm/min), by assuming that the target scour depths had been achieved and the pile would pivot at a depth below ground of approximately 70% of its embedded length. The motor and actuator were attached to a separate scaffold truss crossing the flume to the South of the pit section. A load cell on the actuator was attached to the pile collar by a steel cable. Data were logged at 1613 Hz.

The monotonic loading equipment and *LabVIEW* data acquisition code were developed by Ross McAdam and Brian Sheil.

C.8.2 Data Pre-processing

Initial processing of the monotonic loading data consisted of (i) smoothing the data using a filter window size of 1000 samples (0.62 seconds), and (ii) downsampling by a ratio of 200. Additional processing was performed for some tests to fix specific problem data:

- Low frequency noise was present in the signal of the top LVDT (z = 2.4 m) in Tests 1 and 2. These data were smoothed (using *MATLAB* function *smooth*, window = 82 samples ≈ 10 seconds).
- During Test 2 the LVDT voltage periodically stepped up and back down during the test. This was addressed by applying a corrective offset (0.415 mm, 0.027 V) to the affected data segments, and subsequently smoothing the data (using *MATLAB* function *smooth*, window = 82).
- During Test 3 there were fluctuations in the LVDT and H measurements near the start of the test (H < 200 N), due to a slightly loose attachment of the monopile to the loading actuator. This was addressed by smoothing the LVDT data (*MATLAB* function *smooth*, window = 82).

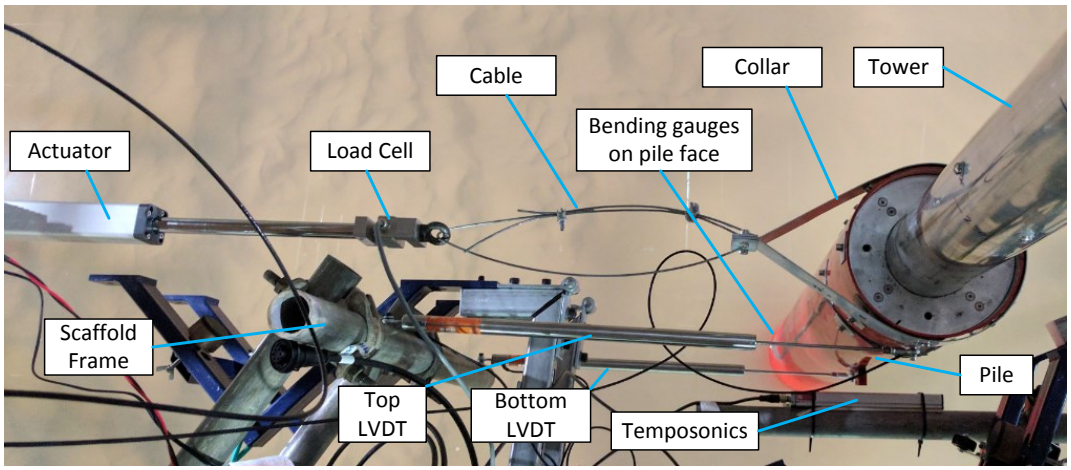

Figure C.8.1. Photograph of the monotonic loading equipment setup

C.8.3 Analysis Method

The analysis of ground level displacements follows the methodology adopted for the analysis of field tests in the PISA JIP (Burd et al., 2019), which used Timoshenko beam theory. Displacement measurements from the LVDTs were used to calculate the ground level ($z' = 0$) displacement, v_G, rotation of the pile neutral axis, θ_G, and rotation of the pile cross-section, ψ_G. The lever arm, h, is defined relative to the median local bed level from the bathymetry analysis (Paper 3). For the applied loading (Figure 2.23), the bending moment, M, and shear, V, in pile above soil level are,

$$M = H(h - z') \tag{C.8.1}$$

$$V = H \tag{C.8.2}$$

Figure C.8.2 presents the kinematics governing Timoshenko beam theory (after Burd, 2018), where θ is the rotation of the pile neutral axis (clockwise negative), and ψ is the rotation of the pile cross-section (clockwise positive). These kinematic relationships are,

$$w(y', z') = w_0 + \psi(z')y' \tag{C.8.3}$$

$$v(y', z') = v_0(z') \tag{C.8.4}$$

where w and v are the vertical and lateral displacements respectively at a point in the pile.

The adopted sign convention in Figure C.8.2 implies the moment and shear force definitions,

$$\frac{M}{EI} = -\frac{d\psi}{dz'} \tag{C.8.5}$$

$$\frac{V}{\kappa AG} = +\gamma_{yz} = +\frac{\partial w}{\partial y'} + \frac{\partial v}{\partial z'} = \psi + \theta \tag{C.8.6}$$

where κ is the shear coefficient for Timoshenko beam theory. Combining the previous relationships

gives expressions for rotation of the pile neutral axis, θ, and lateral displacements, v,

$$\frac{M}{EI} = -\frac{d\psi}{dz'} = -\frac{d}{dz'}\left[\frac{V}{\kappa AG} - \theta\right] \qquad \text{therefore} \qquad \frac{d\theta}{dz'} = \frac{M}{EI} + \frac{d}{dz'}\left[\frac{V}{\kappa AG}\right] \tag{C.8.7}$$

$$\theta = \int \frac{M}{EI}dz' + \frac{V}{\kappa AG} = \int \frac{H(h-z')}{EI}dz' + \frac{H}{\kappa AG} = \left(\frac{H}{EI}\right)\left(hz' - \frac{z'^2}{2}\right) + \frac{H}{\kappa AG} - \psi_G \tag{C.8.8}$$

$$v = \int \theta\, dz' = \left(\frac{H}{EI}\right)\left(\frac{hz'^2}{2} - \frac{z'^3}{6}\right) + \left(\frac{H}{\kappa AG} - \psi_G\right)z' + v_G \tag{C.8.9}$$

Using the two measured LVDT displacements v_1 and v_2 at elevations of z'_1 and z'_2, this is solved to find θ_G and v_G,

$$v_2 - v_1 = \left(\frac{H}{EI}\right)\left(\frac{h(z'^2_2 - z'^2_1)}{2} - \frac{(z'^3_2 - z'^3_1)}{6}\right) + \left(\frac{H}{\kappa AG} - \psi_G\right)(z'_2 - z'_1) \tag{C.8.10}$$

$$\frac{H}{\kappa AG} - \psi_G = \theta_G = \frac{\left(\frac{H}{EI}\right)\left(\frac{h(z'^2_2 - z'^2_1)}{2} - \frac{(z'^3_2 - z'^3_1)}{6}\right) + v_1 - v_2}{z'_1 - z'_2} \tag{C.8.11}$$

$$v_1 + v_2 = \left(\frac{H}{EI}\right)\left(\frac{h(z'^2_1 + z'^2_2)}{2} - \frac{(z'^3_1 + z'^3_2)}{6}\right) + \left(\frac{H}{\kappa AG} - \psi_G\right)(z'_1 + z'_2) + 2v_G \tag{C.8.12}$$

$$v_G = \left(\frac{H}{EI}\right)\left(\frac{(z'^3_1 + z'^3_2)}{12} - \frac{h(z'^2_1 + z'^2_2)}{4}\right) - \theta_G\frac{z'_1 + z'_2}{2} + \frac{v_1 + v_2}{2} \tag{C.8.13}$$

The shear terms drop out of the solutions for θ_G and v_G, given these shear terms are constant above ground and are accounted for as a constant increase in the ground level pile neutral axis rotation θ_G.

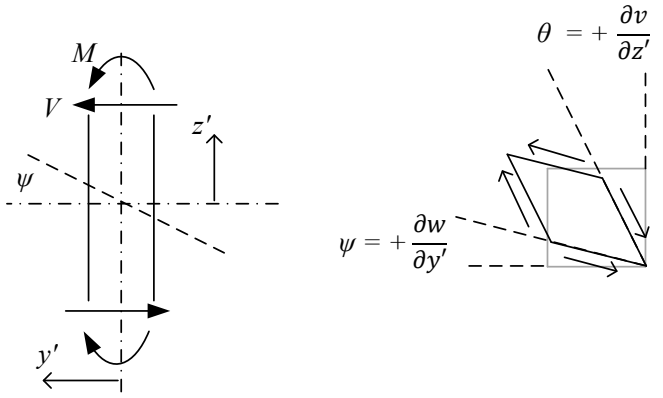

Figure C.8.2. Timoshenko beam theory; kinematics and adopted sign conventions

C.9 Results Tables

C.9.1 Scour Depth Results Table

Table C.9.1. Median Local and Global Bed Levels

		Median Local Bed Level					Median Global Bed Level				
Subset Zone		**-**	**N**	**S**	**W**	**E**	**-**	**N**	**S**	**W**	**E**
Min angle		**180**	**315**	**180**	**225**	**45**	**180**	**315**	**180**	**225**	**45**
Max angle		**360**	**360**	**225**	**315**	**225**	**360**	**360**	**225**	**315**	**225**
FFF Test[a]	T_f [b] **[mins]**	$\frac{z}{D}$	$\frac{z}{D}$	$\frac{z}{D}$	$\frac{z}{D}$	$\frac{z}{D}$	$\frac{z}{D}$	$\frac{z}{D}$	$\frac{z}{D}$	$\frac{z}{D}$	$\frac{z}{D}$
1	0	4.52	4.53	4.51	4.52	4.53	4.56	4.58	4.49	4.56	4.43
	166	3.65	3.76	3.66	3.62	-	4.54	4.56	4.52	4.54	-
	498	2.97	3.12	2.88	2.97	3.03	4.41	4.36	4.61	4.39	-
	996	2.49	-	2.49	2.70	1.92	4.31	4.05	4.48	4.30	-
	1494	2.89	2.92	2.91	2.86	2.92	4.05	4.18	3.88	4.16	-
	1992	2.24	2.26	2.20	2.24	2.13	3.99	3.40	4.14	4.28	-
2 (R-TFN)	0	4.57	4.57	4.57	4.55	4.53	4.61	4.58	4.60	4.64	-
	83	3.95	3.97	4.08	3.92	3.95	4.61	4.58	4.61	4.64	-
	498	3.03	3.18	2.90	3.01	3.00	4.52	4.36	4.59	4.53	-
	498 [c]	4.26	4.39	4.21	4.20	-	4.52	4.36	4.59	4.54	-
	996	3.85	3.81	-	3.89	-	4.42	4.15	4.42	4.53	-
	1494	3.75	-	3.79	3.68	-	4.22	4.26	3.95	4.41	-
	1992	3.81	3.83	3.61	3.76	4.02	4.18	3.94	4.18	4.29	-
3 (R-RF1)	0	4.64	4.64	4.64	4.63	4.65	4.57	4.56	4.58	4.58	-
	498	3.08	3.26	2.99	3.07	3.02	4.36	4.31	4.48	4.33	-
	498 [c]	3.89	3.79	4.18	3.91	3.89	4.36	4.31	4.48	4.33	-
	996	3.86	3.79	4.05	3.87	3.85	4.33	4.32	4.32	4.37	-
	1494	3.86	3.78	4.04	3.86	3.88	4.34	4.32	4.31	4.41	-
	1992	3.87	3.81	4.03	3.86	3.84	4.27	4.29	4.16	4.38	-
4 (R-RF2)	0	4.56	4.58	4.56	4.56	4.58	4.55	4.57	4.56	4.55	-
	166	3.88	4.03	3.87	3.85	3.95	4.56	4.58	4.57	4.55	-
	166 [c]	4.42	4.47	4.38	4.43	4.35	4.56	4.58	4.57	4.55	-
	664	4.32	4.36	4.08	4.32	4.34	4.41	4.33	4.33	4.52	-
	1162	3.97	3.82	3.98	3.99	3.88	4.26	4.28	3.99	4.43	-
	1660	3.83	3.82	3.65	3.85	3.80	4.18	4.01	4.15	4.34	-
5 (P-RA)	0 [c]	4.85	4.86	4.84	4.85	4.88	4.57	4.61	4.56	4.57	-
	498	4.85	4.86	4.84	4.83	4.86	4.43	4.37	4.41	4.55	-
	996	4.84	4.88	4.84	4.83	-	4.43	4.52	4.33	4.59	-
	1494	4.84	4.89	4.85	4.83	4.82	4.36	4.18	4.51	4.52	-
	1992	4.84	4.86	4.85	4.82	4.80	4.11	3.99	4.04	4.34	-
6 (R-RF3)	0	5.63	5.63	5.64	5.62	5.64	5.61	5.62	5.59	5.61	-
	166	4.89	5.00	4.84	4.87	4.94	5.63	5.62	5.61	5.64	-
	498	4.10	4.20	3.99	4.07	-	5.46	5.29	5.62	5.45	-
	498 [c]	5.12	5.07	5.10	5.14	-	5.46	5.29	5.62	5.45	-
	966	5.09	5.04	5.08	5.11	-	5.33	5.06	5.46	5.47	-
	1494	5.09	-	-	5.09	-	5.13	5.14	5.07	5.31	-
	1992	5.06	5.03	5.02	5.09	-	4.80	4.49	4.82	5.04	-
	2490	5.05	5.02	5.03	5.07	-	4.06	4.03	4.01	4.15	-
	2988	5.05	5.02	5.04	5.07	4.89	3.82	3.64	3.84	3.86	-

[a] Test matrix is provided in Table 3 in Paper 3
[b] T_f is elapsed flow time (see Paper 3)
[c] indicates first measurement after installing scour protection

C.9.2 Structural Dynamics Results Tables (Impulse Tests)

Table C.9.2 to Table C.9.4 provide the full set of mean natural frequency and damping results for modes 1 to 3. Due to the exclusion criteria (described in Appendix C.6) there is one data point missing for mode 2 and five data points missing for mode 3.

Table C.9.2. Mode 1 Mean Natural Frequency and Damping (Impulse Tests)

Parameter		f_m				ζ_m			
Num. Top Masses:		0	1	3	6	0	1	3	6
FFF Test[a]	T_f [b] [mins]	[Hz]	[Hz]	[Hz]	[Hz]	[%]	[%]	[%]	[%]
1	0	6.499	5.029	3.718	2.846	1.57	0.79	0.48	0.51
	166	6.285	4.899	3.630	2.785	1.42	0.99	0.63	0.56
	498	5.958	4.706	3.532	2.716	1.75	1.37	0.77	0.75
	996	5.845	4.630	3.472	2.679	1.78	1.50	0.97	0.84
	1494	5.878	4.647	3.481	2.686	2.02	1.56	1.08	0.86
	1992	5.740	4.587	3.451	2.668	1.70	1.26	0.92	0.80
2 (R-TFN)	0	6.532	5.034	3.709	2.846	2.25	2.13	1.38	1.31
	83	6.419	4.960	3.668	2.812	2.13	2.13	1.26	1.32
	498	6.149	4.791	3.575	2.741	2.48	2.18	1.55	1.25
	498 [c]	6.167	4.791	3.567	2.739	2.24	2.14	1.25	1.28
	996	6.159	4.818	3.585	2.745	2.74	2.03	1.35	1.40
	1494	6.166	4.747	3.582	2.753	2.60	2.04	1.32	1.28
	1992	6.182	4.825	3.596	2.755	2.70	2.27	1.41	1.45
3 (R-RF1)	0	6.593	5.077	3.755	2.863	1.01	0.97	0.88	1.06
	498	6.189	4.867	3.639	2.774	0.93	0.77	1.10	0.99
	498 [c]	6.236	4.886	3.654	2.786	1.25	1.07	1.17	1.28
	996	6.367	4.949	3.685	2.812	1.37	1.15	1.44	1.27
	1494	6.297	4.907	3.649	2.799	1.45	1.19	1.20	0.98
	1992	6.309	4.910	3.656	2.797	1.43	1.27	1.15	1.05
4 (R-RF2)	0	6.489	5.032	3.746	2.842	1.15	0.89	1.00	0.91
	166	6.426	4.991	3.725	2.841	1.14	0.52	0.58	0.39
	166 [c]	6.445	5.020	3.735	2.852	1.14	0.55	0.57	0.39
	664	6.360	4.956	3.679	2.810	1.58	1.02	0.82	0.78
	1162	6.299	4.905	3.648	2.790	1.44	1.03	0.85	0.85
	1660	6.283	4.901	3.644	2.787	1.50	1.07	0.86	0.81
5 (P-RA)	0 [c]	6.542	5.046	3.728	2.837	1.66	1.19	0.96	0.96
	498	6.531	5.036	3.714	2.832	1.51	1.10	0.95	0.89
	996	6.534	5.038	3.716	2.831	1.62	1.19	0.98	0.93
	1494	6.540	5.029	3.708	2.837	1.52	1.09	1.03	0.85
	1992	6.556	5.054	3.742	2.851	1.40	0.98	0.83	0.64
6 (R-RF3)	0	6.751	5.166	3.799	2.894	1.71	1.16	0.94	0.89
	166	6.618	5.082	3.751	2.857	1.59	1.12	0.81	0.87
	498	6.417	4.975	3.690	2.810	1.39	1.12	0.81	0.83
	498 [c]	6.518	5.030	3.716	2.836	1.89	1.21	1.04	0.97
	966	6.626	5.104	3.785	2.878	1.36	1.06	0.80	0.66
	1494	6.616	5.106	3.787	2.887	1.31	0.88	0.75	0.56
	1992	6.561	5.074	3.752	2.862	1.44	1.02	0.82	0.64
	2490	6.545	5.061	3.757	2.866	1.12	0.92	0.63	0.57
	2988	6.501	5.036	3.744	2.852	1.35	1.10	0.66	0.63

[a] Test matrix is provided in Table 3 in Paper 3
[b] T_f is elapsed flow time (see Paper 3)
[c] indicates first measurement after installing scour protection

Table C.9.3. Mode 2 Mean Natural Frequency and Damping (Impulse Tests)

Parameter		f_m				ζ_m			
Num. Top Masses:		0	1	3	6	0	1	3	6
FFF Test[a]	T_f [b] [mins]	[Hz]	[Hz]	[Hz]	[Hz]	[%]	[%]	[%]	[%]
1	0	19.24	18.26	17.60	17.20	0.66	0.75	0.75	0.93
	166	17.16	15.81	15.12	14.81	1.23	1.10	0.71	1.64
	498	16.76	13.95	13.31	13.43	1.40	0.27	1.99	1.13
	996	14.29	13.86	12.43	13.00	1.69	1.09	1.38	1.04
	1494	15.89	13.88	-	13.11	2.34	1.03	-	0.98
	1992	13.65	12.79	12.07	11.95	1.64	1.18	1.66	1.46
2 (R-TFN)	0	19.25	17.54	17.03	16.81	1.48	1.30	1.60	1.30
	83	17.53	16.57	15.91	15.63	1.52	1.25	1.53	1.19
	498	16.15	14.55	14.00	13.69	1.35	0.41	1.02	0.32
	498 [c]	16.02	14.76	14.25	13.71	1.31	1.06	1.36	0.99
	996	16.14	14.92	14.17	13.73	1.78	1.26	1.28	0.51
	1494	15.63	14.64	14.22	13.99	1.87	1.28	1.45	0.86
	1992	15.86	14.79	14.30	13.77	1.59	1.39	1.71	0.59
3 (R-RF1)	0	19.51	18.47	18.01	17.65	0.78	0.83	0.71	1.34
	498	16.19	15.32	14.80	14.56	0.73	0.51	0.50	0.47
	498 [c]	16.22	15.41	14.90	14.82	1.98	1.03	1.64	2.05
	996	17.09	16.12	15.81	15.24	1.42	1.46	1.64	1.51
	1494	17.59	15.66	15.74	15.52	1.21	1.02	1.78	1.43
	1992	17.24	16.60	15.84	15.75	1.74	1.95	2.39	1.53
4 (R-RF2)	0	18.53	17.80	17.33	16.81	1.52	1.20	1.12	1.26
	166	18.02	17.04	16.53	16.21	0.63	0.50	0.49	0.52
	166 [c]	18.17	17.45	16.90	16.62	0.74	0.64	0.60	0.56
	664	18.02	16.98	16.32	15.99	1.98	1.26	1.29	1.37
	1162	17.31	16.24	15.64	15.32	1.53	1.63	1.29	1.09
	1660	17.07	16.14	15.53	15.00	1.69	1.43	1.22	0.96
5 (P-RA)	0 [c]	19.51	18.65	18.49	17.62	0.29	1.67	1.10	1.38
	498	19.62	19.07	18.47	17.86	0.60	1.58	0.25	1.25
	996	19.74	19.15	18.54	17.95	0.62	1.20	0.17	1.17
	1494	19.79	19.06	18.49	18.05	0.83	1.39	1.01	1.28
	1992	19.91	19.08	18.74	18.13	0.81	1.12	0.82	1.20
6 (R-RF3)	0	20.58	20.67	19.71	20.16	1.81	1.16	1.30	0.69
	166	19.71	19.30	18.78	18.55	1.09	1.06	0.74	1.33
	498	18.32	17.28	16.82	16.41	1.08	1.27	0.98	0.90
	498 [c]	19.51	18.11	18.20	17.25	0.72	1.97	0.80	1.50
	966	20.12	19.33	18.74	18.48	1.75	1.64	2.29	1.33
	1494	20.13	19.59	19.30	18.80	1.88	1.48	0.92	1.20
	1992	19.78	18.98	18.90	18.15	0.81	1.59	1.01	1.27
	2490	19.56	18.70	18.20	17.90	0.68	1.39	0.93	1.10
	2988	19.18	18.14	17.83	17.40	1.88	1.64	1.13	1.29

[a] Test matrix is provided in Table 3 in Paper 3
[b] T_f is elapsed flow time (see Paper 3)
[c] indicates first measurement after installing scour protection

Table C.9.4. Mode 3 Mean Natural Frequency and Damping (Impulse Tests)

Parameter		f_m				ζ_m			
Num. Top Masses:		0	1	3	6	0	1	3	6
FFF Test[a]	T_f [b] [mins]	[Hz]	[Hz]	[Hz]	[Hz]	[%]	[%]	[%]	[%]
1	0	47.66	44.02	41.62	40.84	0.78	1.42	1.56	1.44
	166	44.94	42.16	-	38.11	1.99	0.72	-	1.49
	498	38.18	37.76	37.23	35.58	1.92	1.83	1.68	0.62
	996	40.61	36.68	35.68	34.83	0.62	2.24	1.53	0.44
	1494	40.72	37.29	-	35.04	0.54	1.26	-	1.53
	1992	39.37	36.76	35.35	34.45	1.30	1.28	1.18	1.20
2 (R-TFN)	0	45.04	42.92	41.02	39.51	1.33	0.94	0.63	0.63
	83	44.62	42.21	39.97	38.47	0.33	1.25	1.46	1.09
	498	41.98	39.38	37.97	36.50	0.37	1.00	0.63	1.19
	498 [c]	41.41	39.32	37.54	36.69	1.78	1.82	0.49	0.75
	996	43.62	43.60	38.53	36.31	1.32	0.46	1.54	1.08
	1494	41.37	38.92	37.62	36.61	0.68	1.95	1.91	0.98
	1992	42.30	-	38.11	36.87	1.27	-	0.79	2.02
3 (R-RF1)	0	47.78	44.56	41.49	41.68	1.09	0.69	0.96	0.85
	498	43.84	40.28	38.39	37.39	1.39	0.70	0.89	0.93
	498 [c]	43.19	40.55	39.06	37.49	2.20	1.43	0.66	0.86
	996	45.45	41.26	39.49	38.37	1.65	0.91	0.84	1.20
	1494	43.42	40.07	39.66	38.63	1.40	0.93	0.23	3.10
	1992	43.15	40.82	-	38.08	1.90	1.58	-	1.17
4 (R-RF2)	0	47.40	43.52	41.59	39.22	1.80	0.72	1.48	0.56
	166	46.82	43.20	40.94	39.50	0.90	0.59	1.14	1.16
	166 [c]	46.41	43.48	41.29	39.54	1.61	0.80	1.33	1.04
	664	42.46	42.28	40.14	38.51	0.47	0.83	1.16	1.01
	1162	43.14	41.32	39.00	37.80	0.79	0.85	1.13	1.29
	1660	44.32	40.80	39.11	38.30	1.72	1.48	1.15	1.05
5 (P-RA)	0 [c]	47.33	44.22	42.23	41.13	0.72	0.52	1.16	0.97
	498	46.60	42.40	41.92	41.84	0.49	0.44	0.60	1.44
	996	44.77	46.44	42.11	43.10	0.57	1.79	1.44	0.98
	1494	47.76	43.39	42.13	42.54	0.26	0.69	0.33	1.14
	1992	47.45	45.65	40.78	42.39	0.88	1.04	1.39	1.31
6 (R-RF3)	0	49.02	45.21	43.92	42.51	1.44	1.00	1.26	1.27
	166	48.56	45.09	42.27	40.95	2.48	1.44	0.59	1.12
	498	46.52	44.79	40.79	39.17	0.89	1.43	1.26	0.65
	498 [c]	46.05	-	40.01	-	1.20	-	1.65	-
	966	46.72	43.45	42.74	41.23	1.13	1.32	0.71	2.57
	1494	48.20	44.89	43.01	41.65	1.49	1.99	2.12	1.71
	1992	46.28	44.34	40.55	39.84	1.17	1.17	0.55	0.83
	2490	46.75	44.18	40.92	40.32	1.37	1.11	0.74	1.39
	2988	44.47	40.26	40.64	40.86	1.00	1.77	2.74	0.67

[a] Test matrix is provided in Table 3 in Paper 3
[b] T_f is elapsed flow time (see Paper 3)
[c] indicates first measurement after installing scour protection

C.10 Lessons from Experimental Programme

Table C.10.1. Summary of lessons from experimental programme and analysis

Activity	Description of Issue Encountered / Lesson Learned
Debugging activities	The flume experiments were preformed over a limited timeframe in the summer of 2017. A significant effort went into performing debugging activities and trial runs of the majority of the testing activities in order to de-risk the experimental programme. Some of these were performed at earlier stages at Oxford University. These activities were continued in a sand box provided by HR Wallingford (2018) adjacent to the flume whilst flume operation was tested.
Sand bed saturation	During the initial sand bed preparation for Test 1, there were multiple occurrences of piping when attempting to saturate the sand bed. These were initiated around features connecting to the gravel layer in the base of the pit section of the flume where the water found a preferential route to the surface.
Sand bed compaction	An initial sand compaction for Test 1 used 250 mm thick compacted layers, which a CPT showed to have noticeable 250 mm layers. The bed for Test 1 was re-prepared in 50 mm thick compacted layers, which produced a more uniform profile and was adopted as the preparation method for all tests.
CPT relative density calibration	CPT relative density calibrations in saturated and dry conditions produce differing relationships with normalised cone resistances.
Soil sampling	A small sample tube was used to make density measurements by push sampling at the end of Test 6. The density measurements were ultimately considered unreliable as they were much lower than those produced from the CPT results.
Pile driving	During pile driving there was a tendency for the pile to rotate about the vertical axis.
Scour protection modelling	The total mass of installed scour protection rock was not measured directly, which required estimation based on the installation records.
Bathymetry measurement	The use of fine sand in live bed conditions caused visibility issues, which limited the measurement range of the underwater laser scanner and added programme delays in attempts to improve the water clarity.
Global scour development	The global scour development was most successful in the final stages of Test 6, when an alternate flow regime was used, informed by test experience.
Structural dynamics testing	Tests performed with a modal shaker attached to the top of the tower produced different natural frequency results than with no shaker attached. The shaker used had a large mass relative to the measured structure, which may have been a contributing factor.

Appendix D Scour Protection Properties with Accreted Sand

This Appendix presents a method of calculating the unit weight and voids ratio for scour protection with accreted sand.

D.1 Voids Ratio and Density Calculation Method

Excavation following tests in which scour protection was placed demonstrated sand accretion into the scour protection matrix (see Paper 3). The scour protection properties are required for numerical modelling activities, however the properties of scour protection with accreted sand are uncertain. To allow the bulk properties to be assessed, the scour protection-soil-voids composition was treated as a three-phase material as shown in Figure D.1.1.

The voids ratio of the scour protection material, e_{SP}, is assumed to remain at the as-installed value,

$$e_{SP} = \frac{V_{v,SP}}{V_{SP}} = \frac{V_{sand} + V_v}{V_{SP}} \tag{D.1.1}$$

The voids ratio of the deposited sand, e_{sand}, was defined by disregarding the presence of the scour protection material,

$$e_{sand} = \frac{V_v}{V_{sand}} = \frac{V_v}{e_{SP}V_{SP} - V_v} \tag{D.1.2}$$

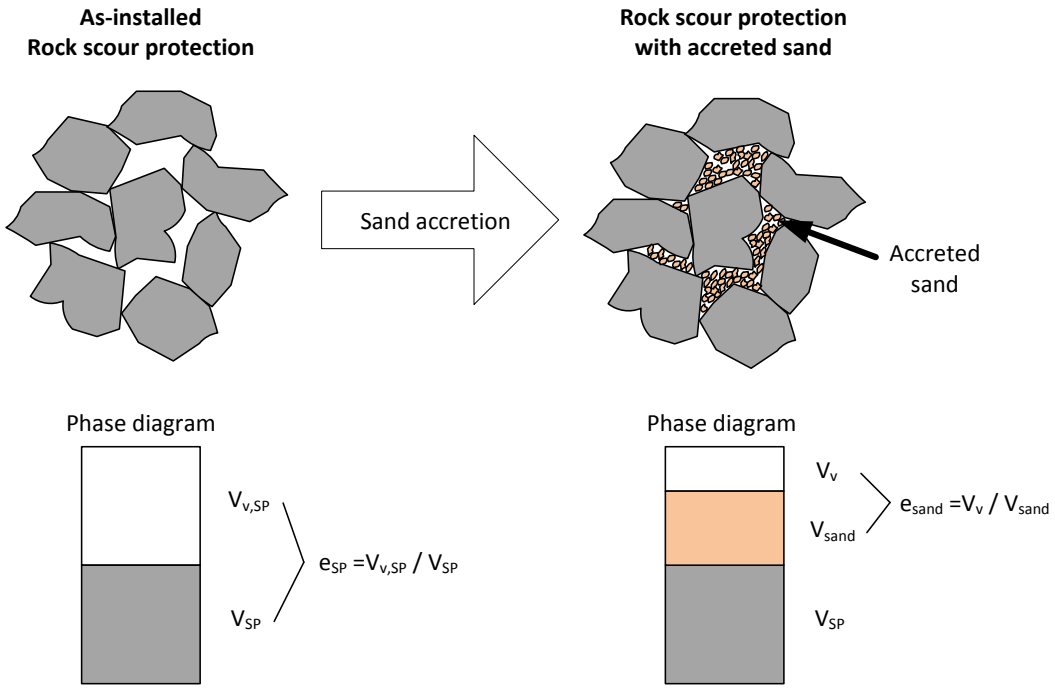

Figure D.1.1. Grain structures and phase diagrams for scour protection rock without and with accreted sand

The bulk voids ratio, e_{bulk}, and density, ρ_{bulk}, properties of the scour protection-soil-voids composition were then defined,

$$e_{bulk} = \frac{V_v}{V_{SP} + V_{sand}} \tag{D.1.3}$$

$$\rho_{bulk} = \rho_w \frac{G_{S,SP}V_{SP} + G_{S,sand}V_{sand} + V_v}{V} \tag{D.1.4}$$

Using the above expressions, the bulk properties are defined as a function of the scour protection and sand properties,

$$e_{bulk} = \frac{e_{SP}e_{sand}}{1 + e_{SP} + e_{sand}} \tag{D.1.5}$$

$$\rho_{bulk} = \rho_w \frac{G_{S,SP}(1 + e_{sand}) + G_{S,sand}e_{SP} + e_{SP}e_{sand}}{1 + e_{SP} + e_{sand} + e_{SP}e_{sand}} \tag{D.1.6}$$

The proportion by mass of sand particles, p_{sand}, in the sand-scour protection material is:

$$p_{sand} = \frac{M_{sand}}{M_{sand} + M_{SP}} = \frac{G_{S,sand}V_{sand}}{G_{S,SP}V_{SP} + G_{S,sand}V_{sand}} = \frac{G_{S,sand}e_{SP}}{G_{S,sand}e_{SP} + G_{S,SP}(1 + e_{sand})} \tag{D.1.7}$$

D.2 Example Values for Flume Experiments

The bulk properties of the scour protection with accreted sand have been estimated in Table D.2.1, presented for accreted sand with a relative density of 0% and 100% since the true value is unknown.

Table D.2.1. Scour Protection Properties with Accreted Sand

Test (Table 5 in Paper 3)	**Scour Protection**	$D_{R,sand} = 0\%$			$D_{R,sand} = 100\%$		
		e_{bulk}	γ_{bulk}	p_{sand}	e_{bulk}	γ_{bulk}	p_{sand}
		[-]	**[kN/m³]**	**[%]**	**[-]**	**[kN/m³]**	**[%]**
2 (TFN)	Tyre-filled nets	0.556	17.8	86.2	0.385	19.1	87.9
3 (R-RF1)	Rock armour in fully-formed scour hole	0.265	23.4	34.0	0.195	24.1	37.5
4 (R-RF2)	Rock armour in partially-formed scour hole	0.260	23.4	33.3	0.191	24.2	36.8
5 (P-RA)	Pre-installed rock armour	0.298	23.0	38.2	0.217	23.8	41.9
6 (R-RF3)	Rock armour in fully-formed scour hole	0.275	23.2	35.3	0.202	24.0	38.9

Appendix E Macro Element Stiffness Derivation from 1D FE Model

This Appendix presents a method of calculating the stiffness of coupled and uncoupled macro element models from a one-dimensional (1D) finite element (FE) stiffness matrix.

E.1 Coupled Spring Macro Element

The stiffness for a macro element, $\mathbf{K_{0D}}$, at ground level is equivalent to the stiffness matrix from a 1D finite element model, $\mathbf{K_{1D}}$:

$$\mathbf{K}_{0\mathrm{D}} = \begin{bmatrix} K_H & K_{HM} \\ K_{HM} & K_M \end{bmatrix} = \left[\left[\mathbf{K}_{1\mathrm{D}} \right]^{-1} (dofs, dofs) \right]^{-1} \tag{E.1.1}$$

where K_H, K_M, and K_{HM} are the horizontal, moment and cross-coupling stiffness parameters respectively, and $dofs$ indicates the displacement and rotation degrees of freedom at ground level.

E.2 Uncoupled Spring Macro Element

The 2x2 macro element stiffness $\mathbf{K_{0D}}$ can be converted to the equivalent uncoupled lateral and rotational stiffness, $K_{H,v}$ and $K_{M,\theta}$ respectively,

$$H \begin{bmatrix} 1 \\ h \end{bmatrix} = \begin{bmatrix} K_H & K_{HM} \\ K_{HM} & K_M \end{bmatrix} \begin{bmatrix} v_G \\ \theta_G \end{bmatrix} = \begin{bmatrix} K_{H,v} v_G \\ K_{M,\theta} \theta_G \end{bmatrix} \tag{E.2.1}$$

The equality on the left in (E.2.1) produces a relationship between v_G and θ_G, as a function of the components of $\mathbf{K}_{0\mathrm{D}}$ and the lever arm, h,

$$H.h = (K_H v_G + K_{HM} \theta_G) h = K_{HM} v_G + K_M \theta_G \tag{E.2.2}$$

$$v_G (K_H h - K_{HM}) = \theta_G (K_M - K_{HM} h) \tag{E.2.3}$$

The equality on the right in (E.2.1) produces the solutions for $K_{H,v}$ and $K_{M,\theta}$,

$$K_{H,v} = K_H + K_{HM} \frac{(K_H h - K_{HM})}{(K_M - K_{HM} h)} \quad \text{and} \quad K_{M,\theta} = K_M + K_{HM} \frac{(K_M - K_{HM} h)}{(K_H h - K_{HM})} \tag{E.2.4}$$